DISSERTATION

PRECIPITATION MAPPING AT LOCAL, REGIONAL AND GLOBAL SCALE

Submitted by

Shashank S. Joshil

Department of Electrical and Computer Engineering

In partial fulfillment of the requirements

For the Degree of Doctor of Philosophy

Colorado State University

Fort Collins, Colorado

Fall 2022

Doctoral Committee:

Advisor: V. Chandrasekar

Margaret Cheney
S. Ryan Gooch
Susan P. James

ABSTRACT

PRECIPITATION MAPPING AT LOCAL, REGIONAL AND GLOBAL SCALE

It is well established that the Earth's water cycle is accelerating, and extreme precipitation events are becoming more common. While we cannot avoid this issue, we can be better prepared to handle it if we can obtain accurate observations of precipitation for use in short-term and long-term prediction models. Various remote sensing instruments are available to obtain precipitation data. In this research work, mapping precipitation at local, regional and global scales is studied. The technology of precipitation mapping at these scales is very different and elaborated. Examples of precipitation measurements from these scales are discussed.

At the local scale, rain gauges and disdrometers are two prominent instruments that are utilized for precipitation measurement. Precipitation observations captured from these two instruments are introduced. Millimeter wave radars have been previously used in various domains, and extensive research is currently in progress to improve this technology. This research will present the potential of using automobile class radars to obtain local surface precipitation. Since the maximum range of an automobile radar is within a few hundred meters, we can consider the observations to be at a local scale. With the help of signal modeling, methods to obtain the rainfall rate at the millimeter wave band by using radar parameters, such as reflectivity and attenuation are discussed. A simulation tool is developed that generates the radar signals at the millimeter wave frequency band. The various parameters which are used in the signal simulations are explained in detail, and the simulation results are presented. Experiments for mapping precipitation using a current state-of-the-art automobile radar are carried out, and the results are discussed. The reflectivity value obtained from the experiment using automobile radar is compared to the NWS reflectivity mosaic and the results match within a couple of decibels (dB).

Weather radars are remote sensing instruments that provide precipitation observations at a regional scale. They provide data at a large spatial extent. Weather radar observations obtained at various frequency bands for mapping precipitation is discussed with examples. The current networks of instruments and system architectures that provide precipitation information at a regional scale are discussed. The precipitation data obtained from individual automobile radars is considered as a local data point, and precipitation maps at the regional scale are constructed. The system analysis of using a network of automobile radars for mapping precipitation is discussed with the help of simulations. The Dallas-Fort-Worth urban region is considered for the simulation study, and the potential of using millimeter wave radars to create precipitation maps is presented. Three different interpolation techniques, linear, nearest-neighbor and natural are explored to study the reconstruction of precipitation maps. A system architecture for precipitation mapping using automobile radars is also discussed.

The attenuation of radar signals has to be addressed and corrected to obtain accurate precipitation information from radar data. The attenuation correction in weather radars for rain hydrometeors is well studied in the literature, but attenuation correction for snow is limited. This is due to the fact that snow does not attenuate much at lower frequency bands like S and C bands and because the snow particles vary in their particle size distributions and have complex shapes. Theoretical relationships between specific phase and attenuation are developed using signal simulations. This research will introduce a new algorithm that corrects radar signal attenuation in rain and snow. The attenuation correction method developed is applied to X-band and Ku-band radar data, and the results are discussed.

It was observed from the data for snow cases that the path integrated attenuation at the X-band reached up to 2 dB and, at the Ku-band, it reached up to 8 dB.

Mapping precipitation at a global scale is a challenging task. The Dual Precipitation Radar (DPR) is a spaceborne instrument providing valuable precipitation information at the global scale, but the observations from this instrument suffer from poor spatial and range resolutions. Synthetic Aperture Radars (SAR) are well known for providing high spatial resolution data. In the past, SARs have been deployed on airborne and spaceborne platforms for mapping land cover and constructing surface elevation models. The potential of using SAR for mapping precipitation is not widely explored. In this research, SAR signal simulations are carried out to observe precipitation from spaceborne platforms. The mathematical framework for monostatic and bistatic SAR is discussed. The simulation results for two specific spaceborne SAR architectures are discussed in detail. The variation of precipitation parameters such as velocity and spectral width are studied using simulations.

This dissertation presents the roles and challenges of observing precipitation at the three scales, with suggestions for future research.

Acknowledgments

The graduate school experience at Colorado State University has been extremely valuable. I am thankful and indebted to my advisor Dr. V. Chandrasekar for his kindness, support, guidance and encouragement throughout my graduate study. Also, I would like to thank Dr. Margaret Cheney, Dr. S. Ryan Gooch and Dr. Susan P. James for serving as my committee members. I would like to thank Dr. Mohit Kumar and Dr. Renzo Bechini for their guidance and input in my research. I would like to thank Dr. Kevin Maschhoff and Dr. Martin Ryba for all the helpful discussions during my research. I would like to thank all the current and past members of the radar group at Colorado State University, Dr. Yanting Wang, Dr. Robert Beauchamp, Dr. Haonan Chen, Sounak Biswas, Ivan Arias, Dr. Yingzhao Ma, Dr. Chandraekar Radhakrishnan, Dr. Minda Le, Amit Dutta, Sergio Graniello, Jacob Garcia, Pratik Ramdasi, Zach Mendez, Alexander Morin, Juhyup Kim, Saurabh Magodia, Ragesh Gopalakrishnan Jayalalithaa, Shweta Haran, Mateo Lovato and Eun Yeol Kim for your help during my graduate studies.

I would like to thank David Wolff and D3R staff at Wallops Flight facility for their encouragement and support during my graduate work. I would also like to thank Dr. Manuel Vega for his input during my graduate work. I would like to express my gratitude to the staff at the CSU-CHILL radar facility, Dr. Francesc Junyent, Jim George and Dr. Patrick Kennedy, for their help during my graduate studies. I would like to thank all my colleagues during my internships at NASA Jet Propulsion Laboratories. I would like to thank the administrative staff of Electrical and Computer Engineering (ECE), Engineering Technology Services (ETS) and Engineering Business Office (EBO) at Colorado State University for all the help during my graduate school.

I am deeply grateful to my parents, wife, friends and family for their love, support and encouragement throughout the years of my graduate studies.

This research is supported by NASA through a combination of different projects including GPM Ground Validation program and IIP program.

TABLE OF CONTENTS

ABSTRACT ii

ACKNOWLEDGEMENTS v

LIST OF TABLES x

LIST OF FIGURES xi

CHAPTER 1. INTRODUCTION 1

1.1. REMOTE SENSING INSTRUMENTS 1

1.2. URBANIZATION AND CLIMATE STUDIES 3

1.3. PROBLEM STATEMENT 5

1.4. RESEARCH OBJECTIVES 9

1.5. ORGANIZATION OF THE DISSERTATION 12

CHAPTER 2. PRECIPITATION MAPPING AT LOCAL SCALE 15

2.1. RAIN GAUGES 15

2.2. DISDROMETERS 18

CHAPTER 3. AUTOMOBILE RADARS FOR PRECIPITATION MEASUREMENT 22

3.1. INTRODUCTION TO AUTOMOBILE RADARS 22

3.2. AUTOMOBILE RADARS FOR PRECIPITATION MEASUREMENT 27

3.3. AUTOMOBILE RADARS AS RAIN GAUGES 29

3.4. TIME-SERIES SIMULATION STUDY 43

3.5. METHOD OF SIMULATING TIMESERIES USING DIRECT VOLUME OF PARTICLE BACKSCATTERING METHOD 44

3.6. CURRENT TECHNOLOGY OF AUTOMOBILE RADARS 53

3.7. precipitation measurement experiment and results 56

Chapter 4. Precipitation mapping at regional scale 66

4.1. Weather radars for remote sensing of atmosphere 66

4.2. precipitation information from weather radar data 75

4.3. Current systems of precipitation mapping 79

Chapter 5. Attenuation correction in weather radars 85

5.1. Current methods for attenuation correction in weather radars .. 87

5.2. Attenuation correction for ice hydrometeors 93

5.3. The New attenuation correction algorithm 100

5.4. Attenuation correction for Ku band data 104

5.5. Attenuation correction for X band data 117

Chapter 6. System analysis of automobile radars for precipitation mapping at regional scale 128

6.1. Simulation studies of precipitation mapping using automobile radar network 128

6.2. Study area considered for simulation 130

6.3. Precipitation map simulation studies considering automobile radars 131

6.4. Proposed system of precipitation mapping using automobile radars 144

Chapter 7. Precipitation mapping at global scale 146

7.1. Synthetic aperture radars for mapping precipitation 149

7.2. Mathematical framework for monostatic and bistatic SAR for observing precipitation targets 153

7.3. SAR simulation package 162

7.4. Simulations of SAR in monostatic mode for observing precipitation target 165

7.5. Simulations of SAR in bistatic mode for observing precipitation target 179

7.6. SAR simulations considering input weather radar data 183

Chapter 8. Summary and future work 186

8.1. Summary 186

8.2. Future work 191

Bibliography 193

Appendix A. Parameters for relationship between specific phase and specific attenuation for different hydrometeors at X band 202

Appendix B. Parameters for relationship between specific phase and specific attenuation for different hydrometeors at Ku band 203

List of tables

3.1 The relationships obtained from simulations at various frequencies for $Z = A(RR)^B$. 42

3.2 The relationships obtained from simulations at various frequencies for $Att = C(RR)^D$. 42

3.3 Radar parameters considered for the simulation. 52

3.4 Parameters of the TI AWR1642 radar evaluation module. 57

3.5 Computing reflectivity from rain rate values obtained. 65

6.1 Vehicle ownership in the U.S. as of 2016 130

7.1 GPM Ku radar parameters. 166

7.2 Summary of the simulation outputs obtained for stripmap and spotlight mode of SAR. 173

A.1 X band, horizontal polarization - Values for a and b from 0° elevation to 45° elevation 202

A.2 X band, vertical polarization - Values for a and b from 0° elevation to 45° elevation 202

B.1 Ku band, horizontal polarization - Values for a and b from 0° elevation to 45° elevation 203

B.2 Ku band, vertical polarization - Values for a and b from 0° elevation to 45° elevation 203

List of figures

1.1 Classification of remote sensing instruments. 1

1.2 Urban and rural population trend from 1950-2050 [1]. 4

1.3 Illustration of observation gaps due to the radar beam propagation in the atmosphere. 7

1.4 The three key aspects of designing and implementing a system. 10

2.1 Daily precipitation accumulation data from CSU-Fort Collins weather station between 2019-2021. 17

2.2 Data from the OTT Parsivel recorded during a rain event on November 10, 2017. 19

2.3 Data from the OTT Parsivel recorded during a snow event on February 28, 2018. 20

3.1 Diagram illustrating different types of automobile radars and their uses. [2]. 23

3.2 Basic block diagram of an automobile radar operating at 77 GHz. 25

3.3 Automobile radars for measuring precipitation - concept diagram. 29

3.4 Atmospheric attenuation at various frequencies [3]. 30

3.5 Rain attenuation versus frequency for different rain rates. 31

3.6 Scattering regions at 77 GHz. 36

3.7 Scatterplots of reflectivity versus rain rate from signal simulations at (a) 10 GHz, (c) 24 GHz and (e) 77 GHz. Scatterplots of attenuation versus rainrate from signal simulations at (b) 10 GHz, (d) 24 GHz and (f) 77 GHz. The red line indicates the power-law fit in all the plots. 38

3.8 (a) Scatterplot of reflectivity versus rain rate from signal simulations using Maetzler toolbox at 77 GHz. (b) Scatterplot of attenuation versus rain rate from signal simulations using Maetzler toolbox at 77 GHz. The red line indicates the power-law fit in all the plots. 42

3.9 Random collection of the precipitation particles in the radar resolution volume whose instantaneius locations are described by the set of vectors r_k relative to the radar. 46

3.10 Complex plane plot of the instantaneous sum of the elemental phasors. 47

3.11 The exponential DSD considering 5000 rain particles in the radar resolution volume 49

3.12 Block diagram of the simulation program. 51

3.13 Statistics of the simulated timeseries IQ data. (a) Histogram of I data, (b) Histogram of Q data, (c) Histogram of $I^2 + Q^2$ and (d) Scatterplot of I and Q data. 54

3.14 Magnitude spectrum of the simulated timeseries signal. 55

3.15 TI AWR1642 automobile radar block diagram [4]. 56

3.16 TI AWR1642 evaluation module [4]. 57

3.17 Graphical illustration of the experiment setup for checking the evaluation module to observe water droplets. 58

3.18 (a) scene of observation and (b) Snapshot of water being poured in front of the automobile radar evaluation board. 59

3.19 Results of the experiment where water is poured in front of the automobile radar evaluation board. 60

3.20 Graphical illustration of the experiment setup for precipitation measurement, the radar is placed in front side of the automobile. 61

3.21 (a) Scene of observation and (b) Setup of automobile radar evaluation module inside the car. 61

3.22 Results of using automobile radar evaluation board for observing precipitation.... 62

3.23 Difference in power level long the range from the data collected using automobile radar evaluation board observing precipitation. 63

3.24 Screenshot of the National Weather Service (NWS) reflectivity mosaic over the CSU campus. The region in the black circle is where the data was collected. 64

4.1 The radar resolution volume ranging from (r, r+Δr), the received voltage at the radar are due to scattering of particles located within this volume. 68

4.2 Illustration of range-time axis and sample-time axis for received radar signal (pulse repetition time of T_s). 68

4.3 NEXRAD S-band radar (KDAX) reflectivity (left) and estimated rain rate (right) at Sacramento, California. 76

4.4 The X-band (XSCV) radar output at Santa Clara, California. (a) radar reflectivity, (b) specific phase and (c) rain rate. 77

4.5 D3R Ku-band radar reflectivity (left) and estimated rain rate (right) during a rain event at ICE-POP field campaign. 78

4.6 D3R Ku-band radar reflectivity (left) and estimated snow rate (right) during a snow event at ICE-POP field campaign. 78

4.7 The architecture of the Distributed Collaborative Adaptive Sensing (DCAS) system used in the CASA radar network. [5]. 80

4.8 The architecture of the NEXRAD system [6]. 82

4.9 A snapshot of the CoCoRaHS network's 24-hour precipitation data from the Denver and Fort Collins taken on February 17, 2021. 84

5.1 Snow attenuation versus frequency for different snow rates. 86

5.2 Attenuation coefficient versus frequency for dry ice spheres and ice spheres with water shell [7]. 87

5.3 Steps for hydrometeor classification in DROPS2.0 algorithm. 90

5.4 CASA IP1 RHIs of dual-polarization variables at 04:14 UTC 20 May 2011, along the azimuth 101.6°: (a) observed Z_h, (b) attenuation corrected Z_h, (c) Z_{dr}, (d) ρ_{hv}, (e) K_{dp} and (f) final hydrometeor classification [8]. 91

5.5 Rainfall rate estimates comparisons using different rainfall rate computation algorithms along with the corresponding radar moments data for NPOL radar data at 03:30 UTC 20 May 2013: (a) Z_h, (b) Z_{dr}, (c) ϕ_{dp}P, (d) ρ_{hv}, (e) NEXRAD Z-R, (f) NEXARD DP, (g) DROPS1.0 and (h) DROPS2.0 [5]. 93

5.6 The snow crystal morphology diagram [9]. 94

5.7 Parameters considered for T-matrix simulations for different hydrometeor particles. 95

5.8 Scatter plots of specific phase versus specific attenuation for different hydrometeors at 0° elevation angle at the X band (a) Rain, (b) Snow aggregate, (c) Crystals, (d) Graupel and (e) Hail. The red line represents the power-law fit line. 98

5.9 Scatter plots of specific phase versus specific attenuation for snow aggregates at the X band (a) 0° elevation angle, (b) 20° elevation angle, (c) 45° elevation angle. 99

5.10 Scatter plots of specific phase versus specific attenuation for different hydrometeors at 0° elevation angle at the Ku band (a) Rain, (b) Hail, (c) Graupel, (d) Snow aggregate, (e) Crystals and (f) Dendrites. The red line represents the power-law fit line. 101

5.11 Scatter plots of specific phase versus specific attenuation for snow aggregates at the Ku band (a) 0° elevation angle, (b) 20° elevation angle, (c) 45° elevation angle. 102

5.12 The new algorithm for attenuation correction for all hydrometeors. 103

5.13 The D3R radar deployed on a rooftop of a building in PyeongChang region, South Korea during the ICE-POP field campaign. Credits: Aron Dabrowski. 105

5.14 The maximum unambiguous range coverage of the D3R radar during ICE-POP field campaign. Credits: Google Earth. 106

5.15 Radar moments for the D3R Ku band for RHI scan data collected on November 10, 2017 at 07:34 UTC. (a) Observed Reflectivity, (b) Observed Differential reflectivity, (c) Specific phase, (d) Copolar correlation (e) and (f) Hydrometeor classification output. 108

5.16 Radar moments for the D3R Ku band for RHI scan data collected on November 10, 2017 at 07:34 UTC. (a) Observed Reflectivity, (b) Observed Differential reflectivity, (c) Path integrated attenuation - H Pol, (d) Path integrated attenuation - V Pol, (e) Corrected reflectivity and (f) Corrected differential reflectivity. 109

5.17 Radar moments for the D3R Ku band for RHI scan data collected on February 28, 2018 at 11:25 UTC. (a) Reflectivity, (b) Differential reflectivity, (c) Specific phase, (d) Copolar correlation (e) and (f) Hydrometeor classification output. 111

5.18 Radar moments for the D3R Ku band for RHI scan data collected on February 28, 2018 at 11:25 UTC. (a) Observed Reflectivity, (b) Observed Differential reflectivity, (c) Path integrated attenuation - H, (d) Path integrated attenuation - V, (e) Corrected reflectivity and (f) Corrected differential reflectivity. 112

5.19 Comparison of attenuation corrected reflectivities considering rain attenuation parameters for the complete scan versus the new method for attenuation correction (a) and (b) November 10, 2017 at 07:34 UTC case, (c) and (d) February 28, 2018 at 11:25 UTC case. 114

5.20 Comparison of observed reflectivity and attenuation corrected reflectivity of D3R data with reflectivity from a Parsivel disdrometer 116

5.21 (a) X-band radar deployed at Santa Clara, California and (b) X-band radar deployed at Mt. Crested Butte, Colorado 117

5.22 The X-band radar data and DROPS output for rain case on February 8, 2019 at 22:38 UTC. (a) uncorrected reflectivity, (b) uncorrected differential reflectivity (c) Specific phase, (d) Copolar correlation, (e) and (f) Hydrometeor classification output. 118

5.23 The X-band radar data and attenuation corrected output for rain case on February 8, 2019 at 22:38 UTC. (a) uncorrected Reflectivity, (b) uncorrected Differential reflectivity, (c) Path integrated attenuation - H, (d) Path integrated attenuation - V, (e) Corrected reflectivity and (f) Corrected differential reflectivity. 119

5.24 The X-band radar data and DROPS output for rain case on January 8, 2022 at 20:30 UTC. (a) uncorrected reflectivity, (b) uncorrected differential reflectivity (c) Specific phase, (d) Copolar correlation, (e) and (f) Hydrometeor classification output. 121

5.25 The X-band radar data and attenuation corrected output for rain case on January 8, 2022 at 20:30 UTC. (a) uncorrected Reflectivity, (b) uncorrected Differential reflectivity, (c) Path integrated attenuation - H, (d) Path integrated attenuation - V, (e) Corrected reflectivity and (f) Corrected differential reflectivity. 122

5.26 The X-band radar data and DROPS output for rain case on December 24, 2021 at 08:28 UTC. (a) uncorrected reflectivity, (b) uncorrected differential reflectivity (c) Specific phase, (d) Copolar correlation, (e) and (f) Hydrometeor classification output. 125

5.27 The X-band radar data and attenuation corrected output for rain case on December 24, 2021 at 08:28 UTC. (a) uncorrected Reflectivity, (b) uncorrected Differential reflectivity, (c) Path integrated attenuation - H, (d) Path integrated attenuation - V, (e) Corrected reflectivity and (f) Corrected differential reflectivity. 126

6.1 Observed precipitation map for May 30, 2020 for the continental United States [10]. 129

6.2 A Google earth view of the Dallas-FortWorth (DFW) region considered for the simulation study. Credits: Google Earth. 131

6.3 Primary and secondary road data for the DFW region. 132

6.4 All roads data for a part of the DFW region which was highlighted in red in Figure 6.3. 133

6.5 Ten thousand random points generated on the DFW area which are considered for the study. 134

6.6 Distance to the nearest road for the ten thousand simulation points considered. . 135

6.7 Merged radar rainrate map from the CASA radar network on May 29, 2015 at 05:30 UTC. 135

6.8 Rain rate values corresponding to the selected points on/near the roads. 136

6.9 Performance of the three different interpolation methods used in this study, the magenta circles are the data points (a) Exact solution for sin(x) + cos(y) (b) Linear interpolation (b) Nearest neighbour interpolation and (d) natural neighbour interpolation 137

6.10 Rain map output after using linear interpolation method for the simulated data points. 138

6.11 Rain map output after using nearest neighbour interpolation method for the simulated data points. 139

6.12 Rain map output after using natural neighbour interpolation method for the simulated data points. 140

6.13 Rain map output after using natural neighbour interpolation method for the simulated data points, considering all ten thousand points. 141

6.14 Description of data points from the resolution volume - concept diagram. 142

6.15 Proposed system architecture of using automobile radar network for obtaining precipitation information. 143

7.1 The GPM DPR radar and its specifications [11]. 147

7.2 The GPM DPR radar data over the Dallas-Fort Worth (DFW) region collected on 18th March 2015 at 08:56 UTC, the range ring of the DFW NEXRAD radar is also shown for reference, (a) Ku band data and (b) Ka band data. 148

7.3 SAR scanning modes, (a) Stripmap SAR, (b) ScanSAR and (c) Spotlight SAR. . . 151

7.4 SAR architecture, (a) Side view and (b) 3-D view. 153

7.5 SAR architecture for bistatic case, (a) Side view and (b) 3-D view. 158

7.6 Block diagram of the SAR simulation architecture. 161

7.7 Monostatic SAR simulation output for a fixed target case, (a) raw received signal (b) Processed SAR signal and (c) Azimuth cut along range 0m of the processed SAR signal. 167

7.8 Monostatic SAR simulation output for a 1 bin weather target case, (a) raw received signal (b) Processed SAR signal and (c) Azimuth cut along range 0m of the processed SAR signal. 168

7.9 Monostatic SAR simulation outputs for varying velocity of the precipitation particles. (a), (b) and (c) processed SAR signal corresponding to velocities -5 m/s, 0 m/s and 10 m/s. (d), (e) and (f) Azimuth cuts along range 0m corresponding to velocities -5 m/s, 0 m/s and 10 m/s. 169

7.10 Monostatic SAR simulation outputs for varying spectral widths of the precipitation particles. (a), (b) and (c) processed SAR signal corresponding to spectral widths 0.5 m/s, 1 m/s and 2 m/s. (d), (e) and (f) Azimuth cuts along range 0m corresponding to spectral widths 0.5 m/s, 1 m/s and 2 m/s. 170

7.11 Theoretical and output values from simulations for azimuth resolution with varying spectral widths for monostatic SAR. 172

7.12 Monostatic SAR simulation output for a 1 resolution volume of 500 m weather target case, (a) raw received signal (b) Processed SAR signal and (c) Azimuth cut along range 0m of the processed SAR signal. 174

7.13 SAR architecture for spotlight mode - front view. 176

7.14 SAR architecture for pseudo-spotlight mode - front view. 176

7.15 Monostatic SAR simulation output for a fixed target case - pseudo-Spotlight mode, (a) raw received signal (b) Processed SAR signal and (c) Azimuth cut along range 0m of the processed SAR signal. 177

7.16 Monostatic SAR simulation output for a 1 bin weather target case - pseudo-Spotlight mode, (a) raw received signal (b) Processed SAR signal and (c) Azimuth cut along range 0m of the processed SAR signal. 178

7.17 Bistatic SAR simulation output for a fixed target case, (a) raw received signal (b) Processed SAR signal and (c) Azimuth cut along range 0m of the processed SAR signal. 179

7.18 Bistatic SAR simulation output for a 1 bin weather target case, (a) raw received signal (b) Processed SAR signal and (c) Azimuth cut along range 0m of the processed SAR signal. 181

7.19 Bistatic SAR simulation output for a 1 resolution volume of 500 m weather target case, (a) raw received signal (b) Processed SAR signal and (c) Azimuth cut along range 0m of the processed SAR signal. 182

7.20 RHI plot of CHILL S-band radar data considered for the simulation case. 184

7.21 Azimuth compressed SAR output image for simulation considering profile of reflectivity. 185

7.22 (left) Azimuth cut of input reflectivity profile and (right) azimuth cut of output SAR processed image corresponding to range 0 meters 185

Chapter 1

Introduction

1.1. Remote sensing instruments

The Earth's atmosphere and atmospheric process play a crucial role in the natural life on the planet. Various atmospheric parameters, such as water vapor, precipitable water, temperature, and pressure, affect the climate, climate change, and many other aspects. It is important to measure and understand the various parameters, processes, and interactions in the atmosphere to ensure Earth is sustainable. Remote sensing plays an important role in measuring the parameters of the Earth's atmosphere. Remote sensing is the acquisition of information about an object, area, or phenomenon without being physically present at the point of measurement. Remote sensing plays a prominent role in various fields, such as meteorology, geology, hydrology, and climate studies. This research concentrates on remote sensing instruments, used for mapping precipitation. The various remote sensing instruments used for this purpose can be broadly classified into active and passive remote sensing instruments, as shown in Figure 1.1.

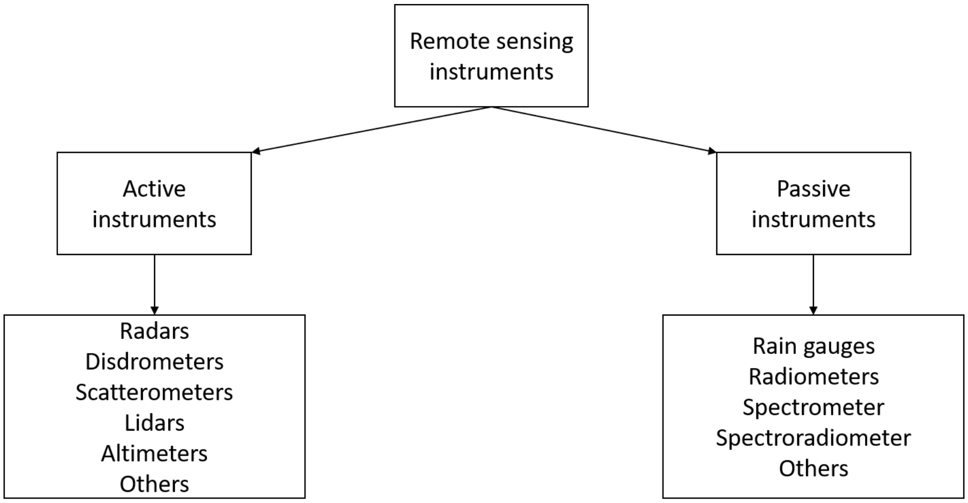

Figure 1.1. Classification of remote sensing instruments.

The active remote sensing instruments use their energy source to illuminate the target or region of interest. The energy transmits in the direction of the target, and the instrument collects the reflected or backscattered radiation. Most of the remote sensing instruments used for mapping precipitation employ microwave signals. The active remote sensing techniques vary by what they transmit, such as light or electromagnetic waves and what information is collected by the instrument, such as precipitation and distance to the target. Researchers and scientists use a wide variety of active remote sensing instruments, such as radars, lidars, and scatterometers. Weather radars are widely used among the active remote sensing instruments present for mapping precipitation.

The passive remote sensing instruments do not transmit their own energy to illuminate the target or region of interest. Instead, they detect the natural energy reflected or emitted from the scene. The passive remote sensing instruments sense only the radiation emitted by the target being viewed or reflected from a source other than the instrument. There are various passive remote sensing instruments, such as radiometers and sounders. Some passive remote sensing instruments widely used for measuring precipitation are rain gauges and radiometers.

Remote sensing instruments can be classified further in various ways based on whether the instrument is collecting point measurement or volume measurement or whether the instrument is ground-based or space-based. Specifically, for measuring the quantity and microphysical parameters of the precipitation, the main instruments widely used are rain gauges, disdrometers, weather radars, and meteorological satellites. Synthetic aperture radars (SAR) have also been used for precipitation measurement in the past few years. In this dissertation, the various remote sensing instruments are classified based on the scale at which we obtain the precipitation information; they are broadly classified into local, regional, and global scales. The precipitation mapping obtained at these three scales is also discussed in detail.

1.2. Urbanization and climate studies

Urbanization is a complex socio-economic process that transforms the environment of a particular area, especially the infrastructure, converting the rural areas which reside around an urban region to urban settlements and shifting the population towards the urban regions from rural regions. Therefore, urbanization plays an important role in the development of any country or region.

The world is growing rapidly in the twenty-first century. Considering various factors, such as job opportunities and quality of lifestyle, people are moving towards urban regions at an alarming rate. In 2018, 55 percent of the world's population resided in urban areas. As of 2018, 4.2 billion people resided in urban settlements compared to 3.4 billion in rural areas. The trend of urban and rural populations from 1950 to 2050 is shown in Figure 1.2 [1]. From this figure, it can be seen that the urban population is continuously increasing while the rural population trend is decreasing. With more people moving to urban areas, scientists across numerous disciplines need to better plan for these regions, as sustainable urbanization is the key to successful development. Various factors must be considered for the well-being of the people.

Multiple aspects need to be considered for the positive development of urban regions; the climate is one of the factors which needs to be accounted for in urban environments. Accurate measurement and modeling of climate parameters are required for the safety of the people. The interaction between precipitation and surface runoff varies with time and geography.

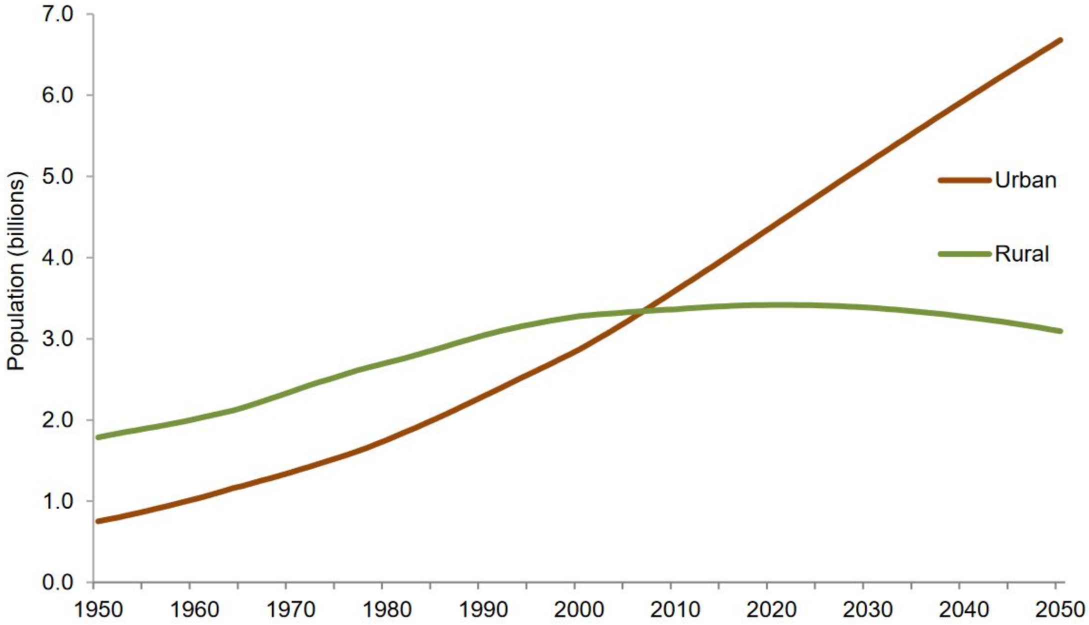

FIGURE 1.2. Urban and rural population trend from 1950-2050 [1]

.

It is crucial to track water because water is always on the move. The water in a distant ocean might fall as rain today in the urban regions. The rainwater may turn out to be snow on a high mountaintop. This process of the water in different states and moving to various places is known as the water cycle. The changes in the climate directly impact the water cycle. Global precipitation numbers are on the rise every year. The global water cycle is accelerating and caused by natural processes and artificial processes. Climate change is one of the factors accelerating the water cycle. Global warming, which is increasing at an alarming rate due to human influence, will directly affect the global water cycle. Statistics show it will get much worse in the next 100 years. The warming of global temperatures will increase the rate of evaporation which will cause parts of the water cycle to speed up.

The intensifying water cycle around the world will have a direct impact on the intensity of the storms. As the water cycle model gets affected, storms will become bigger and more intense. The higher evaporation and precipitation rates are not evenly distributed around the world. Some areas may experience higher precipitation, while others may be prone to droughts. Even today, there are a lot of regions around the world that are affected by flooding. However, we cannot prevent natural processes from happening, but we can better prepare to handle such situations.

It has become an urgent necessity to map and study the precipitation so that accurate hydrological mapping and future predictions could be done. The hydrological and meteorological models rely on data available to be used in the models. The accuracy of the data plays an important role in these models. The accuracy of the data plays an important role in these models. The water cycle at a global scale, especially in urban regions should be researched further to have a better understanding of the climate.

The current state-of-the-art technology to capture precipitation information uses various instruments which were mentioned in the previous section. However, these instruments have certain shortcomings in accurately providing data at the surface level in urban areas and remote regions, such as over oceans or remote mountains. The problems encountered by the remote sensing instruments and the problem statement of this research are described in the next section.

1.3. Problem Statement

The point precipitation measurement instruments like rain gauges and disdrometers require a small area for setup and operations, which is an advantage in both remote and urban areas; they can be installed on top of buildings as well. The data collected by these instruments are at the surface or near-surface level and are considered to be accurate. In the past, weather radars have used data from rain gauges and disdrometers for calibration purposes. These remote sensing instruments, as standalone or groups of them, are used effectively to map precipitation at the local scale. Though these instruments provide an accurate measurement at a local scale, they are held back by several disadvantages for getting precipitation values over a large area. One disadvantage is external factors, such as wind, might affect the accurate measurement of the precipitation. The second disadvantage is that they are point measurements, meaning they cannot map precipitation over large areas. Even if we deploy many precipitation instruments, they cannot accurately capture the spatial variability of precipitation events. When a localized storm confined to a small region, these point instruments may miss capturing the precipitation values if the precipitation event does not overlap on these instruments.

Measuring the precipitation event using volume instruments will overcome the many disadvantages mentioned above, such as weather radars and meteorological satellites deployed at regional and global scales. The ground-based weather radars provide information on the precipitation on a regional scale. Even though accurately calibrated weather radars provide good quality data over a large area, they are limited by certain aspects when measuring precipitation in urban areas and areas with complex terrain.

One of the issues is the observation gaps in the measured data due to the radar beam propagation in the atmosphere. This is illustrated in Figure 1.3. In this figure, taking into account the curvature of the earth, the radar beam as it propagates with distance is represented for various elevation angles; the elevation angles are considered based on the volume scan from NEXRAD radars [12]. From the Figure 1.3, it can be seen that even for the lowest elevation angle, as we move away in range, we can notice the observation gap increases. Observations at the surface level are required as input for hydrological models, especially in urban regions. To obtain this, we should place radars closer to the urban regions.

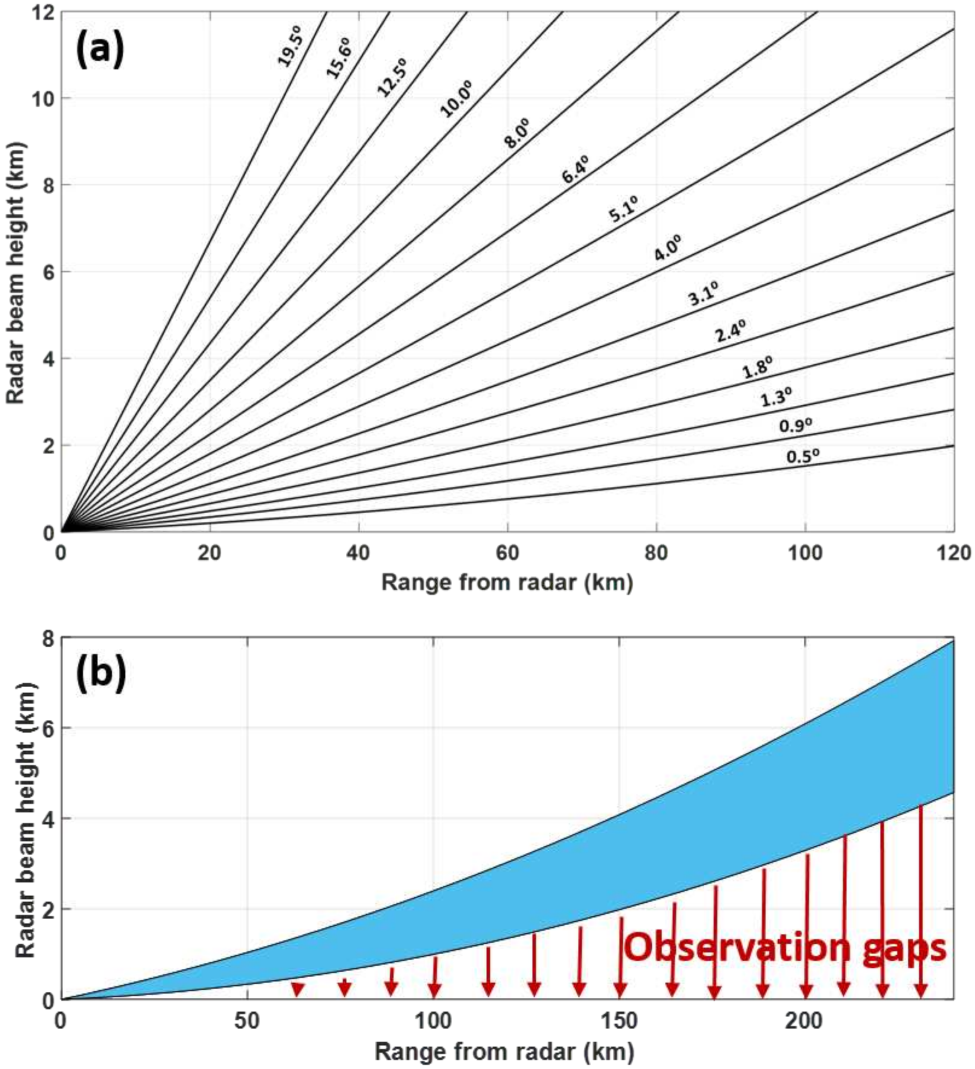

Figure 1.3. Illustration of observation gaps due to the radar beam propagation in the atmosphere.

.

Another concern is the radar beam blockage due to structures or terrain blocking the radar path. Large buildings and towers usually limit the radar observation volume in urban areas. Any structure will reflect the radar energy and appear as a blockage sector in the radar scan output. If the radar is deployed close to the ground, the probability of having beam blockage will be high. If the radar signal is blocked, we cannot get any reliable measurement further in that particular direction of the radar beam propagation. To overcome the beam blockage, weather radars are usually deployed on top of tall buildings or towers, which in turn limits the observation measurement values close to the ground. Weather radars deployed in areas with complex terrain, such as mountain ranges, will also have beam blockage limiting the radar beam propagation.

Remote sensing instruments deployed on satellites, such as precipitation mapping radars, will provide data on a global scale. It is essential to consider that they provide data over remote regions, such as mountains or oceans, and precipitation data over urban regions. One such satellite which maps the precipitation around the world is the Global Precipitation Measurement (GPM) core satellite, which has the dual-precipitation radar (DPR) operating at Ku and Ka frequency bands on board. This satellite containing the DPR provides 3D measurements of rain and snow. Satellites cannot provide continuous coverage over the same area. They will scan the region according to the orbit in which they are traveling and usually have a fixed swath width. Useful information for continuous urban area precipitation measurement would not be possible using satellites because the precipitation events usually last for hours, and satellites can capture data for a few minutes over the same region. Also, the resolution of the data from the satellite is very coarse. It will yield inaccurate precipitation measurements if there is a large variability in the vertical structure of the storm. The GPM radar resolution is 250 meters vertically. Data obtained at this resolution is not useful for surface precipitation measurements.

Accounting for the limitations of the different point and volume remote sensing instruments mentioned above for precipitation mapping, new methods for measuring accurate precipitation information in remote areas and at the surface level in urban regions are required. Any new techniques or systems for urban precipitation mapping must provide accurate data and be feasible to be deployed in urban areas. A method of using automobile radars operating at the millimeter wavelength to map precipitation at a regional scale is discussed in this dissertation. The potential of using synthetic aperture radars (SARs) for observing precipitation data is also discussed.

The accuracy of the weather radar data also plays an important factor in obtaining the true precipitation values from the remote sensing instruments. The remote sensing instruments have to be calibrated, and the data have to be quality controlled to obtain high-quality data. The precipitation values in the radar domain are estimated using the radar moments. The accuracy of the radar moments directly influences the correctness of the precipitation values. An attenuation-correction algorithm that corrects for rain and snow attenuation in weather radars is discussed, which will provide accurate precipitation rate estimates.

1.4. Research objectives

One of the main scientific objectives of this research is to explore the potential of using the network of automobile radars that operate in the millimeter wave band for accurate precipitation estimation at the surface level and subsequently use this information to create precipitation maps at the regional scale. This precipitation information obtained can be used along with weather radar data to improve the various hydrometeor estimation products.

Using automobile radar networks for precipitation mapping is an emerging research area. To the best of my knowledge, this is among the first few works that use a network of automobile radar for precipitation mapping. For any idea to be successful and implemented in the real world, three different aspects must be considered. As shown in Figure 1.4 science, technology and system are the three key areas that need to be researched and addressed to

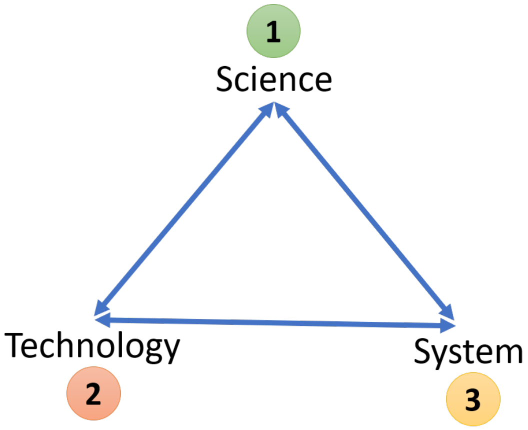

FIGURE 1.4. The three key aspects of designing and implementing a system.

.

bring the idea to reality. As seen in the figure, the three areas share feedback for building a successful end product. The detailed research and analysis for these three areas with respect to precipitation mapping using automobile radars are discussed in detail in this dissertation.

The second scientific objective of this research is to accurately account for attenuation encountered in weather radars signal when observing rain and snow particles and correct them. Previous attenuation correction methods have shown excellent attenuation correction in the rain, but there are only a few research works that address attenuation correction for snow in weather radars. A new algorithm that corrects for attenuation in rain and snow particles is developed based on the Dual-Processing Radar Operational Processing System (DROPS) algorithm and signal simulations. This new attenuation correction can be implemented for various frequency bands of weather radars.

The third scientific objective of this research is to study simulations of precipitation from a SAR platform deployed on a spaceborne platform. SAR operates in different modes. The most common modes of operation of spaceborne SAR are the stripmap and spotlight modes. In this research, SAR scanning in stripmap mode is considered. SAR architectures for both monostatic and bistatic are used to study the effect of varying parameters of precipitation, such as the velocity and spectral width of the precipitation particles.

Within these three scientific objectives, specific research goals are devised, including:

(1) Millimeter wave radars for precipitation mapping

    (a) Research on the radar signals at millimeter wave frequencies which automobile radars use, obtain relationships between the radar observed products with precipitation.

    (b) Technology demonstration of an automobile radar for obtaining precipitation information using a state-of-the-art automobile radar available in the market.

    (c) Complete system design and analysis of using automobile radar data for generating precipitation maps which are provided to the end user.

(2) Attenuation correction in weather radars for rain and snow particles

    (a) Determine the particle size distribution for the various hydrometeors and get the relationships between attenuation and specific phase using signal simulations.

    (b) Development of the new attenuation correction algorithm and initial test cases.

    (c) Apply the attenuation correction algorithm for weather radar data collected at different frequency bands.

    (d) Validation of the results obtained using the attenuation correction algorithm.

(3) Precipitation study using SAR

    (a) Development of simulation code for SAR observing precipitation in monostatic and bistatic modes.

(b) Carry out signal simulations for a spaceborne case of SAR and study the simulation results. For the simulations involving bistatic case a specific SAR architecture is considered.

(c) Study the influence of the precipitation parameters such as velocity and spectral width on the simulation results.

1.5. Organization of the dissertation

Subsection 1.1 provides a brief introduction to the various types of instruments used to collect data in remote sensing domain. In subsection 1.2 the urbanization prospects of the current world and the climate studies are briefly introduced. Subsections 1.3 and 1.4 describe the problem faced in precipitation measurement in urban areas and the limitations of different remote sensing instruments for mapping surface precipitation. The three main objectives of this research study, along with the specific goals of this work are also described.

Chapter 2 introduces the various remote sensing instruments used to map precipitation at the local scale. Data from rain gauges and disdrometers are briefly discussed considering actual data collected during precipitation events. The advantages and disadvantages of using these instruments for precipitation mapping is also described.

Chapter 3 starts with an introduction to automobile radars. Next, in this chapter, the various relationships for mapping precipitation at the millimeter wave frequencies are derived based on simulation studies. The relationships between the rainfall rate and radar parameters such as reflectivity and attenuation are introduced. This chapter also focuses on the technological aspect of millimeter wave radars. A timeseries simulation tool that can generate pulsed radar signal at millimeter wave band is introduced and discussed in detail. The current technology and various automobile radars available in the market are briefly introduced. The experiments conducted to map precipitation using automobile radars are also presented.

Chapter 4 introduces weather radars and the various estimated products obtained from radars in meteorology. Weather radar data from multiple radars are considered and the precipitation maps obtained at the regional level are presented. The chapter also briefly introduces the current systems at a regional scale which are available for precipitation mapping.

Chapter 5 describes the attenuation problem due to ice hydrometeors in weather radars in detail. The existing algorithms, DROPS1.0 and DROPS2.0, which deal with attenuation for rain hydrometeors, are described. Theoretical simulations are carried out using the T-matrix method for the ice hydrometers are explained from which relationships are obtained and used for attenuation correction. Next, this chapter presents the proposed attenuation correction algorithm for ice hydrometeors. The Ku-band and X-band radar data are used to show the performance of the algorithm and the results are discussed.

Chapter 6 focuses on the method of using automotive radars for creating precipitation maps at a regional scale. The simulation results of creating precipitation maps using automobile radars are explained step by step. This chapter also discusses the various challenges and problems encountered in the simulation study. A potential system architecture that can be deployed is also discussed in this chapter.

Chapter 7 starts with a brief introduction of using satellites for precipitation measurement on a global scale. SAR simulations are carried out in various modes of the radar for a precipitation target and the results are discussed. In this chapter, the effect of variation of weather parameters on the SAR processed signals are also presented.

Finally, Chapter 8 summarizes the research work and the results corresponding to the three main research objectives. The chapter ends with suggestions for future work.

Chapter 2

Precipitation mapping at local scale

The rain gauges and disdrometers fall under the category of point measurement instruments. In the point measurement class of instruments we get a data value at a point in the geological location. A network of these instruments is usually deployed to obtain data values over a large region. A rain gauge is an instrument that gives us data on the amount of precipitation collected during a precipitation event. There are a wide variety of rain gauges varying from manual to automatic. Another type of point instrument which gives additional information on particle size and density along with the amount of precipitation is disdrometers. Disdrometers are useful as we can obtain microphysical information about the occurring precipitation event. Disdrometers are broadly classified into three main types, video, acoustic, and impact disdrometers. Each has its own operation technology and advantages for obtaining accurate measurements. A brief discussion on the rain gauge and disdrometers will be provided in this chapter.

2.1. Rain gauges

Rain gauges are remote sensing instruments that provide data specific to geolocation. Most of these instruments are located at the surface level and provide accurate estimates of the precipitation information on the surface. The variety of rain gauges depends on the technology of the operation. The manual rain gauges require operators to record gauge data and manually empty the gauge to start the next observation. Researchers rarely use manual rain gauges. There are many types of automatic rain gauges present today. The following section provides a brief overview of some of the most common rain gauges:.

(1) Weighing rain gauge: These gauges operate on the principle of the instrument weighing the rainwater. The rain measurement is the difference in the values in the time intervals. A weighing rain gauge's accuracy is dependent on the precision of the water accumulation measurement.

(2) Tipping-bucket rain gauge: In this type of rain gauge, the rainwater is collected in a bucket of known size and capacity. After a given amount of water is collected, the bucket tips and drains. Each bucket tip occurrence sends a signal to the measurement device using a switch. These instruments are usually deployed for recording precipitation information on the land surface.

(3) Optical rain gauges: Optical rain gauges measure the scintillation in an optical beam produced by the shadows of the rain drops falling between a light source and an optical receiver. The light source can be a light-emitting-diode (LED). The intensity of variation caused by the natural raindrops is proportional to the rainfall rate [13].

(4) Capacitance rain gauge: The capacitance rain gauge was developed for potential use on buoys at sea [14]. The rainwater is collected in a chamber, and the capacitance varies based on the height of the water present in the chamber. This capacitance is converted to a voltage proportional to the height of the water in the chamber. The difference in the rainwater accumulation is used for measuring the amount of precipitation in a given time interval. More details regarding this can be found in [15].

Other types of rain gauges operate on the principle of sound, known as acoustic rain measurement system [15]. Various organizations deploy a large number of rain gauges across the globe to capture precipitation information, particularly at a local scale. The Global Historical Climatology Network (GHCN)-Daily is a database that addresses the critical need

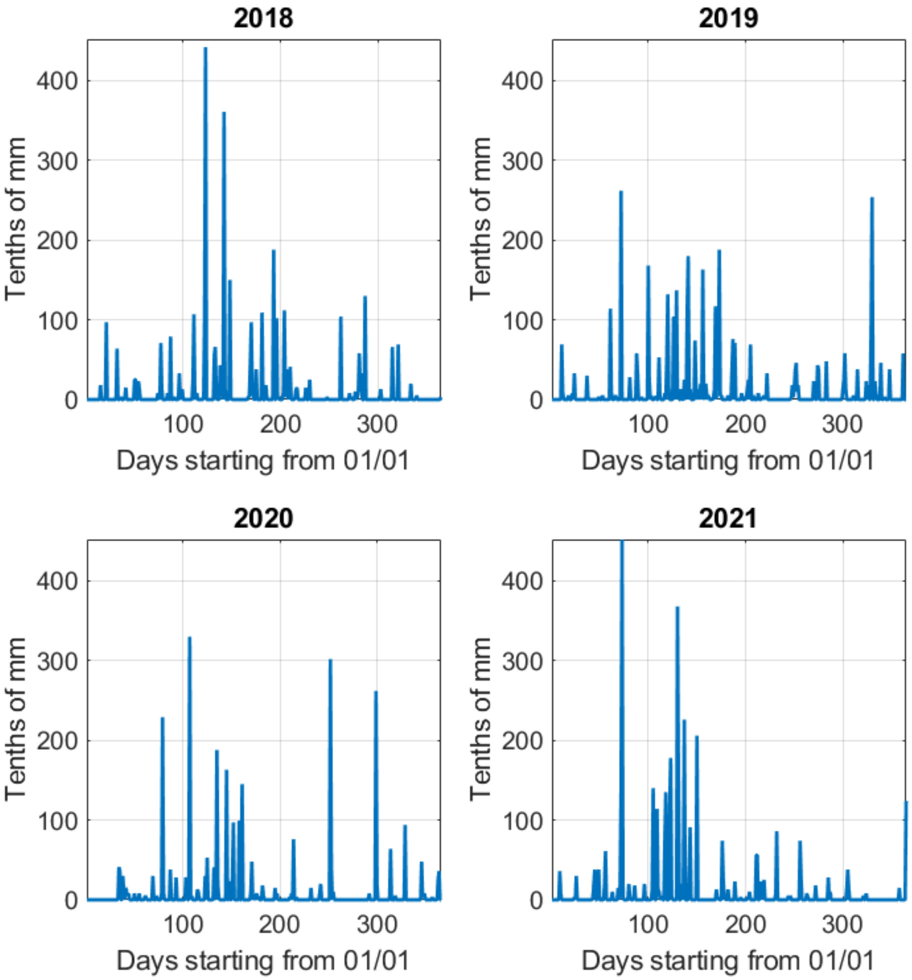

Figure 2.1. Daily precipitation accumulation data from CSU-Fort Collins weather station between 2019-2021.

for historical daily temperature, precipitation, and snow records over global land areas. The precipitation gauge deployed at the Colorado State University (CSU) main campus uses a precipitation gauge to gather the total daily precipitation accumulation data for the past four years, as shown in Figure 2.1. This figure shows that the amount of precipitation varies from year to year. We observe that the data over the four-year period has a similar trend, such as precipitation values, which are maximum between day 100-200. The information from the precipitation gauge and data from other instruments, such as temperature, can be used for studying seasonal patterns and climate studies.

2.2. DISDROMETERS

Similar to rain gauges, disdrometers are surface measurement instruments. Their main difference is that they provide information, such as the drop size distribution (DSD), in addition to the rainfall accumulation estimates. In addition, disdrometers measure other precipitation particle types, such as snow and hail. Disdrometers are grouped broadly based on their technology of operation into three groups. Some of the most common disdrometers include:

(1) Impact disdrometers: This type of disdrometers measures the precipitation information based on the impact of the precipitation particles on the measuring surface of the disdrometer. One popular impact disdrometer is the Joss-Waldvogel Disdrometer (JWD), which has an impact-type electromechanical counter considered as a reference instrument for drop size distribution (DSD) measurements. The JSD has been commercially available for over 30 years, and researchers have widely used it in many field campaigns to complement validation efforts of radar rainfall estimation. The GPM ground validation program uses this instrument [16] [17].

(2) Acoustic disdrometers: Different sized raindrops splashing on a water surface produce sound underwater that is distinctive and can be used to measure the drop size distribution in the rain [16]. The acoustic disdrometers are based on this principle and were designed to obtain measurements of rainfall in remote oceanic regions.

(3) Optical disdrometers: Optical disdrometers with laser-based sensors measure precipitation by determining the size and velocity of raindrops when falling through

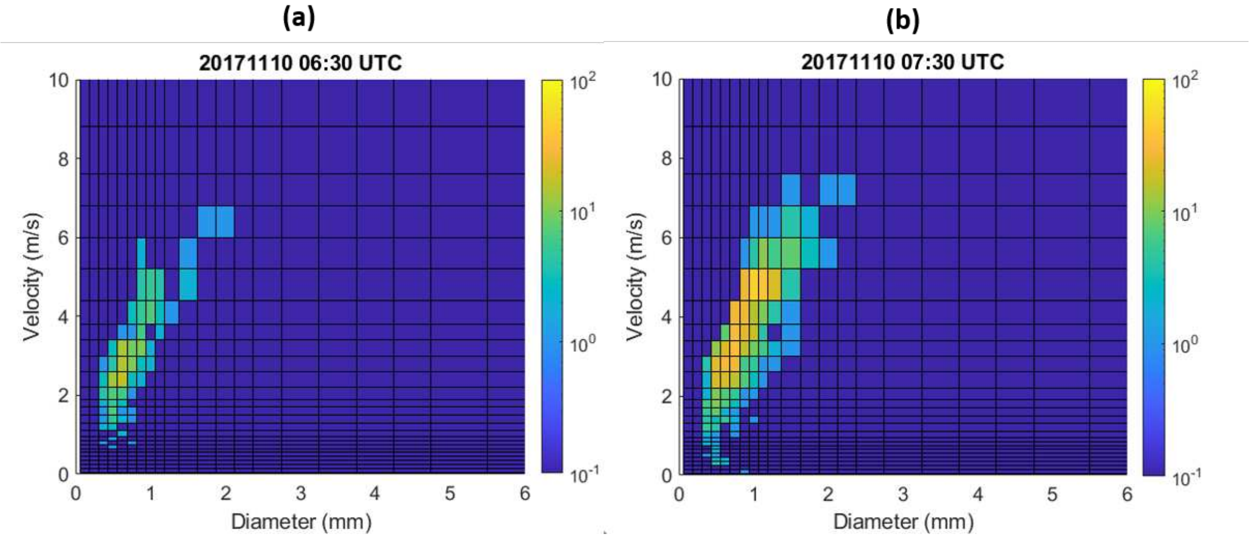

FIGURE 2.2. Data from the OTT Parsivel recorded during a rain event on November 10, 2017.

the measuring area. These types of disdrometers are the most widely used and are classified further into three types: light occlusion, linear scanning and planar imaging. Two-dimensional video disdrometer (2DVD) and OTT Particle size velocity (Parsivel) are two well-known optical disdrometers. The 2DVD uses two high-speed line scan cameras to provide continuous measurements of size distribution, shape, and fall velocities of all precipitation particles and types. The OTT Parsivel measures the properties of the precipitation particles based on the signal loss due to light occlusion and determines the size and fall velocity of raindrops [17].

Datasets of OTT Parsivel disdrometer are considered for rain and snow events and the information obtained from the instrument is briefly discussed. The data shown here were collected from the disdrometer at the YongPong Observatory (YPO) in South Korea during the ICE-POP field campaign.

Figure 2.2 shows snapshots of the data collected by the OTT Parsivel disdrometer during a rain event on November 10, 2017. Two cases of data are considered one hour apart. The

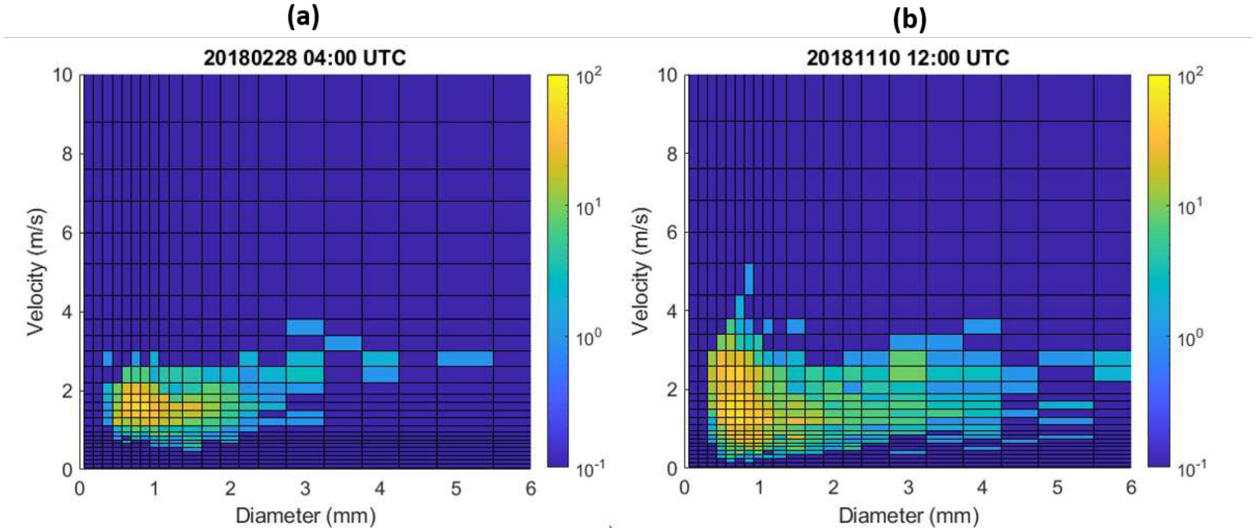

Figure 2.3. Data from the OTT Parsivel recorded during a snow event on February 28, 2018.

first case was collected during the initial phase of the rain event where light rain was present, and the second case was taken when there was significant rain in the region. Figure 2.2 (a) shows the data collected during the initial phase of the rain event. The figure shows that the drop size is concentrated between 0.3 mm to 1.2 mm in diameter and 1 m/s to 5 m/s in velocity. Figure 2.2 (b) shows the data collected during the heavy phase of the rain event. The figure shows that the drop size is concentrated between 0.3 mm to 2 mm in diameter and 1 m/s to 7 m/s in velocity. From these two figures, we can understand the drop size distributions during the different phases of the rain event. This data gives us information for the validation of other instruments and algorithms.

Next, Figure 2.3 shows the data collected by the OTT Parsivel disdrometer during a snow event on the February 28, 2018 The snow event lasted several hours on this day with varying precipitation particle types. Two cases of data are considered eight hours apart. The first case was collected during the initial phase of the snow event, where light snow was present and the second case was taken when there was significant snow in the region with large aggregates. Figure 2.3 (a) shows the data collected during the initial phase of the snow event. The figure shows that the drop size is concentrated between 0.45 mm to 2 mm in diameter and 1 m/s to 2.5 m/s in velocity. Figure 2.3 (b) shows the data collected during the heavy phase of the snow event; from the figure, we can see that the drop size is concentrated between 0.3 mm to 4 mm in diameter and 0.25 m/s to 3.8 m/s in velocity. From these two figures, we can understand the drop size distributions during the different phases of the snow event. During the initial phase, smaller particles are detected compared to the heavy phase. We can infer that larger aggregate particles are formed during the heavy phase of the snow event, which increases the particle size of the snow. We explore more details on the computation of the reflectivity from the OTT Parsivel data in Chapter 5.

From the rain and snow disdrometer data, we can see that the velocity of rain particles is larger than that of snow particles. Both rain gauges and disdrometers are widely used across the globe for getting precipitation measurements and particle size distributions. With the technology improving rapidly, there is the capability of obtaining precipitation information using other instruments primarily used for applications other than precipitation mapping. The potential is using automobile radars, which operate at the millimeter wave frequencies for precipitation mapping, is explained in the next chapter.

CHAPTER 3

AUTOMOBILE RADARS FOR PRECIPITATION MEASUREMENT

The potential use of automobile radars for mapping precipitation is an emerging field of study. This chapter will discuss the introduction to automobile radars from a science and technology perspective. The block diagram of an automobile radar and the use of automobile radars as rain gauges are discussed in detail in this chapter. Signal simulations are carried out to obtain the relationship between reflectivity, attenuation, and rain rates at frequencies in which automobile radars operate. A new simulation tool developed at the CSU radar group for millimeter wave pulsed radars based on the total volume of particles backscattering method is also discussed, with simulation results carried out at 77 GHz. This chapter also provides a short overview of the automotive radar sensors available in the market. Finally, a field experiment using automotive radars to measure precipitation and recorded results are discussed.

3.1. INTRODUCTION TO AUTOMOBILE RADARS

Automobile radars have been an integral part of the majority of modern automobiles. Most of the current automobile radars work on the principle of millimeter wave technology, meaning the wavelength of the transmit signal from the radar is a few millimeters. The initial usage of millimeter wave technology dates back to the early 1970s. Many companies and research labs were working on small-scale radars which could detect distance from automobiles. Due to the lack of technology and cost constraints at that time, it was not until 1999 that the first automotive sensors were built. High-end cars were equipped with automotive radars which performed simple operations like cruise control. As years passed

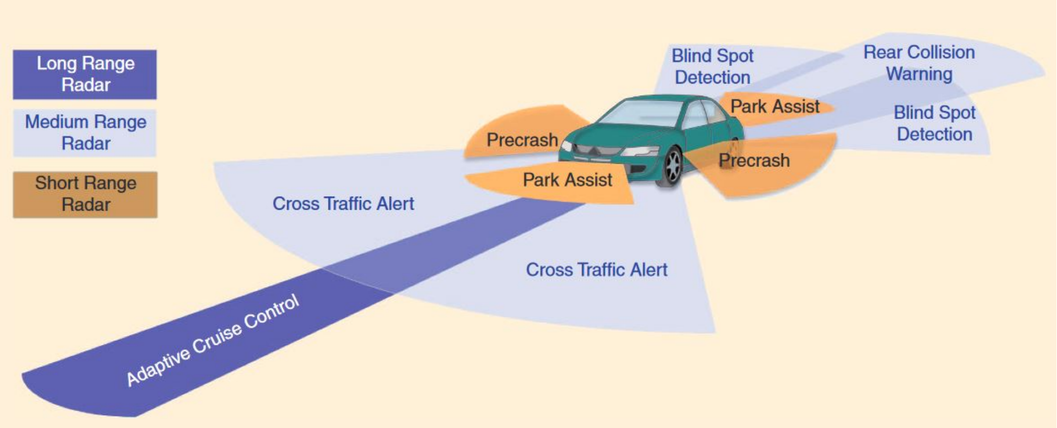

Figure 3.1. Diagram illustrating different types of automobile radars and their uses. [2].

by, in the current world, most cars have more than a hundred sensors including automotive radars on them, which carry out various functionalities.

Initially, automotive radars were working in the 24 GHz band. Due to the advantages of the 76-81 GHz frequency band, automotive radars later shifted from 24 GHz to the 76-81 GHz frequency band. The advantages of using the 76-81 GHz frequency band over the 24 GHz band include wide bandwidth, smaller system size, high range resolution and accuracy, and increased velocity resolution and accuracy [20]. Due to these additional advantages, most of the automotive radars currently in the market operate at the higher frequency band of 76-81 GHz. Few automobile radars are still operational at the 24 GHz band. Other radar frequency bands such as the 10 GHz (X-band) are being considered for automobile radar applications and the research is currently in progress.

Various sensors are available in the market now used for automotive radar purposes. Major electrical and electronic manufacturing companies are constantly updating the technology of automobile sensors to increase their capability and efficiency. The automotive radars are used for various operations, including driving assistance, cruise control, parking assistance, and lane change assistance. Different automotive radars, such as long-range radars, medium-range radars, and short-range radars, suit specific applications. Figure 3.1 presents different automotive radars and their applications. The various radar sensors present in automobiles have unique systems and technical specifications. For example, in long-range radars, the range is given priority over the field of view, which is used for applications, such as adaptive cruise control. In short-range radars, the radar design is prioritized based on the field of view rather than the distance of the radar range.

The early generation automobile radar sensors were significantly larger than the industry's current automobile radars. The semiconductor technology has developed to the point that automotive radar sensors are available on a single chip within a few millimeters. Companies like Texas Instruments and Analog devices are actively involved in research to expand the capabilities of automotive radar sensors. Various system blocks of the automobile radars are similar to that of any other radar system, such as the antenna module and the transceiver module, which houses the transmitter and the receiver, the signal processing module and the data storage and communication module.

Initially, automotive radar technology started by transmitting continuous waves (CW) of electromagnetic signals. Since then various methods of transmitting signals such as pulsed Doppler, Frequency Modulated Continuous Wave (FMCW) and Phase Modulated Continuous Wave (PMCW) have been developed and used. In automobile radars, the maximum range of detection of the targets lies within a few meters to a few hundred meters. A continuous wave transmission is preferred for short-range radars, which can detect within a few meters. For this purpose, FMCW technology is still widely used in automobile radars. The basic idea of FMCW radars is to generate a linear frequency ramp for transmitting the radar signal. Since the transmitted signal varies only with frequency, the amplitude modulation of

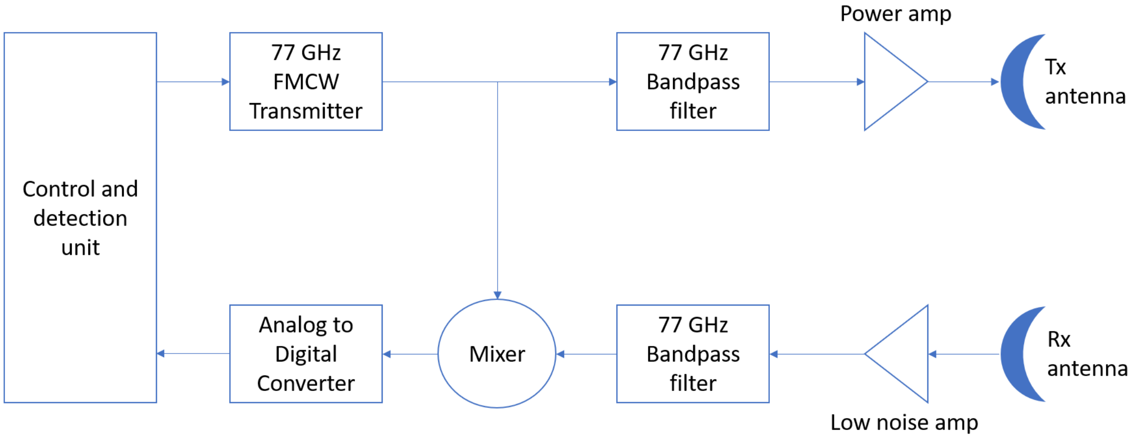

Figure 3.2. Basic block diagram of an automobile radar operating at 77 GHz.

the signal is not required. The use of FM allows the transmit circuit to operate in saturation, which is the most efficient mode for any RF amplifier.

Detailed information regarding the FMCW for automotive radars can be found in [18]. Pulsed radars are also considered and used in automobile radars. However, pulsed radars were not commonly used for automobile radar applications previously. With the advancement in technology and efficient design principles, pulsed Doppler radars have the potential to be used in all automobile radars.

There are various block diagrams for automobile radars available in the literature such as the one shown in [19]. A basic block diagram of an FMCW automobile radar operating at 77 GHz is shown in Figure 3.2. The architecture of the radar using FMCW is much simpler compared to pulsed radars. The control block, along with the 77 GHz FMCW transmitter, generates the transmitted signal required according to the design specification required for the radar. The signal is then sent through the bandpass filter, which transmits only the required band of frequencies (i.e., an approved band of frequencies around 77 GHz). It should be noted that appropriate licensing should be obtained before transmitting electromagnetic signals in the atmosphere. The frequency bands from 76-81 GHz have been approved for automobile radars by the United States Federal Communications Commission.

The next stage in the radar block diagram is the power amplifier, where the radar signal power is amplified before transmission. The signal is amplified based on the receiver characteristics and the application in which the radar is used.

Separate antennas are used for the transmission and reception of the radar signals since the block diagram of the radar shown here is an FMCW radar. The isolation between the transmission and receiver antenna should be considered when designing the radar system. This isolation directly influences any signal leakage from the transmitter to the receiver and will affect the system's performance. After the receiver antenna receives the signal, the first stage the signal passes through is the low noise amplifier. In this stage, the received signal is amplified. Then the signal is passed through a bandpass filter where the unwanted signal components are cut off. Next, the signal is sent to a mixer stage, where the signal is brought down from the carrier frequency of 77 GHz to the baseband.

In some cases, using the mixer, the radar signal is brought down to the intermediate frequency (IF), and then another mixer is used to bring the signal down to the baseband. In a weather radar system the carrier signal is brought down to the baseband using two mixing stages. Next, the signal is converted into digital samples using an analog-to-digital (ADC) converter. After which, the signal is filtered using a digital low-pass filter and then the Fast Fourier Transform (FFT) for the signal is done to get the frequency components of the received signal. This signal is then processed to extract the range and Doppler information. These processes are carried out in the control and detection unit of the radar system. More details on the process of detecting range and Doppler for automotive radar can be found in [18].

The antenna assembly on an automotive radar is an important factor to be considered. An advanced antenna system can perform multiple operations and increase the efficiency of the radar. The antenna system can be broadly classified into four categories: quasi-optical beamforming, digital beamforming, analog beamforming and mechanical scanning. Each of these antenna systems has advantages over the other. While most automotive sensors avoid mechanical scanning antennas, they do exist. Phased arrays are gaining popularity in this domain and many radar systems are being developed based on this technology.

More advanced and current research topics like Multiple Input Multiple Output (MIMO) and Virtual array concepts are also gaining popularity in the automotive radar field and systems are designed based on them. Two linear, orthogonally placed arrays are used to simultaneously achieve azimuth and elevation angle measurements. [20]. More current research on two-dimensional digital beamforming for automotive radars can be found in [21]. All the currently ongoing research for automobile radars indicates a promising future for this technology.

3.2. AUTOMOBILE RADARS FOR PRECIPITATION MEASUREMENT

The majority of the existing precipitation measurement and monitoring methods are precipitation gauges, weather radars, and meteorological satellites. Most of the radars which operate for meteorological purposes are independent instruments operating at the S-, C-, X-, Ku-, Ka- and W-band frequencies. These instruments provide good quality data but are limited in observations of urban regions, as explained in Chapter 1. The meteorological satellites have poor resolutions in mapping precipitation in urban areas. To map the precipitation accurately in urban areas, we can use other sensors in the region. Each automobile is equipped with more than a hundred sensors, so automobile radars can be a perfect fit for mapping precipitation in urban regions. As mentioned previously, automobile radars are used for many applications such as assistance and safety for the driver. By modifying certain parameters of the operation of automobile radar and using them as systems of systems, we can use the automobile radar to map precipitation.

Research on using automobile radars to measure precipitation is in the initial stages and there are only a couple of prior literature available currently. Using automobile radar to measure precipitation, we can get a more accurate value of precipitation rate at the surface level. The concept of using automobile radars for measuring precipitation is a new and emerging technology. There are thousands of automobiles going around in each urban city. We can take this as an advantage to measure accurate precipitation in cities that are densely populated. Since automobile radars operate at 24 GHz and 77 GHz frequencies, the radar signal characteristics at these frequencies should be studied theoretically to understand the scope of the problem. Although most automobile radars operate at millimeter wavelength, i.e., around 77 GHz, in this study results of 10 GHz, 24 GHz and 77 GHz are discussed with respect to automobile radars.

Figure 3.3 illustrates the application of automobile radars for measuring precipitation. The automobile radars have the capability to scan in a couple of different modes. Although mechanical scanning is avoided, using the antenna configuration electronic scanning is possible. In the fixed mode, the azimuth and elevation angles are fixed. In the partial plan position indicator (PPI) mode, the radar scans a sector in azimuth with a fixed elevation angle. Scanning a sector in elevation is usually not carried out using automobile radars.

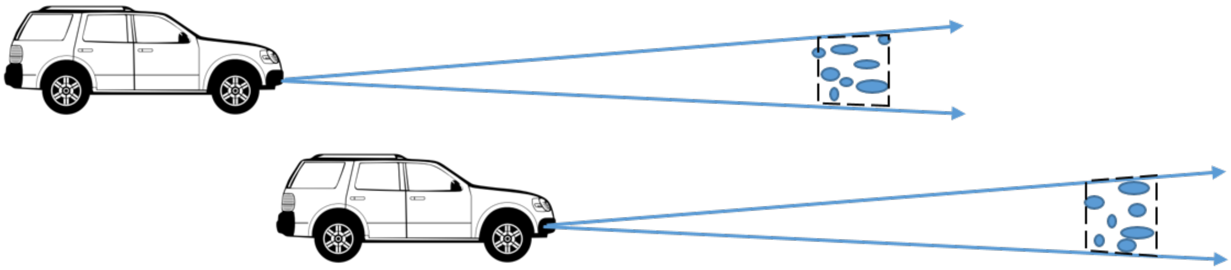

Figure 3.3. Automobile radars for measuring precipitation - concept diagram.

.

However, with the advancements in phased array radar technology, the data along elevation direction will be available in future automobile radars.

If we obtain the precipitation rate from each automobile radar using the information of reflectivity or attenuation, which are explained in the next section, it will be very useful to measure and update rainfall estimations in a very short temporal resolution. Also, these surface precipitation observations could benefit real-time monitoring operations in urban areas. At the same time, it is a challenge to retrieve accurate measurements of meteorological variables using automobile radars. In this research, the use of automobile radars as rain gauges is presented. In the future, the application of automobile radars can be studied for other hydrometeors, such as, snow as well. A detailed description of how automobile radars can be used as a rain gauge is explained in the next section.

3.3. Automobile radars as rain gauges

Automobile radar can be used as a rain gauge to map the precipitation rate during a weather event. To consider automobile radar for measuring rain rate, various radar-derived parameters such as attenuation and reflectivity must be considered. The reflectivity of radar signals which was defined earlier gives us information on the intensity of the precipitation. More details on reflectivity and how it is computed can be found in chapter 4. Attenuation

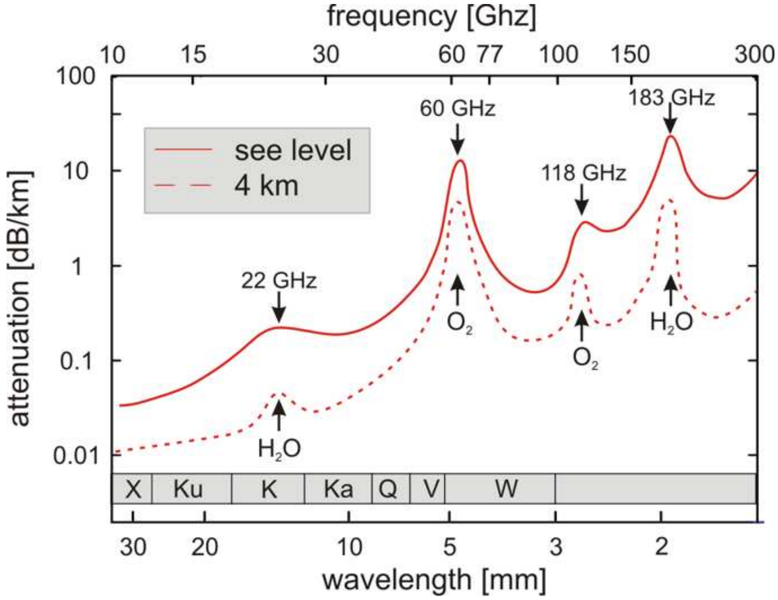

Figure 3.4. Atmospheric attenuation at various frequencies [3].

is weakening of a radar signal beam due to some of the energy being lost due to scattering and absorption as it traverses through the atmosphere. The attenuation of radar signals is caused by precipitation particles, cloud droplets, gases and lithometeors. Attenuation depends primarily upon the wavelength of the radar pulse relative to the particle size and composition. Shorter the wavelength, the greater the attenuation of the radar signal. The attenuation of the radar signal occurs both on the outward path and on the return path. The atmospheric absorption and attenuation must be considered since they can put constraints on the data from the maximum usable range from the radar.

One of the factors on which the attenuation of the radar signal depends is the attenuation due to absorption of the signal by the contents in the atmosphere even though there is no precipitation event. As we all know earth's atmosphere contains gases and water vapor, these contents of the atmosphere will influence the amount of absorption of radar signals. The oxygen and water vapor molecules are the major contributors to the absorption of signals

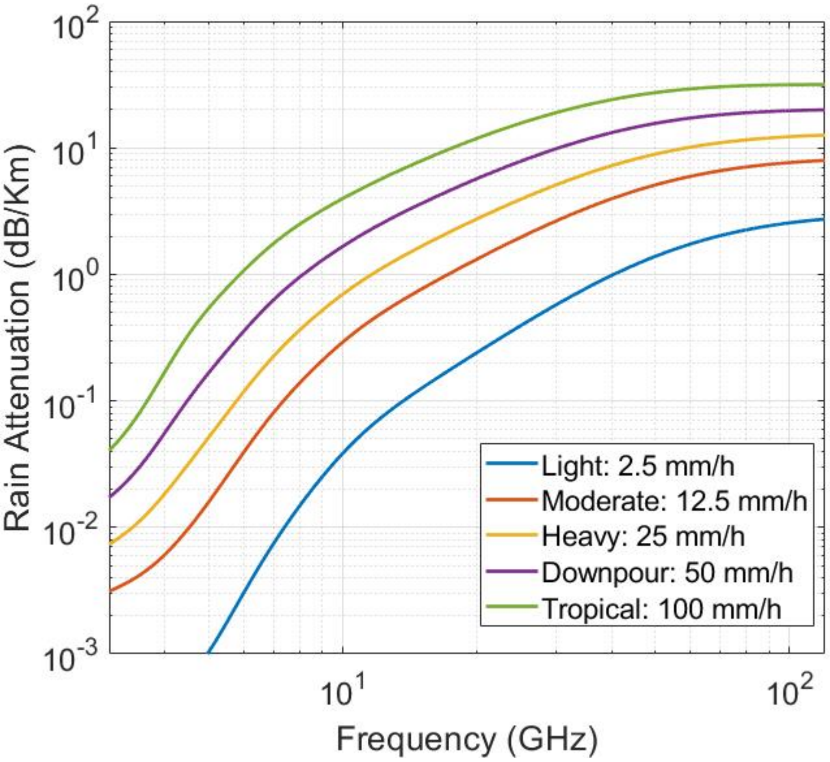

FIGURE 3.5. Rain attenuation versus frequency for different rain rates.

in the atmosphere. The value of attenuation varies depending on the height and humidity present in the atmosphere.

Figure 3.4 shows the atmospheric attenuation at different frequencies [3]. In this figure, it can be seen that the attenuation peaks with water and oxygen molecules at various frequencies. Radars usually avoid these frequencies at which the attenuation peaks. It should also be noted that the attenuation peaks vary with different altitudes. This figure shows attenuation values at sea level and 4 km height. We can see that at sea level, the attenuation is more compared to 4 km in height. Also, it can be seen that the attenuation increases as we go higher in frequency. The atmospheric absorption at the frequency range of 77 GHz is about 1 dB/km. This value is considered sufficiently low for the applications of automotive radar as a rain gauge. Also, considering the atmospheric absorption curve seen in the figure, we can say that 77 GHz absorption is located in one of the minimums.

Along with this attenuation discussed above, attenuation caused by precipitation particles such as rain, snow, and hail during a precipitation event should be considered. The attenuation caused by precipitation particles has a very large value compared to the gaseous atmospheric attenuation. The specific attenuation values are computed for varying intensities of rain and snow hydrometeors to understand the influence of the attenuation caused by precipitation particles on the radar signal. First, the attenuation values are computed for the rain hydrometeors based on the International Telecommunication Union (ITU) specific attenuation model for rainfall [22]. This model considers the radar signal frequency, rainfall rate, polarization and elevation angle and outputs the specific attenuation. The attenuation values are specified in the units of dB/Km. The specific attenuation is modeled as a power-law fit with respect to the rain rate, as shown in Equation 1. The procedure to obtain k and α is provided in detail in [22].

$$SpecificAttenuation(A_h) = k * Rainrate^{\alpha} \tag{1}$$

The range of the rainfall rate can vary from less than 0.25 mm/h for very light rain to over 200 mm/h for extreme rains. The attenuation values for different intensities of rain are considered and the variation of attenuation with frequency for different rain intensities is shown in Figure 3.5. From Figure 3.5, it can be clearly seen that as the intensity of the rain increases, the attenuation also increases. It can also be seen that as the frequency increases, the attenuation values increases. The attenuation is particularly worse for the combination of high frequency and heavy rainfall.

Figure 3.5 shows the rain attenuation around 77 GHz varies from 2 dB/km for light rain with a rain rate of 2.5 mm/hr to 35 dB/km for a downpour with a rain rate of 100 mm/hr.

One of the previous works also mentions that the attenuation varies from 0.4 dB/km for a rain rate of 0.25 mm/h to 42 dB/km for a rain rate of 150 mm/hr [23]. It should also be noted that if both horizontal and vertical polarizations are used, the attenuation in horizontal polarization will be greater than the vertical polarization due to the distribution of the rain drops in the radar resolution volume. But dual-polarization in automobile radars is another new concept that is not covered in this research work. It should also be considered that there will be an attenuation of about 0.07 dB/km caused by dry air and 0.36 dB/km caused by the water vapor component.

Considering the above points regarding attenuation, in most cases, the free space attenuation is less than 0.5 dB/km. When considering a rain rate of around 20 m/hr, the attenuation is less than 15 dB/km. Since we consider only a short distance in front of the radar (usually within a few meters) close to the vehicle, these values do not become a limitation for using automobile radars as a rain gauge. We can utilize this information on signal attenuation to map precipitation rates.

3.3.1. PARTICLE BACKSCATTERING REGION - MIE AND RAYLEIGH.

In addition to the incident electromagnetic wave, the scattering properties of the hydrometeors depend on the size shape and other physical properties of the particles. By studying the characteristics of the scattering waves, we can infer the physical properties of the hydrometeor particles. The radar antenna receives only a part of the electromagnetic wave which was transmitted, this scattered signal from the hydrometeor particles are known as backscattered signals. The backscattered signal depends on the cross-section of the particle from the radar's perspective, known as the backscattering cross-section or the radar cross section. The received signal strength depends on the amount of back scattering ability of the hydrometeor particles.

The dimensionless scale parameter α is a frequently used factor to study physical properties including the backscattering of the particle. It is given as follows;

$$\alpha = \frac{2\pi r}{\lambda} = \frac{\pi d}{\lambda} \tag{2}$$

where r is the radius of the particle, d is the diameter of the particle, λ is the wavelength of the incident electromagnetic signal. The type of scattering also influences the interpretation of the received radar signal. The two most common scattering regions in weather radars are Rayleigh scattering and Mie scattering.

Mie scattering theory was established by Gustav Mie when studying the scattering of colloidal metal particles [24]. Mie derived the exact solution of the scattering wave of a homogeneous spherical particle against a plane electromagnetic wave using Maxwell's equations. The solution is a mathematical series that gives the amplitude of the scattering electromagnetic field of the particle and the amplitude of the electromagnetic field in the particle in far field, called Mie scattering coefficients.

Mie scattering can be used for all particle sizes, but the computation is complex. The Rayleigh scattering is the approximation of Mie scattering and the calculation is much simpler than that of Mie scattering. When the size of the hydrometeor particles is much smaller than the wavelength of the incident electromagnetic wave (scale parameter α is very small), Rayleigh scattering can be used instead of Mie scattering for computations. In other words, in the Rayleigh scattering region, the particle size is considered much smaller than the operating wavelength of the radar. When the particle size is comparable to the wavelength of the radar, then it will fall under the Mie scattering.

The backscattering cross-sections calculated by Mie scattering and Rayleigh scattering are different for the same particle. Rayleigh scattering is the approximation of Mie scattering ignoring the higher order coefficients. It can be found that the calculation of Rayleigh scattering is much simpler than Mie scattering. However, only when the scale of the particle is in certain ranges, can Rayleigh scattering be adopted in computation, otherwise, Mie scattering must be used.

As mentioned earlier, the particle size determines the scattering computation that can be used. Considering a hydrometeor particle of about 1 cm, it will fall in the Rayleigh scattering region when using an X-band radar (around 10 GHz). In contrast, it will be in Mie scattering at the Ka-band (about 35 GHz). The 77 GHz region does not fall in the Rayleigh scattering region when observing the hydrometeor particles. The scattering at 77 GHz will fall in the Mie scattering region and signal properties should be considered appropriately. The scattering regions for the 77 GHz frequency is shown in Figure 3.6. In this figure the three scattering regions, Rayleigh, Mie and Optical are shown with respect to the scale parameter α.

3.3.2. PRECIPITATION RATE ESTIMATION USING REFLECTIVITY AND ATTENUATION.

Estimating the accurate precipitation rate is needed to correctly interpret weather events as they directly impact the hydrometeorological models. Estimation of precipitation rate is well-researched in the field of weather radars. The radar moments, such as reflectivity and specific differential phase, are commonly used for this purpose. Attenuation of radar signal can also be used to estimate the precipitation rate as we go higher in frequencies.

Computing radar parameters at 77 GHz frequency is not straightforward as they lie in the Mie scattering region. In this research work, two simulations programs which account for the particle size distributions of the various hydrometeors are considered and the results are

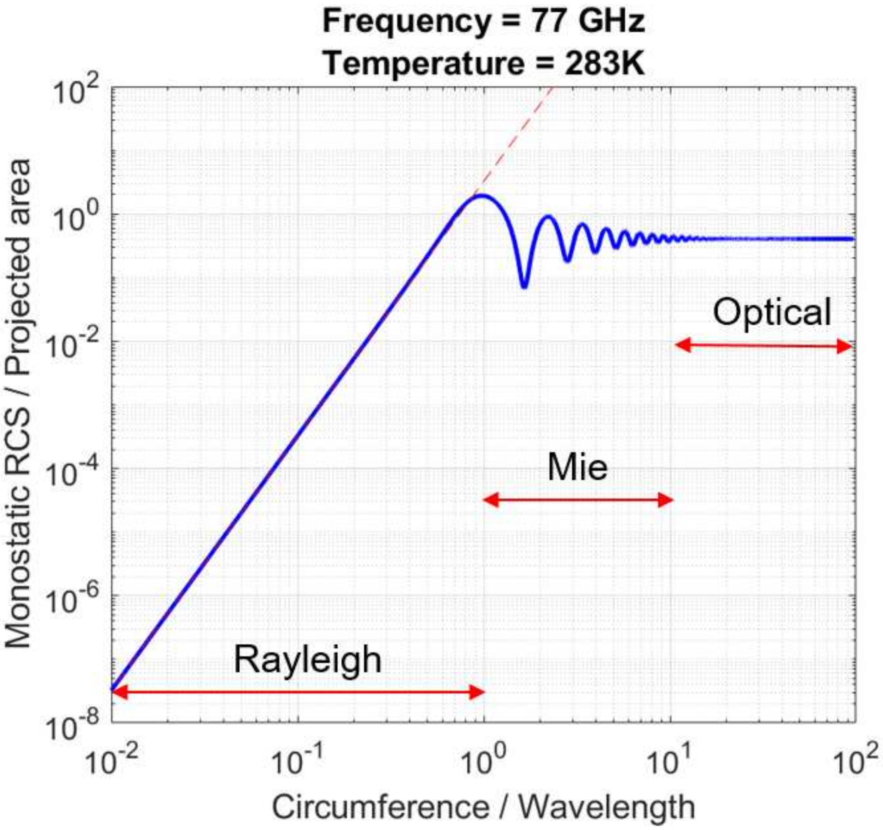

FIGURE 3.6. Scattering regions at 77 GHz.

.

discussed in detail. The first set of simulations are carried out using the T-matrix method. As mentioned before, the raindrops will be considered to be perfect spheres and the signal parameters are computed. This approximation will provide a reasonable estimate for the raindrops and the final results would not vary much due to this assumption. Accounting that the scattering falls into the Mie scattering region, the radar reflectivity equation can be given as in Equation 3.

$$Z = \frac{\lambda^4}{\pi^5 |K|^2} \int_0^{D_{max}} \sigma_{bMie} N(D) dD \tag{3}$$

where K is the absorption coefficient of water, D is the spherical particle diameter, N(D) is the drop size distribution, λ is the wavelength and σ_{Mie} is the radar backscattering cross section of a raindrop calculated according to Mie scattering theory. The σ_{Mie} factor depends on the wavelength at which the radar is operated.

Knowing the drop size distribution of the radar resolution volume, the rainfall rate can be computed using the equation 4.

$$RR = 6\pi 10^{-4} \int_{0}^{D_{max}} D^3 N(D) v(D) dD \tag{4}$$

Where v(D) is the terminal velocity of the rain drops.

The T-matrix code was used to carry out signal simulations from which an equation relating the radar reflectivity and rain rate was determined. This relationship is usually known as the Z-R relationship, as shown in Equation 5. Previously, one of the research works [23] provided a Z-R equation at 77 GHz, it is given as in Equation 6. Similarly, Equation 7 defines the attenuation and rain rate relationship. More details of the attenuation of radar signals is discussed in the next chapter.

$$Z = A(RR)^B \tag{5}$$

$$Z = 130RR^{0.65} \tag{6}$$

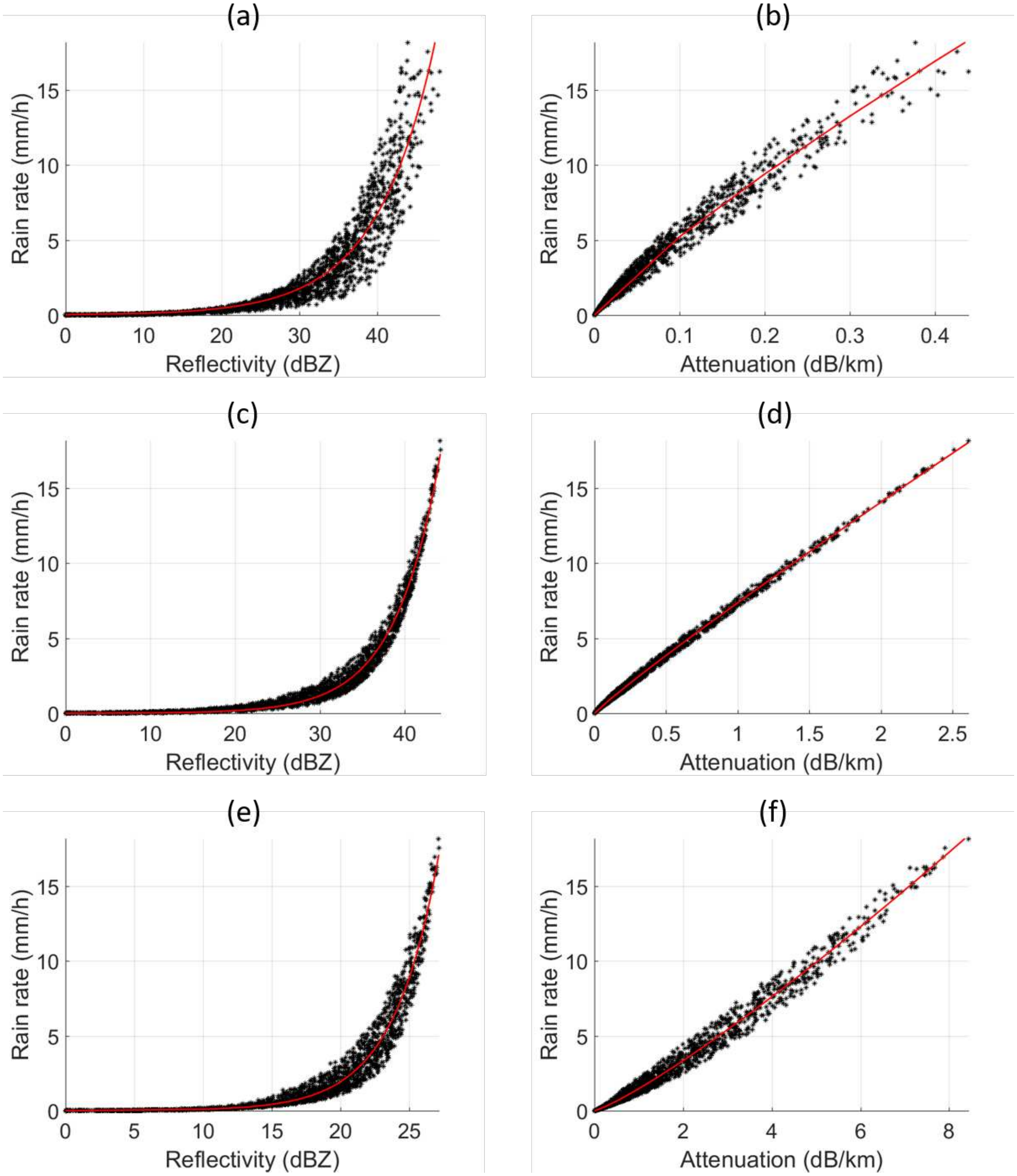

Figure 3.7. Scatterplots of reflectivity versus rain rate from signal simulations at (a) 10 GHz, (c) 24 GHz and (e) 77 GHz. Scatterplots of attenuation versus rainrate from signal simulations at (b) 10 GHz, (d) 24 GHz and (f) 77 GHz. The red line indicates the power-law fit in all the plots.

.

$$Att = C(RR)^D \tag{7}$$

Signal simulations were carried out to obtain the relationships between the rain rate and reflectivity, as well as rain rate and attenuation. The simulation parameters for rain particles considered were as follows. The temperature was set at 10 degrees Celsius and Beard and Chuang axis ratio model was used. The μ parameter was varied between -2 to 5, D_0parameters was varied between 0.2 and 2, and N_w was varied between 200 to 3000. Twenty thousand simulation points were carried out to obtain the scatter plot of the data and then a fit was made using the data points to obtain the relationship.

As mentioned previously, we computed this relationship using signal simulations, which is frequency-dependent. Hence, if the frequency of the radar changes, the respective Z-R relationship should be derived accordingly. The simulations were carried out at the 10 GHz, 24 GHz and 77 GHz frequency bands. Large raindrops were not convergent, so we considered only a small subset of raindrops for the initial simulation.

The scatterplots of reflectivity and rainfall rate were generated for 10 GHz, 24 GHz and 77 GHz frequencies using signal simulations.The scatterplots of simulated data of attenuation and rainfall rate for the three frequencies considered are shown in Figure 3.7. The red line shows the power-law fit to get the parameters of the relationship.

From the power-law fits of the scatter plots, the A and B values for rain rate and reflectivity relationships for simulations using T-matrix are provided in Table 3.1. The C and D values for rain rate and attenuation relationships for simulations using T-matrix are provided in Table 3.2.

The difference in the A and B parameters at 77 GHz from the simulations and the parameters mentioned in the literature [23] may be due to the different range of RR values considered. In that particular research, they considered RR up to 150 mm/hr, whereas the maximum RR in this simulation study goes only up to 26 mm/hr. Further simulation studies will better assess an accurate Z-RR relationship.

The next set of simulations at 77 GHz uses the Maetzler MATLAB toolbox. The Maetler MATLAB toolbox [25], can be used for simulations to obtain reflectivity, attenuation and rainfall rate at 77 GHz. This toolbox handles the Mie scattering of the particles and improves the accuracy of the outputs. In the Maerzler toolbox, a set of Mie functions computes the four Mie coefficients, efficiencies of extinction, scattering, backscattering and absorption. Along with this the asymmetry parameter and two angular scattering functions are obtained.

In this research, the Mie efficiencies and cross sections are considered for computing the radar parameters. The efficiencies are defined as the cross section normalized to the particle cross section. The Mie efficiencies are given as

$$Q_i = \frac{\sigma_i}{\pi a^2} \tag{8}$$

Where i stands for extinction (i=ext), absorption (i=abs), scattering (i=sca) and backscattering (i=b) the radar reflectivity equation can be given as in Equation 3. The efficiency is a unit-less quantity. We must multiply the particle cross section to obtain the back scattering cross section from backscattering efficiency.

In the Maetzler toolbox the backscattering efficiency Q_b, applicable to a monostatic radar is given by:

$$Q_b = \frac{1}{x^2}\left|\sum_{n=1}^{\infty}(2n+1)(-1)^{-n}(a_n - b_n)\right|^2 \tag{9}$$

The reflectivity and rainfall rate are computed using the equations shown in Equations 3 and 4. The equation for the terminal fall velocity considered in the computations is given as below.

$$v(D) = 9.65 - 10.3\exp(-0.6D) \tag{10}$$

The specific attenuation in dB/km is computed using the equation below.

$$Att = \frac{0.01}{ln(10)}\int_0^{D_{max}} \sigma_e N(D) dD \tag{11}$$

The refelctivity, specific attenuation and rainfall rates are computed considering varying drop size distributions. The scatterplot of reflectivity and rainfall rate simulated values and the scatterplot of attenuation and rainfall rate simulated values simulations at 77 GHz are shown in Figure 3.8. The red line shows the power-law fit to get the parameters of the relationship.

From the power-law fits of the scatter plots, the A and B values for rain rate and reflectivity relationships for simulations using computations of Maetzler toolbox are provided in Table 3.1. The C and D values for rain rate and attenuation relationships for simulations with computations from Maetzler toolbox are provided in Table 3.2.

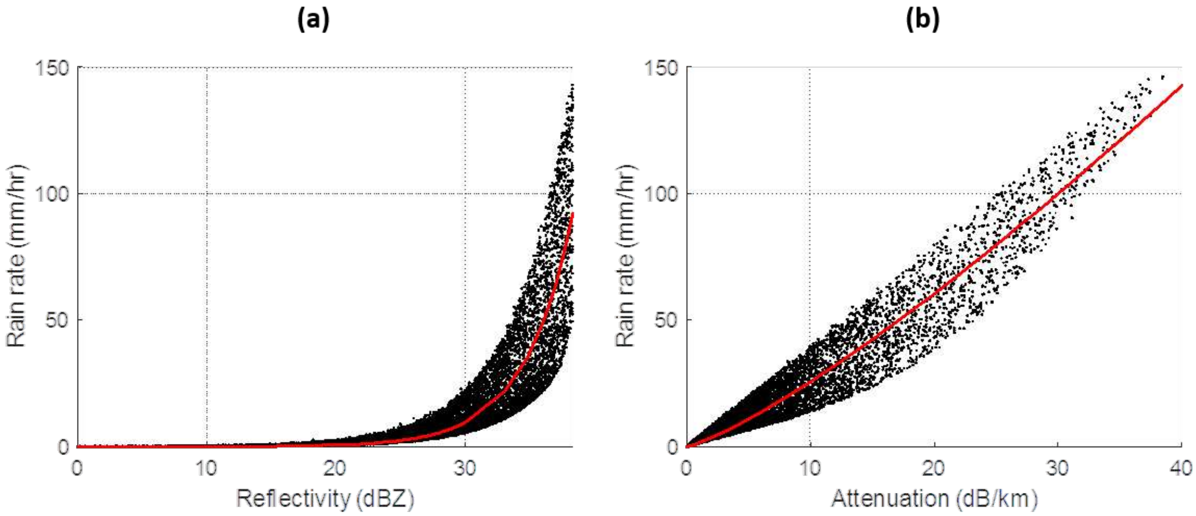

FIGURE 3.8. (a) Scatterplot of reflectivity versus rain rate from signal simulations using Maetzler toolbox at 77 GHz. (b) Scatterplot of attenuation versus rain rate from signal simulations using Maetzler toolbox at 77 GHz. The red line indicates the power-law fit in all the plots.

.

TABLE 3.1. The relationships obtained from simulations at various frequencies for $Z = A(RR)^B$.

Method	Frequency	A	B
T-matrix	10 GHz	687.9	1.39
T-matrix	24 GHz	856.8	1.19
T-matrix	77 GHz	61.8	0.736
Maetzler toolbox	77 GHz	239	0.69

TABLE 3.2. The relationships obtained from simulations at various frequencies for $Att = C(RR)^D$.

Method	Frequency	C	D
T-matrix	10 GHz	0.015	1.147
T-matrix	24 GHz	0.118	1.069
T-matrix	77 GHz	0.729	0.836
Maetzler toolbox	77 GHz	0.718	0.803

3.4. Time-series simulation study

Automobile radars have the potential to be deployed for meteorological purposes. In the previous sections of this chapter, the science aspect of the automobile radars was discussed. The technology of the current automobile radars is briefly introduced in the following sections. The technology of automobile radars has been progressing rapidly in the last decade. With more funding resources directed to the automobile industry for making fully autonomous vehicles, the progress in the automotive radar is looking at an upward trend in the short future. Also, there is active research in the electronic manufacturing companies for accommodating the automotive sensors on a very small-sized chip.

Simulation of radar signals plays a crucial role in radar signal analysis and system design. The simulations of radar signals aid in the testing and comparison of different algorithms or processing techniques in a radar system. Current radar systems have the features of Doppler and polarimetric capabilities. The simulations must account for both these factors to get accurate radar signals. In the current and next section, we will explore the simulation of precipitation echoes from a pulsed Doppler radar, specifically for rain hydrometeors for meteorological applications.

The radar systems having coherent detection techniques are usually based on the use of a couple of phase-sensitive detectors in the horizontal and vertical channels, which provide the in-phase (I) and quadrature (Q) components of the precipitation echo. The IQ data corresponds to the real and imaginary parts of the complex envelope of the received precipitation signal. The radar received signal is a complex voltage signal represented as $V = I + jQ$. An IQ data simulation code will generate the in-phase and quadrature components of the received voltage signal in horizontal polarization and vertical polarization modes. The IQ data samples are obtained at regular intervals of time which depends on the PRT of the radar; the IQ data is also commonly called timeseries data.

Previously, many timeseries simulation programs have been developed which were based on the properties of the precipitation echoes. Some of the earlier methods simulate IQ data with correct marginal and joint densities [26]. The primary assumption for the simulation method is that the precipitation echo is assumed to be a stationary Gaussian process. The precipitation signal can be completely characterized by its covariance matrix and it is sufficient to correctly simulate the autocovariance and mutual covariance between the H and the V channels. At the CSU radar group, a frequency domain algorithm based on statistical properties for the generation of dual-polarized timeseries signal was developed previously and is still used currently. Other methods that use the fast convolution generator were also proposed by [26] [27]. In this research, a timeseries simulation program that accounts for each individual hydrometeor particle in the radar resolution volume is developed. The simulation code accounts for the total volume of the backscatters and the Doppler shift of the particles with time. More details of the timeseries simulation program are described in the next section.

3.5. Method of simulating timeseries using direct volume of particle backscattering method

In the direct volume of particles backscattering method, the timeseries simulation uses the time domain algorithm to generate dual-polarized echoes. Here the primary motivation is to generate the time series corresponding to a specified correlation structure of the precipitation particles. Once a pulse of width τ_p is sent through the atmosphere or precipitation medium, the echo signal is a result of scattering from a large collection of hydrometeors packed in a close volume, known as the radar resolution volume. The radar range resolution, the distance between the start and end of the radar resolution volume, is given as $\frac{c\tau_p}{2}$. The radar resolution volume is defined as in Equation 12.

$$Volume = \frac{R\theta\phi}{8} \tag{12}$$

Where R is the distance to the radar resolution volume θ and ϕ are the beamwidths corresponding to the antenna. The radar resolution volume increases as we go further away from the radar due to the radar beam broadening. The beamwidth of the antenna used for the simulation influences the radar resolution volume considered for the signal simulation.

The received signal, $U_{tr}(t)$, at the radar due to a point scatterer moving at a constant speed is the replica of the transmit waveform scaled to a very small value. This signal will be shifted in time which will correspond to the range-time delay (t_0) and is shifted in frequency which is corresponding to the Doppler shift. The received voltage of this single moving particle is given as.

$$V_r(t) = Ae^{-j2\pi f_0 \tau} U_{tr}(t - \tau) \tag{13}$$

Where A is the scattering amplitude, f_0 is the center frequency and τ is the time delay. In general, precipitation is composed of a large number of hydrometeors extending over a large range with widely different scattering amplitudes moving with different velocities. Now consider the received voltage is obtained due to the scattering of the precipitation particles within a radar resolution volume extending from r to $r + \delta r$ as shown in Figure 3.9. The

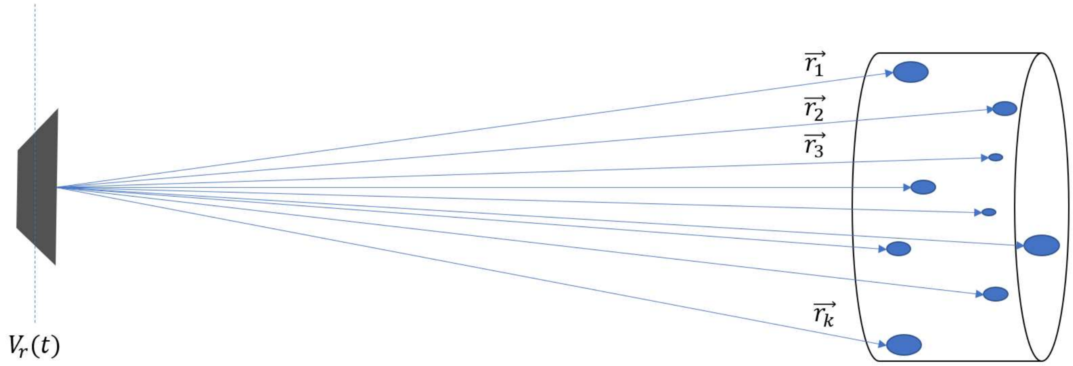

FIGURE 3.9. Random collection of the precipitation particles in the radar resolution volume whose instantaneius locations are described by the set of vectors r_k relative to the radar.

.

received voltage can now be expressed as a discrete sum of the contribution from individual particles in the medium and is given as

$$V_r(t) = \sum_k A_k(\tau_k; t)e^{-j2\pi f_0 \tau_k} U_{tr}(t - \tau_k) \tag{14}$$

Where A_k is the scattering amplitude of the kth particle and $\tau_k = 2r_k/c$.Figure 3.10 illustrates another way of understanding the received voltage at the radar receiver by considering the complex plane consisting of the instantaneous phasors of the scattering particles. Equation 14 represents the received voltage at any instant of time is the instantaneous sum of the elemental phasors. The phase angle θ_k is uniformly distributed in the interval $(-\pi, \pi)$. The resultant phasor has the components I + jQ.

The hydrometeor particles in the radar resolution volume will be scattered following a distribution model. This distribution of particles is known as particle size distribution

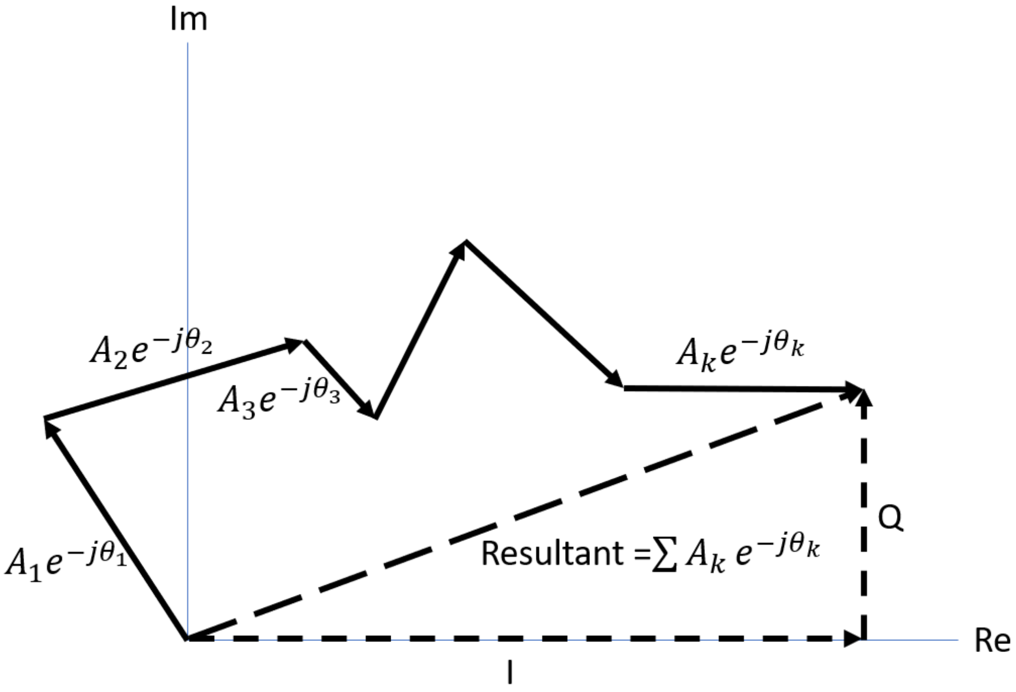

FIGURE 3.10. Complex plane plot of the instantaneous sum of the elemental phasors.

.

(PSD). The PSD within the radar resolution volume should be considered for the correct simulation of the timeseries signals. The distribution for rain hydrometeors is known as drop size distribution (DSD). The DSD varies based on many factors of the weather event, such as the type of the storm and the climatological conditions. The DSD gives us information such as the number of raindrops and mean drop diameter within the radar range resolution cell. There are various DSD defined in the literature, such as the exponential model, the gamma model and the lognormal distribution model.

A DSD model usually contains a few free parameters that should be easy to determine and the model should be capable of capturing the main physical processes and properties [28]. The exponential distribution is the most commonly used distribution model for rain hydrometeors and has two free parameters. Equation 15 defines the exponential distribution model.

$$N(D) = N_0 exp[-3.67\frac{D}{D_0}] \tag{15}$$

Where D_0 is the mean volume diameter in mm and N_0 is the number concentration in $mm^{-1}m^{-3}$. This distribution has only two varying parameters and can be estimated using the radar variables. Ulbrich suggested using the Gamma distribution to represent raindrop spectra as the gamma DSD has a broader variation than the exponential DSD. Equation 16 defines the gamma distribution model.

$$N(D) = N_0 D^{\mu} exp[(-3.67 + \mu)\frac{D}{D_0}] \tag{16}$$

Where μ is the shape parameter of the model. When $\mu = 0$, the DSD is an exponential distribution, this is a special case of the gamma DSD. Estimation of the parameters in the distribution models is carried out using remote sensing data such as disdrometer data and weather radar data. The parameters vary for different climatological conditions and prior works in the literature can be found regarding parameter estimation.

A histogram of the exponential drop size distribution of the rain particles in the radar resolution volume is shown in Figure 3.11. In this figure, the data was generated considering 5000 rain particles in the resolution volume. The minimum size of the drop diameter was 0.1 mm and the maximum drop size was 8 mm. This figure also shows that most of the raindrops are concentrated in the lower diameters below 2 mm.

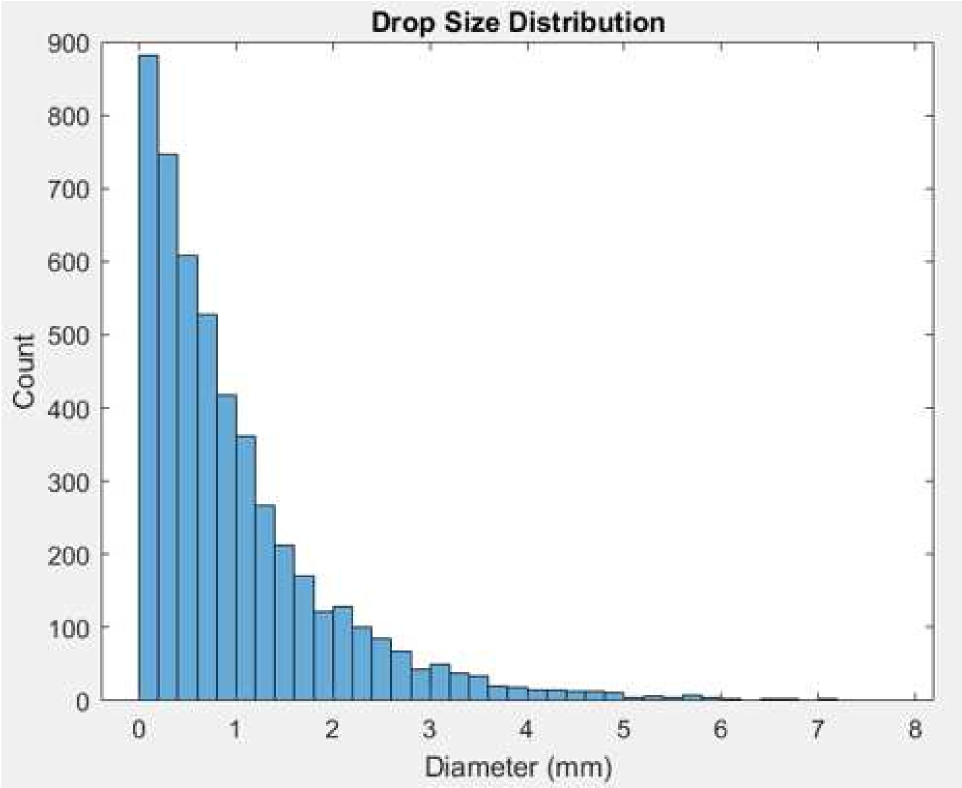

FIGURE 3.11. The exponential DSD considering 5000 rain particles in the radar resolution volume

.

The cross section σ of a scatterer (e.g., hydrometeor) is an apparent area that intercepts a power which, if radiated (i.e., scattered) isotropically, produces at the receiver a power density. The backscattering cross-section of the precipitation particles has to be considered correctly to get accurate simulation output. The backscattering cross section depends on the frequency at which the simulation is carried out. At lower frequency bands, the scattering will fall in the Rayleigh scattering region; this is when particle size is much smaller than the wavelength. As the frequency increases, the wavelength decreases, which will make the scattering shift to the Mie scattering region. We previously saw the dependency of Rayleigh and Mie scattering earlier in this chapter.

The backscattering cross section in the Rayleigh region can be computed directly using Equation 17.

$$\sigma_b = \frac{\pi^5}{\lambda^4}|K_m^2|D^6 \tag{17}$$

where K_m is given as

$$K_m = \frac{m^2-1}{m^2+2} \tag{18}$$

Where m is the complex refractive index, for raindrops the value of $|K_w^2|$ is considered as 0.93. This value is well defined in prior literature [29]. This equation holds good up to the Ku band frequencies. At the millimeter wave frequency band, we have to account for radar scattering due to Mie scattering.

For computing the radar backscattering cross section at Mie scattering, the Maetzler MATLAB toolbox is used. In this toolbox, functions have been developed to compute propagation parameters for freezing rain and melting graupel, assuming Marshall-Palmer drop-size distribution, including functions to compute the complex dielectric permittivities of ice and water. Mie Theory is based on the formulation of Bohren and Huffman (1983), in short, BH. A full detailed description of the computation of the scattering coefficients at the Mie band can be found in [25].

The backscattering efficiency Q_b for the interaction of radiation with a sphere of radius r is the backscattering cross section σ_b (called C_b BH) normalized to the geometrical particle cross-section as provided below:

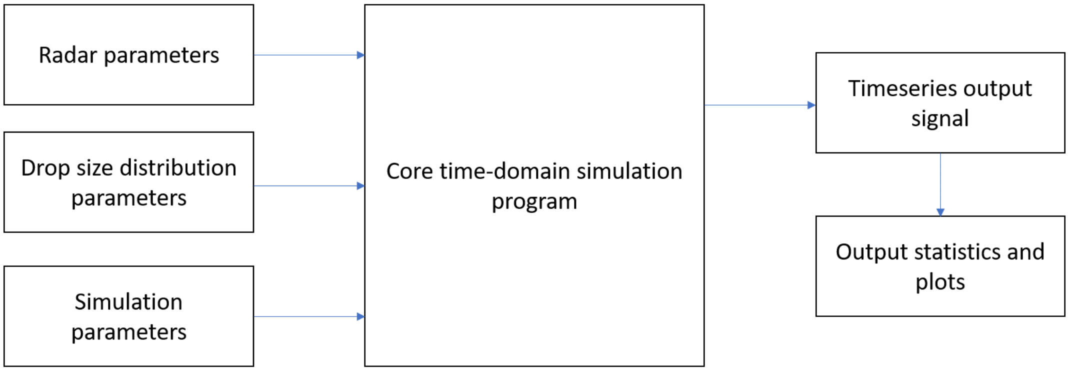

Figure 3.12. Block diagram of the simulation program.

.

$$Q_b = \frac{\sigma_b}{\pi r^2} \tag{19}$$

The backscattering cross section is obtained from the backscattering efficiency depending on the diameter of the rain particle and then used in the simulation program. A look-up table (LUT) is created for various drop diameters and the backscattering coefficient at the frequency band in which simulation is carried out. This LUT is then used to determine backscattering cross-section values.

The various radar parameters such as the frequency of the radar signal, pulse repetition time (PRT), sampling frequency, range resolution and pulse width are given as the input for the simulation program. The various antenna parameters such as beamwidth and antenna size were considered for the signal simulations. Along with these parameters, there are various other simulation parameters such as the number of pulses and start range is also specified.

Table 3.3. Radar parameters considered for the simulation.

Parameter	Value
Pulse repetition frequency	10 KHz
Pulse width	10 ns
Range resolution	3 m
Antenna aperture	0.1 m
Antenna beamwidth	0.1 degrees
Number of pulses	50000
Sampling frequency	200 MHz

The characteristics of the rain particles distributed in the radar resolution volume, such as the mean velocity and spectral width, are also specified for the simulations. We can change the characteristics of the precipitation particles to mimic a real weather event by changing the values of mean velocity and spectral width.

Figure 3.12 shows the overall simulation procedure as a block diagram. The simulation procedure is coded in the MATLAB software. The radar parameters, drop size distribution parameters and simulation parameters are given as input for the core time-domain simulation program. In the core signal simulation program, there are mainly two loops that handle the signal generation: One of the loops iterates over each radar pulse, while the other loop iterates over each particle in the radar resolution volume constructing the received radar signal. The position and velocity of all the particles are initialized before the loop process and the position of each and every drop is updated after each pulse based on the velocity distribution of the particles. This way, the signal simulation considers each individual hydrometeor particle in the radar resolution volume. The time series output is then provided to the output signal averaging, signal statistics and plotting modules for further analysis.

A radar signal simulation at 77 GHz was carried out. The various simulation parameters for the radar signal simulation are specified in Table 3.3.

The noise signal was not considered for the timeseries I and Q data that was generated. The statistics of the I and Q data generated are shown in Figure 3.13. From this figure, it can be seen that the histograms of both I and Q data follow a Gaussian (bell-shaped) distribution centered around zero. The scatterplot of I and Q data is concentrated around the zero value and the histogram of $I^2 + Q^2$ has an exponential distribution. These figures are as expected and can be validated with the literature [29].

The magnitude spectrum of the same data is shown in Figure 3.14. From this figure, it can be seen that the data is centered around the mean velocity of 0 m/s and has a Gaussian distribution. Since we use 50000 pulses for the simulation, we have more number of data points in the magnitude spectrum.

The mean power of the received radar signal is computed by taking the average of all the pulses in the radar resolution volume. The greater the number of pulses, the better the signal quality as the signal to noise ratio increases. There are trade-offs between using more pulses and signal correlation. However, we will not discuss them in this dissertation.

3.6. Current technology of automobile radars

There are various automobile radars available in the market. Usually, the whole assembly of the millimeter wave frequency band radars is accommodated on a single printed circuit board.Having the whole radar system on a single PCB ranging a few centimeters makes deploying in systems with space constraints feasible. This section discusses some of the current automobile radar boards available on the market. A brief discussion on the specifications of the board is also given. Two radar boards from Texas Instruments (TI) and Analog Devices (AD) are introduced. The radar board from TI is studied in detail. Both these boards have been currently used for research and applications in real-time. Other companies are

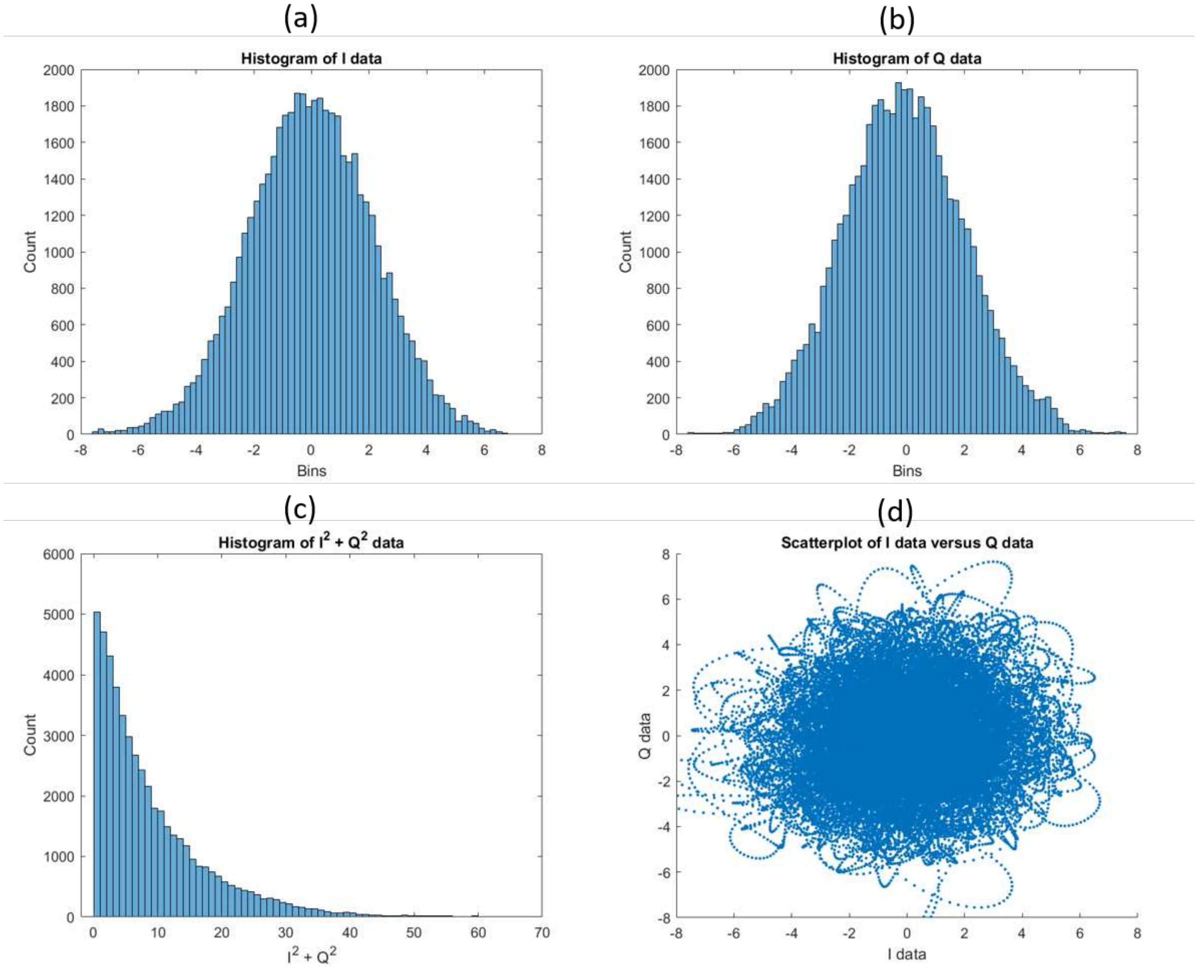

FIGURE 3.13. Statistics of the simulated timeseries IQ data. (a) Histogram of I data, (b) Histogram of Q data, (c) Histogram of $I^2 + Q^2$ and (d) Scatterplot of I and Q data.

.

also actively researching automobile radars, including many small-scale startup companies. However, those are not discussed here due to space constraints.

The analog devices have a radar system on a single board called the Eval-TINYRAD. This radar evaluation system operates in the 24 GHz to 24.25 GHz frequency range and has the capability of multiple input multiple outputs (MIMO) for transmission and reception. The 3dB beamwidth of the system is specified as 75° in azimuth and 15° in elevation. Also, the azimuth resolution using MIMO angle estimation is 20 degrees. The whole system is

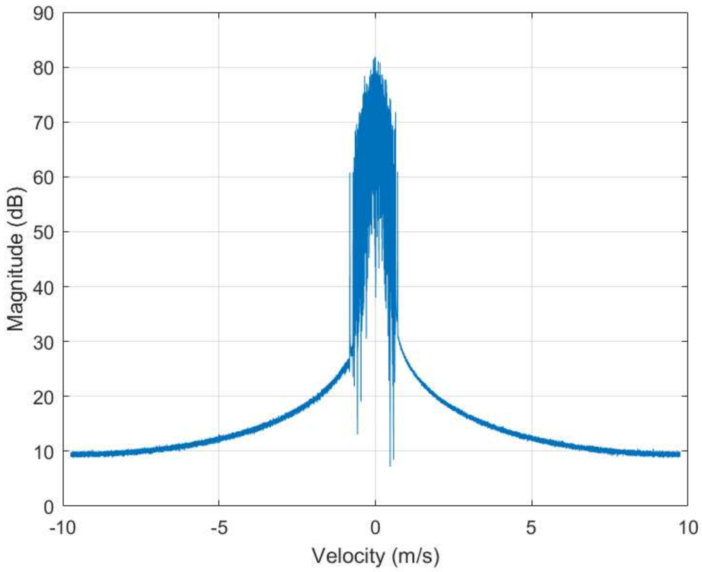

FIGURE 3.14. Magnitude spectrum of the simulated timeseries signal.

.

assembled on a PCB with dimensions of 85 mm × 55 mm. There are two front-side transmit antennas and four front-side receive antennas. More details can be found in [30].

Texas Instruments (TI) have a single chip automobile radar sensor that operates at the millimeter frequency bands. The TI automobile sensor, AWR 1642, is a single chip automotive radar sensor that integrates the digital signal processing (DSP) and microcontroller unit (MCU). The sensor has the capability to operate in the frequency ranges of 76 GHz to 81 GHz. The device is built with TI's low-power 45-nm RFCMOS process and enables unprecedented levels of integration in an extremely small form factor. The AWR1642 is an ideal solution for low-power, self-monitored, ultra-accurate radar systems in the automotive space. This radar chip operates on the FMCW technology and has built-in calibration and self-test technology.

The block diagram of using this sensor for automotive applications is shown in Figure 3.15. With the integration of power management, antenna elements, oscillator, flash memory

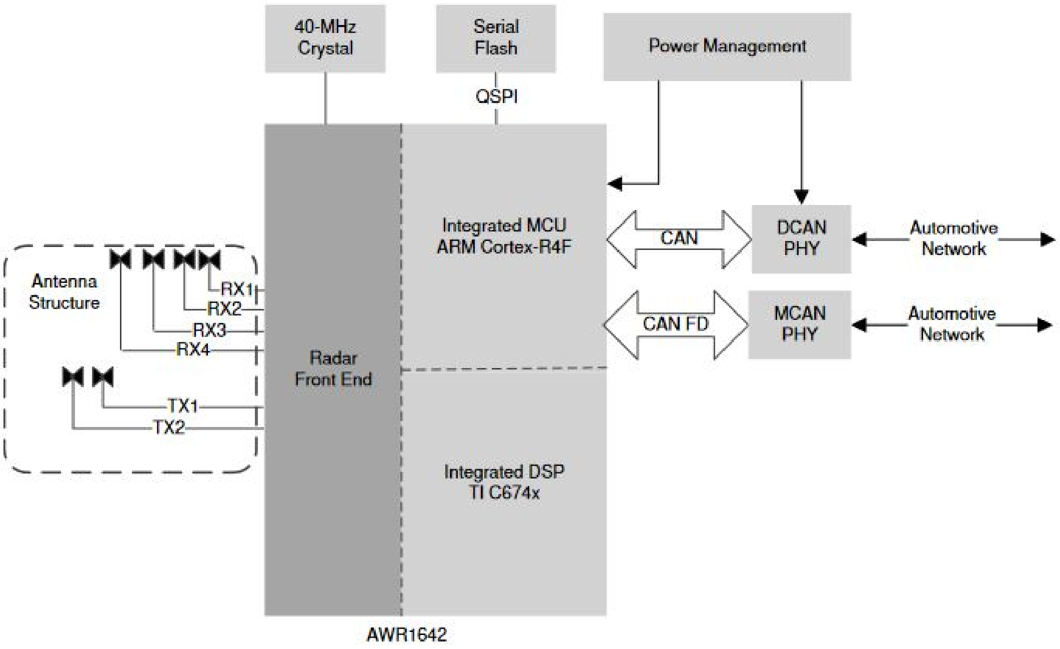

Figure 3.15. TI AWR1642 automobile radar block diagram [4].

and control signals, a fully functional automobile radar unit can be deployed. This automobile radar sensor is integrated with various other interfacing units and it is already being studied using an evaluation module [4]. This evaluation module has all the capabilities to test the automobile radar unit. An external board can be used to acquire the raw radar signals directly from the signal processing unit. A picture of the evaluation module which uses the AWR 1642 is shown in Figure 3.16.

3.7. PRECIPITATION MEASUREMENT EXPERIMENT AND RESULTS

In this section, the millimeter wave automobile radar from TI is used to observe precipitation. The TI AWR1642 boost evaluation module is used for the experiments. The capability of this evaluation module for mapping the rain rate is discussed. Mapping precipitation using the automobile radar is similar to obtaining precipitation information from a precipitation gauge. The range of the automobile radars is in the order of a few tenths

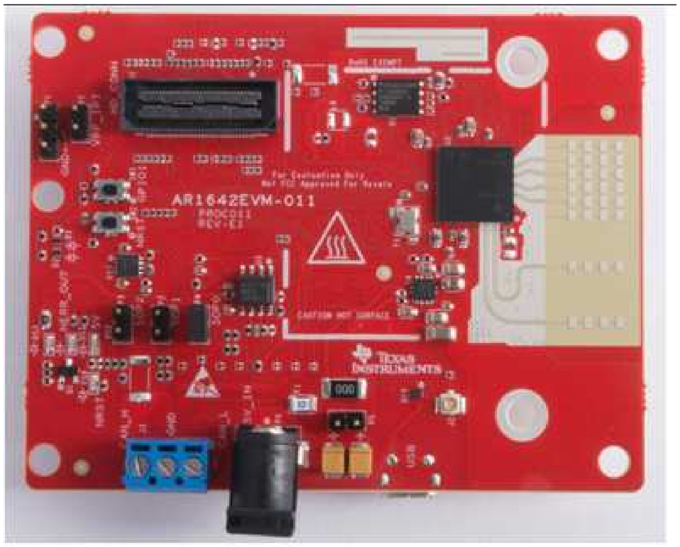

FIGURE 3.16. TI AWR1642 evaluation module [4].

.

of meters to a couple of hundred meters. The precipitation intensity does not vary significantly in such a short range and can be considered constant. With this information that the precipitation values are the same in the observation region of automobile radars, the attenuation encountered by the signal can be measured and the rainfall rates can be derived as explained earlier in this chapter.

TABLE 3.4. Parameters of the TI AWR1642 radar evaluation module.

Parameter	Value
Frequency	77-81 GHz (W band)
Configuration	4 Rx, 2 Tx
Beamwidth	15 degrees
Range resolution	0.4 meters
Max range	50 metres

Next, the operational setup and configuration for the automotive radar to work as a rain gauge is explained. The various parameters of the TI AWR1642 radar evaluation module are given in Table 3.4. From this table, it can be seen that the radar frequency spans from 77-81 GHz and the beamwidth of the antenna elements is about 15 degrees. A suitable power

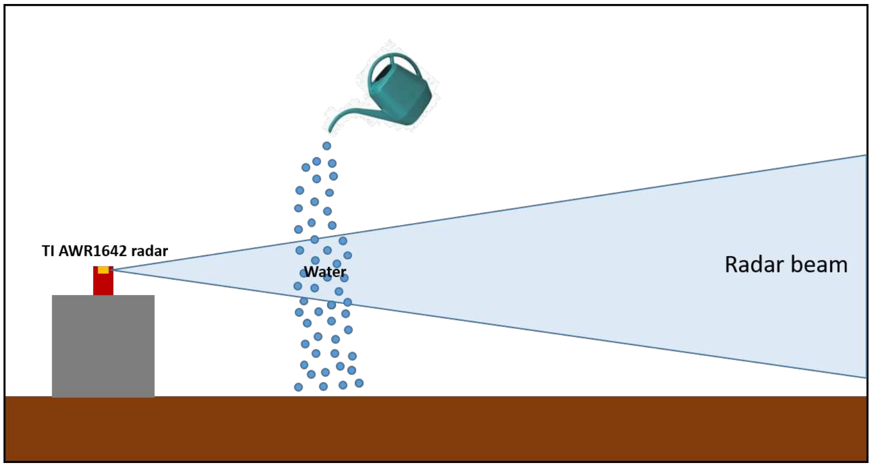

Figure 3.17. Graphical illustration of the experiment setup for checking the evaluation module to observe water droplets.

.

source supplies the power to the evaluation module, and a personal computer that runs the mmWave studio software interfaces with the module

The TI mmWave studio software is a code package with a collection of tools that enhances the evaluation of TI mmWave sensors. These easy-to-use tools provide the capability to experiment with the TI evaluation module on hand. The tools are hosted directly on TI.com. This can be accessed anywhere with the help of a stable internet connection and enable interaction with mmWave sensor evaluation modules. This software is a stand-alone Windows GUI that provides the ability to configure and control mmWave sensor modules. The software is also used for the collection of analog-to-digital (ADC) data for offline analysis. The software also provides basic post-processing and visualization of ADC data. Various parameters required for the operation of the evaluation module can be selected from the dropdown menu in the GUI, which makes it easy to set up and operate the evaluation modules.

To test the sensitivity of the TI automobile radar module for detecting and measuring water particles, an experiment involving artificially putting the water particles in the radar resolution volume was carried out. For this experiment, a garden watering can is used to drop

FIGURE 3.18. (a) scene of observation and (b) Snapshot of water being poured in front of the automobile radar evaluation board.

.

water in the range of the radar and the observed data is stored on the personal computer and analyzed offline. The setup of this experiment is shown in Figure 3.17. The scene of the experiment location and the water being poured using the water can in front of the radar is shown in Figure 3.18.

The expected result from this experiment is when we have water drops in the radar resolution volume. The received power should give a large value corresponding to the targets. The radar scans were first run in a static environment and the noise profile was recorded. Then the water was poured in front of the radar at a distance of 1 meter and the data was recorded. Ten seconds of data was recorded for both cases. The data was analyzed and the output plots obtained are shown in figure 3.19. In this figure, the recorded noise profile is shown in orange, and the data collected when water is present in the resolution volume is plotted in blue. It can be clearly seen from this picture that when water was present in the

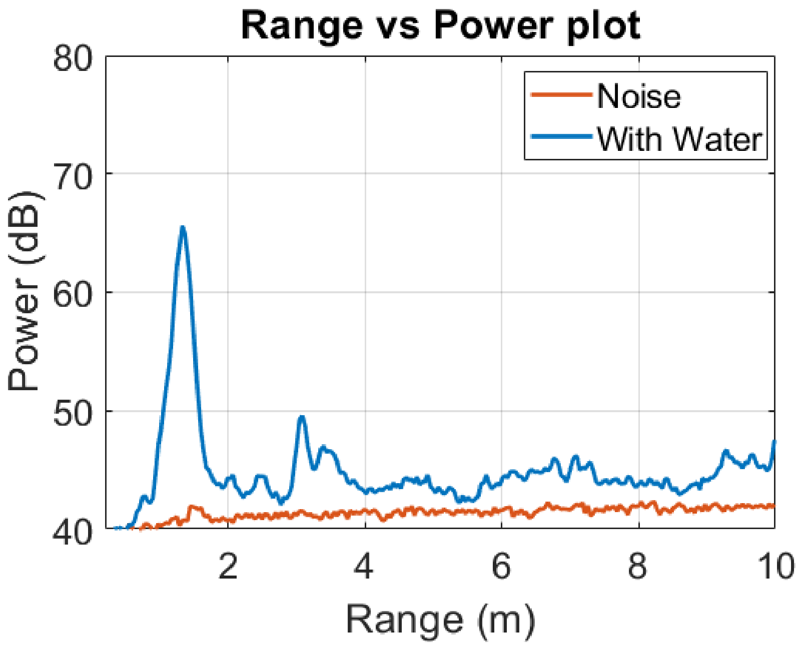

FIGURE 3.19. Results of the experiment where water is poured in front of the automobile radar evaluation board.

.

radar resolution volume, we see a spike in the received power. This corresponds close to 1m in the range where the water was poured. From this experiment, we can conclude that the water articles in the resolution volume can be observed with the automobile radar evaluation board.

Next, the radar evaluation board was installed in front of a car to collect precipitation data. The power supply module for the evaluation board was replaced with a similar module that converts the 12 V output from the car electric port to the 5V, which is required by the evaluation board. The setup of the automobile valuation board for this experiment is graphically illustrated in Figure 3.20.

The experiment data was collected at the Colorado State University (CSU) main campus in one of the parking lots. A very intense storm was passing over the CSU campus on the 15th of July 2022, around 23:00 UTC. The radar evaluation module was set up to collect

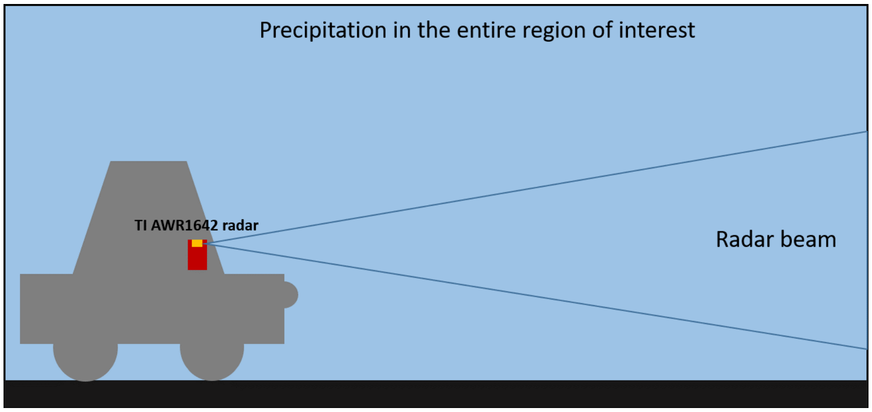

FIGURE 3.20. Graphical illustration of the experiment setup for precipitation measurement, the radar is placed in front side of the automobile.

.

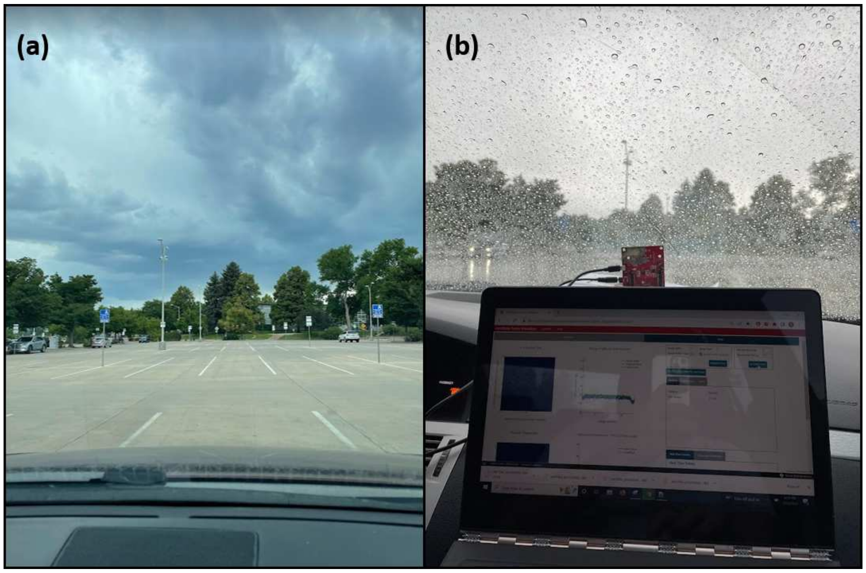

FIGURE 3.21. (a) Scene of observation and (b) Setup of automobile radar evaluation module inside the car.

.

precipitation data from the storm. The scene of precipitation observation and the automobile radar evaluation module connected inside the car is shown in Figure 3.21.

The noise profile for the scene under observation was collected around 22:00 UTC when there was no precipitation event and the precipitation data were collected around 23:00 UTC. Figure 3.22 shows the noise and precipitation data in front of the car. We can clearly see the precipitation data being observed by the evaluation module. It should be noted that the

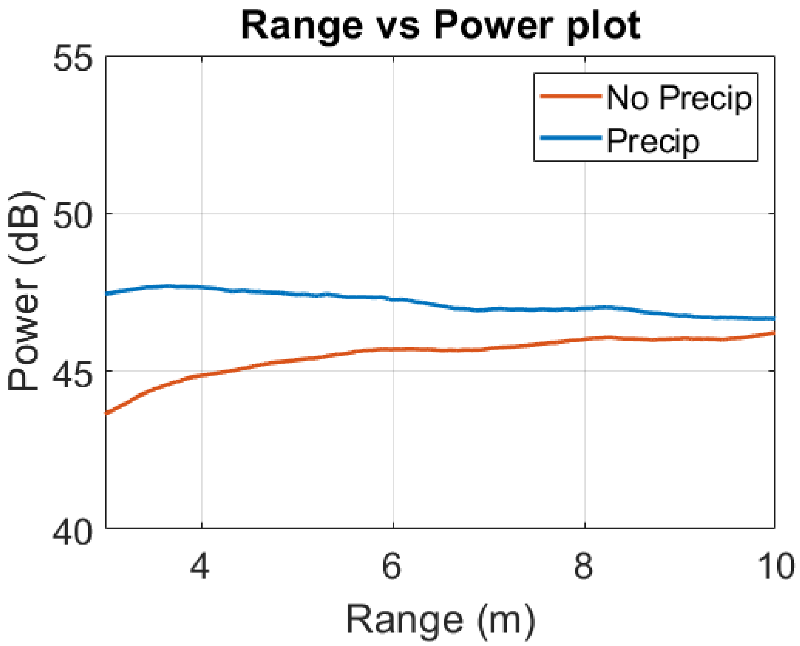

FIGURE 3.22. Results of using automobile radar evaluation board for observing precipitation.

raw radar data obtained from the evaluation board is extracted using a python code package and plotted. Also, a moving window filter is used for smoothing the radar data along the range.

As the radar signal propagates in the range, the data is collected corresponding to the resolution volumes. As the radar signal propagates through the precipitation medium, the radar signal attenuates. Accounting for the two way attenuation encountered by the radar signals, the information on the signal attenuation is used to estimate the rain rate in this experiment. Figure 3.23 shows the data recorded during precipitation. From this figure, it can be seen that the received power peaked at 47.56 dB at 3.5 meters in range and is reducing along the range. The received power reached a value of 46.1 dB at 32 meters. Considering the precipitation in the observed volume does not vary much and the corresponding precipitation rate is constant, the difference in the received power and accounting for two way attenuation will yield the amount of signal attenuation. The difference value of the received power is

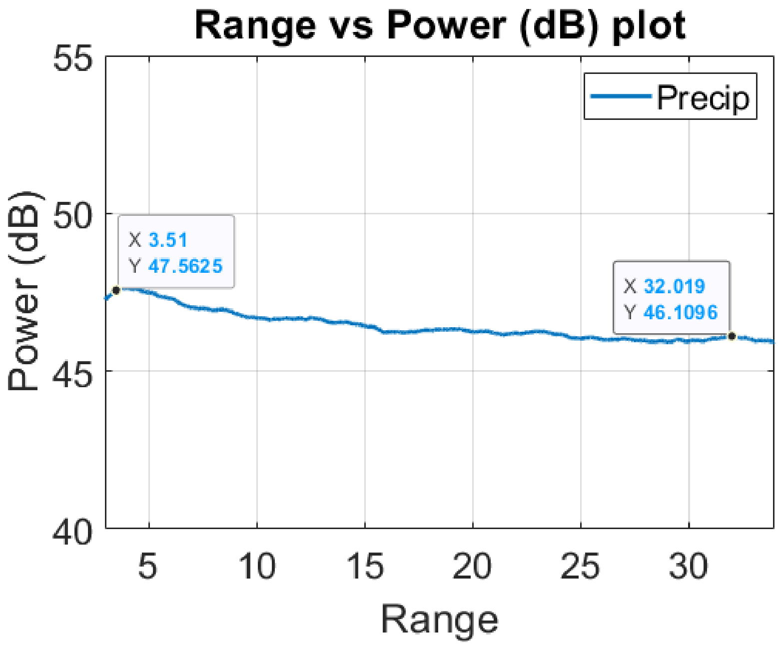

Figure 3.23. Difference in power level long the range from the data collected using automobile radar evaluation board observing precipitation.

.

1.46 dB within 28.5 meters. This corresponds to signal attenuation of 25.5 dB/km due to the rain particles.

A high attenuation value of 25.5 dB/km is obtained from the data collected. Using the Equation 7 and the coefficients obtained using the T-matrix method, we get a rain rate value of 72 mm/hr. Using the Equation 7 and the coefficients obtained using the Maetzler toolbox, we get a rain rate value of 84 mm/hr. The relationship between attenuation and rain rate at 77 GHZ given by the International Telecommunications Union (ITU), a specific attenuation model for rain for use in prediction methods, is shown Equation 20. Using equation 20 the rain rate obtained corresponding to 20.5 dB/km attenuation is 78 mm/hr.

$$Att = 1.132(RR)^{0.7177} \tag{20}$$

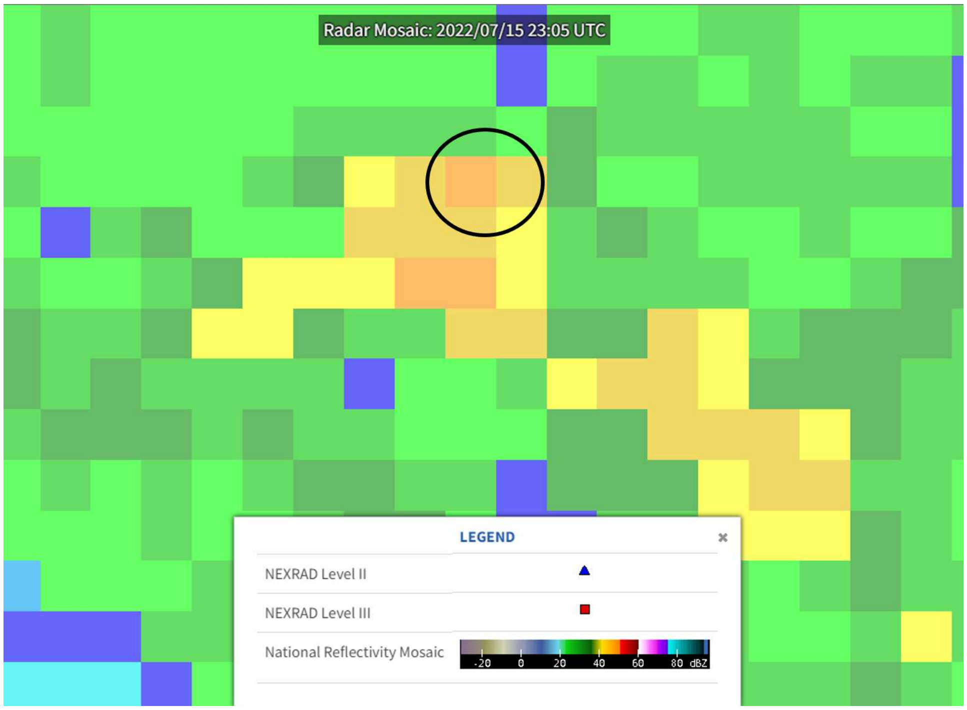

FIGURE 3.24. Screenshot of the National Weather Service (NWS) reflectivity mosaic over the CSU campus. The region in the black circle is where the data was collected.

.

To validate the estimated rain rate, the National Weather Service (NWS) reflectivity mosaic constructed using the NWS S-band weather radar network is considered. The reflectivity mosaic over the CSU campus at 22:03 UTC on the July 15, 2022 is shown in Figure 3.24. The reflectivity value is approximately 52 dB in the region where the experiment was conducted. There are various equations in the literature that are used to compute reflectivity using the rain rate value. Table 3.5 shows three different equations that are used to compute the reflectivity values from the three rain rate values derived earlier. From this table, comparing to the reflectivity value obtained from the reflectivity mosaic, it can be seen that the automobile radar evaluation board can be used to estimate the rain rates. The concept of using a network of automobile radar for mapping precipitation on a regional scale is explained in chapter 6.

Table 3.5. Computing reflectivity from rain rate values obtained.

Relationship	Z corresponding to 72 mm/hr rain rate	Z corresponding to 84 mm/hr rain rate	Z corresponding to 78 mm/hr rain rate
NWS WSR-88D ($Z = 300R^{1.4}$)	50.8 dBZ	51.7 dBZ	51.3 dBZ
Marshall-Palmer ($Z = 200R^{1.6}$)	52.7 dBZ	53.8 dBZ	53.3 dBZ
Rosenfeld Tropical ($Z = 250R^{1.2}$)	46.3 dBZ	47.1 dBZ	46.7 dBZ

CHAPTER 4

PRECIPITATION MAPPING AT REGIONAL SCALE

Precipitation maps at a regional scale have various advantages compared to point measurement instruments. At a regional scale, we can get precipitation information over a large span of area. The climate varies from region to region around the Earth, and the precipitation maps obtained at the regional level are useful for climate studies of that particular region. We need remote sensing instruments that have the capability to observe over large distances to obtain precipitation maps.

Weather radars and meteorological satellites fall under the category of volume measurement instruments. The volume measurement instruments can acquire data over a large area and are useful in tracking the progress of the precipitation event. Weather radars have many advantages. They can provide data over a large area and the time resolution of data obtained is considered good. In addition to the precipitation rate, weather radars can be used for obtaining derived products such as precipitation particle type. More details of weather radars are provided in this chapter. In this research work, the precipitation maps obtained using weather radars are discussed. The meteorological satellites give precipitation information on a global scale and are explained in detail in chapter 7.

4.1. WEATHER RADARS FOR REMOTE SENSING OF ATMOSPHERE

Among the remote sensing instruments, RAdio Detection And Ranging (RADAR) is one of the key instruments. Radars are often preferred in the remote sensing domain due to their spatial and temporal resolution. The research and invention of radar date back to the period of world war II. Since then, with the help of continuous research in the radar field, radars can now detect the target's position, velocity, size and even shape. The applications of radars have found uses in multiple areas such as aviation, object tracking, military, remote sensing and automobiles.

The radar system consists of many complex subsystems such as the transmitter, receiver and antenna. All the subsystems are carefully designed and operated to achieve maximum efficiency. The fundamental concept of radar is to transmit electromagnetic waves in the propagation medium and then extract information from the received electromagnetic wave, which is reflected back from the target. After the electromagnetic wave is transmitted, once it hits the target, the signal is scattered isotropically from the target and a part of the signal travels back towards the radar. The intensity of the received signal, which is also known as the backscattered signal, varies on many factors, such as the transmitted signal power and target properties. Also, the medium in which the electromagnetic wave travels has a direct impact on the strength of the signal received at the radar. Once the signal is received, signal processing methods are applied to extract the desired information. This system described above corresponds to a single polarization radar. In the initial days of radar technology, this simple concept was used to detect the position and intensity of the target. Next, the Doppler technology was introduced in radars which opened doors for single polarization Doppler radars. These radars could measure the velocity of the target along with its position and intensity, the frequency change in the received radar signal was used to determine the velocity. The pulsed radar concept, which sends pulses of electromagnetic energy instead of continuous transmission was the next big step in radar technology. The characteristics of the pulses can be varied to improve the quality of the signal.

Dual-polarization radars in which two polarizations (horizontal and vertical) of signals are transmitted instead of one have various advantages. This also came with additional complexity for the radar system. With the advancement of technology, dual-polarization

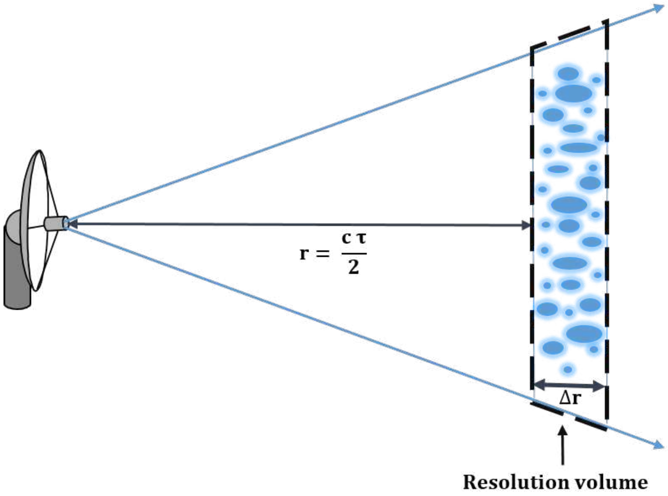

FIGURE 4.1. The radar resolution volume ranging from (r, r+Δr), the received voltage at the radar are due to scattering of particles located within this volume.

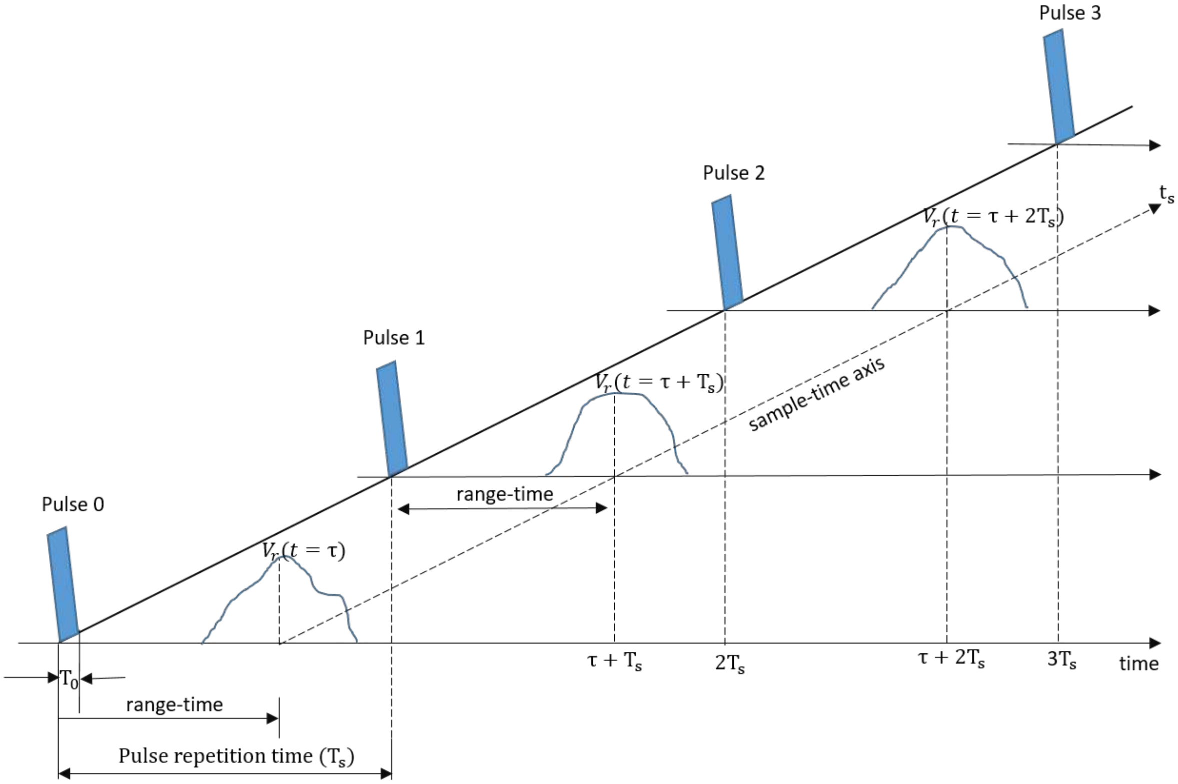

FIGURE 4.2. Illustration of range-time axis and sample-time axis for received radar signal (pulse repetition time of T_s).

radars became operational in the early 1990s. With the dual-polarization capability, it was possible to determine additional features of the target, such as orientation and shape.

The radars which are used to measure and characterize precipitation events are known as weather radars. Today, most weather radars are pulsed radars and have the capability of dual-polarization and Doppler. Weather radars work on the same principle as hard target radars, except that the target here is the precipitation volume. The target is not a single point; rather it is a collective distribution of particles over a volume. The volume at which the radar samples is the range resolution volume, which extends radially from r to r+δr and the received voltage $V_r(t)$ at $t = \tau$ is based on the scattering of particles located within the resolution volume as illustrated in Figure 4.1. Resolution volumes are typically spaced $cT_0/2$ apart, where T_0 is the pulse width [29]. The smaller the range resolution volume, the more information we get about the microphysical process happening in the precipitation event. Pulsed radar transmits a train of pulses at a time interval known as the pulse repetition time (PRT). These trains of pulses are sampled and are divided into range-time and sample-time. For a periodic pulsed train T_s apart, the range-time and sample-time is illustrated in Figure 4.2.

The range-time for a single pulse transmitted is given by $r = 2\tau/c$, and the received voltage $V_r(t)$ at $t = \tau$ is due to back scatter from particles located in the resolution volume at range-time τ. Here, for a periodic train of pulses, the received voltage at the same range-time is given as $V_r(t = \tau)$, $V_r(t = \tau + T_s)$, . . . , $V_r(t = \tau + nT_s)$ which forms a sequence of temporal samples from the same resolution volume. The received voltage value for a given range-time can be viewed as uniformly spaced samples along the sample-time axis t_s. From this we can define the received voltage as a two-dimensional function with respect to range-time and sample-time. Due to the time-varying properties of particles located in the resolution volume, which correspond to τ, we see fluctuations in the sample-time axis.

The signal received by the radar is a complex stochastic signal. For a stochastic signal, the power spectral density provides the decomposition of the signal power into various frequencies contained in the signal. A Gaussian-shaped power spectral density or the Doppler spectrum [29] is given as

$$S(\Omega) = \sum_{n=-\infty}^{\infty} R(n) e^{-j\Omega n} \tag{21}$$

The corresponding Doppler velocity spectrum is given by

$$S(v) = \frac{S_0}{\sigma_v \sqrt{2\pi}} exp[-\frac{(v-\hat{v})^2}{2\sigma_v^2}] \tag{22}$$

The auto-correlation coefficient for a reflectivity weighed velocity spectrum is given as

$$R(n) = |R(0)| e^{-j\frac{4\pi}{\lambda}\hat{v} n T_s} exp(-\frac{8\pi^2}{\lambda^2}\sigma_v^2 n^2 T_s^2) \tag{23}$$

where $\hat{v}$ is the mean Doppler velocity and σ_v is the Doppler spectral width.

Pulsed Doppler weather radars with polarization diversity can transmit and/or receive two orthogonal polarized signals. The transmission and reception of the signal in most pulsed radar systems are achieved through a single antenna. The intrinsic backscattering properties of particles in the resolution volume from the two polarization states enable the measurement of characteristics of the particles such as size, shape, spatial orientation and type. The backscattering covariance matrix is used to describe these characteristics and is given as

$$\Sigma_{BSA} =< \begin{bmatrix} |S_{hh}|^2 & \sqrt{2}S_{hh}S_{hv}^* & S_{hh}S_{vv}^* \\ \sqrt{2}S_{hv}S_{vv}^* & 2|S_{hv}|^2 & \sqrt{2}S_{hv}S_{vv}^* \\ S_{vv}S_{hh}^* & \sqrt{2}S_{vv}S_{hv}^* & |S_{hh}|^2 \end{bmatrix} > \tag{24}$$

Where S_{hh}, S_{hv}, S_{vh} and S_{vv} are the elements of the scattering matrix and angle brackets represent the ensemble averaging. The subscripts vh refers to "transmit horizontal polarization and receive vertical polarization" and vice versa. The $*$ denotes complex conjugate. Polarimetric variables are computed using the backscattering covariance matrix elements. Meteorological moments and polarimetric variables are estimated from the covariance matrix of the vector of received signals. The received signal **Z** and the corresponding covariance matrix **K** are given as follows:

$$\mathbf{Z} = \begin{bmatrix} V_{hh} & V_{hv} & V_{vh} & V_{vv} \end{bmatrix}^T \tag{25}$$

$$\mathbf{K} = E[\mathbf{Z}\mathbf{Z}^{\mathbf{H}}] = E \begin{bmatrix} |V_{hh}|^2 & V_{hh}V_{vh}^* & V_{hh}V_{hv}^* & V_{hh}V_{vv}^* \\ V_{vh}V_{hh}^* & |V_{vh}|^2 & V_{vh}V_{hv}^* & V_{vh}V_{vv}^* \\ V_{hv}V_{hh}^* & V_{hv}V_{vh}^* & |V_{hv}|^2 & V_{hv}V_{vv}^* \\ V_{vv}V_{hh}^* & V_{vv}V_{vh}^* & V_{vv}V_{hv}^* & |V_{vv}|^2 \end{bmatrix} \tag{26}$$

Where T indicates transpose and H is the Hermitian operator. The elements of **K** give us the estimates of Σ_{BSA} . The relationship between **K** and Σ_{BSA} is given by

$$\mathbf{K} = \frac{C\Sigma_{BSA}}{r_0^2} \tag{27}$$

Where C is the radar constant and r_0 is the radar range to the resolution matrix of measurement. The various radar moments are now calculated as explained below

(1) Equivalent reflectivity factor: The radar reflectivity (η) is the backscattering cross-section per unit volume. η is dependent on the number, shape, physical state and their aspect of the hydrometeor particles with respect to the radar. In radar meteorology, it is conventional to represent η in terms of the equivalent reflectivity factor (Z_e). Z_e is the product of the received power, radar constant and the range factor expressed in mm^6m^{-1} or dBZ in the decibel scale. The equivalent reflectivity factor in the decibel scale is given below:

$$Z = P(dBm) + C + 20logr \tag{28}$$

where $P(dBm)$ is the received power, C is the radar constant and r is the range. For a horizontally polarized received signal the received power is given by

$$P^h =< |V_{hh}|^2 > \tag{29}$$

(2) Differential reflectivity: The differential reflectivity (Zdr) gives information on the difference in received energy from the horizontal and vertical polarizations. Positive values of Zdr indicate the hydrometers are larger in the horizontal direction

compared to the vertical. In the decibel scale, Zdr is the difference between the horizontal and vertical received power as given below

$$Zdr = P^h(dB) - P^v(dB) \tag{30}$$

(3) Co-polar correlation: The behavior of the horizontal and vertical polarized pulses within the resolution volume is measured using the Co-polar correlation (ρ_{HV}). The values extend from 0 to 1, with higher values indicating similar behavior and lower values indicating dissimilar behavior. When the same type of hydrometeor particles are present in the radar resolution volume, the value of ρ_{HV} is very close to 1. The co-polar correlation is given as follows:

$$\rho_{HV} = \frac{| < V_{hh} V_{vv}^{*} > |}{\sqrt{P^h}\sqrt{P^v}} \tag{31}$$

(4) Differential phase shift: The phase shift between the horizontal and vertical signal as the signal propagates through the propagation medium gives the differential phase shift (ϕ_{dp}). The two-way attenuation of the radar signal is dependent on ϕ_{dp}. As the radar signal propagates through the propagation volume, it slows down, causing the phase to change. The phase of the complex correlation between the co-polar signals provides the differential phase as below

$$\phi_{dp} = arg[< V_{hh} V_{vv}^{*} >] \tag{32}$$

(5) Specific differential phase: The specific differential phase (K_{dp}) is a derived radar product that indicates the gradient of the differential phase shift.

$$K_{dp}(r) = \frac{1}{2}\frac{d\phi_{dp}(r)}{dr} \tag{33}$$

(6) Radial velocity: The radial velocity is the component of the wind velocity parallel to the direction of the radar beam, either toward or away from the radar. This gives information about the velocity of the precipitation particles. The relationship between the Doppler frequency shift (f_d), wavelength (λ), and radial velocity is given by

$$v_r = -\frac{\lambda f_d}{2} \tag{34}$$

The negative sign in the above equation indicates that the precipitation particles are moving towards the radar. The maximum Doppler shift that can be measured is dependent on the PRT and is given by

$$f_{max} = \frac{1}{2PRT} \tag{35}$$

(7) Spectral width: The spectral width (σ_w) gives information on the distribution of the velocities within a radar resolution volume. The spectral width is computed using the variance and provides information on the spread of the Doppler power spectrum.

(8) Hydrometeor classification: The information on the type of hydrometeor particle present in the radar resolution volume is obtained by hydrometeor classification (HID). The HID is a derived product and there are various algorithms that provide accurate identification of the particle types.

4.2. PRECIPITATION INFORMATION FROM WEATHER RADAR DATA

Weather radars are widely used for precipitation mapping at a regional scale. The operational range of a weather radar increases as the operating frequency of the radar increases [31]. The S-band radars weather radars usually have a very long observational range of around 250 km. An X-band radar deployed in urban regions will have an observation range of about 40 km. A network of radars is deployed to obtain precipitation information over a large area of interest. Some systems that use a network of remote sensing instruments for precipitation mapping are explained later in this chapter.

The National Weather Service (NWS) has more than 160 next-generation S-band weather radars (NEXRAD) deployed all over the continental US. Each radar in the network has an operational range of about 250-300 km. NEXRAD radars perform volume scans every five minutes, and the radar plan position indicator (PPI) plot at a certain elevation angle repeats approximately every five minutes. Precipitation information obtained from each radar is used for constructing the combined precipitation map for all the radars. Figure 4.3shows the reflectivity and rain rate of a NEXRAD S-band radar (KDAX) deployed in Sacramento, CA. In NEXRAD, the rain rate is estimated based on a simple relationship with the reflectivity obtained from the radar. The relationship used to obtain the rain rate is $Z = 300R^{0.4}$. Most NEXRAD radars use this relationship between radar reflectivity and rain rate. Figure 4.3

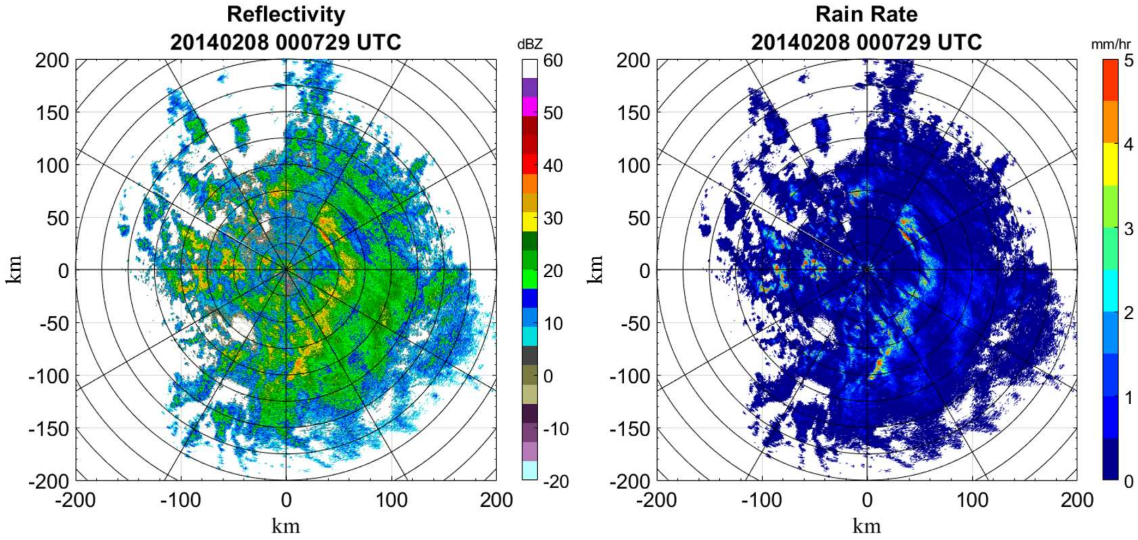

FIGURE 4.3. NEXRAD S-band radar (KDAX) reflectivity (left) and estimated rain rate (right) at Sacramento, California.

(b) shows the corresponding rain rate estimated based on the equation mentioned above. It can be seen from the figure that the higher the reflectivity, the higher the rain rate values.

The specific differential phase (K_{dp}) moment is obtained from dual-polarization radars. Since the K_{dp} is estimated based on the phase change in the received radar signals, it is widely used for obtaining precipitation information. It should be noted that this method is only applicable to dual-polarization radars. Most weather radars today have the capability of dual polarization. Increasing K_{dp} indicates an increase in the size and concentration of raindrops and thus, an increase in the rain rate. Data from the X-band radar (XSCV) deployed in Santa Clara, CA, is considered to discuss the rain rate obtained from K_{dp}. The K_{dp} is obtained from the DROPS algorithm, which uses a robust estimation method [32] more details are provided in the next chapter. Figure 4.4 (a) and (b) show the reflectivity and specific phase of the XSCV radar data taken on the December 17, 2018 at 3:00 UTC. The rain rate shown in Figure 4.4 (c) is estimated based on the equation $RR = 20K_{dp}^{0.65}$

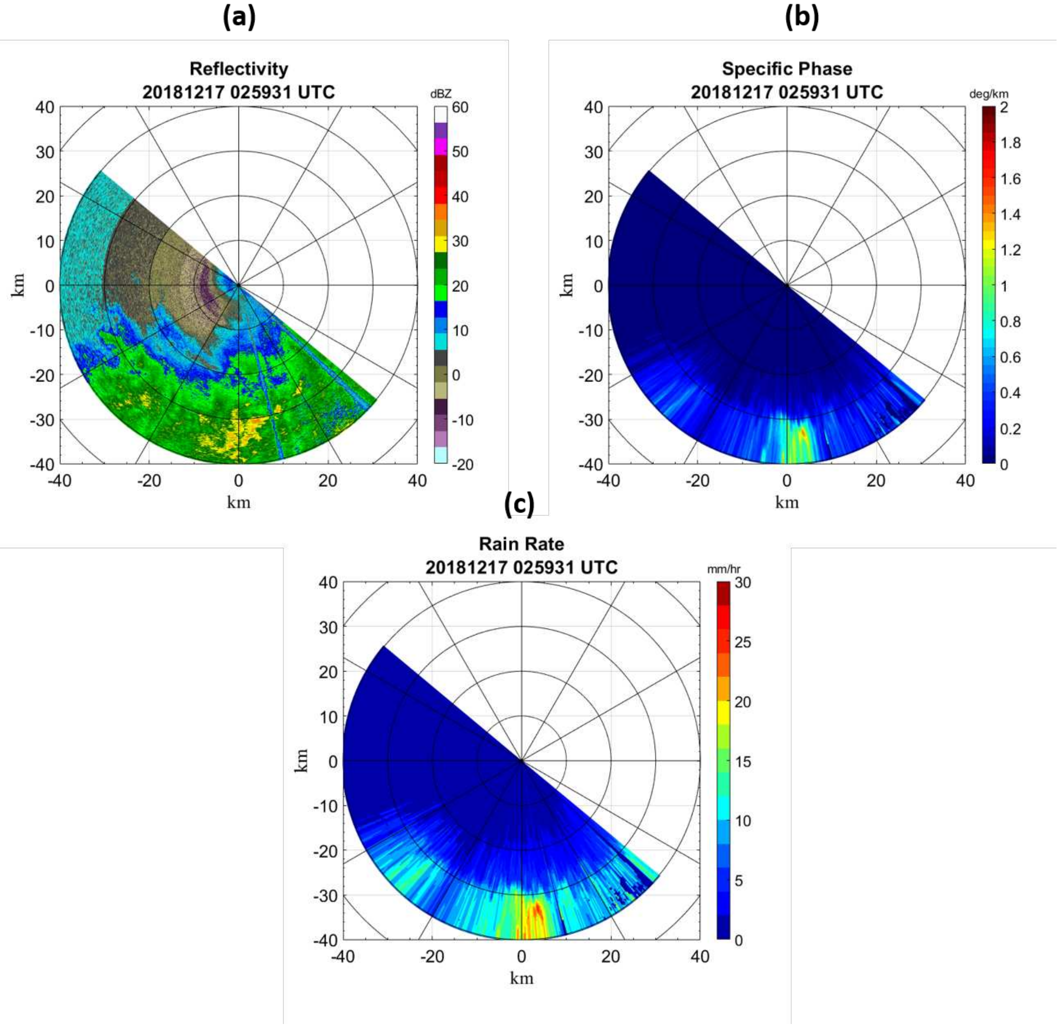

FIGURE 4.4. The X-band (XSCV) radar output at Santa Clara, California. (a) radar reflectivity, (b) specific phase and (c) rain rate.

[33]. More accurate estimates of rain rates are obtained when using specific phase instead of reflectivity when available.

Figure 4.5 shows the reflectivity and rain rate from the dual-frequency dual-polarization Doppler weather radar (D3R) deployed at the ICE-POP field campaign. The DROPS algorithm is used to estimate the rain rate. The data is taken from November 3, 2017 at 17:14 UTC. We see no data in the southeast part of the PPI scan. This lack of data is due to part of the PPI sector being blocked. During this field campaign, the D3R radar collected interesting snow events; research was carried out to estimate the snow rate from D3R by

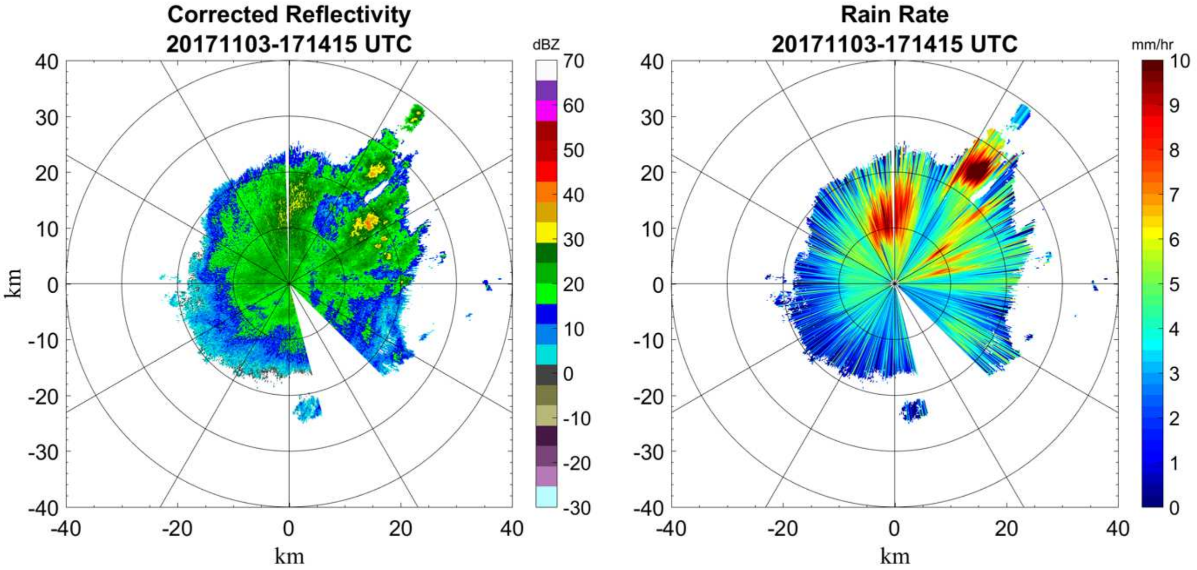

Figure 4.5. D3R Ku-band radar reflectivity (left) and estimated rain rate (right) during a rain event at ICE-POP field campaign.

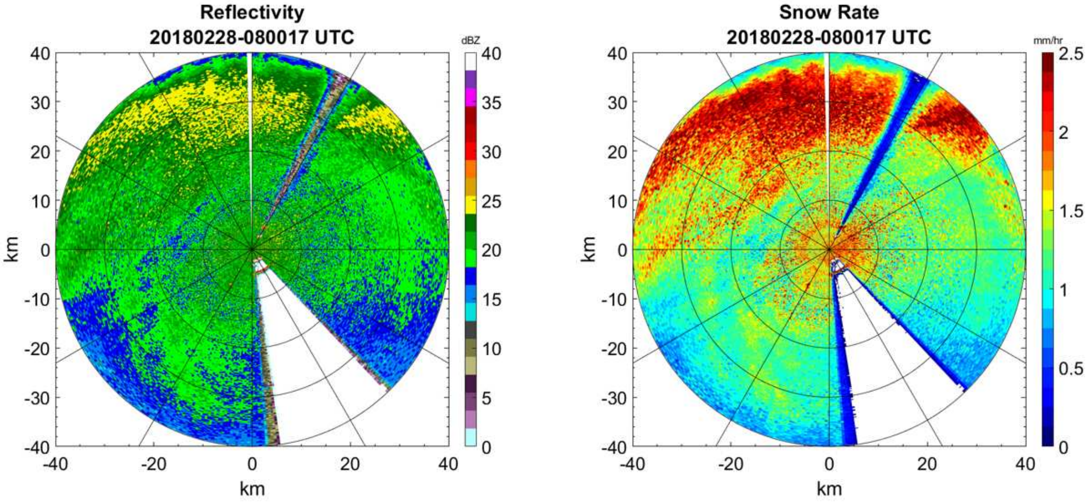

Figure 4.6. D3R Ku-band radar reflectivity (left) and estimated snow rate (right) during a snow event at ICE-POP field campaign.

deriving a relationship between the reflectivity and snow rate for the region where the radar was deployed $SR = 0.0921Z^{0.5809}$. More details regarding the derivation of the relationship can be found in [34]. Figure 4.6 shows the reflectivity and snow rate data taken from the snow event on February 28, 2018 at 08:00 UTC. The figure shows that the snow event covered the entire domain of the radar up to 40 km. The figure also shows that the snow rate increases with the increasing reflectivity values.

4.3. Current systems of precipitation mapping

In today's world, there are various remote sensing system networks that are successfully deployed. A few precipitation measurement systems which are currently active are discussed in this section. Based on the architecture of the various precipitation measurement systems, a system of automobile radar network for mapping precipitation is proposed.

4.3.1. CASA Radar Network. The United States National Science Foundation Engineering Research Center (NSF-ERC) for Collaborative Adaptive Sensing of the Atmosphere (CASA) is dedicated to revolutionizing our ability to observe, understand, predict, and respond to hazardous weather events using a dense network of small, low-power and low-cost X-band radars that can collaboratively and adaptively sense the lower atmosphere [35]. There are many advantages of using multiple X-band radars instead of a S-band radar as deployed by WSR-88D Next Generation Doppler Radar (NEXRAD) such as overcoming the earth-curvature blockage and make up the resolution degradation caused by spreading of radar beams at long ranges and large temporal sampling intervals.

CASA consisting of a system of X-band weather radars, has proposed a new atmospheric sensing paradigm called Distributed Collaborative Adaptive Sensing (DCAS), which adaptively and collaboratively operates the radar network according to real-time changing atmospheric conditions, prevailing weather information, and the needs of various end users [36]. The distributed network primarily refers to the large number of X-band radars deployed in the network. These radars operate collaboratively through the proposed detecting,

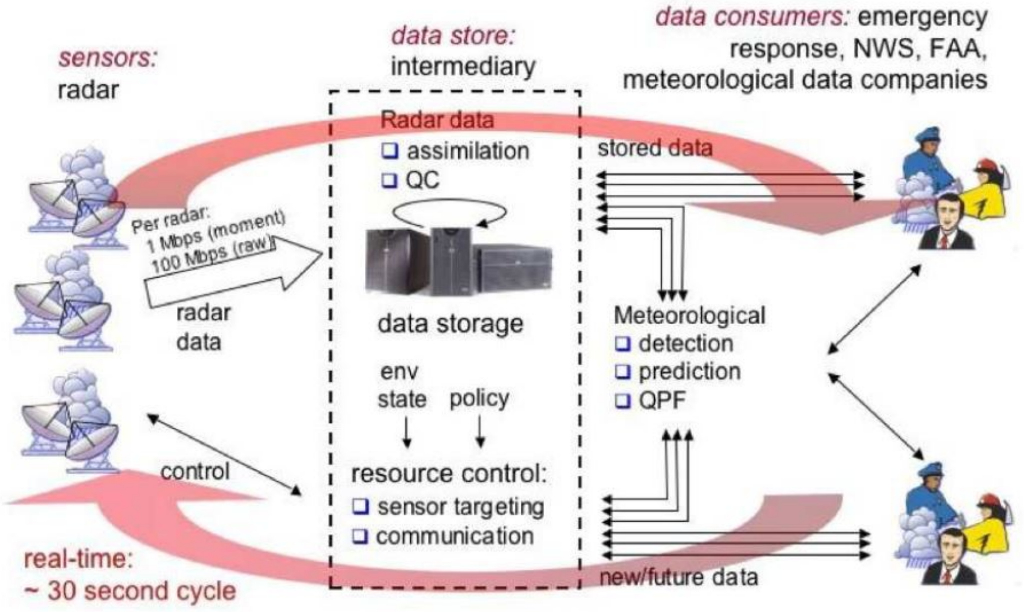

FIGURE 4.7. The architecture of the Distributed Collaborative Adaptive Sensing (DCAS) system used in the CASA radar network. [5].

tracking and predicting schemes. Based on the needs of the various end users, changing weather conditions, prevailing weather data and information and changes in the associated communication and computing resources the system is dynamically adapted.This adaptive nature of the system will provide flexibility in real-world operations. These system aspects of DCAS are shown in Figure 4.7 [5].

In brief, a DCAS system should include remote sensing instruments, algorithms that can detect and predict hydrometeorological hazards such as flash floods and storms, an underlying substrate of distributed computation that will dynamically process the data which is collected and manages the system resources, and user-friendly interfaces which will provide the ability for the end-users to access and interact with the system. The main goal of such a DCAS system is to give accurate information and warning to everyone, which saves lives and reduces property damage. Some of the applications of this type of system is using the system for improving flash flood prediction and reducing the tornado false alarm rate.

4.3.2. NEXRAD radar Network. The Next Generation Weather Radar (NEXRAD) systems are Doppler weather radars that detect and produce over a hundred different long-range and high-altitude weather observations and products, including areas of precipitation, winds, and thunderstorms. NEXRAD is a network of 160 high-resolution Doppler weather radars operated by the NOAA National Weather Service (NWS), the Federal Aviation Administration (FAA), and the U.S. Air Force (USAF). The current NEXRAD system comprises more than 150 sites throughout the United States and a few select overseas locations. Most of the radars in the NEXRAD radar are S-band radars. The NEXRAD radars provide volume data by scanning PPIs at different elevation angles.

Figure 4.8 shows the system architecture of the NEXRAD radar network [6]. Unlike the CASA radar network, the radar scans do not change based on user feedback and the system parameters in the NEXRAD network. Compared to the CASA radar network, the NEXRAD radar network can be considered as a rigid network with minimal changes in operations and data type. The scan strategy of the NEXRAD radars is fixed and will provide data at regular intervals of time (about 5 min interval for each volume scan). However, they have different scan strategies, such as precipitation and clear air modes.

The radar data is then sent for processing and storage through the Internet. The stored data and end products are available to the data users through the Internet. The metadata of the radar scan, such as the radar names are stored separately, which will help in sorting and finding the data easily. The monitor database is used to monitor the radars signal flow and correct any data drops. The data archive system is a pipelined Extraction, Transform, Load (ETL) process. Each module functions independently on input files and communicates with each other using XML. This process allows for high-performance and fault tolerance as the processes can be duplicated and distributed across machines[6].

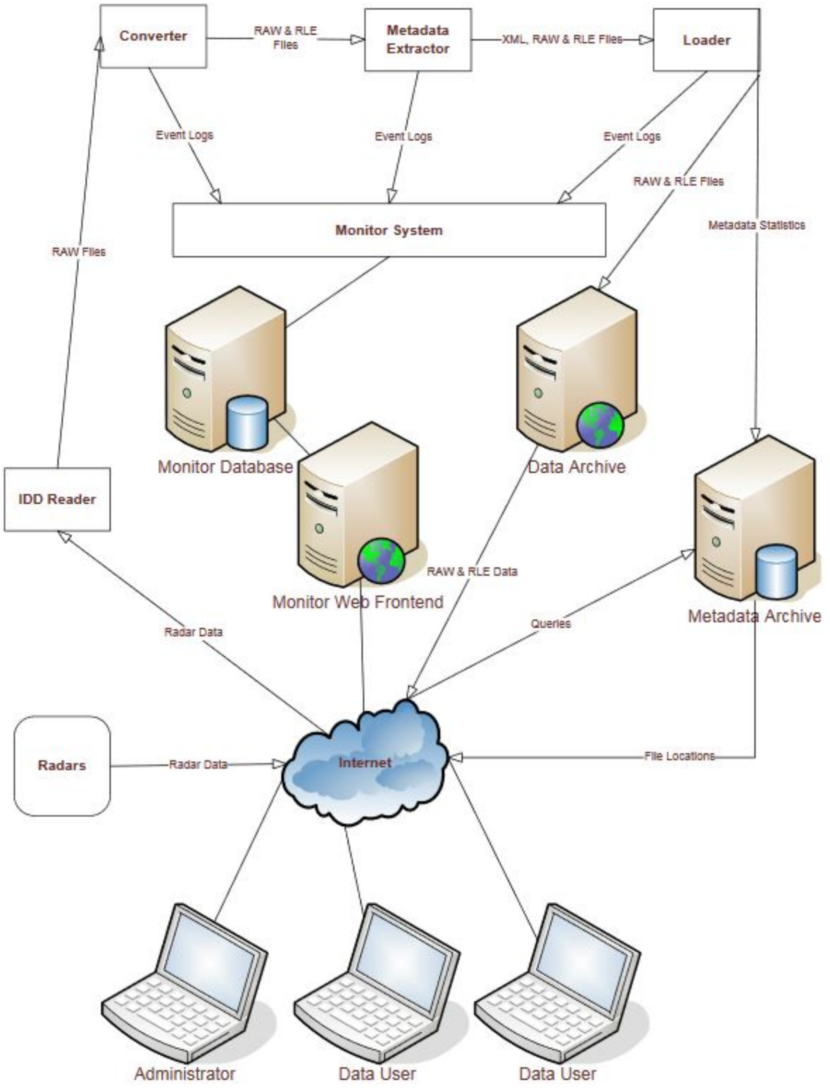

Figure 4.8. The architecture of the NEXRAD system [6].

4.3.3. Point precipitation measurement network. The rain gauge and disdrometer provide point measurements of the precipitation data. However, a single disdrometer or rain gauge fails to give the spatial variability of the storm. Also, a single measurement from these point instruments might be inaccurate in a few instances, such as when the measurements are affected by factors such as wind or mechanical issues with the instrument itself. To overcome the above-mentioned problems, usually a network of point instruments is deployed.

CoCoRaHS, which stands for the Community Collaborative Rain, Hail and Snow Network, is a unique, non-profit, community-based network of volunteers of all ages and backgrounds working together to measure and map precipitation (rain, hail and snow). The measurements in CoCoRaHS mostly comprise measurements from point measurement instruments such as rain gauges.

The system is designed such that anyone with a rain gauge can sign up in the network as a volunteer and update the precipitation information daily. Since this measurement network is completely driven by the users and it has few potential risks. Having multiple measurements in the same region will be helpful in reducing the error estimates. Once there are many volunteers, the network will be able to provide accurate precipitation measurement data. It should be noted that there will be large observation gaps in rural areas and the precipitation data will be more concentrated in urban regions. A snapshot of the CoCoRaHS network's 24-hour precipitation data from the Denver and Fort Collins area is shown in Figure 4.9. From this figure, it can be clearly seen that the precipitation measurements are concentrated in the cities of Denver and Fort Collins. In the remote regions outside the urban areas, the precipitation measurements are less frequent.

Other precipitation networks consisting of rain gauges and disdrometers are present in various parts of the world. In the United States, the rain gauge network at each state level is used along with the NEXRAD radar network to provide accurate estimates of the hydrometeorological products. There are various algorithms that have been researched in the past which interpolated the rain gauge data spatially and temporally. Some of the researchers have also used machine learning to improve rain gauge estimates [37]. The design of the optimal rain gauge network is a topic of active research. There are various statistical methods that are used in the optimal design of a rain gauge network. A review of

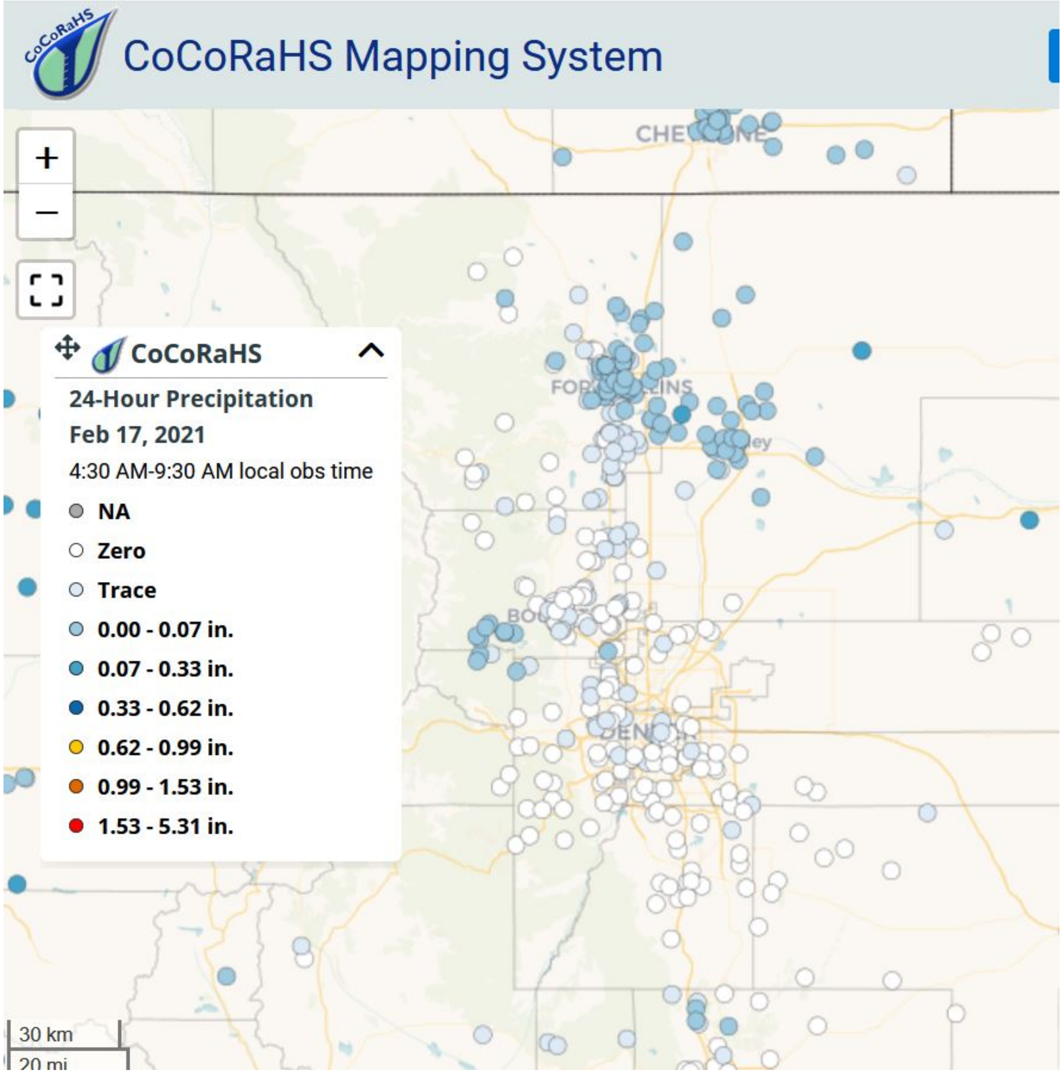

Figure 4.9. A snapshot of the CoCoRaHS network's 24-hour precipitation data from the Denver and Fort Collins taken on February 17, 2021.

all the methods can be found in [38]. The spatial-interpolation methods are most commonly used in the processing of the rain-gauge networks. Geostatistical interpolation methods are stochastic methods, with kriging being the most well-known in this category [39].

Chapter 5

Attenuation correction in weather radars

Weather radars play a prominent role in the remote sensing of the atmosphere. The quality of the radar data should be maintained at the highest standards as they make a direct impact in the models and algorithms where the radar data is used. The end users of radar data like meteorologists would require accurate data to interpret and predict information obtained correctly. There are issues associated with radar data, such as calibration offsets of radar moments; these issues can be solved by periodically calibrating the weather radars. There are various calibration methods that are used to ensure accurate data is measured from the radar [40]. There are other issues in weather radar data that cannot be avoided, but these issues can be considered and corrected. One such issue is the loss of signal power due to attenuation.

The attenuation of radar signals is one is the factors that need to be considered carefully. A brief discussion about the attenuation in radars was provided in chapter 3. Based on the previous literature, the attenuation values for rain can be well defined for different rain rates. The determination of attenuation values for ice hydrometeors is quite tricky. This is because of the varying density of the ice particles and also the amount of water covering the ice particles.

To understand the amount of attenuation encountered by the radar signal beam due to snow particles, the specific attenuation is computed using the Gunn-East model [41]. The computation of specific attenuation based on this model is given in Equation 36. Where RR is the liquid water equivalent (LWE) snow rate and λ is the wavelength. The model used for

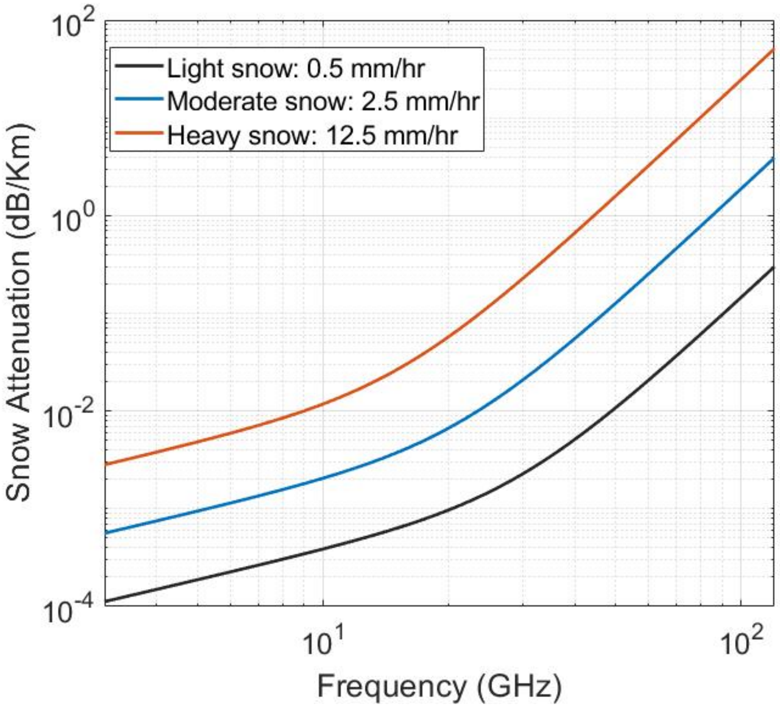

FIGURE 5.1. Snow attenuation versus frequency for different snow rates.

computing the losses due to snow is parameterized by the equivalent liquid content instead of volume. The model assumes $0°C$ with snow particles.

$$A_h = 0.00349\frac{SR^{1.6}}{\lambda^4} + 0.00224\frac{RR}{\lambda} \tag{36}$$

Figure 5.1 shows the variation of snow attenuation with respect to frequency and varying snow rates. For light snow the equivalent liquid water content was considered as 0.1 mm/h, for moderate snow the value was chosen as 1 mm/h and for heavy snow the value was 4 mm/h. The snowfall rates are characterized based on the society of automotive engineers (SAE) [42].

Ice particles can be classified as dry ice and wet ice. In dry ice, there is no influence of water in the liquid state covering the ice particle. As temperature increases, some parts

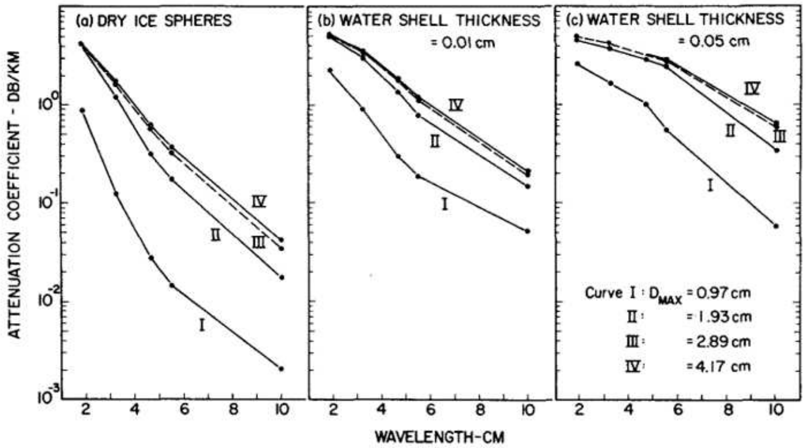

Figure 5.2. Attenuation coefficient versus frequency for dry ice spheres and ice spheres with water shell [7].

of the ice particles begin to melt and a water coating will be present on the ice particles, which we call wet ice. This will further increase attenuation. The attenuation for dry ice spheres and ice spheres with water shells is shown in Figure 5.2. From this figure, it can be seen that the attenuation for dry ice spheres is much lower than the ice spheres with water shells. A complete summary of how the variations of attenuation coefficient with frequency and diameter of the ice spheres can be found in [7].

In this chapter, the attenuation correction in weather radars for rain is introduced. A new method for attenuation correction for ice hydrometeor particles is discussed and the results are presented with the help of the X-band and Ku-band radars. This method of attenuation correction can be used for correcting the received signals at the radar at various frequency bands.

5.1. Current methods for attenuation correction in weather radars

Accounting for attenuation and correcting it for data obtained from weather radars is a challenging task. A procedure based on the combination of a Bayesian changepoint model and ordinary least squares was used to identify attenuation in radar signals [43]. In [44] large attenuation values were observed at the X-band frequencies, which led to large errors in rain estimation techniques. Reflectivity and differential reflectivity are the two radar variables that are affected by attenuation [45]. The problem of attenuation correction in weather radars has been investigated for more than three decades. Various algorithms have been developed for attenuation correction for rain particles and the improvement in the derived products have been published.

Procedures to estimate the specific and differential attenuation using dual-polarization radar moments at C-band frequencies were shown in [46] and [47]. An attenuation correction procedure was developed based on raindrop size distribution (DSD) obtained from disdrometer measurements by [48]. An attenuation correction method developed by [49] was based on the property that the differential propagation phase is nearly linearly proportional to cumulative attenuation in the usual radar frequencies. [50] discusses a self-consistent ZPHI method for attenuation correction of reflectivity and differential reflectivity for rain attenuation. The improved ZPHI method, based on a self-consistent approach for attenuation correction in a practical environment was discussed in [51]. An evaluation of attenuation correction methodology for dual-polarization radars operating at the X band frequencies using a differential phase-based algorithm as well as the range-profiling algorithm are discussed in [52].

Researchers have also used various indirect methods to address the problem of attenuation; some researchers even used microwave links to determine attenuation [53]. In [54], the arbitrarily oriented microwave link is used to optimize the ratio of specific attenuation to a specific differential phase, a key parameter in attenuation correction schemes.

The problem of attenuation correction in weather radars has been researched in the CSU radar group for over three decades. Various algorithms have been developed for attenuation correction for rain particles and improvement in the derived products has been published. The Dual-Polarization Radar Operational Processing System (DROPS), an attenuation correction and quality control algorithm developed at CSU, is widely used to estimate accurate radar moments. The improved radar moments are used for enhancements of the quantitative precipitation estimation (QPE).

There are currently two different versions of the DROPS algorithm. The first version of DROPS is referred to as DROPS1.0. The DROPS1.0 algorithm was invented to ensure quality data is obtained after processing the raw weather radar data. The algorithm estimates the specific phase (K_{dp}) based on a robust method and hydrometeor classification using a bin-based fuzzy logic approach. More details of the DROPS1.0 algorithm can be found in [55]. Rainfall rate estimation was improved after using the DROPS1.0 algorithm. Many prior works validated the results of outputs from the DROPS1.0 algorithm. This was accomplished using the CSU-CHILL and National Weather Service NEXRAD radars.

The improved version of the DROPS1.0 algorithm, referred to as the DROPS2.0 algorithm, provides various advantages and additional features for correcting radar data. The step-by-step procedure of the DROPS2.0 algorithm is explained next. The first step of the DROPS2.0 algorithm involves data quality correction and K_{dp} estimation. The adaptive algorithm developed by [32] is used to estimate the K_{dp} which is then used to filter out non-meteorological echoes and ground clutter. The non-meteorological targets are classified based on characteristics of differential phase and co-polar correlation.

The quality-controlled data is provided as an input to the advanced hydrometer classification module. The hydrometeor classification in the DROPS2.0 is based on region-based classification. This is a semi-supervised hydrometeor classification method that has shown promising results in the past. A brief discussion of the hydrometeor classification is described

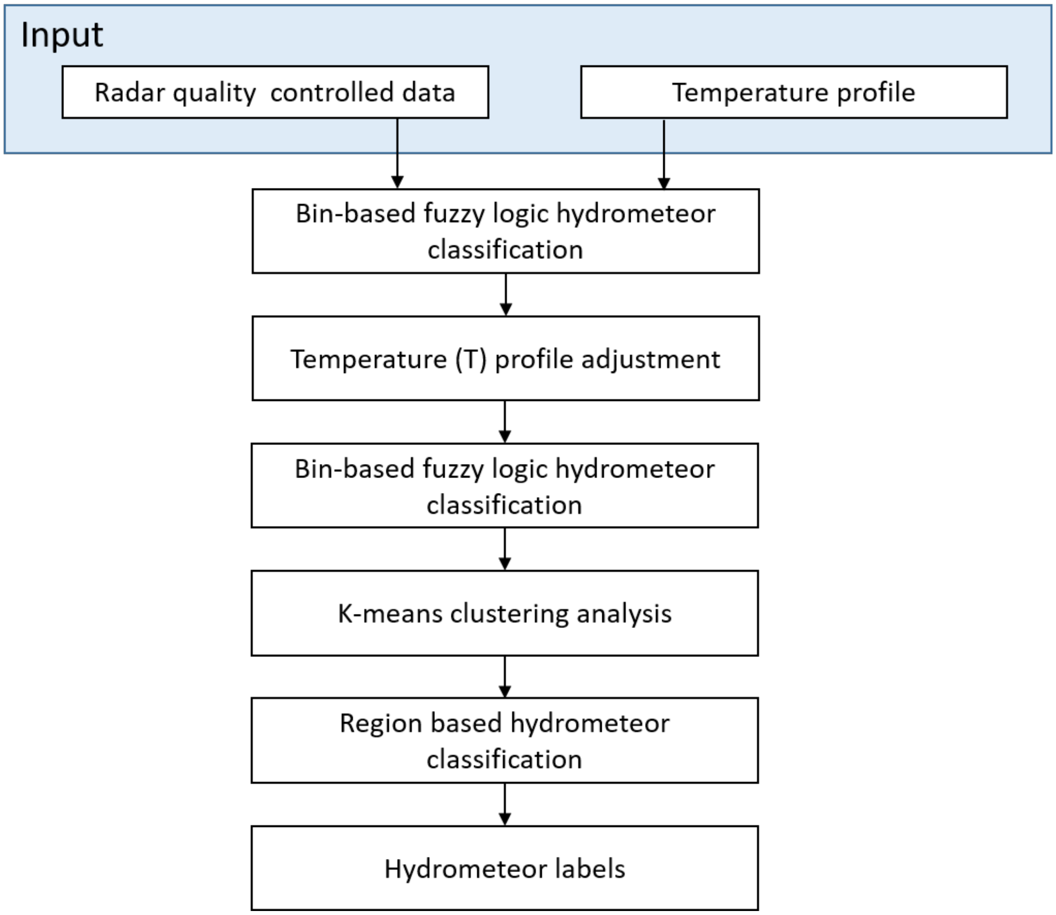

FIGURE 5.3. Steps for hydrometeor classification in DROPS2.0 algorithm.

next as we will be using this output in the proposed algorithm. More detailed information regarding the hydrometeor classification can be found in [8].

The radar quality controlled moments reflectivity (Z_h), differential reflectivity (Z_{dr}), co-pol correlation (ρ_{hv}) and K_{dp} are the inputs for the hydrometeor classification module. The vertical temperature profile obtained using a nearby sounding station is provided as an input to the module. The various steps of the classification module are given in Figure 5.3. As the first step, the bin-based fuzzy logic approach with four general blocks is implemented to get initial hydrometeor classification results [56]. This is a traditional way of obtaining the classification outputs. The quality of wet ice classifications is then used to adjust the temperature profile, which is essentially the average confidence of all the bins identified as

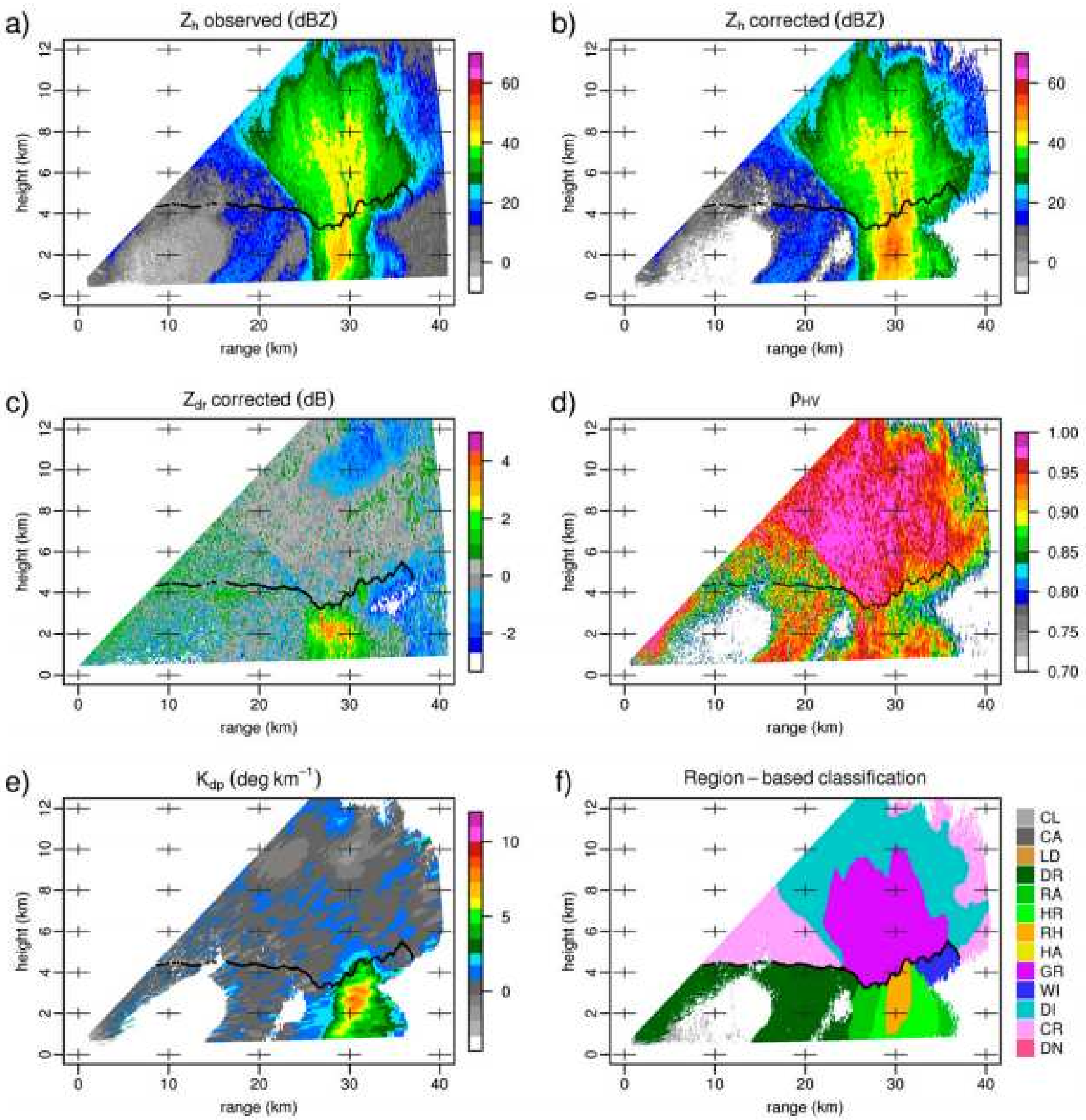

FIGURE 5.4. CASA IP1 RHIs of dual-polarization variables at 04:14 UTC 20 May 2011, along the azimuth 101.6°: (a) observed Z_h, (b) attenuation corrected Z_h, (c) Z_{dr}, (d) ρ_{hv}, (e) K_{dp} and (f) final hydrometeor classification [8].

wet ice based on the inference rule [8]. As a second step to incorporate the spatial continuity and microphysical constraints for each class, a modified K-means clustering technique is applied. The connected component labeling algorithm is then employed to derive connected regions [57], and the final classification is performed over connected regions where unique labeling of regions populated with adjacent bins are assigned to the same hydrometeor type.

In total, sixteen class labels are obtained from the hydrometer output as below: No data, Ground clutter, Non-meteorological clutter, clean air (CA), Attenuation, not classified, large drops (LD), drizzle (DR), rain (RA), heavy rain (HR), rain–hail mixture (RH), hail (HA), graupel (GR), wet ice (WI), dry ice (DI), crystals (CR), and dendrites (DN). This region-based approach is appealing because of its operational application and easy interpretation compared to the conventional fuzzy-logic method. Figure 5.4 illustrates the radar observations and corresponding hydrometeor classification results for a range–height indicator (RHI) scan from CASA IP1 radar on May 20, 2011 at 04:14 UTC. From this figure, it can be seen that the various regions of the storm are classified according to the particle type present. This information will be useful for further interpretation of the data.

Another important feature of the DROPS2.0 algorithm is the rainfall rate estimation. The rainfall rate algorithm uses the information of the corrected radar moments to accurately estimate the values. The comparisons of using DROPS1.0 versus DROPS2.0 is explained with results in [5]. From the comparison, it is mentioned that DROPS2.0 gives better rain rate estimates and cleaner hydrometeor classification. A comparison of rainfall rates computed using various algorithms from NPOL radar data taken on May 20, 2013 at 03:50 UTC is shown in Figure 5.5. From this figure, it can be seen that the DROPS1.0 rainfall rate estimates perform better than the NEXRAD Z-R and NEXRAD DP methods. It is also seen that the DROPS2.0 rainfall rate is better than DROPS1.0 estimated, detailed analysis for this case can be found in [5].

The DROPS2.0 algorithm is used in the proposed method for attenuation correction for ice hydrometeors; this is discussed later in this chapter. Before looking at the new attenuation correction algorithm, it is important to get a basic idea of attenuation correction for ice hydrometeors which is explained in the next section.

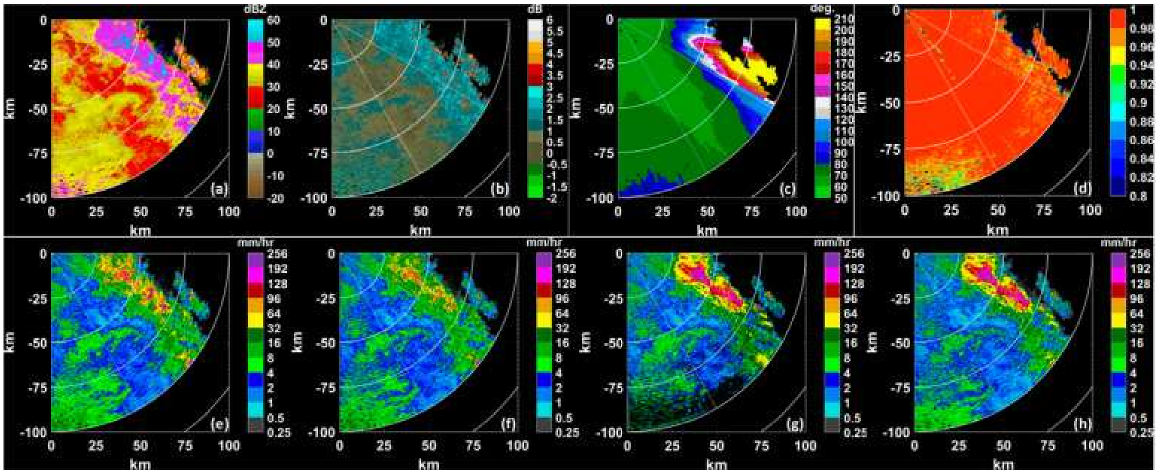

Figure 5.5. Rainfall rate estimates comparisons using different rainfall rate computation algorithms along with the corresponding radar moments data for NPOL radar data at 03:30 UTC 20 May 2013: (a) Z_h, (b) Z_{dr}, (c) ϕ_{dp}P, (d) ρ_{hv}, (e) NEXRAD Z-R, (f) NEXARD DP, (g) DROPS1.0 and (h) DROPS2.0 [5].

5.2. Attenuation correction for ice hydrometeors

It was mentioned earlier that the attenuation values vary for different precipitation particle types. The attenuation depends on the type of precipitation particle present in the atmosphere. Rain particles produce large attenuation values compared to ice particles. Also, ice particles have different shapes and densities, which are related to different environmental factors such as temperature. The snow morphology diagram shown in Figure 5.6 represents various types of ice crystals that are formed in the atmosphere. From this figure, it can be seen that the snow type depends on the temperature and the supersaturation level of the environment. We can also see that different shapes of the ice crystals, such as plates and columns, are present at different temperatures. One or many of these various types of ice hydrometeors can be present during a precipitation event.

Snow aggregates consist of ice crystals merged together. As smaller snow particles such as plates, needles and dendrites fall from the top layer of the atmosphere, they tend to melt a bit and merge with other particles nearby due to the increase in the temperature. This

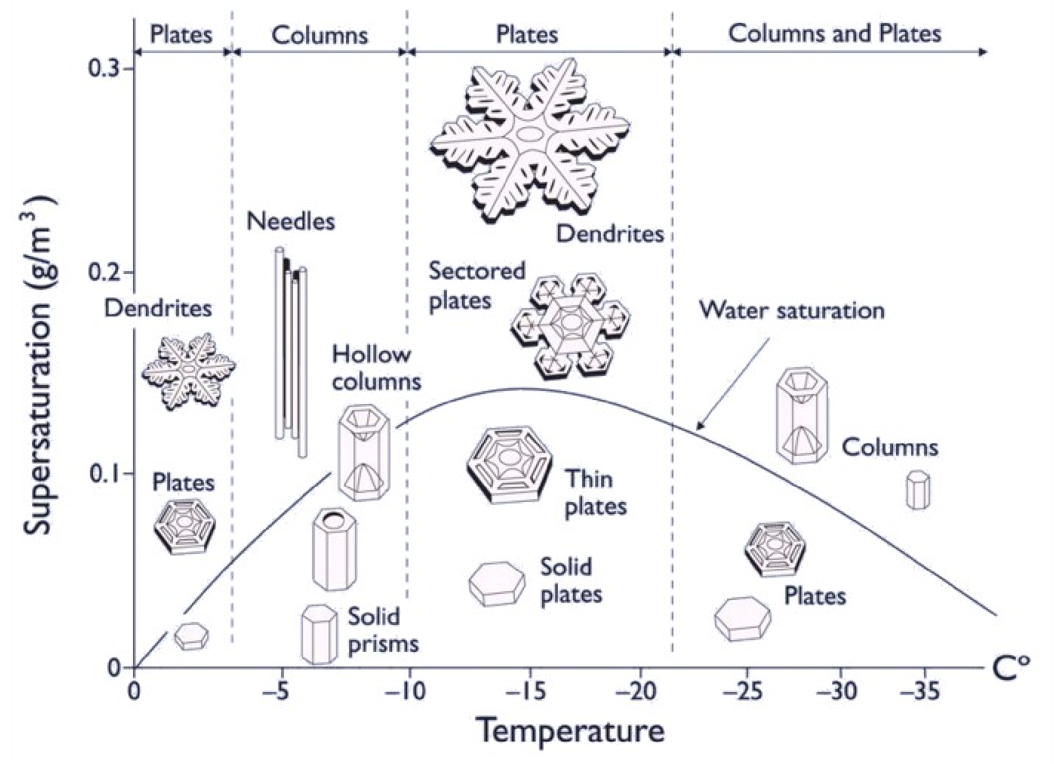

Figure 5.6. The snow crystal morphology diagram [9].

process can happen in various ways. However, we will not discuss them further here. A combination of many ice particles merged together will give us aggregate particles. The density of aggregates is much lower compared to individual ice crystals as aggregates largely contain air due to the packing of the ice particles in a loose manner. Dendrites consist of individual snowflakes, the snowflakes have branches around them and the axis ratio of the dendrites is usually very low. The ice plates and columns have high density and the axis ratio of these particles are very low too. Graupel and hail are bigger particles in size compared to other hydrometeors and their number concentration is very less compared to other ice populations. A particular shape of symmetric graupel with an axis ratio of 0.8 is considered in this research. Hail can be of spherical and conical shape. In this study, only spherical hail is considered.

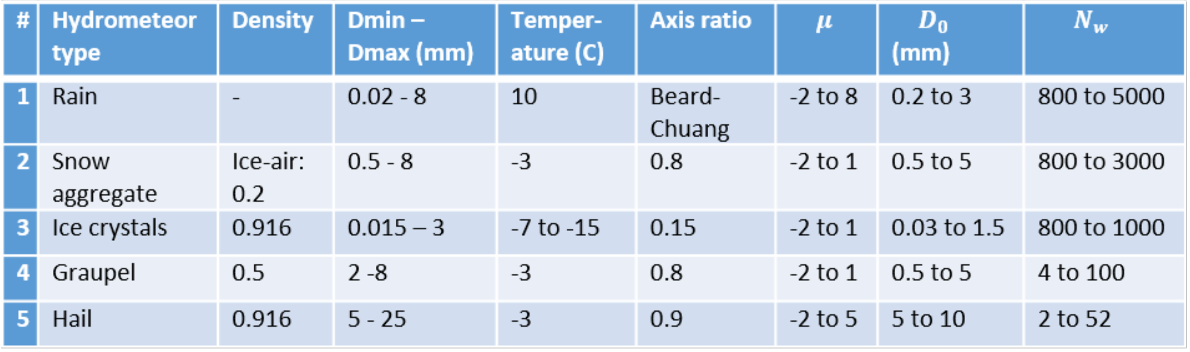

#	Hydrometeor type	Density	Dmin – Dmax (mm)	Temperature (C)	Axis ratio	μ	D_0 (mm)	N_w
1	Rain	-	0.02 - 8	10	Beard-Chuang	-2 to 8	0.2 to 3	800 to 5000
2	Snow aggregate	Ice-air: 0.2	0.5 - 8	-3	0.8	-2 to 1	0.5 to 5	800 to 3000
3	Ice crystals	0.916	0.015 – 3	-7 to -15	0.15	-2 to 1	0.03 to 1.5	800 to 1000
4	Graupel	0.5	2 -8	-3	0.8	-2 to 1	0.5 to 5	4 to 100
5	Hail	0.916	5 - 25	-3	0.9	-2 to 5	5 to 10	2 to 52

FIGURE 5.7. Parameters considered for T-matrix simulations for different hydrometeor particles.

In order to understand the attenuation produced by various precipitation particles, the theoretical results should be studied in detail. Different precipitation particles have different particle size distribution (PSD) and temperature range associated with them. T-matrix simulations were carried out to understand the relationship between various radar moments and specific attenuation. The input for the T-matrix simulations requires distinct particle size distribution and the shape information of the hydrometeors. The particle shape and distribution vary widely for each ice hydrometeor type. There are no fixed values in the literature to characterize each hydrometeor's size, shape and distribution. Most researchers in the past have used observational data to estimate the characteristics of the ice particles. Based on [58], [59], [60], [61] the characteristics of the hydrometeor particles were considered in this work. Figure 5.7 summarizes the various parameters for different hydrometeors considered in this study.

The T-matrix method [62] is considered for simulation of the radar signals. The T-matrix method for computing the scattering properties from a radars perspective is a well-established method. This method was developed in the early 1990s and has proved very useful since then. There are additional code wrappers for the T-matrix code, such as in Python and FORTRAN programming languages. A FORTRAN code is used to obtain the scattering properties of the ice particles in this study. This method assumes the precipitation particles as spheres even if they are of different shapes and computes the scattering coefficients. For ice particles like plates, this will be an approximation, but the results can be used for ice studies.

The simulations presented here are carried out at the Ku and X frequency bands. Simulations for other frequency bands, such as the Ka-band, can be carried out, and the scattering regime of the precipitation particles should be considered when carrying out simulations above Ku band frequencies. The simulation takes a long time to converge for cases in which the hydrometeor particles are very small in size. A shell script was written to run the T-matrix code for twenty thousand instances for each particle type. The particle size distribution was generated randomly within the range corresponding to each particle. The scattering computations are done for each particle and the corresponding radar parameters are computed and stored at the output. Then a MATLAB code was written, which reads the twenty thousand data points and computes the required relationships, and also for generating the scatter plots. Using such a large number of simulation points ensures that there is a minimal error in the retrieved relationships. Also, the simulations were conducted for various elevation angles as the scattering properties vary depending on the radar incidence elevation angle. The radar moments estimated from the simulations will have different values at different elevation angles even if the precipitation particle's characteristics remain the same. Elevation angles from 0 degrees up to 45 degrees in steps of 5 degrees were considered and the simulation outputs were obtained.

Reflectivity (Z), differential reflectivity (Z_{dr}), specific phase (K_{dp}) and specific attenuation (A_h) parameters are obtained from the simulation output. Relationships between A_h

and Z and between A_h and K_{dp} are used to estimate the specific attenuation in weather radar data. The relationship between A_h and K_{dp} is defined in Equation 37.

$$A_h = aK_{dp}^b \tag{37}$$

Since K_{dp} is a derived product obtained using the information of differential phase, it is preferable to use the relationship between A_h and K_{dp} when K_{dp} is available. The K_{dp} estimated by the DROPS2.0 algorithm can be considered very accurate. Hence, this relationship is used in this study. When K_{dp} is unavailable, for example, in single polarization radars, the relationship between A_h and Z can be used to estimate the A_h. The use of the relationship between A_h and Z is not presented in this work.

Figure 5.8 shows the scatter plots of A_h and K_{dp} of both horizontal and vertical polarizations for various hydrometeors at an elevation angle of zero degrees at the X band. The red line in the figures represents the power-law fitted line for these two parameters. The values for parameters a and b obtained from the fit for various hydrometeors and elevation angles are given in Appendix A. The error plots are also shown for the corresponding hydrometeor type in this figure. The errors are low for both polarizations for all hydrometeor types. The results obtained for only zero degrees simulation outputs for all hydrometeors are shown here considering the space constraints.

Figure 5.9 shows the scatter plots of A_h and K_{dp} for three different elevation angles for snow aggregates at the X band. The red line in the figures represents the power-law fitted line for these two parameters. It can be seen from this figure that as the elevation angle increases, for the same A_h value, the K_{dp} value decreases, and the decreasing K_dp values are more prominent at higher elevation angles around 45 degrees.

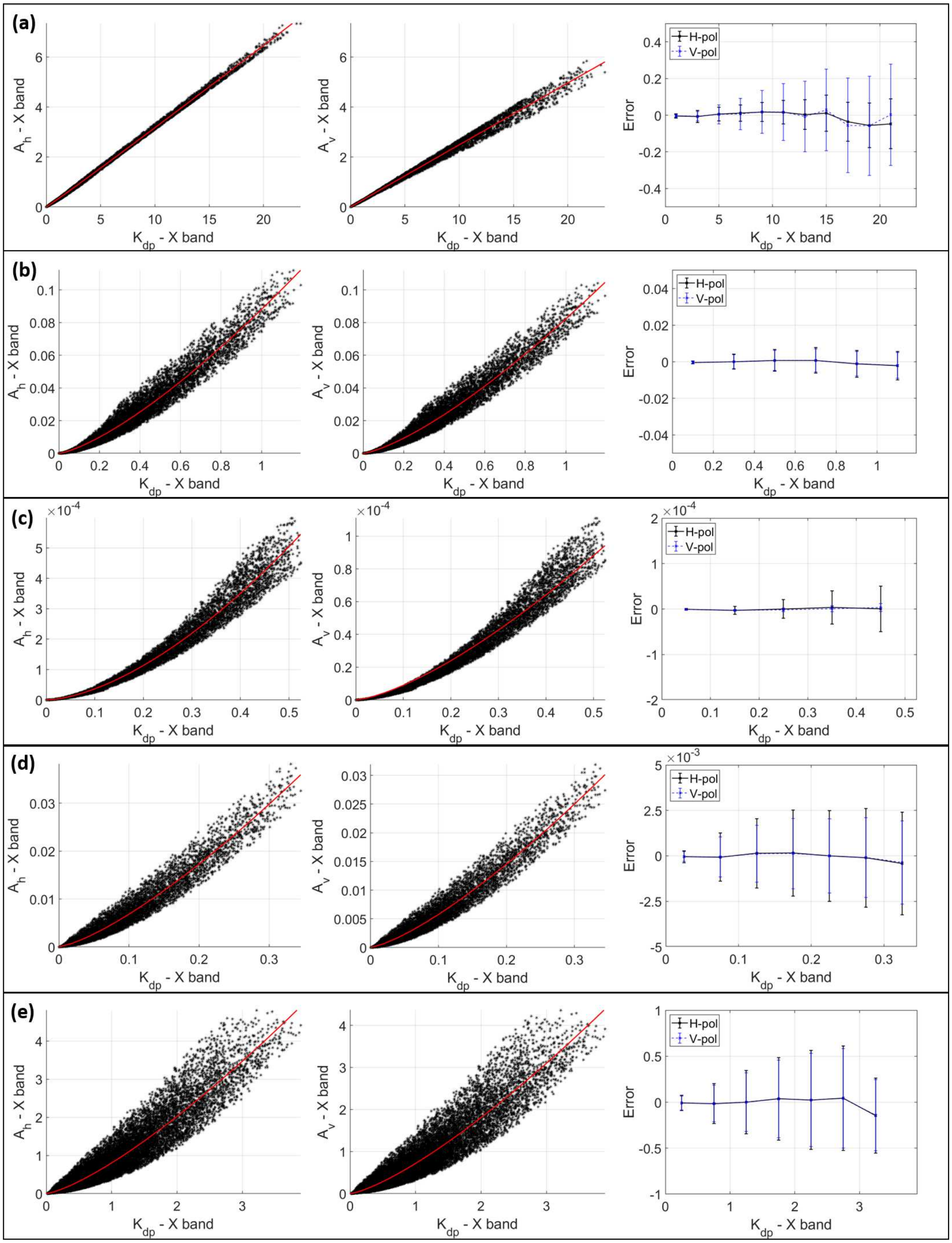

FIGURE 5.8. Scatter plots of specific phase versus specific attenuation for different hydrometeors at 0° elevation angle at the X band (a) Rain, (b) Snow aggregate, (c) Crystals, (d) Graupel and (e) Hail. The red line represents the power-law fit line.

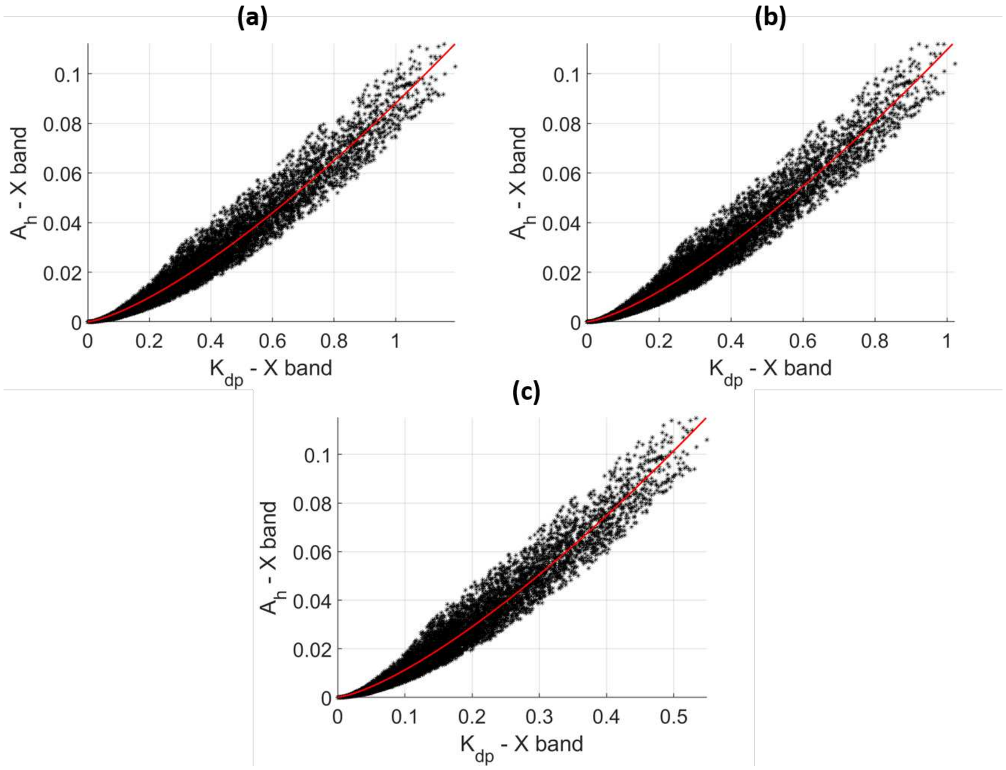

FIGURE 5.9. Scatter plots of specific phase versus specific attenuation for snow aggregates at the X band (a) 0° elevation angle, (b) 20° elevation angle, (c) 45° elevation angle.

Figure 5.10 shows the scatter plots of A_h and K_{dp} of both horizontal and vertical polarizations for various hydrometeors at an elevation angle of zero degrees at the Ku band. The red line in the figures represents the power-law fitted line for these two parameters. The values for parameters a and b obtained from the fit for various hydrometeors and elevation angles are given in Appendix B. The error plots are also shown for the corresponding hydrometeor type in this figure; the errors are very low for both polarizations for all hydrometeor types. The results obtained for only zero degrees simulation outputs for all hydrometeors are shown here considering the space constraints. For getting a correct relationship, the exact PSD and particle characteristics used for X band simulations were used for the Ku band simulations. Twenty thousand data points were simulated at the Ku band frequency as well.

Figure 5.11 shows the scatter plots of A_h and K_{dp} for three different elevation angles for snow aggregates at the Ku band. The red line in the figures represents the power-law fitted line for these two parameters. It can be seen from this figure that as the elevation angle increases, for the same A_h value, the K_{dp} value decreases, and the decreasing K_dp values are more prominent at higher elevation angles around 45 degrees. The relationships obtained for various hydrometeor types at both horizontal and vertical polarizations are used in the attenuation correction algorithm explained in the next section.

5.3. The New attenuation correction algorithm

In this section, a new algorithm used for attenuation correction, which will work for rain as well as ice hydrometeors is introduced. The attenuation correction for rain particles was discussed previously. With the information from the theoretical simulations using the T-matrix and the DROPS2.0 algorithm, a new algorithm which corrects for attenuation for all types of hydrometeors is developed in this work. Figure 5.12 shows the flowchart of the new proposed attenuation correction algorithm.

The first step of the algorithm involves providing the observed data from the radar to the DROPS2.0 algorithm. The DROPS2.0 algorithm estimates the specific phase for the full radar scan. The additional feature as explained earlier, is that the DROPS2.0 algorithm outputs specific attenuation variables for only rain particles. In other words, the specific attenuation values are obtained for all the rain particles below the melting layer in the data. The DROPS2.0 also outputs the hydrometeor classification in sixteen different classes. These hydrometeor class are further simplified to six different classes to be used in the proposed algorithm. The six different classes are Rain, Hail, Graupel, Crystals and Snow aggregates. This information of hydrometeor classification along with specific phase is used to determine

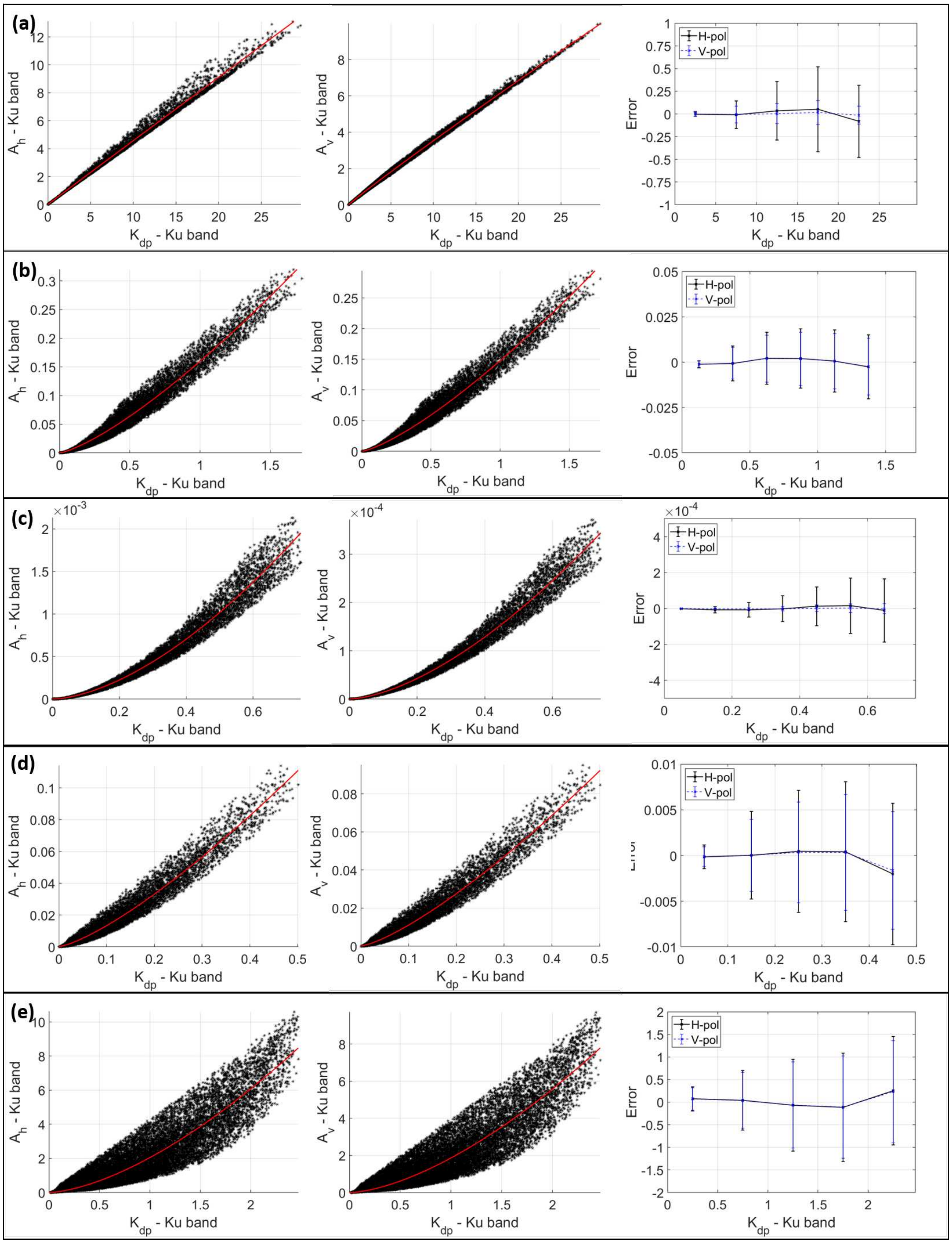

FIGURE 5.10. Scatter plots of specific phase versus specific attenuation for different hydrometeors at 0° elevation angle at the Ku band (a) Rain, (b) Hail, (c) Graupel, (d) Snow aggregate, (e) Crystals and (f) Dendrites. The red line represents the power-law fit line.

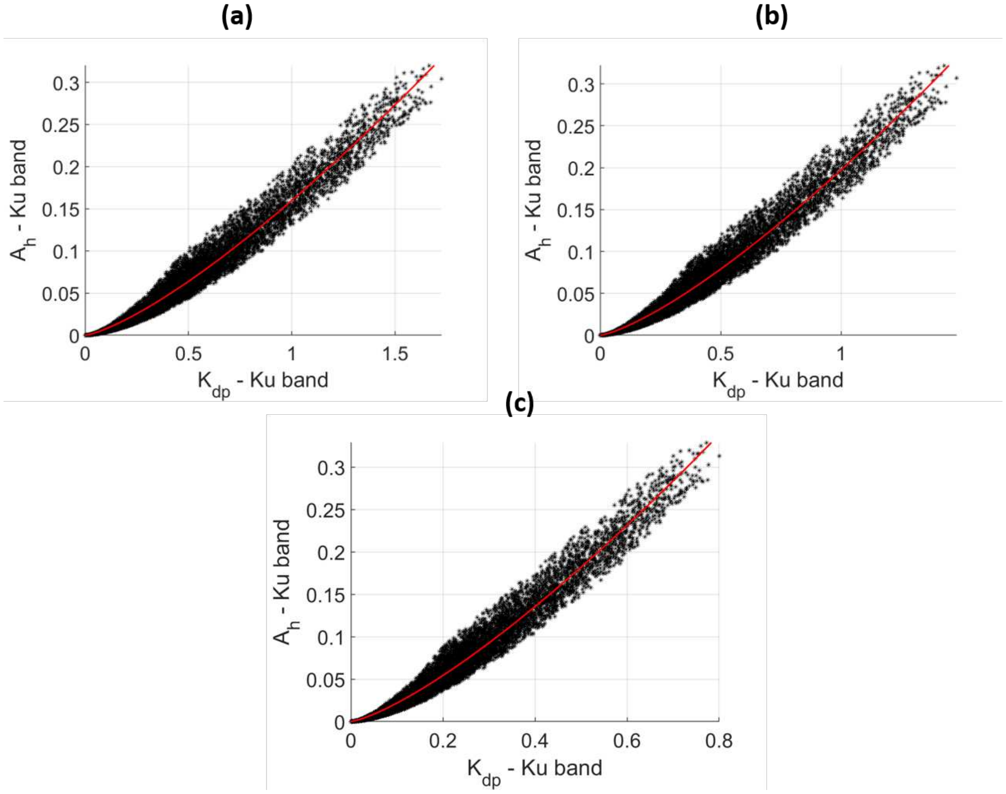

FIGURE 5.11. Scatter plots of specific phase versus specific attenuation for snow aggregates at the Ku band (a) 0° elevation angle, (b) 20° elevation angle, (c) 45° elevation angle.

the specific attenuation for all the hydrometeors. The specific attenuation is related to the specific differential phase as shown in Equation 37.

The simulation studies discussed in the previous section are used to obtain the parameters a and b used in the above equation, which depend on the type of precipitation particle, polarization and elevation angle. Based on the elevation angle, the specific attenuation is computed for all resolution volumes in the radar data. The rain attenuation is directly taken from the DROPS2.0 algorithm as they have proved to be robust in prior research works.

Once we have the specific attenuation values, the Path Integrated Attenuation (PIA) is computed for each ray of the radar data. A ray of radar data corresponds to all the radar resolution volumes along the range for a particular azimuth or elevation, which depends on

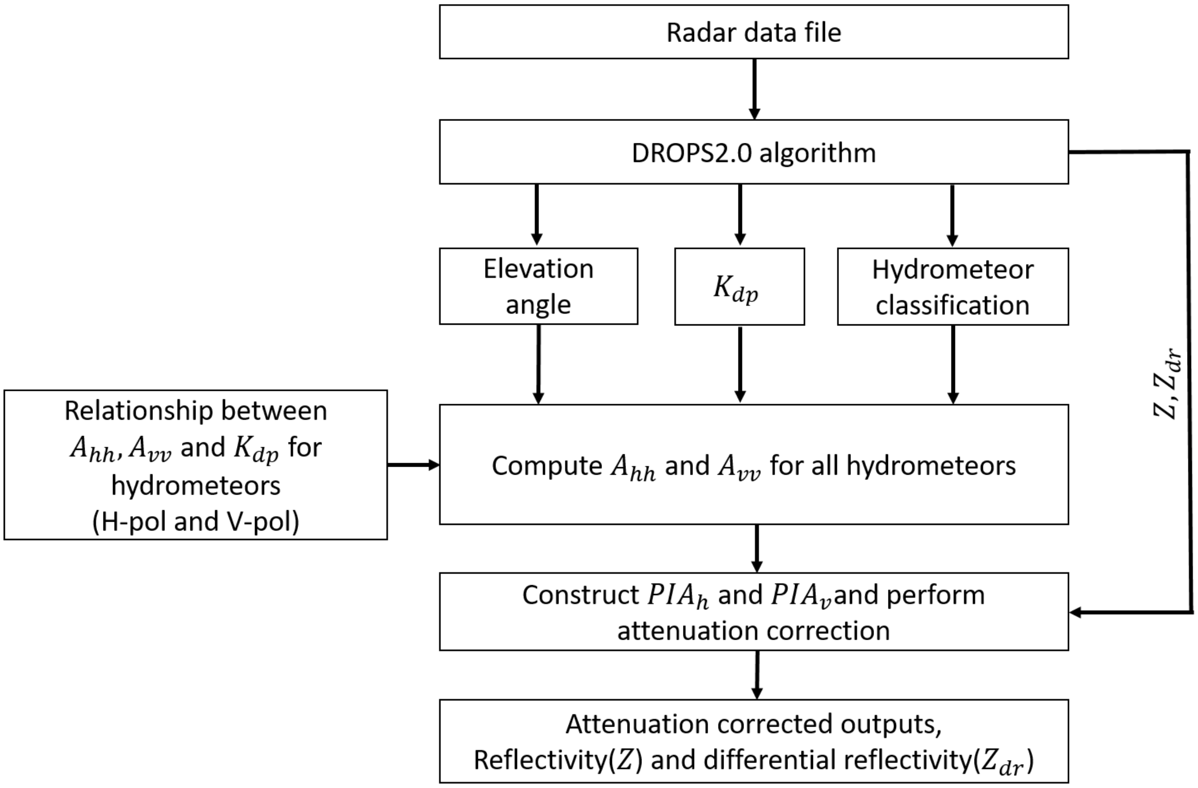

Figure 5.12. The new algorithm for attenuation correction for all hydrometeors.

whether the radar collected data in Plan Position Indicator (PPI) or Range Height Indicator (RHI) scan. The PIA of radar resolution volume is the sum of the attenuation values (two-way) of all the preceding resolution volumes. The PIA for the horizontal polarization and vertical polarization are defined in equation 38 and 39 respectively.

$$PIA_h(r) = 2\int_0^r A_h(s)ds \tag{38}$$

$$PIA_v(r) = 2\int_0^r A_v(s)ds \tag{39}$$

Where r is the range, s is the propagation interval path length and PIA (r) is in decibels. Once the PIA is obtained for all the resolution volumes, the attenuation values are corrected in the radar variables. Reflectivity and differential reflectivity are the two variables in which attenuation should be corrected. The attenuation corrected reflectivity is computed using Equation 40.

$$Z_h(corr) = Z_h + PIA_h \tag{40}$$

The attenuation corrected differential reflectivity is obtained according to Equation 41.

$$Z_{dr}(corr) = Z_{dr} + PIA_h - PIA_v \tag{41}$$

The attenuation corrected reflectivity and corrected differential reflectivity are more accurate values for data interpretation than the direct radar moments. The validation of the radar reflectivity values is shown in this research work. This method can be applied to radars operating at any frequency band which lies in the Rayleigh scattering region. Although we only show the relationships developed in this work for the Ku and X-bands, we can explore further research for obtaining relationships for the Ka-band radars. We can apply this algorithm to both PPI and RHI scan data.

5.4. ATTENUATION CORRECTION FOR KU BAND DATA

5.4.1. D3R RADAR DATA AND ICE-POP 2018 FIELD CAMPAIGN.

The dual-frequency, dual-polarization, Doppler weather radar (D3R) was developed by NASA, Colorado State

Figure 5.13. The D3R radar deployed on a rooftop of a building in PyeongChang region, South Korea during the ICE-POP field campaign. Credits: Aron Dabrowski.

University and Remote Sensing Solutions as a collaborative effort to support the Global Precipitation Measurement (GPM) mission. The D3R radar operates at the frequency bands of Ku (13.9 GHz) and Ka (35.5 GHz). Some of the main features of the D3R include the use of a solid-state amplifier and a novel waveform composed of two consecutive, frequency modulated, frequency separated pulses [63]. The D3R radar operating at these high frequencies is affected by attenuation. The attenuation in the Ka band is much worse compared to the Ku band in the rain, but Ka band radar has the advantage of observing smaller ice hydrometeors. This advantage is because as the wavelength of the radar increases the ability to detect smaller size hydrometeors increases. So the Ka-band radar is much more useful for capturing snow observations.

FIGURE 5.14. The maximum unambiguous range coverage of the D3R radar during ICE-POP field campaign. Credits: Google Earth.

During the past seven years, the D3R has participated in various field campaigns collecting quality data [64]. The various field campaigns in which D3R participated include the GPM Cold-season Precipitation Experiment (GCPEx), Olympic Mountain Experiment (OLYMPEX), Integrated Precipitation and Hydrology Experiment (IPHEx), Iowa Flood Studies (IFloodS) and International Collaborative Experiment during the PyeongChang Olympics and Paralympic winter games 2018 (ICE-POP). In this work, the data collected during the ICE-POP field campaign is discussed.

The ICE-POP field campaign held in the PyeongChang region of South Korea had many weather sensing instruments from around the globe to capture and understand winter precipitation better. The D3R radar which operates at Ku and Ka was also deployed, which had the advantages of high-frequency radar with large spatial coverage for capturing remote sensing observations of both rain and snow. The picture of D3R deployed at the DaegwallYeong Weather Office is shown in Figure 5.13. The 40 km unambiguous range coverage of the D3R radar is shown in Figure 5.14. Studying winter precipitation using D3R radar opens doors for many research fields. Therefore, providing accurate data for researchers and scientists around the world is a priority task. Though the D3R radar was well calibrated during the campaign, the effects of attenuation need to be corrected to provide quality data to end users. The D3R Ku band radar data is used here to present the performance of the attenuation correction algorithm.

The new algorithm for attenuation correction for all hydrometeors used on the D3R Ku band radar is explained next and the performance is studied. The algorithm performs attenuation correction as explained in Section 5.3, but the theoretical relationships between attenuation and specific phase is based on simulations at Ku band. Also, it should be noted that no prior work has been done to correct for attenuation for ice hydrometeors in the D3R radar.

To study the performance of the algorithm, we present two case studies from ICE-POP campaign data in this work. The first case study is for a rain case which was captured in early November and the second case study was captured in late February, when it was the peak snow season in PyeongChang region. Figure 5.15 shows the various radar moments from an RHI scan corresponding to a rain case. This data was collected on November 10, 2017 at 07:34 UTC. From this figure, we can see that the storm is extending up to 6 km in height. The melting layer of this case is around 1200 m. The specific phase and hydrometeor classification outputs are obtained after applying the DROPS2.0 algorithm to the data.

From the Figure 5.15 (a), it can be seen that the reflectivity values go up to 40 dBZ below the melting layer around 5 km in range. Regions with high reflectivity values will cause the radar data to get attenuated as they pass through the peak region of the storm. It should also be noted that in the Figure 5.15 the data at low elevation angles after 10

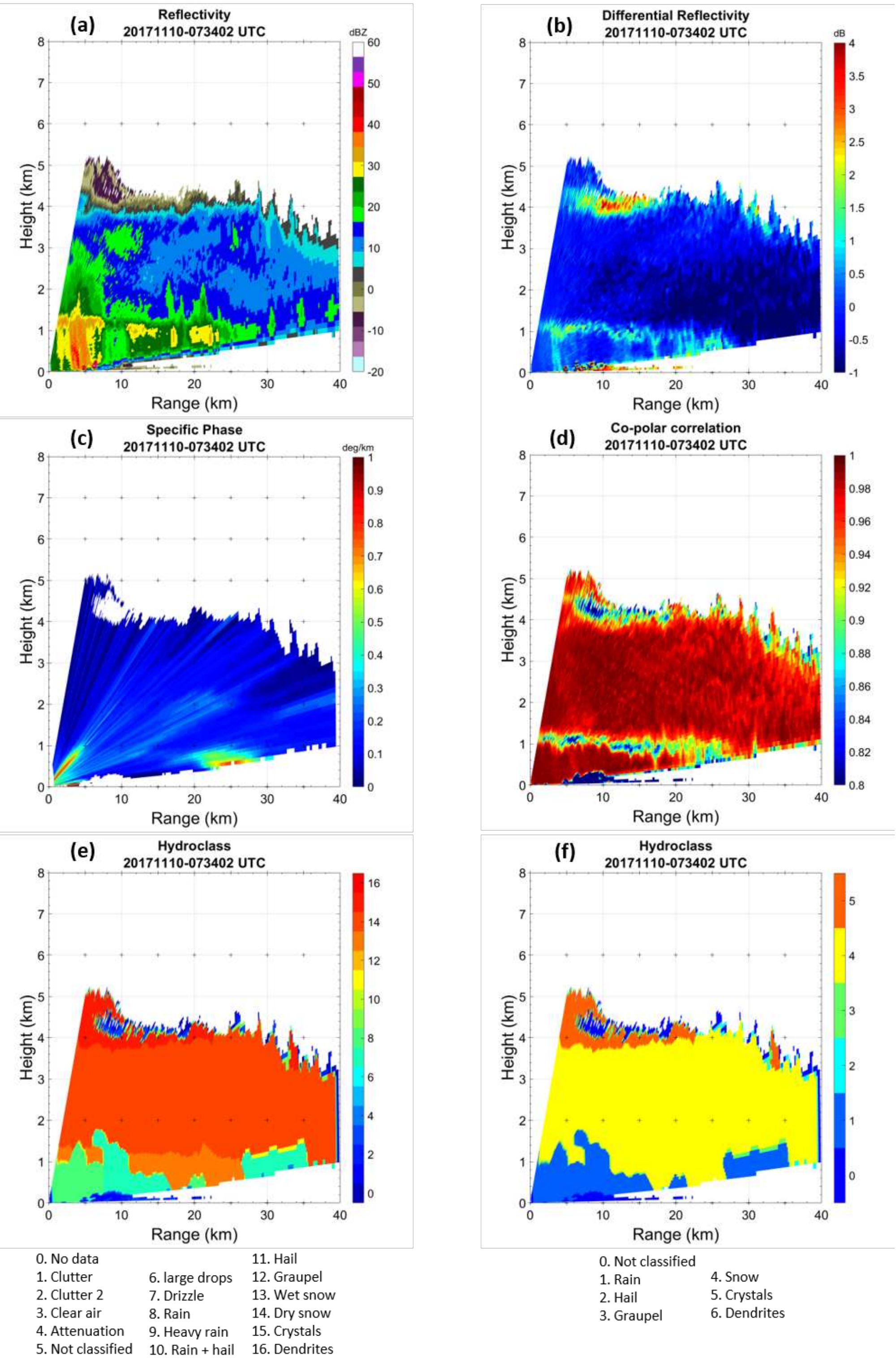

Figure 5.15. Radar moments for the D3R Ku band for RHI scan data collected on November 10, 2017 at 07:34 UTC. (a) Observed Reflectivity, (b) Observed Differential reflectivity, (c) Specific phase, (d) Copolar correlation (e) and (f) Hydrometeor classification output.

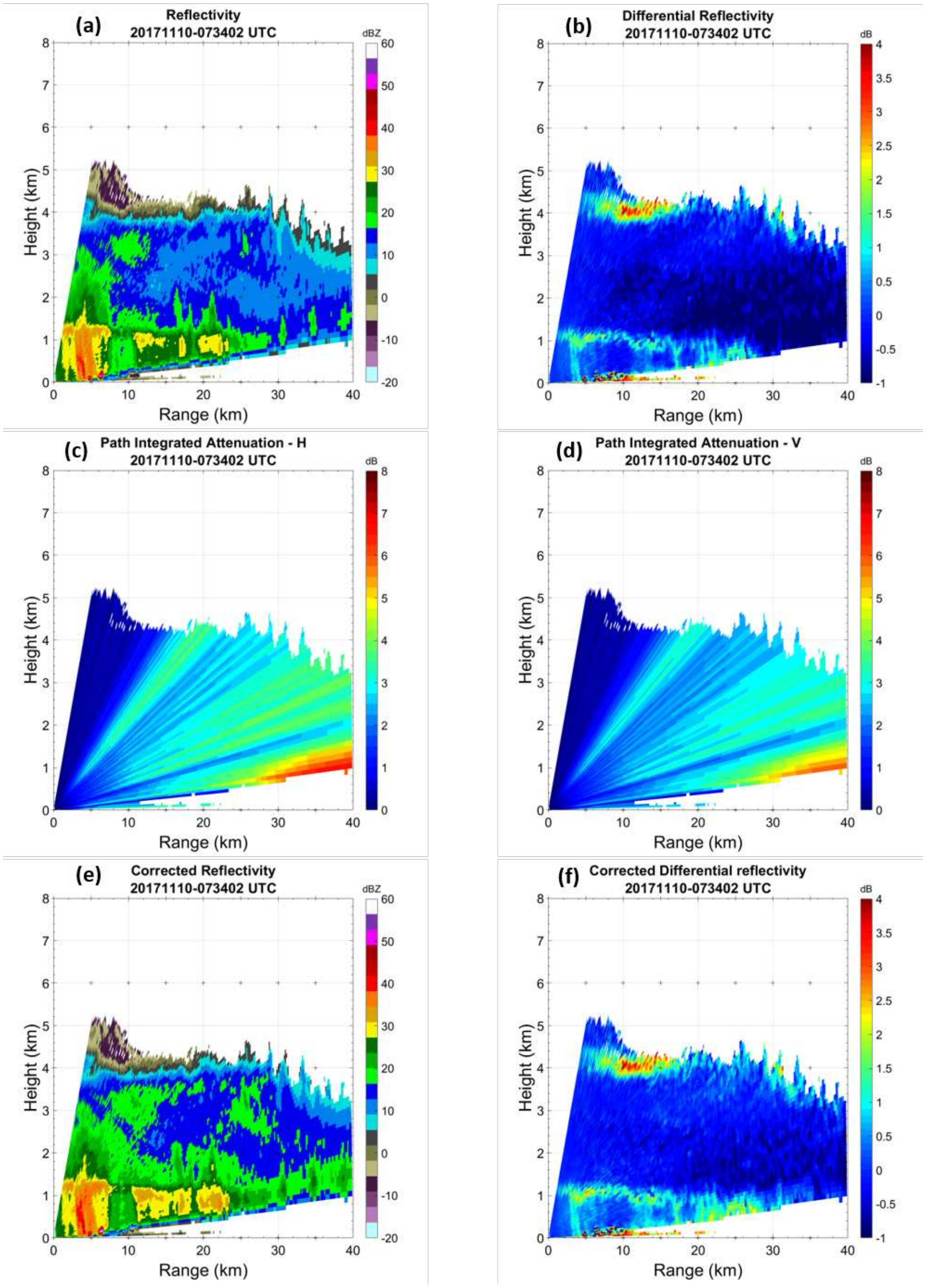

Figure 5.16. Radar moments for the D3R Ku band for RHI scan data collected on November 10, 2017 at 07:34 UTC. (a) Observed Reflectivity, (b) Observed Differential reflectivity, (c) Path integrated attenuation - H Pol, (d) Path integrated attenuation - V Pol, (e) Corrected reflectivity and (f) Corrected differential reflectivity.

km range is not present. This is due to the blockage of the radar beam by the mountains present in the region. The other moments captured by the radar are also shown. We can clearly see the melting layer in the differential reflectivity and co-polar correlation pictures. The differential reflectivity is shown in Figure 5.15 (b); the values are higher below the melting layer compared to above the melting layer. Figure 5.15 (e) shows the hydrometeor classification of all 16 classes from the DROPS2.0 algorithm, Figure 5.15 (f) shows the simplified hydrometeor classification, used to obtain the attenuation parameters and correct the data.

Figure 5.16 shows the attenuation parameters and the corrected reflectivity computed using the new algorithm. Figures 5.16 (c) and (d) shows the path integrated attenuation at horizontal and vertical polarizations. The specific attenuation in the rain region is greater compared to the snow region. As seen in the equation earlier, the specific attenuation values get added to construct the path integrated attenuation. It can be seen from this figure that as the elevation angle increases, the attenuation decreases, which is dependent on the specific phase. Also, the PIA increases as we go along the range which is as expected. Figure 5.16 (e) shows the attenuation corrected Ku band reflectivity. Comparing this figure with 5.16 (a), it can be seen that the rain attenuation and the snow attenuation have been corrected and the results look visually better. Figure 5.16 (f) shows the attenuation corrected Ku band differential reflectivity. Comparing this figure with 5.16 (b), it can be seen the value are slightly increased in the farther range bins.

The second case study considered is for a snow case captured during a huge snow storm on the February 28, 2018. The RHI scan considered here is taken during the peak time of the snow storm. Figure 5.17 shows the various radar moments from this RHI scan. This data was collected at 11:25 UTC. For this snow storm, the vertical profile extended up to 8

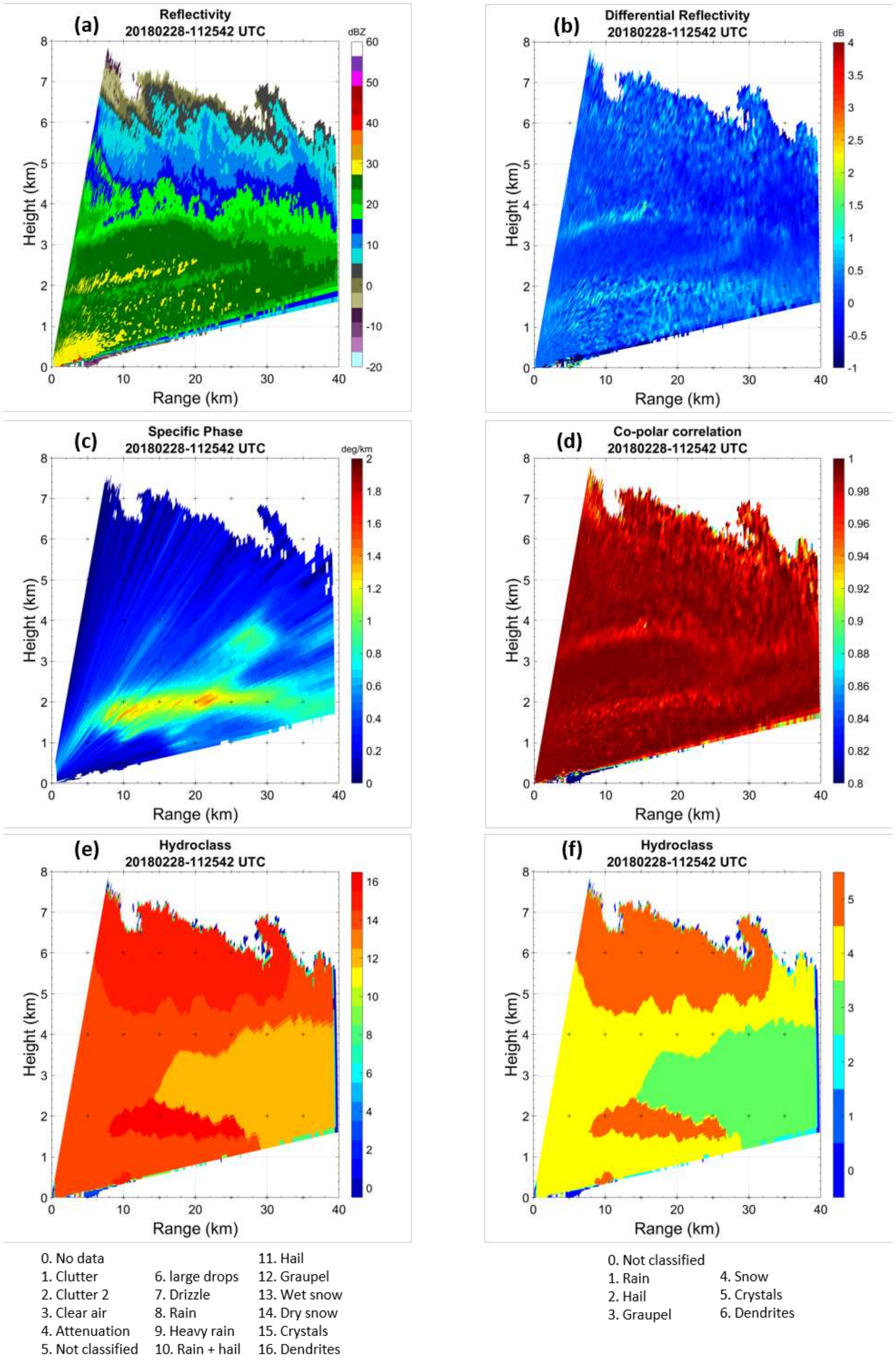

FIGURE 5.17. Radar moments for the D3R Ku band for RHI scan data collected on February 28, 2018 at 11:25 UTC. (a) Reflectivity, (b) Differential reflectivity, (c) Specific phase, (d) Copolar correlation (e) and (f) Hydrometeor classification output.

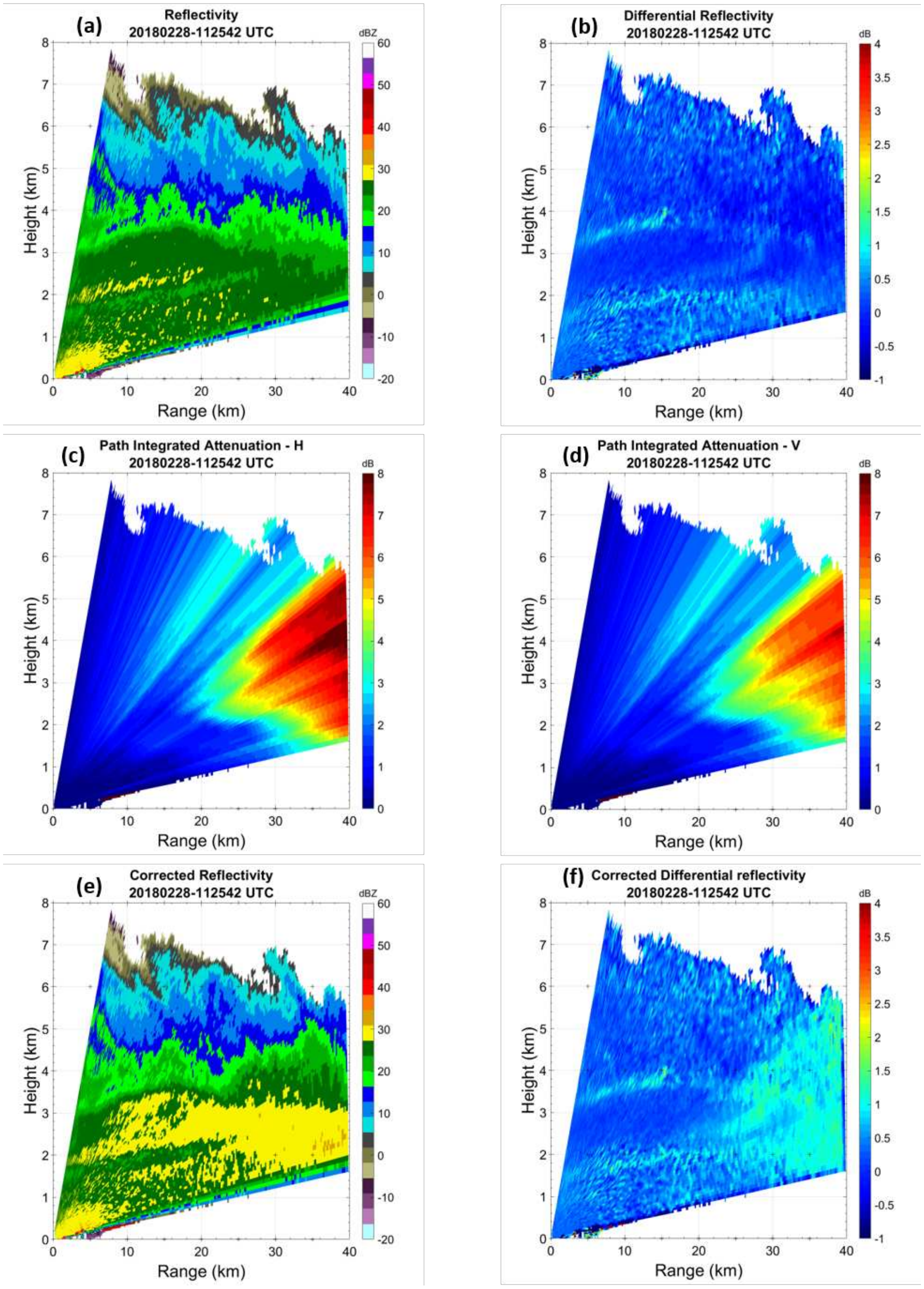

Figure 5.18. Radar moments for the D3R Ku band for RHI scan data collected on February 28, 2018 at 11:25 UTC. (a) Observed Reflectivity, (b) Observed Differential reflectivity, (c) Path integrated attenuation - H, (d) Path integrated attenuation - V, (e) Corrected reflectivity and (f) Corrected differential reflectivity.

km in height. Data up to 6 km is shown in this figure. Since this is a snow case, the melting layer can be considered to be below the surface of the ground. The specific phase and hydrometeor classification outputs are obtained after applying the DROPS2.0 algorithm for the data. Since DROPS2.0 corrects attenuation only until the melting layer for rain particles, no attenuation data from DROPS2.0 is used in the new algorithm for this case.

From the Figure 5.17 (a) we can see reflectivity values going up to 30 dBZ. These reflectivity values are sufficient enough to get noticeable attenuation in the snow at far ranges. It should also be noted that in the figure, the data at low elevation angles after 5 km range is not present. This is due to the blockage of the radar beam by the mountains for this scan. From figures 5.17 (b), (c) and (d), we can see a band of bright specific phase. In the same band, the differential reflectivity increases and the co-polar correlation decreases. This corresponds to a mixture of ice crystals and aggregates present. More details regarding this study can be found in [65]. Figure 5.17 (e) shows the hydrometeor classification of all 16 classes from the DROPS2.0 algorithm, figure 5.17 (f) shows the simplified hydrometeor classification which was used to obtain the attenuation parameters and correct the observed radar data.

Figure 5.18 shows the attenuation parameters and the corrected reflectivity computed using the new algorithm. It was observed from the specific attenuation obtained for different ice hydrometeors that the attenuation is peaking near the band where ice crystals and aggregates are present; this corresponds to the peak in specific phase. Figure 5.18 (c) and (d) show the path integrated attenuation for horizontal and vertical polarizations. It can be seen from this figure that as the elevation angle increases, the attenuation decreases as expected with the theoretical simulations. As expected, the PIA increases as we go along the range. Figure 5.18 (e) shows the attenuation corrected Ku band reflectivity. Comparing this figure

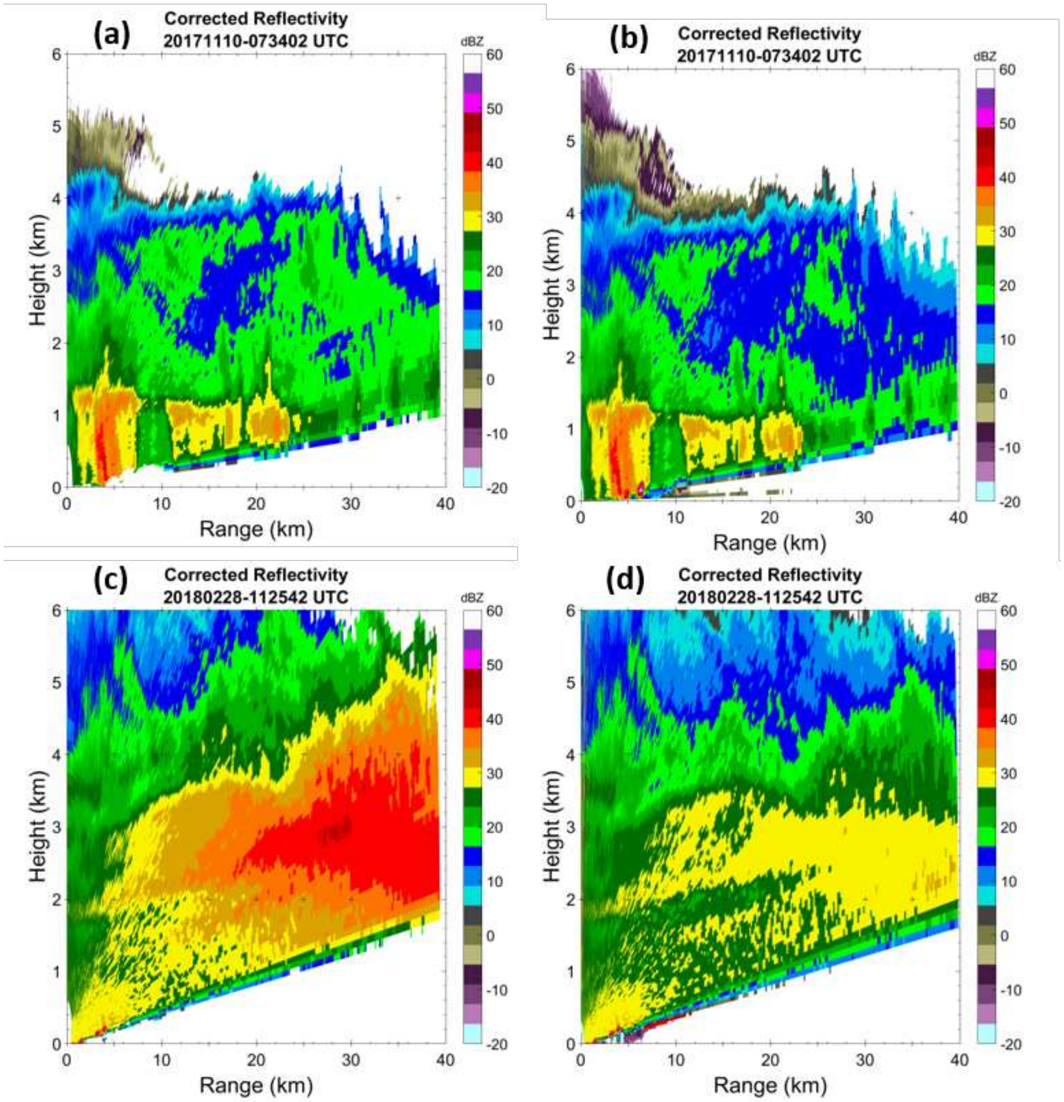

Figure 5.19. Comparison of attenuation corrected reflectivities considering rain attenuation parameters for the complete scan versus the new method for attenuation correction (a) and (b) November 10, 2017 at 07:34 UTC case, (c) and (d) February 28, 2018 at 11:25 UTC case.

with 5.18 (a), it can be seen that the snow attenuation has been corrected and the results look better. Figure 5.18 (f) shows the attenuation corrected Ku band differential reflectivity. Comparing this Figure with 5.18 (b), it can be seen the value are slightly increased in the farther range bins.

In prior literature, many researchers correct the attenuation caused by hydrometeors for the full scan (all hydrometeors) using the rain attenuation parameters determined. This way of attenuation correction will yield large or incorrect results in the ice region. Other researchers do only attenuation correction until the melting level where the rain hydrometeors end. This method will give correct results only till the melting layer and the data in the ice region will still be inaccurate. The new algorithm in this work which corrects the attenuation for rain and ice regions effectively will provide a more accurate data set to be used. Figure 5.19 shows the comparison of the results of attenuation correction considering rain parameters for the full scan and using the new algorithm for rain and snow cases. From these figures, it can clearly be seen that using rain parameters for the full scan overestimates the reflectivity value in the ice region. With the new algorithm, the results look reasonable.

Comparing the radar attenuated corrected values to the actual truth value of reflectivity is a challenging task. Direct and indirect methods are used to check the accuracy of attenuation correction which was done for the radar data. In the direct way of comparison, the attenuated corrected values such as reflectivity are compared with reflectivity data from other instruments such as disdrometers or other radars. It should be noted that the system bias should be accounted for when comparing the data using two different platforms. The indirect way of comparison involves comparing the derived products such as rain rate, which use the attenuated corrected variables. For example, the rain rate obtained using the attenuated corrected reflectivity could be compared to the rain gauges. A close match would indicate correct attenuation correction has been done for the data.

To check the accuracy of attenuation correction done for reflectivity data of the D3R Ku band, data from a Parsivel disdrometer which was located at YongPyong Cloud Physics Observatory (YPO) is considered. This disdrometer is located 5.7 km away and approximately at 233 degree azimuth from the location of the D3R radar. The disdrometer's reflectivity values were computed using the Equation 42.

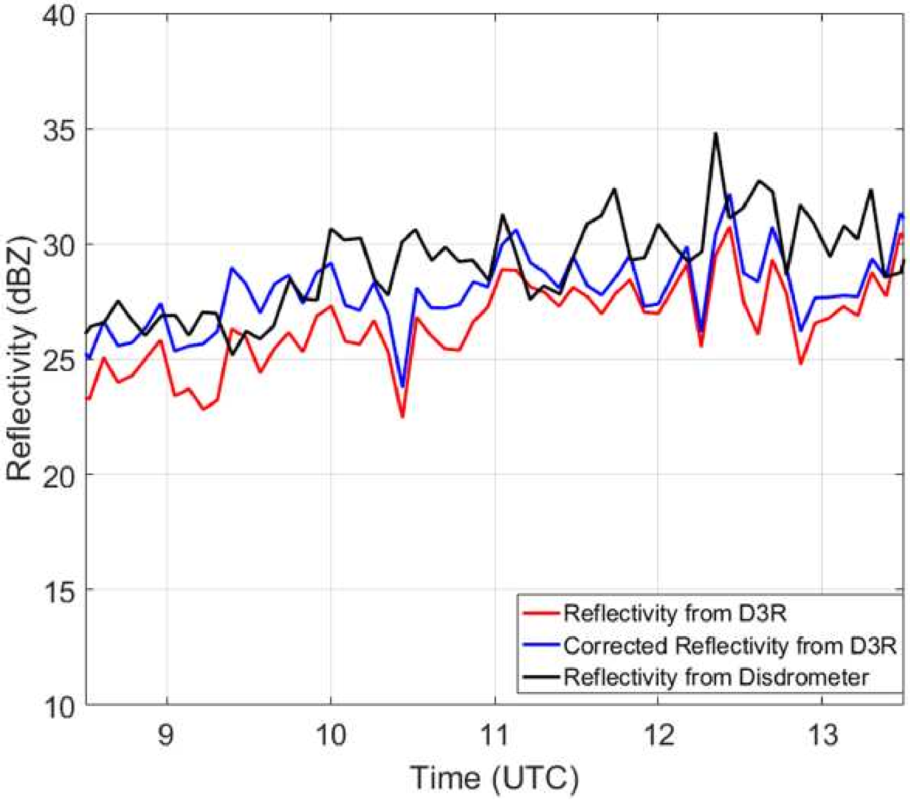

FIGURE 5.20. Comparison of observed reflectivity and attenuation corrected reflectivity of D3R data with reflectivity from a Parsivel disdrometer.

$$Z_h = \frac{\lambda^4}{\pi^5 |k_w|^2} \int \sigma_h(D) N(D) dD \tag{42}$$

where k_w is the dielectric factor of water, λ is the wavelength and σ_h is the radar cross section, which is computed using the scattering model.

In Figure 5.20, the reflectivity data taken on February 28, 2018 from 08:30 to 13:30 UTC is considered. This is the same day from which the snow case for attenuation correction was considered. From the Figure 5.20, it can be seen that the uncorrected reflectivity from D3R has lower values than the corrected reflectivity. Also, the attenuated corrected reflectivity

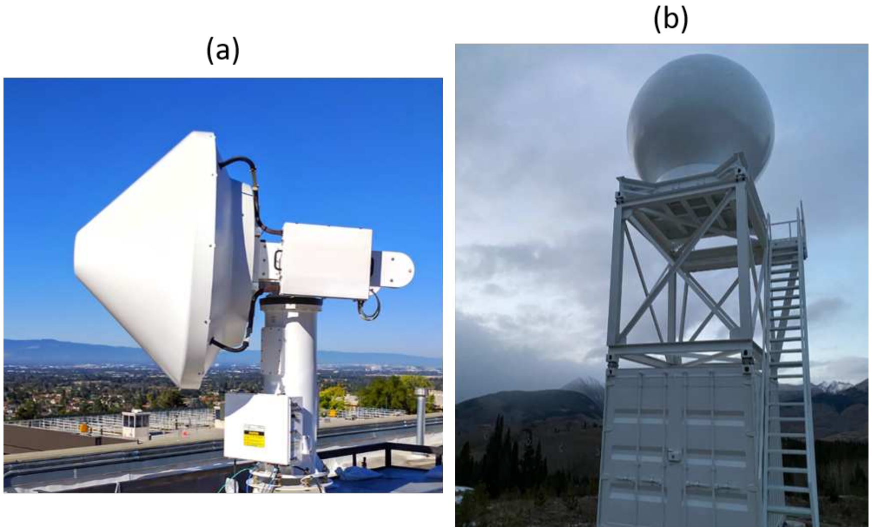

Figure 5.21. (a) X-band radar deployed at Santa Clara, California and (b) X-band radar deployed at Mt. Crested Butte, Colorado.

values are much closer to the disdrometer-derived reflectivity values which indicate that the attenuation correction gives us more accurate data.

5.5. Attenuation correction for X band data

In this section, the attenuation correction results obtained for the X-band radar data are discussed. The X-band radars deployed at Santa Clara, California (XSCV) and Mt. Crested Butte, Colorado (SAIL) are considered to study the performance of the attenuation correction algorithm at the X-band. The pictures of both the radars are shown in Figure 5.21.

The first case is taken from the XSCV radar; more details on this radar can be found in [33]. A stratiform precipitation case from this radar is considered here. The case study is for a rain case that was captured in early February. The data is taken from the February 8, 2019 at 22:38 UTC. We can see stratiform rain events in this region with a clear melting layer during the timeframe of the data.

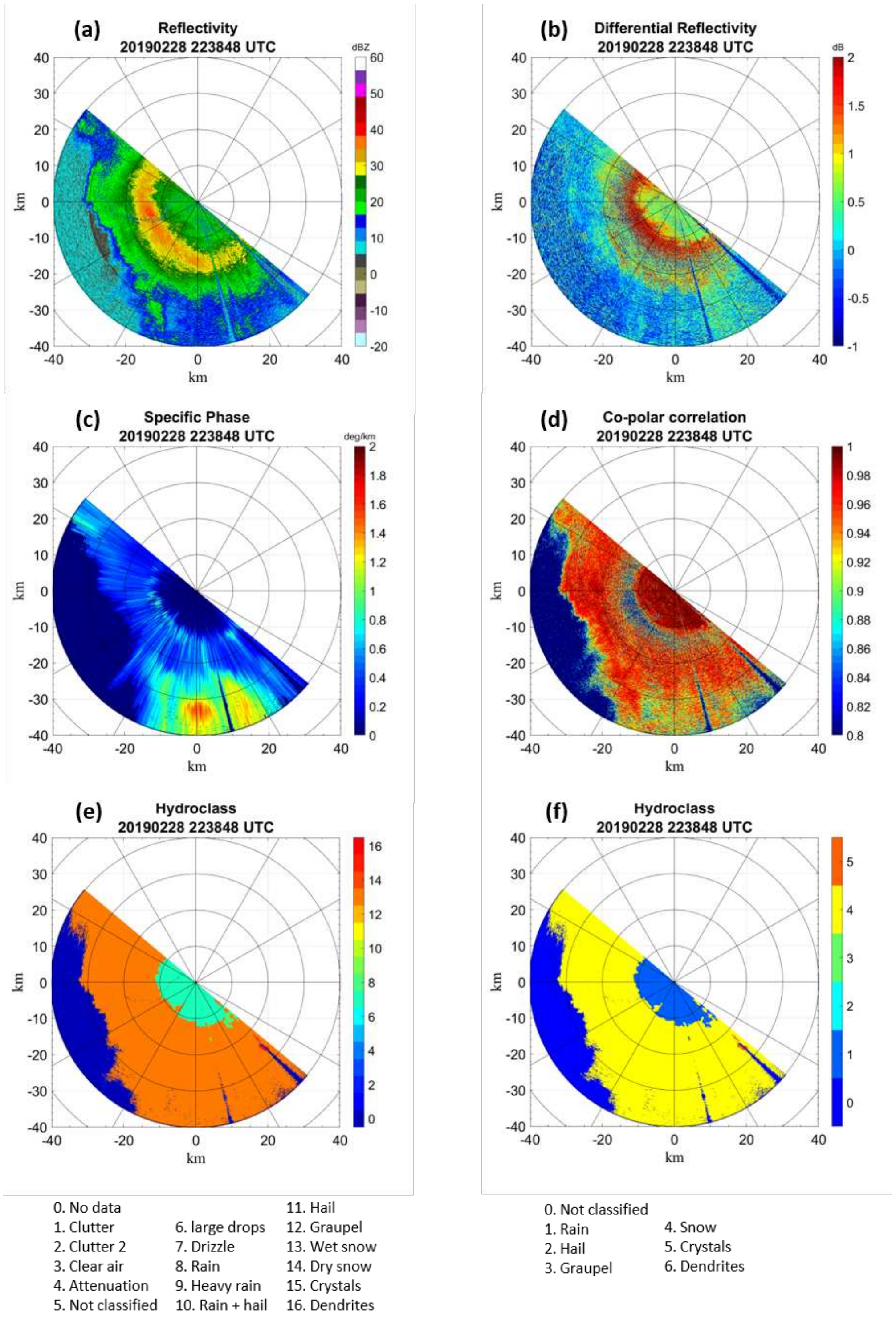

FIGURE 5.22. The X-band radar data and DROPS output for rain case on February 8, 2019 at 22:38 UTC. (a) uncorrected reflectivity, (b) uncorrected differential reflectivity (c) Specific phase, (d) Copolar correlation, (e) and (f) Hydrometeor classification output.

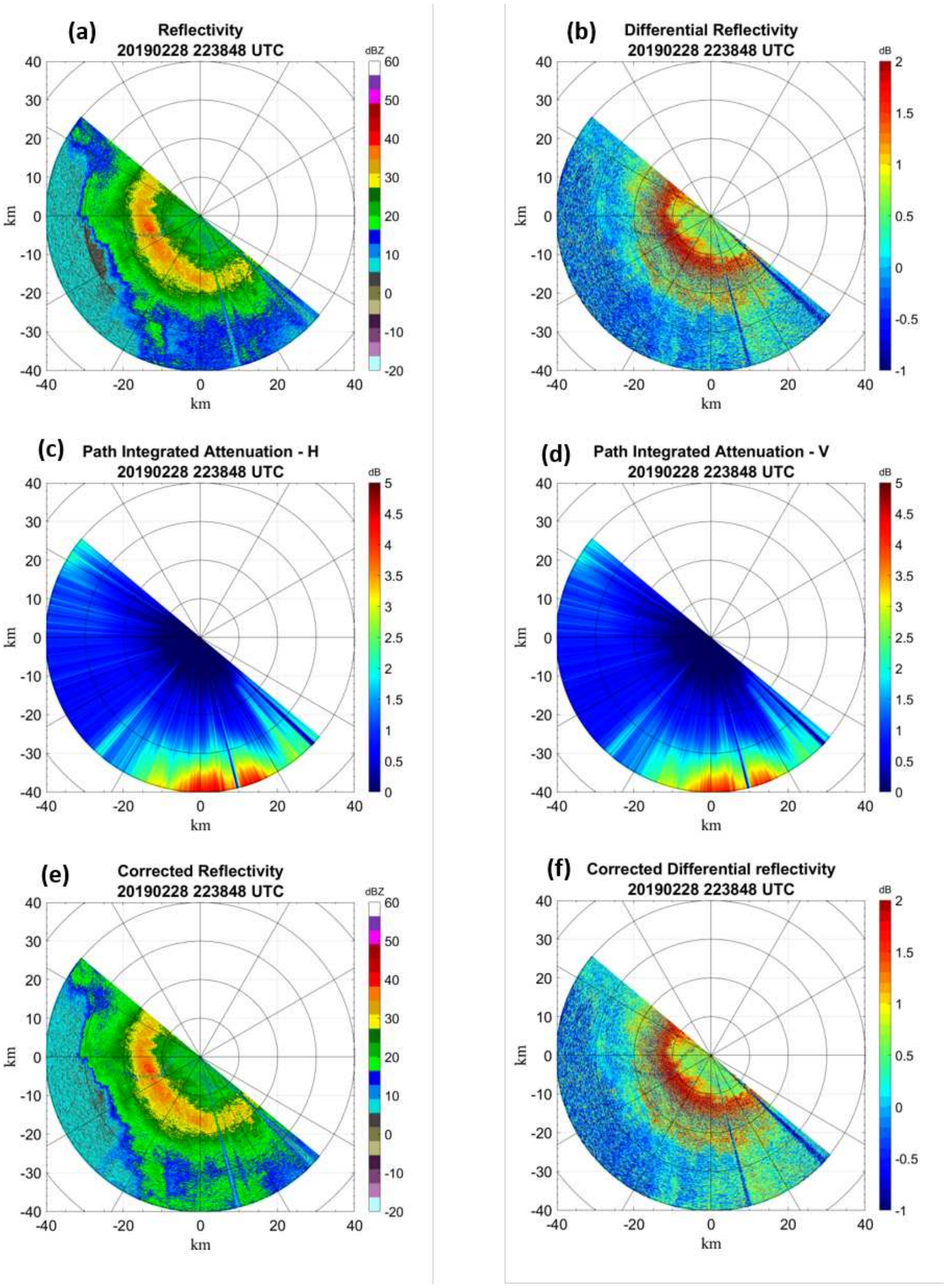

Figure 5.23. The X-band radar data and attenuation corrected output for rain case on February 8, 2019 at 22:38 UTC. (a) uncorrected Reflectivity, (b) uncorrected Differential reflectivity, (c) Path integrated attenuation - H, (d) Path integrated attenuation - V, (e) Corrected reflectivity and (f) Corrected differential reflectivity.

Figure 5.22 shows the PPI plots of the original data and the results obtained from the DROPS algorithm. Each range ring in the figure corresponds to 10 km in range. Figure 5.22 (a) shows the radar reflectivity without accounting for attenuation correction; this will be addressed as uncorrected/observed reflectivity from here on. It can be seen in this figure that a bright band is present in the data approximately 15 km in range. Figure 5.22 (b) shows the differential reflectivity, Figure 5.22 (c) show the specific phase and Figure 5.22 (d) shows the copolar correlation. The hydrometeor classification output from the DROPS2.0 algorithm is shown in Figures 5.22 (e) and (f). From the figures, it can be seen that closer to the radar, rain is present and then the snow takes over the PPI scan.

Figure 5.23 shows the attenuation parameters and the corrected reflectivity computed using the new algorithm. The specific attenuation was computed for this radar scan using the information of elevation angle, hydrometeor classification and specific phase. Since the specific phase values are greater in the southern region, it was observed that the specific attenuation values are higher here compared to other regions. Figure 5.23 (c) and (d) show the path integrated attenuation for horizontal and vertical polarizations. It can be seen from this figure that as the elevation angle increases, the attenuation decreases as expected with the theoretical simulations. Also, the PIA increases as we go along the range which is as expected. Figure 5.23 (e) shows the attenuation corrected X band reflectivity. Comparing this figure with 5.23 (a), it can be seen that the snow attenuation has been corrected and the results look better. Figure 5.23 (f) shows the attenuation corrected X band differential reflectivity. Comparing this figure with 5.23 (b), it can be seen the values are slightly increased based on the difference in path integrated attenuation at H and V polarizations.

The second and third cases are taken from the SAIL X-band radar. Snow cases are considered from the radar data during peak winter in Colorado region. The second case

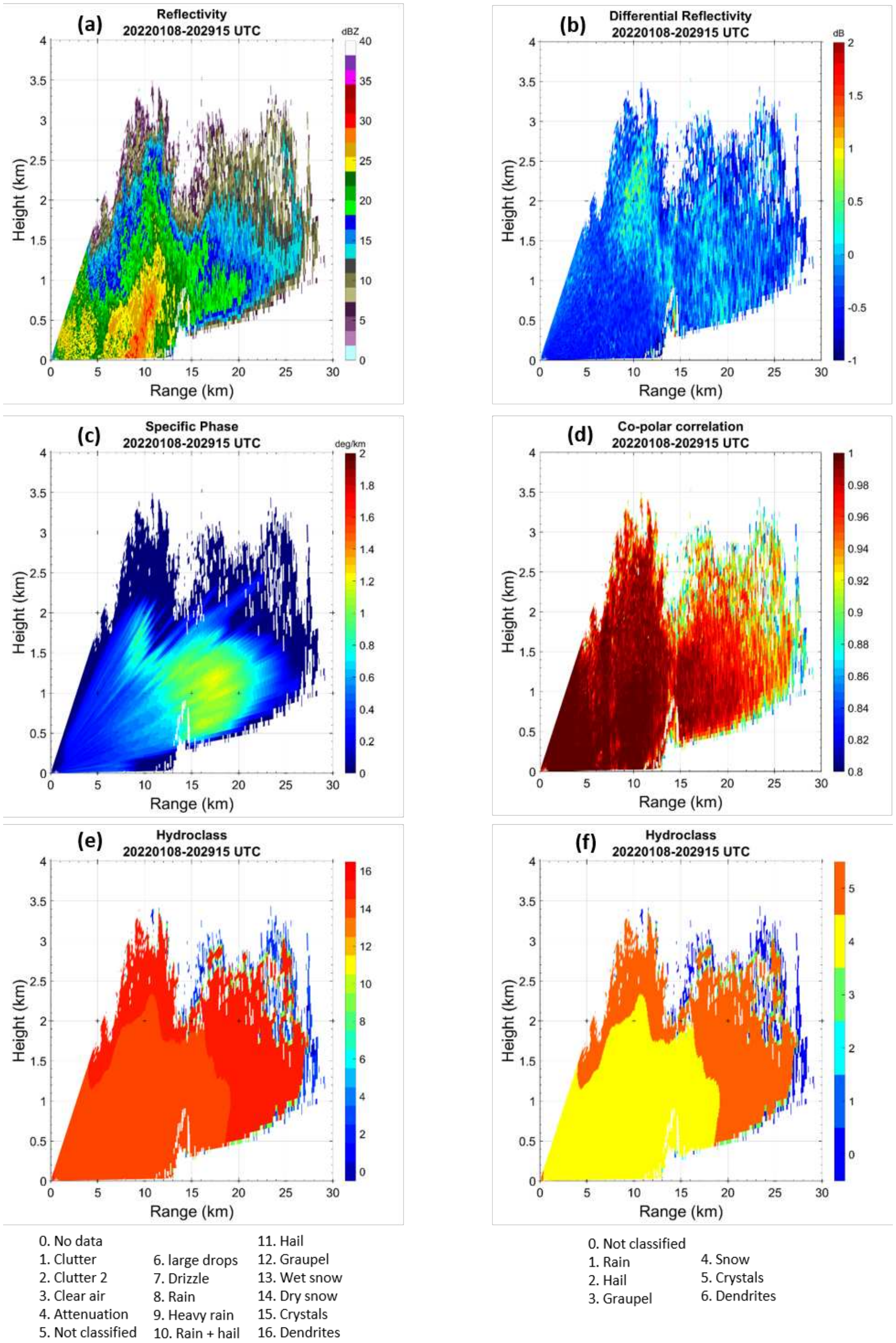

Figure 5.24. The X-band radar data and DROPS output for rain case on January 8, 2022 at 20:30 UTC. (a) uncorrected reflectivity, (b) uncorrected differential reflectivity (c) Specific phase, (d) Copolar correlation, (e) and (f) Hydrometeor classification output.

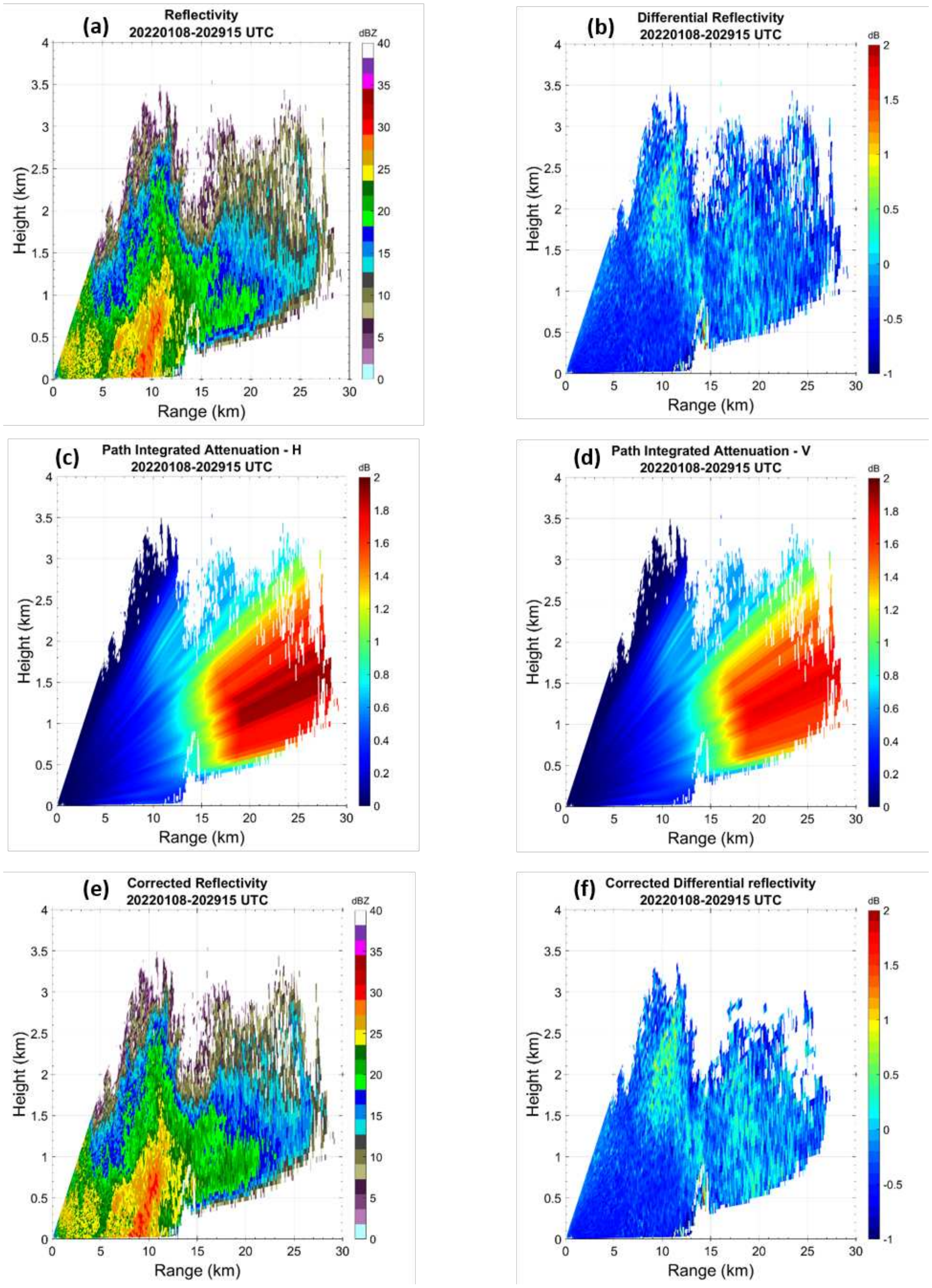

FIGURE 5.25. The X-band radar data and attenuation corrected output for rain case on January 8, 2022 at 20:30 UTC. (a) uncorrected Reflectivity, (b) uncorrected Differential reflectivity, (c) Path integrated attenuation - H, (d) Path integrated attenuation - V, (e) Corrected reflectivity and (f) Corrected differential reflectivity.

data is taken from the January 8, 2022 at 20:30 UTC. We can see from the case data that the snow storm is going up to 3 km in height and is present up to 30 km of observational range of the radar.

Figure 5.24 shows the PPI plots of the original data and the results obtained from the DROPS algorithm. The maximum unambiguous range of the radar is 40 km. Data until 30 km is shown in the radar plots. Figure 5.24 (a) shows the radar reflectivity without accounting for attenuation correction. It can be seen in this figure that the reflectivity values are higher in the lower heights, which may indicate the snow aggregation process taking place and large snow aggregates present. Figure 5.24 (b) shows the differential reflectivity, Figure 5.22 (c) show the specific phase and Figure 5.24 (d) shows the copolar correlation. The hydrometeor classification output from the DROPS2.0 algorithm is shown in figures 5.24 (e) and (f). From the figures, it can be seen that at lower heights, snow aggregates are present and at higher heights ice crystals are present.

Figure 5.25 shows the attenuation parameters and the corrected reflectivity computed using the new algorithm. The specific attenuation was computed for this radar scan using the information of elevation angle, hydrometeor classification and specific phase. Figure 5.25 (c) and (d) show the path integrated attenuation for horizontal and vertical polarizations. It can be seen from this figure that as the elevation angle increases, the attenuation decreases as expected with the theoretical simulations. Also, the PIA increases as we go along the range which is as expected. We can see attenuation of about 2 dB in the radar scan, which needs to be corrected. Figure 5.25 (e) shows the attenuation corrected X band reflectivity. Comparing this figure with 5.25 (a), it can be seen that the snow attenuation has been corrected and the results look better. Figure 5.25 (f) shows the attenuation corrected X band differential reflectivity. Comparing this figure with 5.25 (b), it can be seen the values are slightly increased based on the difference in path integrated attenuation at H and V polarizations.

The third case data is taken from the December 24, 2021 at 08:28 UTC. We can see from the case data that the snow storm is going up to 3 km in height and is present in the entire observational range of the radar.

Figure 5.26 shows the PPI plots of the original data and the results obtained from the DROPS algorithm. The maximum unambiguous range of the radar is 40 km. Figure 5.26 (a) shows the radar reflectivity without accounting for attenuation correction. It can be seen in this figure that the reflectivity values are lower compared to the previous case considered. Figure 5.26 (b) shows the differential reflectivity, Figure 5.26 (c) show the specific phase and Figure 5.26 (d) shows the copolar correlation. The hydrometeor classification output from the DROPS2.0 algorithm are shown in figures 5.26 (e) and (f). From the figures, it can be seen that at lower heights, snow aggregates are present and at higher heights ice crystals are present.

Figure 5.27 shows the attenuation parameters and the corrected reflectivity computed using the new algorithm. The specific attenuation was computed for this radar scan using the information of elevation angle, hydrometeor classification and specific phase. Figure 5.27 (c) and (d) show the path integrated attenuation for horizontal and vertical polarizations. It can be seen from this figure that as the elevation angle increases, the attenuation decreases as expected with the theoretical simulations. Also, the PIA increases as we go along the range which is as expected. We can see attenuation close to 2 dB in the radar scan present which needs to be corrected. Figure 5.27 (e) shows the attenuation corrected X band reflectivity. Comparing this figure with 5.27 (a), it can be seen that the snow attenuation has been corrected and the results look better. Figure 5.27 (f) shows the attenuation corrected X

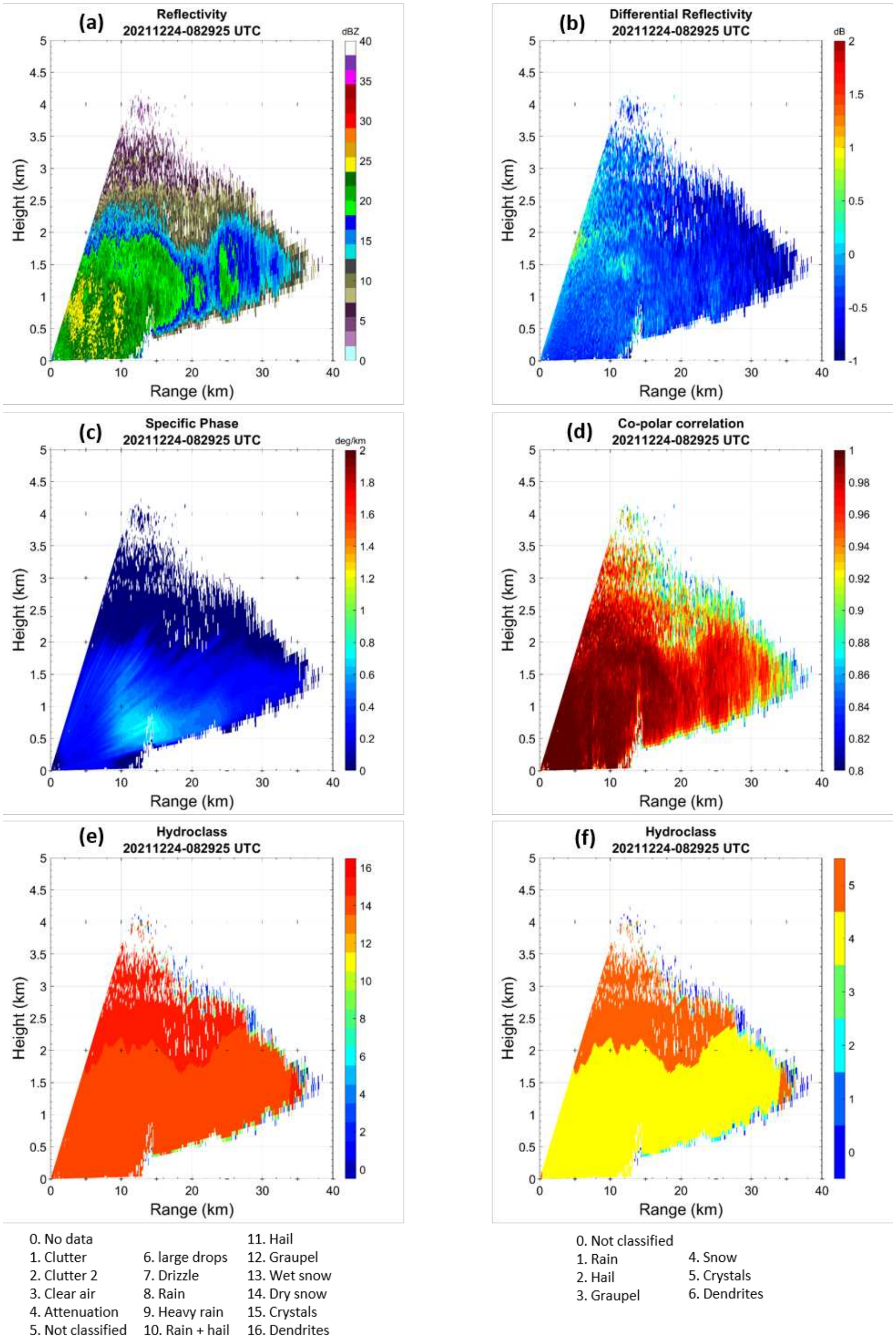

Figure 5.26. The X-band radar data and DROPS output for rain case on December 24, 2021 at 08:28 UTC. (a) uncorrected reflectivity, (b) uncorrected differential reflectivity (c) Specific phase, (d) Copolar correlation, (e) and (f) Hydrometeor classification output.

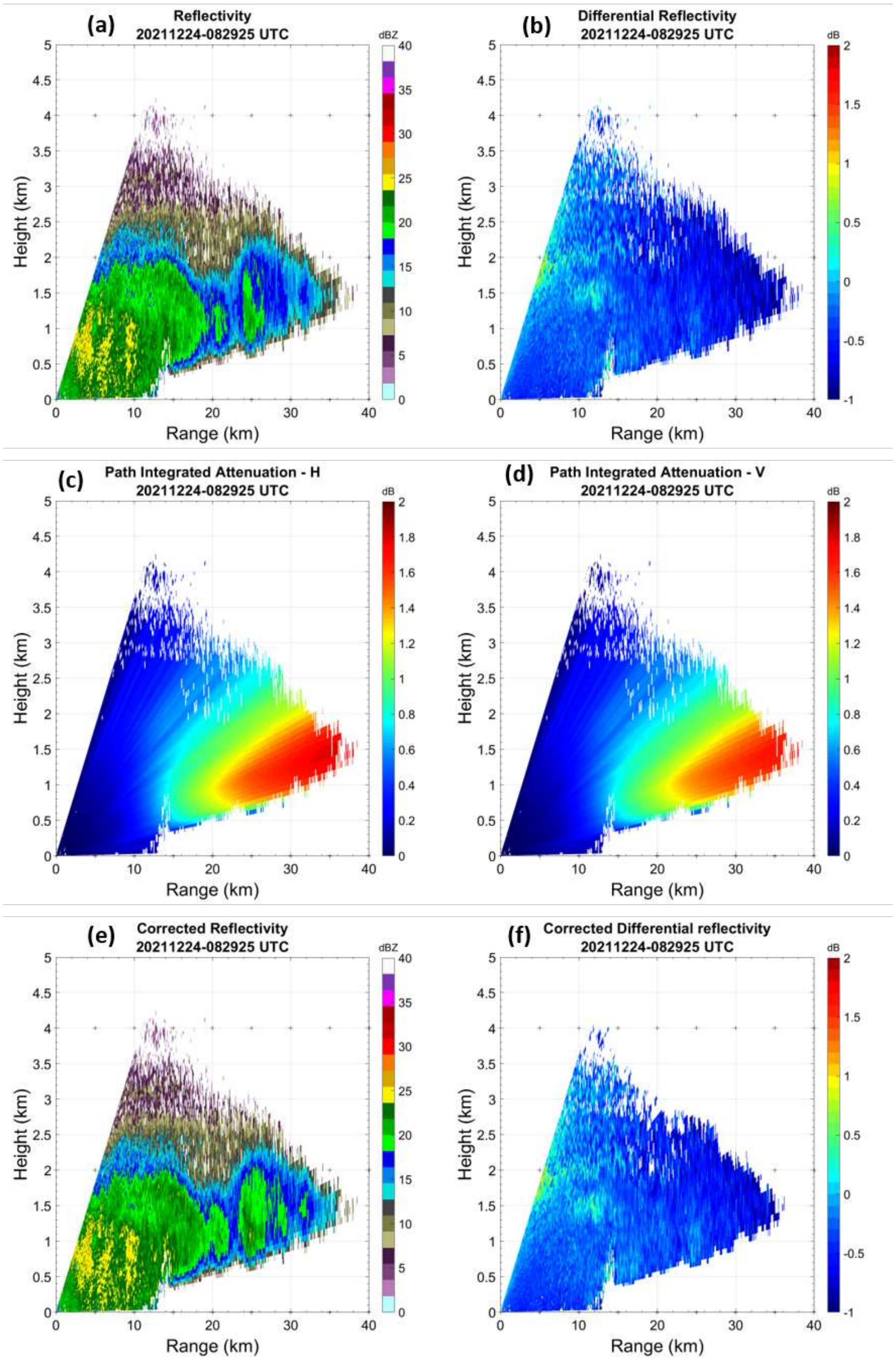

Figure 5.27. The X-band radar data and attenuation corrected output for rain case on December 24, 2021 at 08:28 UTC. (a) uncorrected Reflectivity, (b) uncorrected Differential reflectivity, (c) Path integrated attenuation - H, (d) Path integrated attenuation - V, (e) Corrected reflectivity and (f) Corrected differential reflectivity.

band differential reflectivity. Comparing this figure with 5.27 (b), it can be seen the values are slightly increased based on the difference in path integrated attenuation at H and V polarizations.

Chapter 6

System analysis of automobile radars for precipitation mapping at regional scale

Previously in this dissertation, a brief introduction to automobile radars was provided. In the previous chapters, the science and technology aspects of using automobile radar for meteorological applications were explained in detail. In this chapter, the systems aspect of the automobile radar for meteorological applications, in specific obtaining precipitation maps are discussed. Simulation studies are carried out and a potential system of automobile radar network for precipitation mapping is also discussed.

6.1. Simulation studies of precipitation mapping using automobile radar network

Precipitation maps are images or data of the amount of precipitation over a particular geographical area of interest. Previous studies for mapping precipitation used many methods, including nowcasting algorithms [66]. Short-term forecasting, also known as nowcasting of rainfall typically within a few hours is widely used in providing early warning and therefore, has many practical applications [67]. Although it is common for these maps to represent rain rate or rain accumulation, we can also obtain snow rates and snow accumulation. In this study, the focus is limited to rain hydrometeors.

Precipitation maps obtained at the ground level are a very useful tool for hydrologists as they can use this to compute the amount of surface runoff and map the water levels in the urban regions. There are various ways to obtain precipitation maps. To obtain coverage

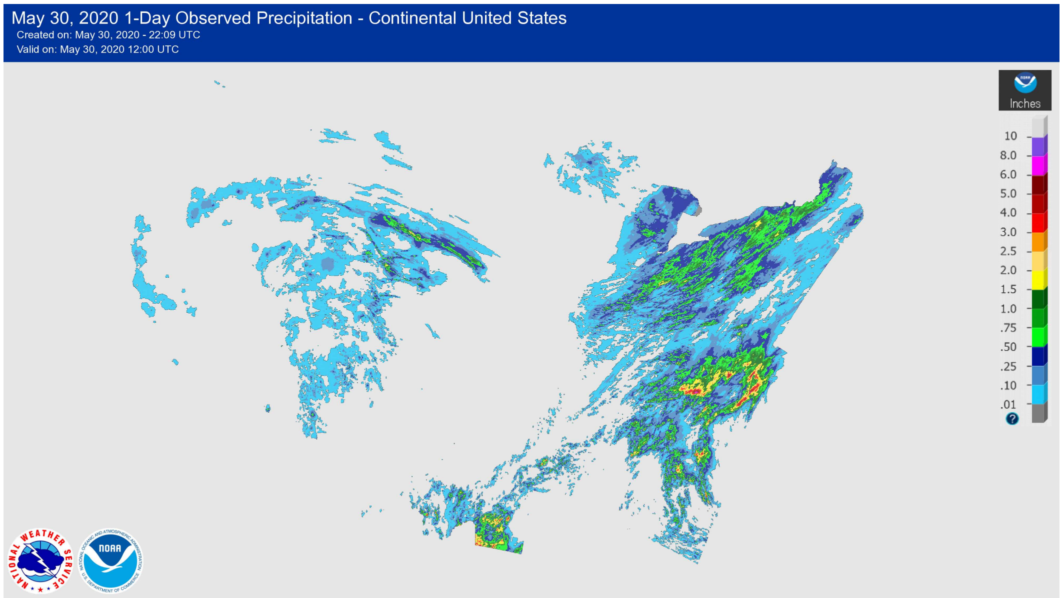

FIGURE 6.1. Observed precipitation map for May 30, 2020 for the continental United States [10].

over a large area, weather radars and satellites are the most preferred tools used for this purpose.

Many real-time systems which are currently operating provide real-time rain rates and accumulation in various parts of the USA. The NSF and NOAA have a webpage that puts out the observed precipitation map over the continental United States constantly. An image of the quantitative precipitation accumulation is shown in Figure 6.1. From this figure, it can be seen that using this information; one can obtain the amount of rain in a particular region/area. It should be noted that the resolution as we zoom the image to any particular city will be limited.

Simulation studies are essential before deploying any system in the real-world. Using simulations, we can study and modify the influence of various parameters on the system. Simulation studies gives us useful information to design an efficient and robust system. The potential use of a network of automobile radars for precipitation mapping is looked at by

Table 6.1. Vehicle ownership in the U.S. as of 2016

Jurisdiction	2016 households without vehicles (%)	2016 vehicles per household (%)
New York, New York	54.4	0.63
Jersey City, New Jersey	37.1	0.85
San Francisco, California	29.9	1.10
Miami, Florida	18.6	1.24
Atlanta, Georgia	16.4	1.28
Los Angeles, California	12.2	1.62
Tempe, Arizona	9.4	1.65
Dallas, Texas	9.1	1.59
FortWorth, Texas	4.8	1.83

performing simulations at the system level. The detailed discussion on the simulations is explained next.

6.2. Study area considered for simulation

For studying the potential of using automobile radars to map precipitation in urban areas, the Dallas-FortWorth (DFW) urban region is considered in this study. There are many reasons which are explained next as to why DFW area was chosen for this study. Some of the vehicle statistics support that the DFW region has a large number of automobiles on the road. According to the statistics of automobiles report, there are more than 22 million automobiles on the road in Texas as of 2018 [68]. Table 6.1 shows a 2016 vehicle ownership report that indicates that the DFW region has more number of vehicles per household compared to other major urban cities in the U.S.

Also, the DFW region is a perfect location to study urban precipitation as it houses many precipitation instruments, including weather radars, rain gauges and disdrometers. The CASA X-band radar network is also located in this region. The CASA radar network comprises eight X-band radars. Additionally, the National Weather Service KFWS S-band radar is present in the region. This radar network produces precipitation accumulation

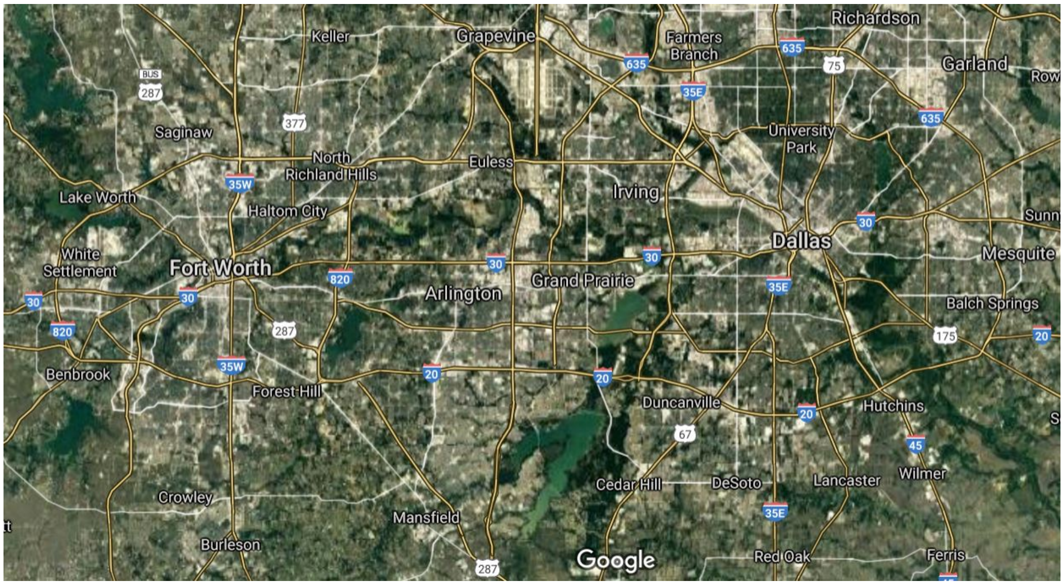

Figure 6.2. A Google earth view of the Dallas-FortWorth (DFW) region considered for the simulation study. Credits: Google Earth.

every 1 min, 30-min and hourly. More information about the CASA radar network and the precipitation maps generated can be found in [69].

For the simulation study the DFW area between 32.5 N to 33 N degree latitudes and 96.5 W to 97.5 W longitudes is considered. A google map image of this area is shown in the Figure 6.2.

6.3. Precipitation map simulation studies considering automobile radars

As explained earlier in the dissertation, considering each automobile produces a rainfall rate estimate, we end up with a large number of rainfall rate estimates from a small region. This is considering the automobiles have radars installed on them and have the capability to estimate precipitation values. For simulating the radar data from automobiles, the road data of the particular region of interest should be obtained as the first step.

The US road map data can be obtained from the United States Census Bureau [70] for any particular region free of cost. This source provides data on primary and secondary roads

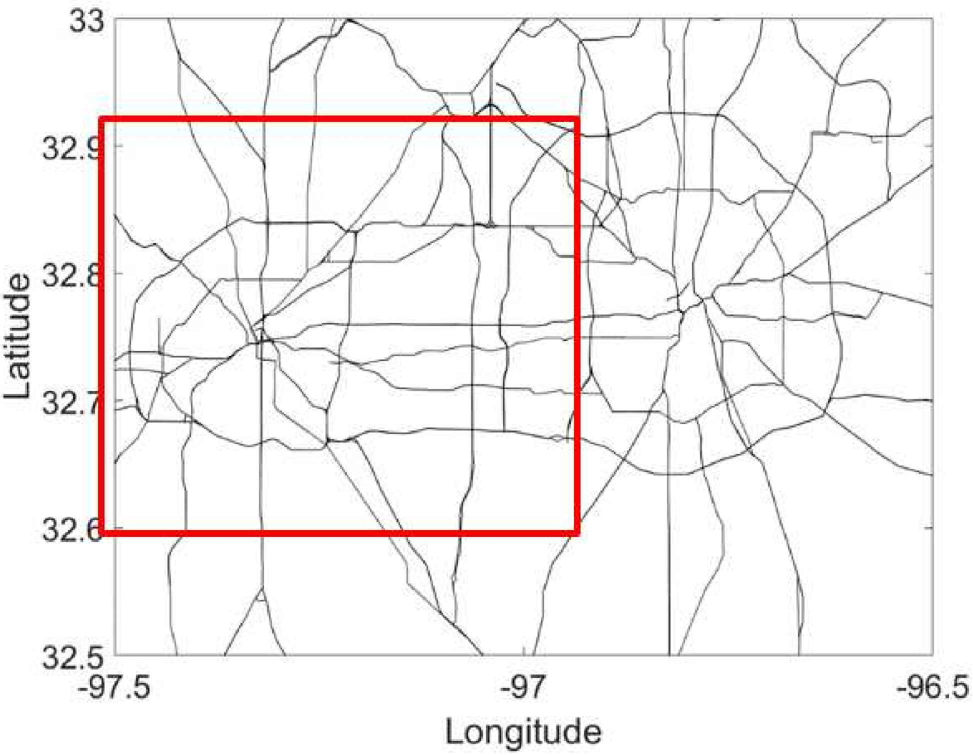

Figure 6.3. Primary and secondary road data for the DFW region.

as well as data of all the roads present in the region. The data for the DFW region was downloaded and the road data plot of primary and secondary roads are shown in Figure 6.3. The road data for all roads for a small sub-region highlighted in red color in Figure 6.3 is shown in Figure 6.4. We can see from this figure that if we consider all the roads, the simulation points obtained will be a huge number. So, for simplifying the simulation, only primary and secondary roads considered in figure 6.3 are used for this study. However, it should be noted that we can expect much larger data for the simulation points if all the roads are considered.

Next, the simulation steps are explained in detail. Once the road data is obtained, a fixed number of points are randomly generated for the area of DFW considered. In this simulation study, ten thousand data points are randomly generated. The randomly generated points can be seen in Figure 6.5. The reason for considering these points is because we can represent the

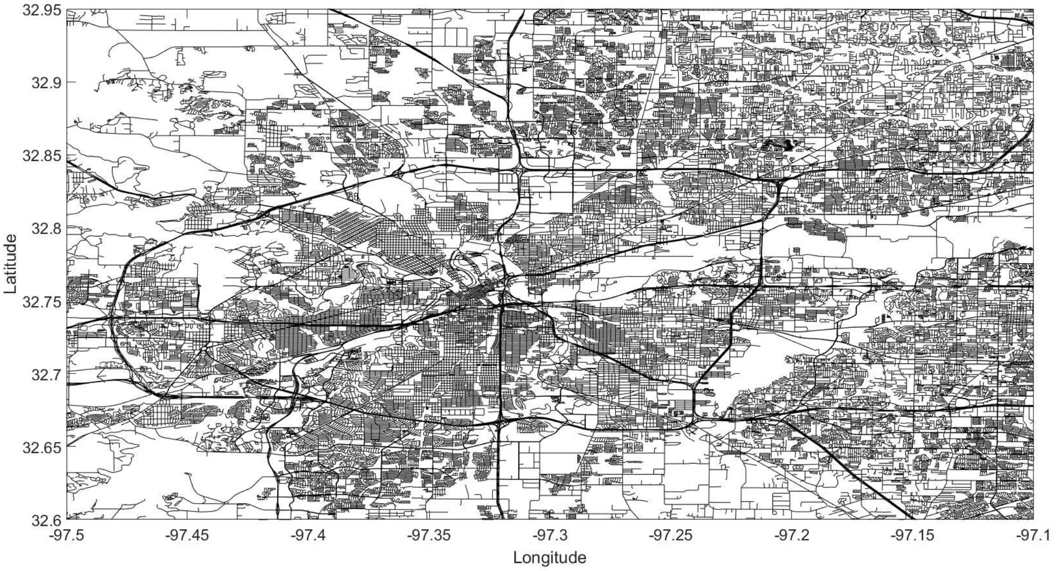

FIGURE 6.4. All roads data for a part of the DFW region which was highlighted in red in Figure 6.3.

automobiles in the region with these points. Since automobiles cannot be randomly spread across the region, there should be a method to consider only the points on the road and remove the remaining points from the simulation.

To consider the points nearest to the road and remove the remaining data points, the distance between the randomly generated points and the nearest road should be computed. To get the distance, each randomly generated point is checked for the distance with the road locations; the minimum distance is recorded for that particular point using the distance formula. Once the distances for all the randomly generated points are computed, we can filter out the points which are very near to the road and eliminate the remaining points. A picture of the distance of the point to the nearest road is shown in Figure 6.6. Note that in this figure, the units for distance in degree units of latitude or longitude. For simplicity in this study, the distance between 1 degree latitude and longitude is considered as 100 km.

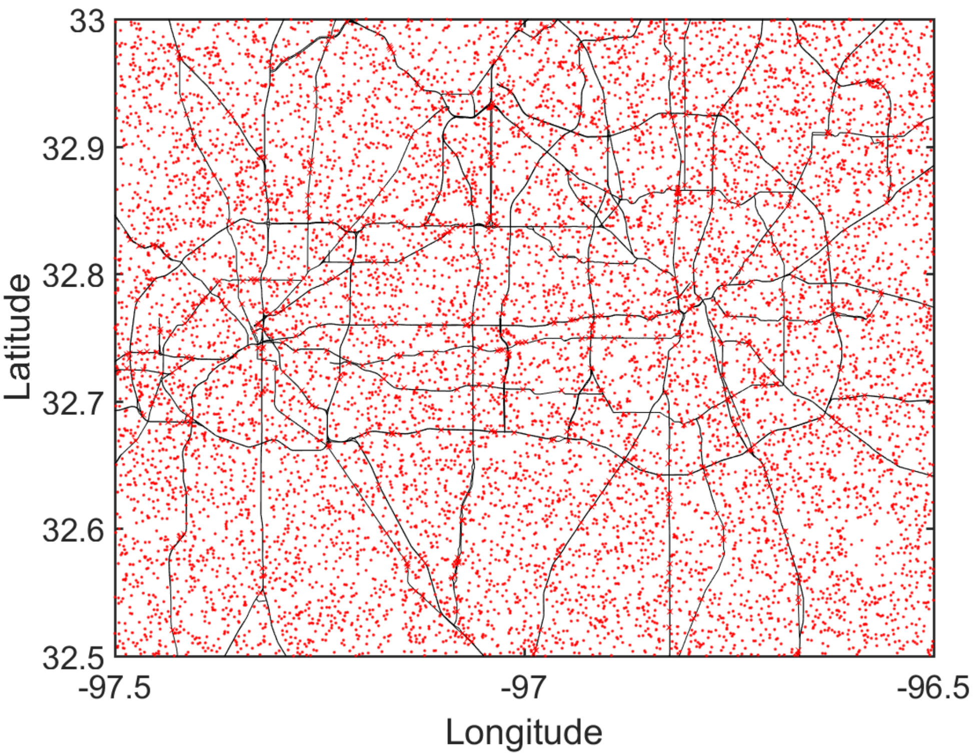

Figure 6.5. Ten thousand random points generated on the DFW area which are considered for the study.

A threshold of 0.001 is applied to the computed distance points to extract only the points closer to the road. Points that have a distance value greater than 0.001 are removed from the study. A distance of 0.001 degrees from the road corresponds to 100 meters. The reason for choosing such a large threshold value was because we have considered only 10000 points for simulation. If more data points are to be considered, then the threshold can be set to a very small value.

A rain map had to be considered to assign the actual weather data to these points which will then give a simulated data set of automobile radar data. The CASA radar network outputs the merged rain rate product, this data was considered for this study. On May 29, 2015, a large storm spread across the DFW area was captured by the network of radars, the Quantitative Precipitation Estimation (QPE) output was obtained for this day. A rain

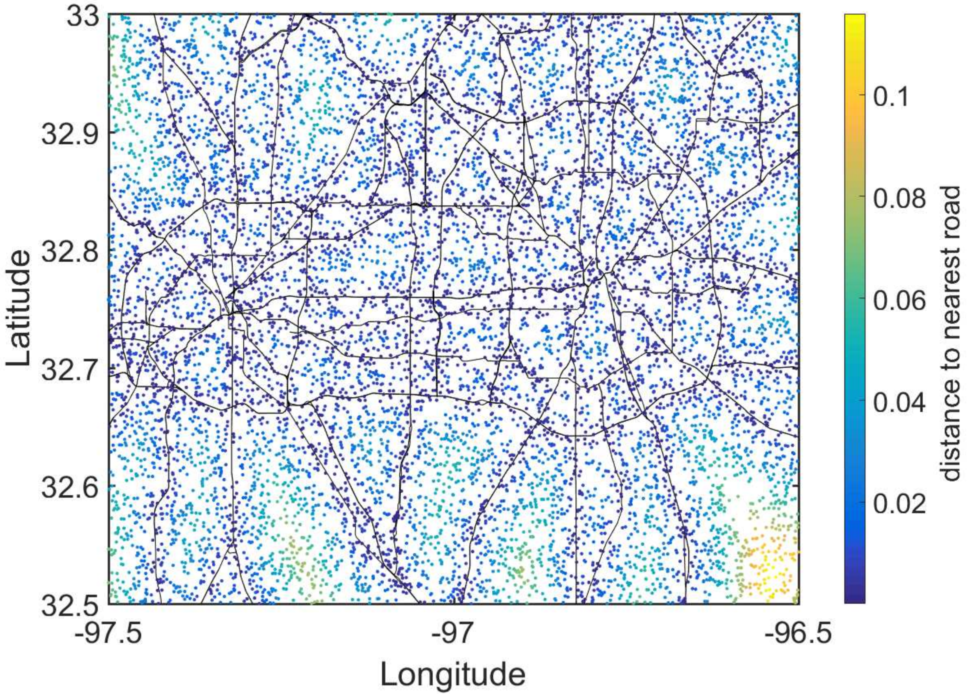

FIGURE 6.6. Distance to the nearest road for the ten thousand simulation points considered.

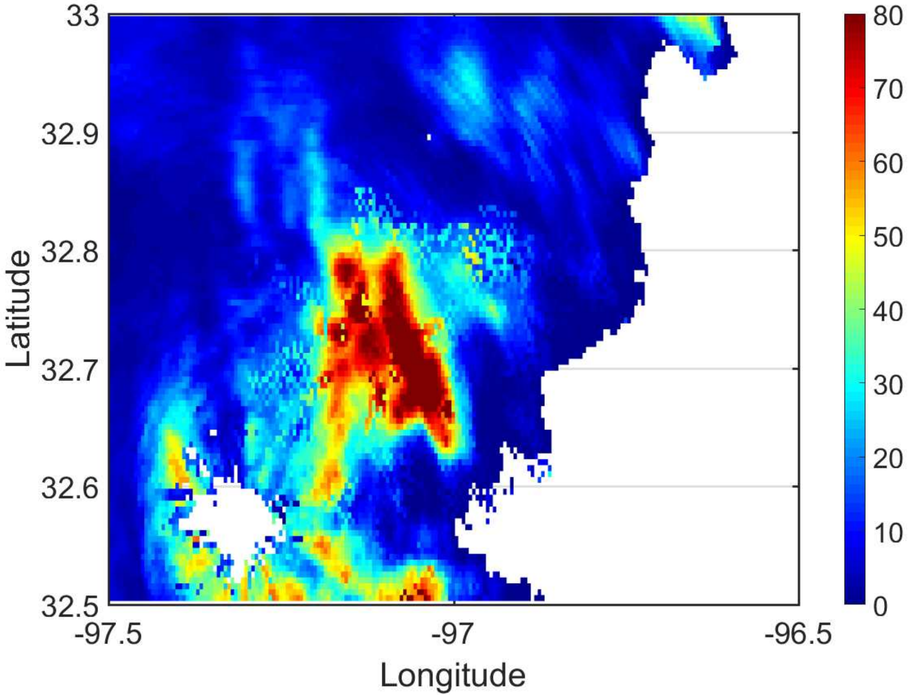

FIGURE 6.7. Merged radar rainrate map from the CASA radar network on May 29, 2015 at 05:30 UTC.

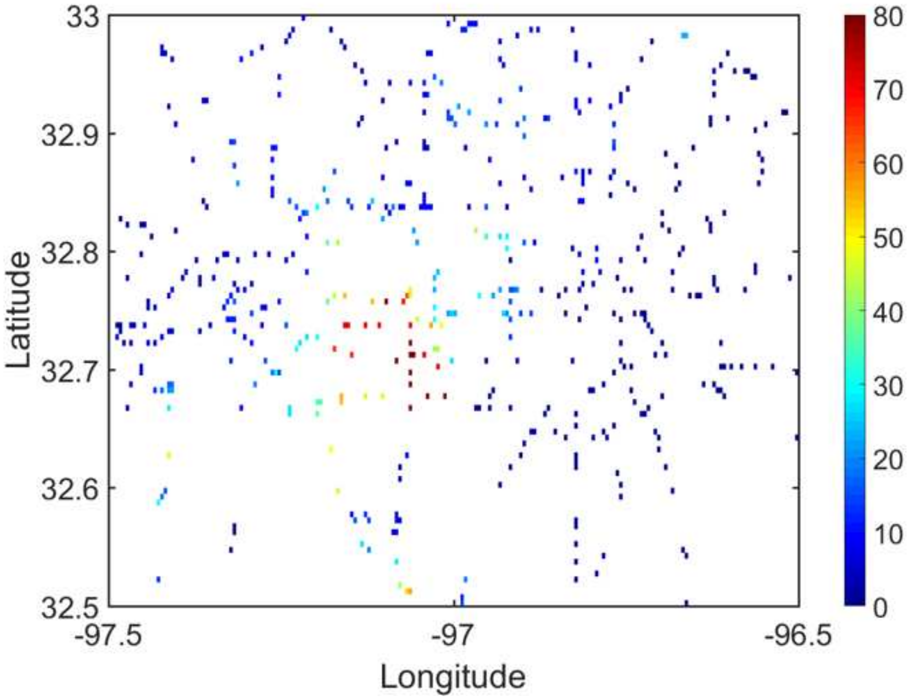

FIGURE 6.8. Rain rate values corresponding to the selected points on/near the roads.

intensity frame around 05:30 UTC was used to obtain the rain rate values for the simulation points. The merged radar rain rate product at 05:30 UTC for our simulation area is shown in Figure 6.7. The corresponding data points nearest to the road are assigned with the rain rate values from the merged radar rain rate; these rain rate values are shown in Figure 6.8. From these data points, we can see that they represent rainfall rate values according to the merged rainfall rate from the CASA radar network output. Note that the rain rate scale in the figures is in mm/hr.

The next part of the simulation study shows how we can use these data points, which represent the automobile radars on the road, to recreate the precipitation map. To obtain the continious precipitation maps from data points, data processing techniques such as interpolation can be applied. Interpolation of the data has to be done in two dimensions to create the rainfall map. There are various interpolation methods in the literature. In this study,

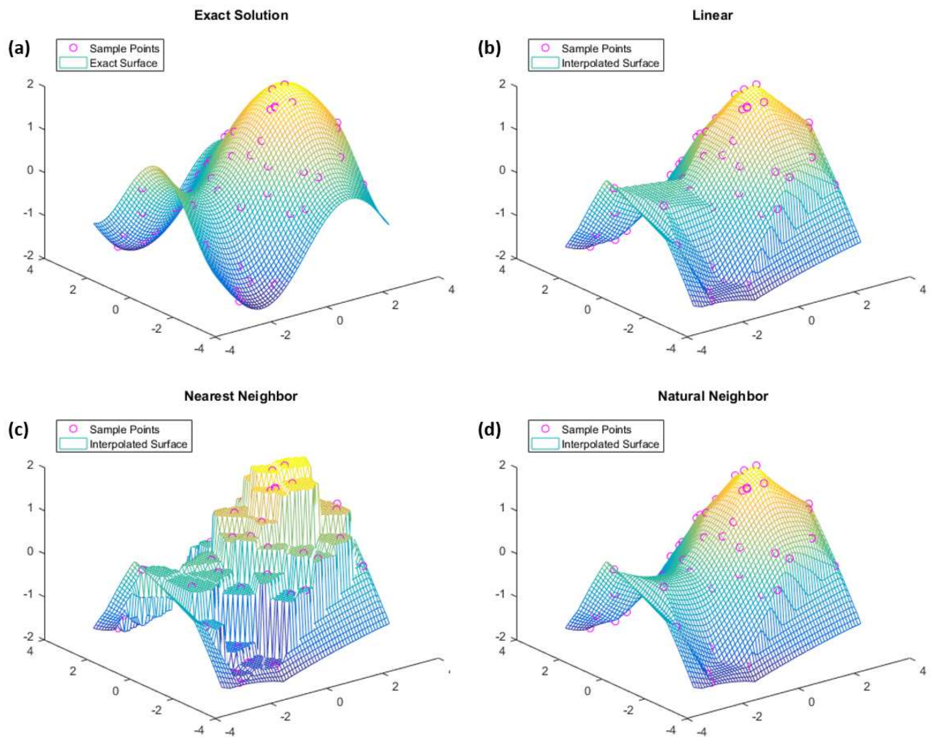

Figure 6.9. Performance of the three different interpolation methods used in this study, the magenta circles are the data points (a) Exact solution for sin(x) + cos(y) (b) Linear interpolation (b) Nearest neighbour interpolation and (d) natural neighbour interpolation

we examine three types of interpolation methods. The three interpolation methods linear interpolation, nearest interpolation and natural interpolation which is used in this study are explained next.

To understand the performance of the three interpolation methods used in this study. First the function $f(x, y) = sin(x)+cos(y)$ is considered, fifty random points are constructed for x and y in the interval [-3,3]. The exact solution for this function and the random points generated are shown in Figure 6.9 (a). Using these fifty data points, the interpolation methods are used for filling the data between the points and the output results are discussed. For the linear interpolation output, as shown in Figure 6.9 (b), it can be seen that the interpolation method captures most of the trend of the exact solution, but there are more sharp edges in the interpolation output. For the nearest neighbor interpolation output, as

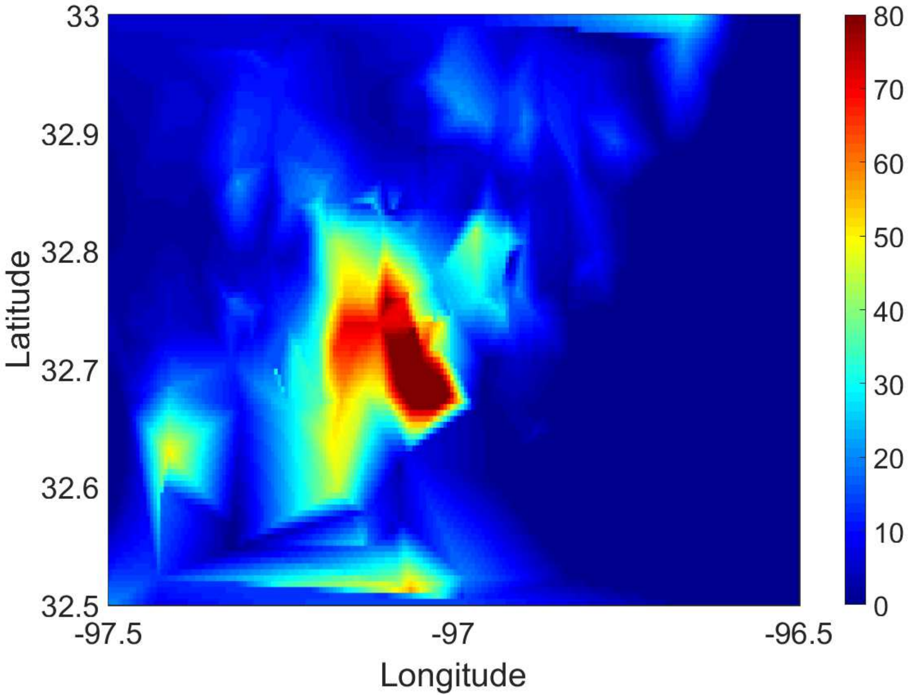

FIGURE 6.10. Rain map output after using linear interpolation method for the simulated data points.

shown in Figure 6.9 (c), it can be seen that the interpolation method captures the trend of the exact solution in a step manner. It performs worse than linear interpolation output. For the natural neighbor interpolation output, as shown in Figure 6.9 (d), it can be seen that the interpolation method captures almost all of the trend of the exact solution and there are fewer sharp edges compared to the linear interpolation. Overall among the three methods, the natural neighbor performs well. Next, these interpolation methods are applied for the precipitation simulation points created and the results are discussed.

For the precipitation point values shown in Figure 6.8, if we apply the linear interpolation method to create a rain map, then we obtain the output as shown in Figure 6.10. From this figure, it can be seen that the features of the storm are captured, but sharp edges along the data is also observed.

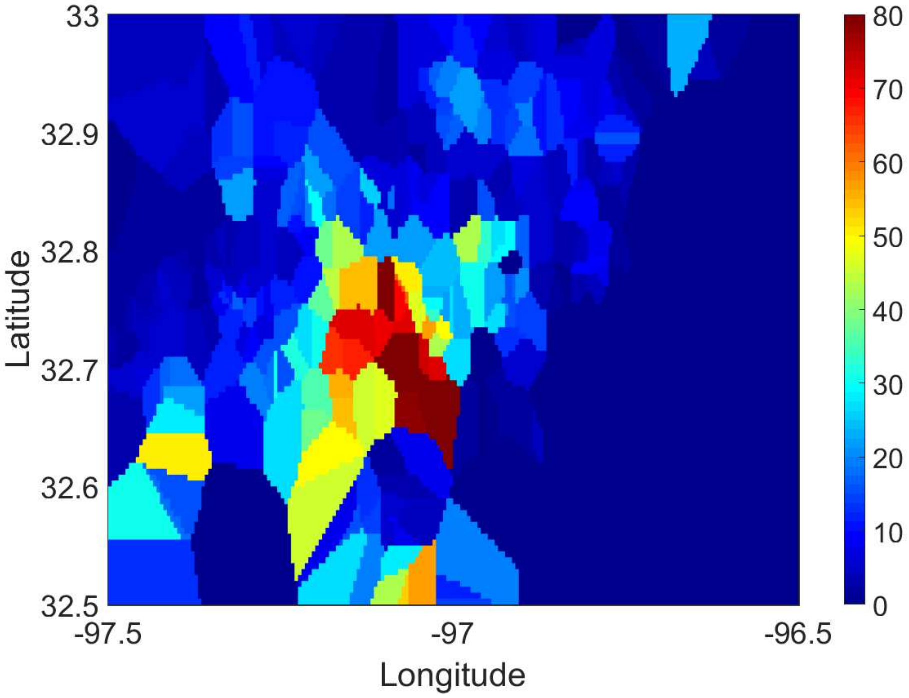

FIGURE 6.11. Rain map output after using nearest neighbour interpolation method for the simulated data points.

When the nearest neighbor interpolation method is used, the output obtained is shown in Figure 6.11. From this figure, we can see that there are definite polygon types of structures for a particular data value. This interpolation method is not smooth over all the data values and performs worse than the linear interpolation method.

The output when the natural neighbor interpolation method is used is shown in Figure 6.12. This interpolation method performs the best among the three interpolation methods discussed until now. The features of the storm are captured well. Compared to the original rainfall map image, the nearest neighbor method is still misses a few features. This is because of the limited number of points used for the data simulation.

To asses whether we need to increase the data points for getting a better reconstructed rain map.

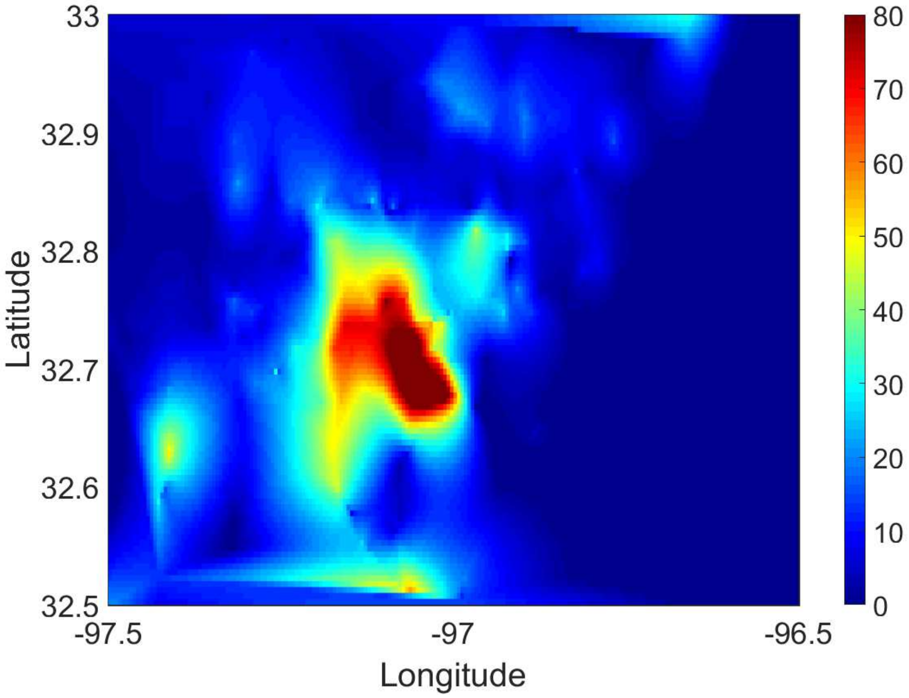

FIGURE 6.12. Rain map output after using natural neighbour interpolation method for the simulated data points.

To asses whether we need to increase the data points for getting a better reconstructed rain map. The natural neighbor interpolation result shown above is compared with the output obtained from natural neighbour interpolation utilizing the complete ten thousand points. The result of using natural neighbor interpolation with all ten thousand points is shown in Figure 6.13. Clearly, from this figure, we can see that increasing the number of points of simulation will yield us a better-reconstructed rain map. As mentioned before, we have considered only primary and secondary roads for this study. If we had used all roads, the results would have been similar to Figure 6.13. This can be studied in the future using data from actual radars and applying advanced image processing techniques.

In all the simulation studies shown above, we assess 200 bins along the x-axis (longitude) and 100 bins along the y-axis (latitude). If we approximate the 1 degree latitude and longitude to 100 km, each resolution bin is $0.5km^2$. The consideration for multiple automobiles in

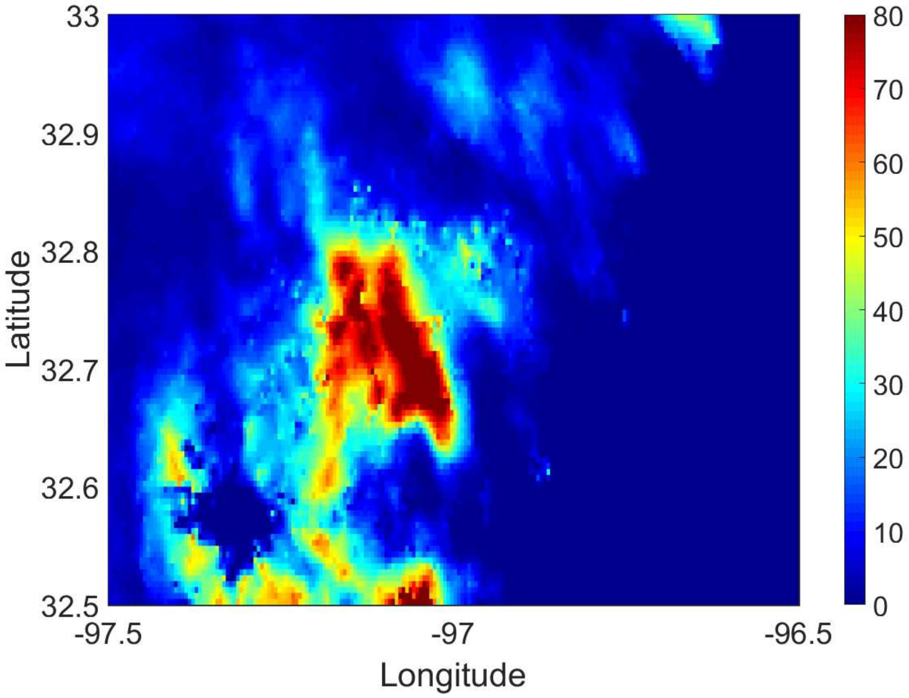

FIGURE 6.13. Rain map output after using natural neighbour interpolation method for the simulated data points, considering all ten thousand points.

single resolution volumes should be studied as well. In Figure 6.14 we can see two resolution volumes. In the first resolution volume, there is only one car, and in the second resolution volume, there are six cars. Considering each of these cars are having radars on them and we obtain the rain rate from all of them, a suitable method should be applied to obtain one single value for the rain rate from each resolution bin. In reality, there will be multiple cars in a single resolution volume.

Some of the methods to obtain a single value for the resolution cell when we have multiple data points inside the resolution volume are given below:

- Maximum value
- Mean value
- Weighted data point value

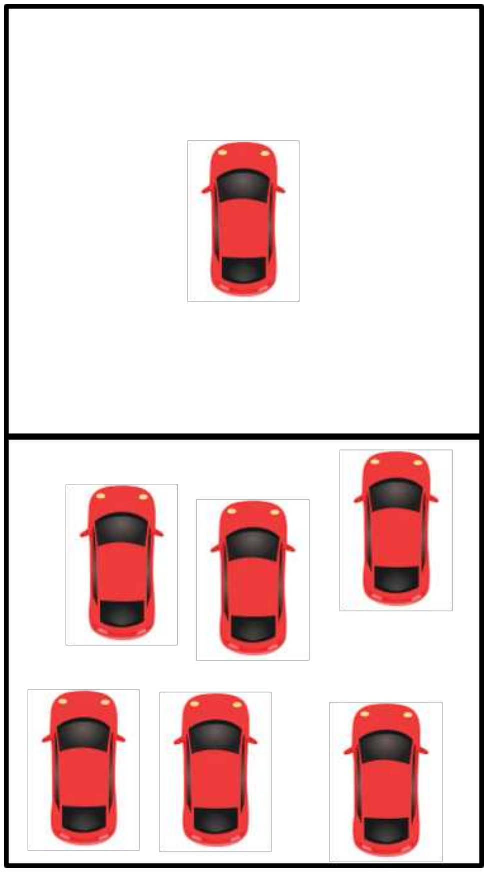

Figure 6.14. Description of data points from the resolution volume - concept diagram.

In the above simulation study, we use the maximum value method. In this method, if there are more than one data point (rain rate values) inside a single resolution volume, then the maximum value of the available data points are considered. For the mean value method, the mean of the available data points is considered. If there is only one data point present in the resolution volume, it will be considered directly. If there are no data points then the resolution cell will be marked as no data present. Obtaining a single value for the resolution cell using the above mentioned methods will influence accuracy of the rain rate spatially, but the values do not vary significantly as the rain rates will be similar within a resolution volume.

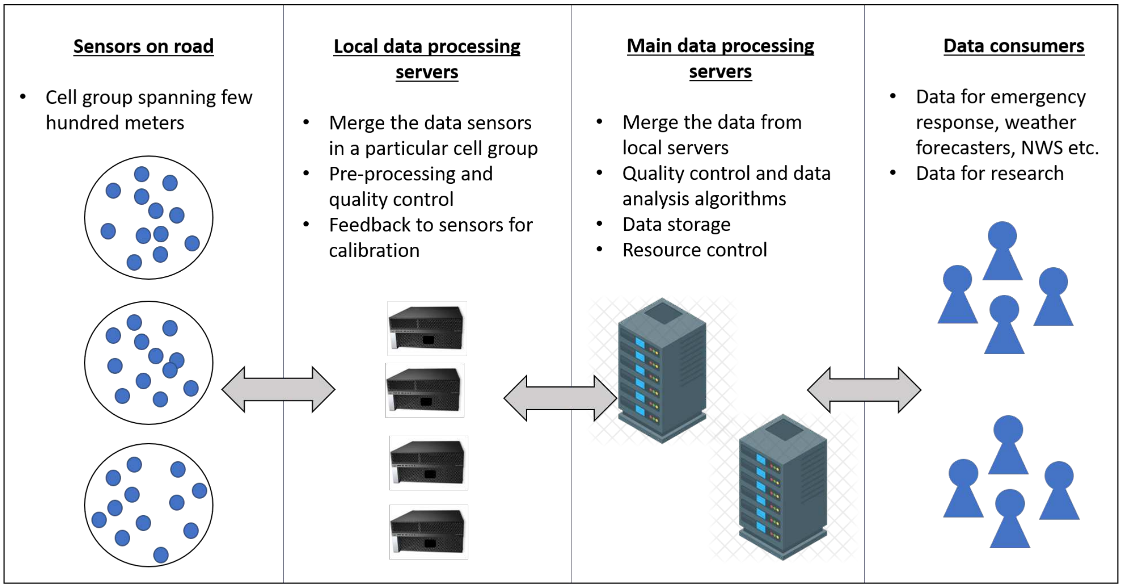

FIGURE 6.15. Proposed system architecture of using automobile radar network for obtaining precipitation information.

Various other factors have to be considered and studied further for these simulations. A couple of considerations are described briefly next. Accurate calibration of the radars will influence the correct estimation of the precipitation. When automobile radars are not correctly calibrated for precipitation, we may get data that are incorrect. These data points can be considered as outliers as till be different from the remaining data. Integrating the outliers points for the estimation of the rain rate within the resolution cell might give incorrect values of output rain rates. These outliers in the data should be handled correctly. In short, further ideas should be explored to correctly handle data quality and quantity. Other aspects to consider is the system configurations to get the rain rate from automobile radars, such as the refresh rate of the rain map and the memory requirements.

6.4. PROPOSED SYSTEM OF PRECIPITATION MAPPING USING AUTOMOBILE RADARS

The system of automobile radar network should be designed efficiently. Various system designs were looked into, as discussed earlier in this chapter for obtaining precipitation products and sending it to the end user. Based on the knowledge of prior systems, a proposed system architecture for obtaining precipitation information using automobile radars is discussed in this section. The system architecture diagram is shown in Figure 6.15.

Most of the time, automobiles are constantly on the move. It is necessary to group the radar data obtained from each automobile into groups assigned to a particular region. These groups can be spread over a few tenths or a few hundred meters, depending on the region of interest. The data from these groups are collected and sent to the local data processing server. This local data processing server should have the capability to connect many groups. We do not need to uniformly distribute the concentration of the local servers over a geographical region. For sending the data from each automobile to the local data processing server, we can make use of the Internet, or with the advancement of embedded systems and smart cities, data can be sent to the local data processing servers directly from the automobiles with the least latency time. Considerations should be given to the geolocation of the automobiles and the geolocation information has to be sent to the local servers. This is because the automobile can be in one group at an instant of time and can move to a different group after a few seconds. The GPS devices present on automobiles can be used for this purpose. The geolocation of the automobile and the data latency plays a crucial factor. The most accurate information would be necessary for the system to be working successfully.

Once the data from each automobile arrives at the local data processing station, the data is pre-processed. The pre-processing of the data includes removing any data points which are incorrect. The data is also quality corrected to include any known bias in the system. These local data processing servers can also provide calibration information to the automotive radar sensors. Then the data in each group are merged together based on the resolution requirement and then transferred to the main data processing servers.

The main data processing server receives and stores all the data obtained from the local data processing servers. The server then merges the data again based on the resolution requirement of the end user. The main data processing servers control many local servers ranging up to a few hundred kilometers. Once the server generates the data processing and meteorological products, the data is stored and transmitted to the end users.

The end users include emergency response service members, weather forecasters, National Weather Service (NWS) and research groups. The data can be transmitted to them over the Internet by accessing the main data storage servers. Feedback from the end users to the main data processing servers is considered and the parameters of the data processing and data collection can be updated. Overall, the system will improve the data product by collecting feedback and changing the system dynamically.

CHAPTER 7

PRECIPITATION MAPPING AT GLOBAL SCALE

Precipitation mapping at the global scale is useful for studying the climate and variation in the seasons across the globe. However, it is very challenging to gather data on such a large scale. Precipitation mapping using remote sensing instruments deployed on satellites has proven to be very useful for various applications. Various precipitation products in multi-scale and multi-time have been developed using the data collected from the satellite remote sensing instruments. Remote sensing data from satellites play a crucial role in mapping remote areas where ground-based instruments cannot be deployed, such as over the ocean or over large mountains. The Low Earth Orbit (LEO) and Geosynchronous Equatorial Orbit (GEO) meteorological satellites orbiting the Earth can sense the radiation emitted or reflected by atmospheric hydrometeors from space. The infrared data from satellites are also used for precipitation measurements [71].

One of the well-known radar instruments deployed on a satellite is the Global Precipitation Measurement (GPM) mission's Dual-frequency Precipitation Radar (DPR) which operates at the Ku and Ka band frequencies. The GPM mission was initiated by the National Aeronautics and Space Administration (NASA) and the Japan Aerospace Exploration Agency (JAXA). The GPM mission comprises of many satellites carrying remote sensing instruments to collect remote sensing data. The DPR is deployed on the core GPM satellite. The swath width of both the Ku and Ka radars is 245 km, with a range resolution of 250 m and spatial resolution of 5 km. Figure 7.1 shows a graphical picture of the GPM DPR [11]. Some of the main goals of the GPM mission include a better understanding of Earth's water

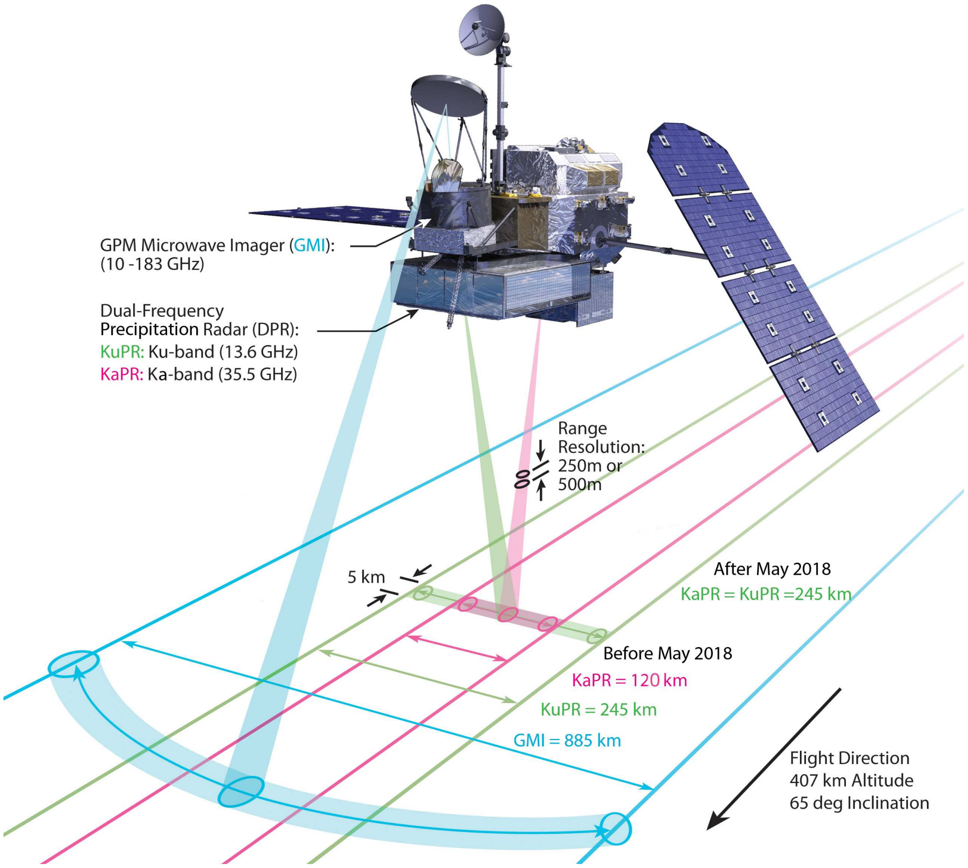

Figure 7.1. The GPM DPR radar and its specifications [11].

cycle and climate change, calculating better rainfall rate estimates and improving winter precipitation measurement.

A picture of data collected from the GPM DPR Ku and Ka band radars is shown in Figure 7.2. The data was collected near the Dallas-Fort Worth region on the March 18, 2015 at 08:56 UTC. The Ku band radar had a larger swath width compared to the Ka band at that time. The ground-based NEXRAD radar's range ring is also shown in this figure, from which we can see the benefits of the satellites in obtaining precipitation information over a large area spatially.

Some methods combine data from satellites and other ground-based remote sensing instruments to obtain precipitation maps at the global scale. The National Oceanic and

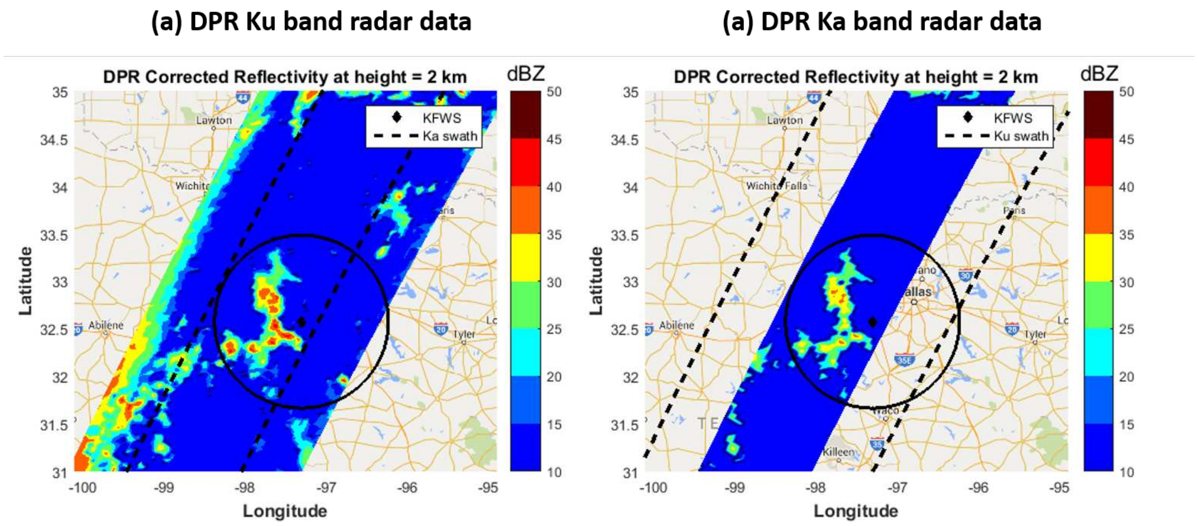
(a) DPR Ku band radar data

(a) DPR Ka band radar data

Figure 7.2. The GPM DPR radar data over the Dallas-Fort Worth (DFW) region collected on 18th March 2015 at 08:56 UTC, the range ring of the DFW NEXRAD radar is also shown for reference, (a) Ku band data and (b) Ka band data.

Atmospheric Administration (NOAA) Climate Prediction Center have developed a morphing technique (CMORPH) to produce global precipitation products by combining existing space-based observations and retrievals. The infrared (IR) brightness temperature information observed by geostationary satellites and passive microwave (PMW)-based precipitation retrievals from low earth orbit satellites are used to derive the CMORPH products. The data is reprocessed on a global grid with an 8km by 8km spatial resolution. The temporal resolution is 30 minutes [72].

With the advantage of space-based precipitation products serving as an excellent tool for hydrologic and climate studies, their accuracy is limited due to restrictions of spatial and temporal sampling and the applied parametric retrieval algorithms, particularly for light precipitation or extreme events such as heavy rain. Currently, researchers are working on developing novel methods which improve the spatial and temporal sampling of precipitation measurements from spaceborne instruments. Synthetic aperture radars (SAR) to observe precipitation is an emerging research field. In this research work, the feasibility of using

SAR for observing precipitation is introduced with simulation results from a spaceborne perspective.

7.1. SYNTHETIC APERTURE RADARS FOR MAPPING PRECIPITATION

For more than three decades, Synthetic Aperture Radars (SAR) have been widely used for remote sensing of the Earth. In the past, spaceborne synthetic aperture radars (SAR), which operate at various frequencies, have been deployed on airborne and spaceborne platforms supporting various missions. SAR systems are preferred for imaging the Earth as they provide data in high resolution and they are invariant with respect to the time of the day (day or night). Obtaining high-resolution images/output of the scene under observation is one of the main advantages of SAR. SAR is basically an imaging radar mounted on a moving platform. The data is collected for an appropriate coherent time, during which many data samples are collected at different positions of the SAR. The coherent combination of the data collected is used to construct a virtual aperture that is much larger than the physical antenna length. This basic attribute of SAR constitutes the name "synthetic aperture."

SAR is used for a wide variety of applications such as interferometry and tomography. More than twenty SAR systems have been successful in the past in imaging the Earth. The applications of SAR include vegetation mapping, landcover monitoring and earth imagery. SAR systems have also been used for planetary exploration missions and 4-D mapping of the Earth. The SAR instruments operate over a wide range of frequencies specific for the applications.

SAR systems have a side-looking imaging geometry and are based on a pulsed radar installed on a platform with a forward movement [73]. SAR can operate in multiple modes, such as stripmap and spotlight modes of operation. The spotlight mode of operation is used to obtain higher resolution images compared to the images obtained when using stripmap mode at the expense of not obtaining the images continuously. In the stripmap mode of SAR, the platform moves along the azimuth direction, scanning one swath of the ongoing weather event. Thus, this mode can be considered as a continuous strip of scan data. In the spotlight mode of SAR, the SAR scanning the weather event will be fixed to a particular area as the platform moves. In this mode, the SAR antenna is moved physically or electronically in the azimuth direction to sample the same region of the observed weather storm. There are other modes of SAR that are not considered in this research work such as the scan SAR mode, in which the SAR platforms scan the imaging scene along the swath as it moves in azimuth. A picture of the SAR platforms in the stripmap, spotlight and scanSAR modes are shown in Figure 7.3.

The SAR systems are also widely classified into monostatic and bistatic SAR, which are based on the locations of antennas used for signal transmission and reception. In the monostatic SAR, the transmission and reception of the radar signal are accomplished using one radar platform with one antenna. In a bistatic SAR, the transmission and reception of the radar signals are accomplished using two separate antennas, typically the antennas are located on different platforms. It should be noted that there are various missions of SAR that involve multiple satellite platforms for transmission and reception. We do not consider these SAR missions in this dissertation.

Understanding the precipitation event at a microphysical scale is important in atmospheric sciences and meteorology. SAR deployed on satellites can be a potential tool for capturing precipitation data and providing data globally. The precipitation data captured by a spaceborne SAR will have a high resolution compared to data captured by other spaceborne platforms. Since SAR can obtain data at very high resolution, understanding the

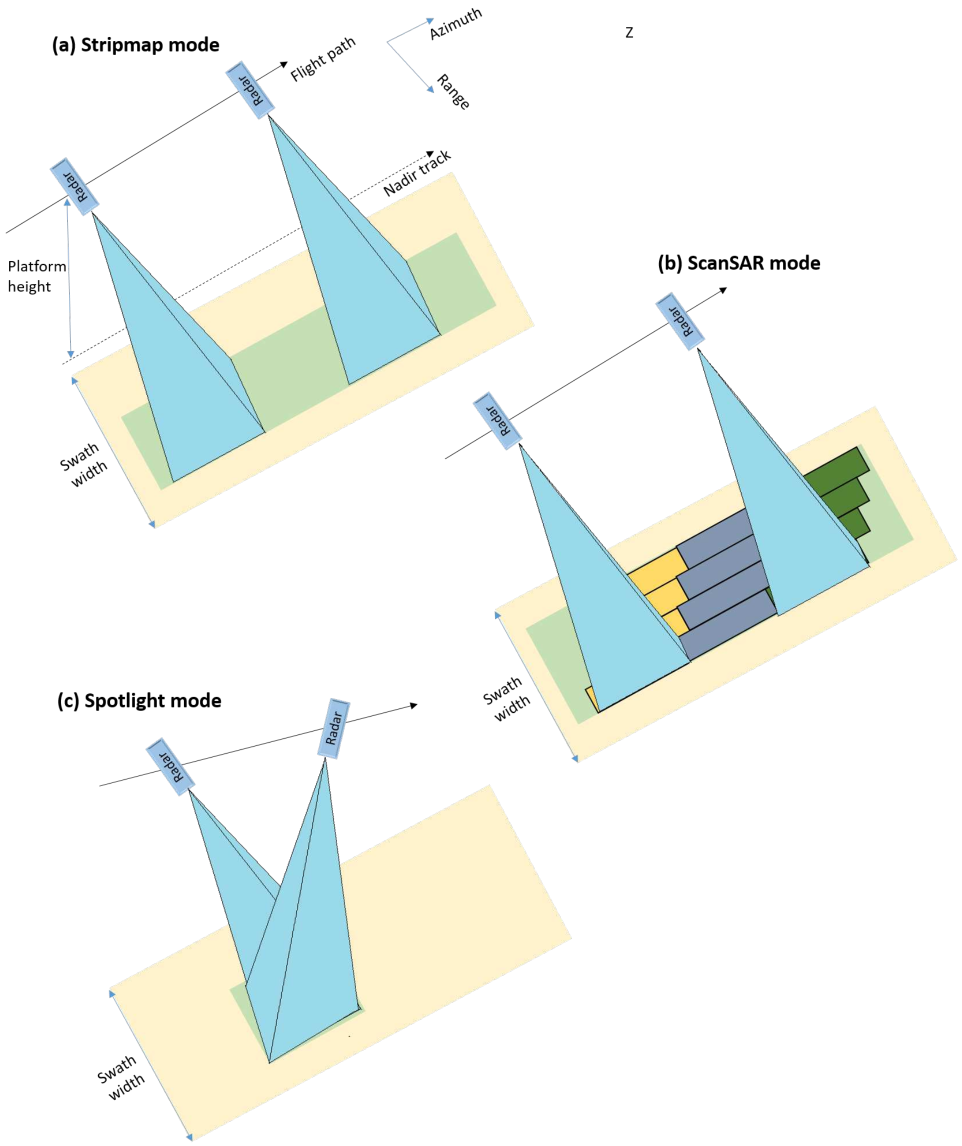

FIGURE 7.3. SAR scanning modes, (a) Stripmap SAR, (b) ScanSAR and (c) Spotlight SAR.

precipitation process at microphysical levels will be possible. The potential for using SAR for meteorological applications is yet to be explored. Currently there are no satellites with SAR which is dedicated to this purpose. In the future, there is a high possibility that SAR systems will be deployed on satellites for studying precipitation.

Simulation studies will aid in understanding meteorological targets from a SAR's perspective and to support future deployments of SAR systems for mapping precipitation. SAR simulation studies are necessary to fully understand the different operating modes and signal processing which is carried out for precipitation targets. This simulation study is focused on understanding how SAR will benefit precipitation observations.

Researchers in the past have worked on the problem of mapping precipitation from SAR platforms [74]. Both airborne and spaceborne platforms were utilized for this purpose. Some researchers have even considered other instruments such as weather radars to study precipitation from a SAR's perspective [75]. This work introduces a simulation tool for the spaceborne SAR platform observing precipitation.

It is important to simulate the realistic scenario of mapping precipitation from SAR platforms to help design future SAR missions and understand the effects of varying parameters in the SAR system. Simulation studies are required to fully understand the influence of SAR system parameters and the various signal processing algorithms which are used to obtain the final output. A simulation program written in MATLAB programming language is considered in this study. The simulation program was developed based on the mathematical framework described in the next section.

In this simulation study, first, the stripmap mode of the SAR is studied in detail for fixed and weather targets, then the simulation study for the pseudo-spotlight mode is briefly introduced. First we study the SAR simulations for the monostatic case, in which transmit and receive are from the same antenna located on a spaceborne platform. Then we study the bistatic case where there transmit and receive antennas are on different spaceborne platforms. The results are studied in detail and a comparison between the stripmap and pseudo-spotlight mode of operation is also presented.

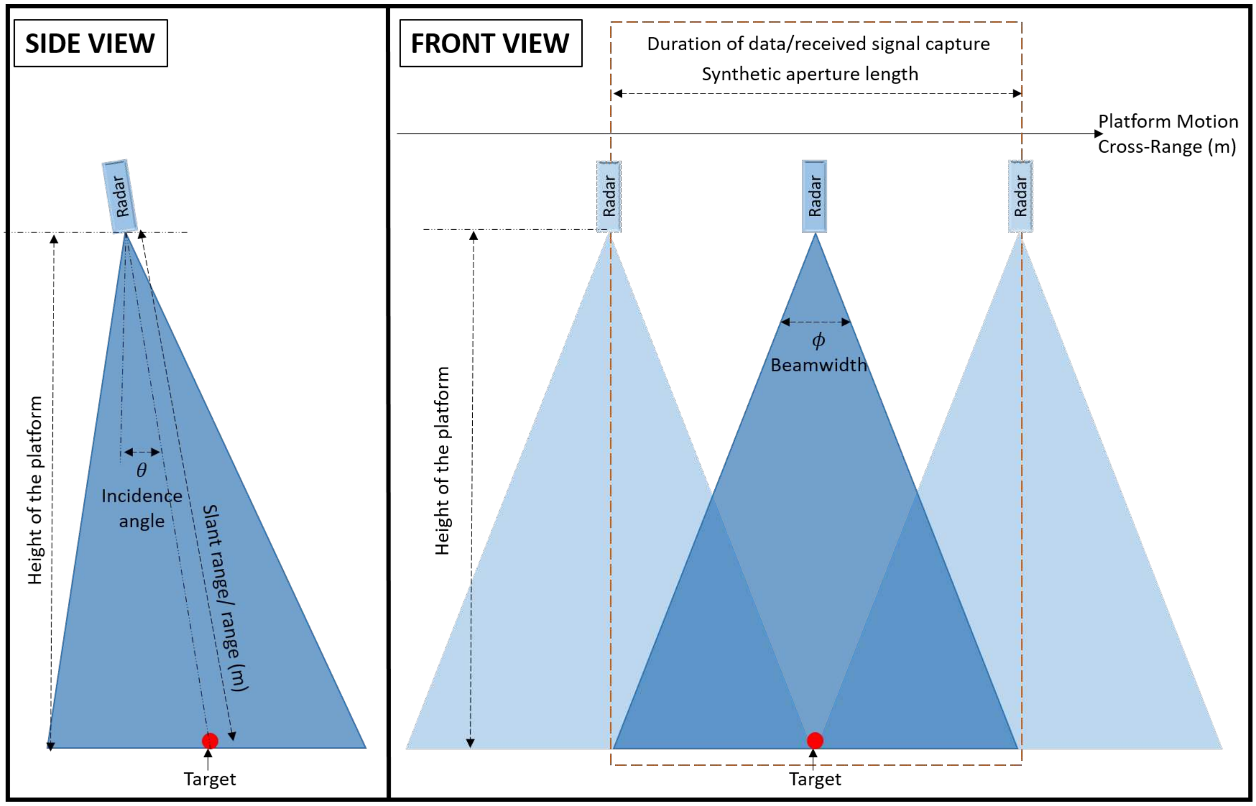

FIGURE 7.4. SAR architecture, (a) Side view and (b) 3-D view.

7.2. MATHEMATICAL FRAMEWORK FOR MONOSTATIC AND BISTATIC SAR FOR OBSERVING PRECIPITATION TARGETS

In this section, the relevant mathematical framework used in this SAR study is briefly discussed for both monostatic and bistatic modes of SAR operation. The simulation program developed is based on the framework described in this section. The SAR architecture for monostatic and bistatic are also presented. There can be many possibilities for the bistatic SAR architecture, simple architecture of bistatic SAR is considered for the simulations presented in this work.

7.2.1. MATHEMATICAL FRAMEWORK FOR MONOSTATIC SAR. The monostatic SAR transmits and receives the radar signal from the same platform. Considering the SAR architecture shown in Figure 7.4, the platform is located at a height H from the surface of the

Earth and is moving at a speed of V_a m/s. Figure 7.4 shows both the side-view as well as the 3-D view of the SAR architecture for clarity. The SAR platform is scanning pointing toward the surface of the Earth at an angle of θ with respect to the nadir. This angle is referred to as the incidence angle. The time in the range direction (direction of transmission of pulses) is usually referred to as fast-time. The time in the azimuth or cross-range direction (direction of movement of the platform) is usually referred to as slow time. The beamwidth of the antenna is represented by ϕ. In the architecture considered, the platform moves in the azimuth direction. The slant range is the distance perpendicular to the radar flight path.

The cross-range resolution δ_a is given by the smallest separation between two point targets that can be detected by the radar. For a given cross-range resolution δ_a, the antenna length in meters (d_a) is 2 δ_a.

The beamwidth of the antenna Θ_a in radians can be approximated by λ/d_a, where λ is the wavelength

The corresponding synthetic aperture length in meters is given by:

$$L_{sa} = \Theta_a \; R = \frac{\lambda \; R}{d_a} \tag{43}$$

where R is the distance to the target

At any time t, the distance between the radar moving at constant velocity V_a and a point on the ground, described by its coordinates $(R, 0, H)$ is easily obtained applying Pythagoras' theorem

$$r(t) = \sqrt{R^2 + V_a^2 t^2} \approx R + \frac{V_a^2 t^2}{2R} \; for \; vt/r_0 \ll 1 \tag{44}$$

where V_a is the SAR platform velocity in cross-range direction. At any time t, the received signal at SAR is given by:

$$s(t) = exp\{j2\pi f(t - \frac{2R}{c})\}exp\{-j2\pi \frac{V_a^2}{\lambda R}t^2\} \tag{45}$$

where c is the speed of light, f is the center frequency

The Doppler frequency is given by:

$$f_{dk} = \frac{2V_a^2}{\lambda R}t \tag{46}$$

The Doppler rate is given by:

$$f_d = \frac{2V_a^2}{\lambda R} \tag{47}$$

The Doppler bandwidth is given by:

$$f_b = \frac{V_a}{\delta_a} \tag{48}$$

The synthetic time is given by:

$$T_d = \frac{f_B}{f_{dk}} = \frac{L_{sa}}{V_a} = \frac{\lambda R}{2V_a\delta_a} \tag{49}$$

Range compression and azimuth compression have to be carried out on the received SAR signal to get the final output. We have not considered range compression in the simulation module. The equations to carry out range compression using the range compression filter along with the equation to get the range compression output is shown below.

$$p(t_r) = \exp\{j\pi \frac{BW}{t_p} {t_r}^2\} \qquad for - \frac{t_p}{2} \leq t_r \leq \frac{t_p}{2} \tag{50}$$

$$RC_{output} = \mathscr{F}^{-1}\{\mathscr{F}(s) * (\mathscr{F}(p))^*\} \tag{51}$$

The equations to carry out azimuth compression using the azimuth compression filter along with the equation to get the azimuth compression output is shown below. If range compression is not used for the simulations, then the received SAR signal can be directly given as the input for the azimuth compression module to get the final SAR processed image.

$$az(t_a) = \exp\{j\pi f_{dk} {t_a}^2\} \qquad for - \frac{T_d}{2} \leq t_a \leq \frac{T_d}{2} \tag{52}$$

$$AZ_{output} = \mathscr{F}^{-1}(\mathscr{F}(RC_{output}) * (\mathscr{F}(az))^*) \qquad if\, range\, compression\, used \tag{53}$$

$$AZ_{output} = \mathscr{F}^{-1}(\mathscr{F}(s) * (\mathscr{F}(az))^*) \qquad if\, range\, compression\, is\, not\, used \tag{54}$$

We make a few assumptions to modeling the SAR received signal from the precipitation (rain) medium. The first assumption is that the random volume of the SAR received signal consists of spherical raindrops in the entire range resolution volume. The second assumption is that the raindrops have zero mean radial velocity with a Gaussian spectrum distribution. A detailed mathematical framework on the backscattering properties from a volume of precipitation particles can be found in [29].

The received SAR signal observing a precipitation medium can be given as:

$$s^P(t) = s(t)\Sigma_k a_k exp\{-j4\pi \frac{V_k(t)}{\lambda} t\} \tag{55}$$

For a sidelooking, broadside SAR, considering the Doppler spectrum of rain medium, the coherency time is given as below which needs to compare with T_d

$$T_c = \frac{\lambda}{2\sqrt{2}\pi\sigma_v} \tag{56}$$

The corresponding expected Doppler bandwidth is

$$f_B^{'} = f_k T_c = \frac{V_a^2}{\sqrt{2}\pi R \sigma_v} \tag{57}$$

Now we get the expression for expected resolution from the SAR received signal when observing a precipitation target as below.

$$\delta_a^{'} = \frac{V_a}{f_B^{'}} = \frac{\sqrt{2}\pi R \sigma_v}{V_a} \tag{58}$$

7.2.2. Mathematical framework for bistatic SAR. The mathematical framework which is used in the simulation study for bistatic SAR is discussed in this section. It

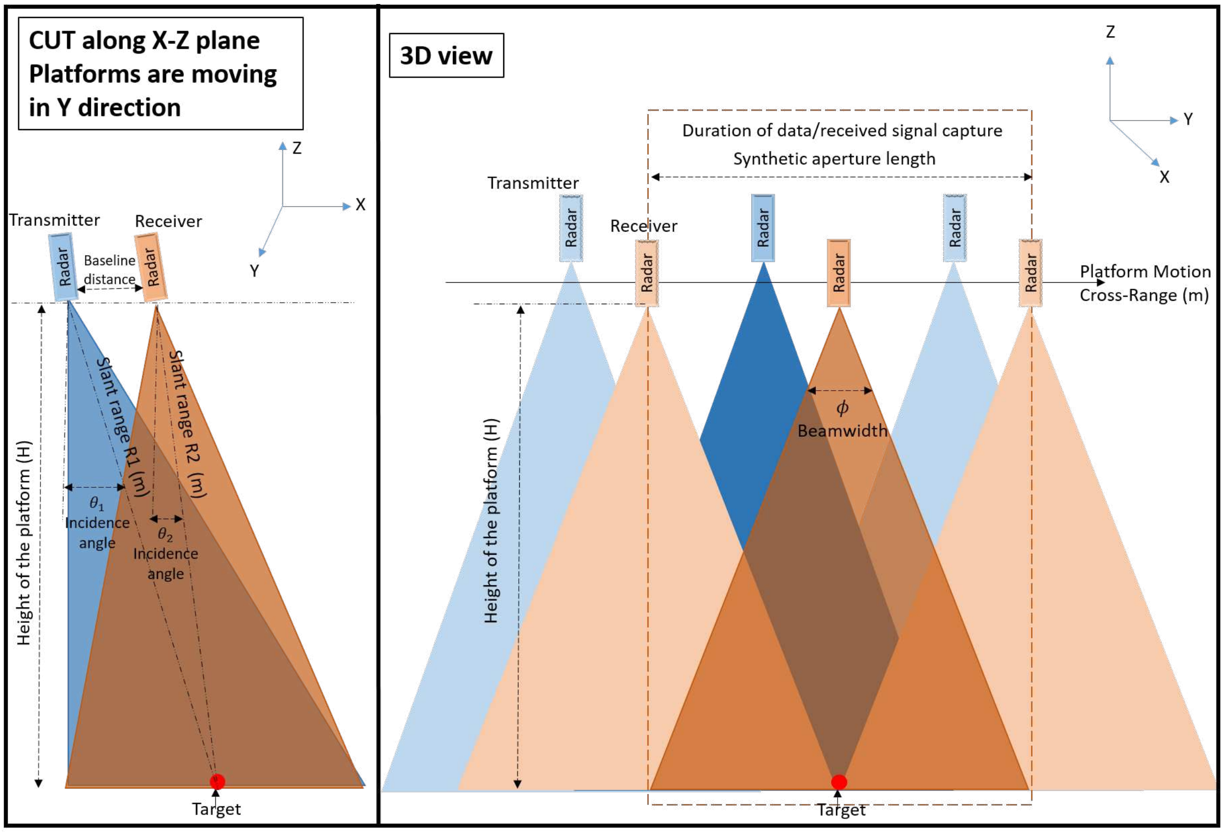

Figure 7.5. SAR architecture for bistatic case, (a) Side view and (b) 3-D view.

should be noted that the mathematical framework is developed based on the architecture of the bistatic SAR considered. The architecture of the bistatic SAR is shown in Figure 7.5. The transmit and receive platforms are located at a height H m from the surface of the earth. Both the platforms are moving at the same speed of V_a m/s. Considering the SAR platforms are focused on a target which is located at [tx, ty, tz]. The SAR transmit platform is pointing towards the target with an incidence angle of θ_1 with respect to the nadir. The SAR receive platform is pointing towards the target with an incidence angle of θ_2 with respect to the nadir. The baseline distance is the distance between the transmitter and receiver locations.

At any time t, the total distance between the transmit radar and receive radar, both moving at a constant velocity V_a along cross-range, and a target on the ground, described by its coordinates $(R, 0, H)$, is given by

$$r_1(t) + r_2(t) \approx R_1 + \frac{V_a^2 t^2}{2R_1} + R_2 + \frac{V_a^2 t^2}{2R_2} \tag{59}$$

where R_1 is the distance from transmitter to the target and R_2 is the distance from the target to the receiver. At any time t, the received signal at SAR is given by:

$$s(t) = exp\{j2\pi f(t - \frac{R_1 + R_2}{c})\}exp\{-j\pi \frac{V_a^2 t^2}{\lambda}(\frac{1}{R_1} + \frac{1}{R_2})\} \tag{60}$$

where c is the speed of light, f is the center frequency

The Doppler frequency is given by:

$$f_d = -\frac{V_a^2}{\lambda}(\frac{1}{R_1} + \frac{1}{R_2})t \tag{61}$$

The Doppler rate is given by:

$$f_{dk} = -\frac{V_a^2}{\lambda}(\frac{1}{R_1} + \frac{1}{R_2}) \tag{62}$$

The corresponding synthetic aperture length in meters is given by:

$$L_{sa} = min(R_1, R_2)\theta_w \tag{63}$$

where θ_w is the antenna beamwidth

Using a patch antenna with beamwidth $theta_w = \lambda/L$ The synthetic time is given by:

$$T_d = \frac{L_{sa}}{V_a} = \frac{\lambda}{L}\frac{min(R_1, R_2)}{V_a} \tag{64}$$

The Doppler bandwidth is given by:

$$f_b = |f_k T_d| = \frac{V_a}{d_a}(\frac{1}{R_1} + \frac{1}{R_2})min(R_1, R_2) \tag{65}$$

The azimuth resolution for a stationary target is given by:

$$\delta_a = \frac{V_a}{f_B} = \frac{L}{min(R_1, R_2)}\frac{R_1 R_2}{R_1 + R_2} \tag{66}$$

The range and azimuth compression for the bistatic case is similar to the monostatic case, so the equations similar to the monostatic case can be considered for processing.

For modeling the SAR received signal from precipitation (rain) medium, we make a few assumptions similar to the monostatic case. The first assumption is that the random volume of the SAR received signal consists of spherical raindrops. The second assumption is that the raindrops follow a Gaussian spectrum distribution. The mean velocity of the simulations is varied and studied accordingly. The received signal for the precipitation target is constructed similar to the monostatic case.

Considering the Doppler spectrum of the particles in a rain medium, the coherency time needs to compare with T_d. The coherency time is given using the equation below.

$$T_c = \frac{\lambda}{2\sqrt{2}\pi\sigma_v} \tag{67}$$

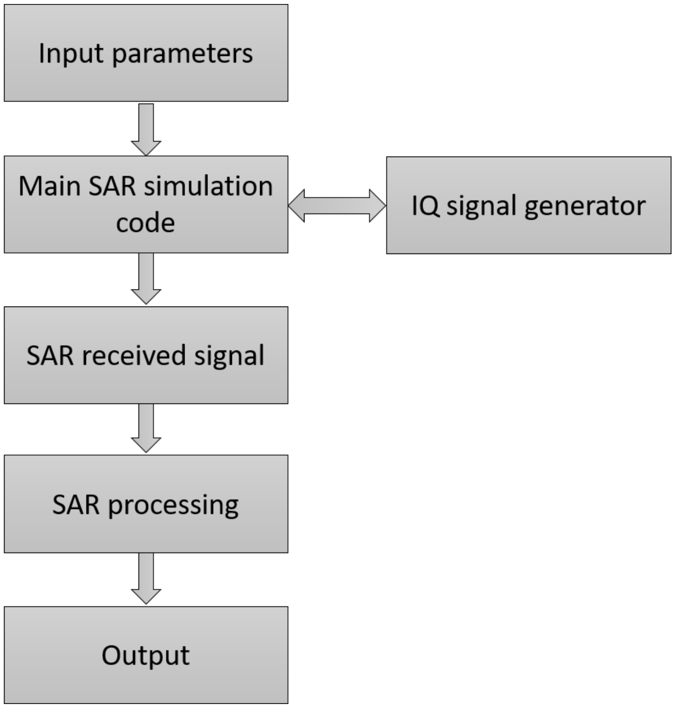

FIGURE 7.6. Block diagram of the SAR simulation architecture.

The corresponding expected Doppler bandwidth is

$$f_B' = |f_k T_c| = \frac{V_a^2}{2\sqrt{2}\pi\sigma_v}\frac{R_1 + R_2}{R_1 R_2} \tag{68}$$

Now we get the expression for expected resolution of a rain medium for a bistatic case from the SAR received signal as below:

$$\delta_a' = \frac{V_a}{f_B'} = \frac{2\sqrt{2}\pi\sigma_v}{V_a}\frac{R_1 R_2}{R_1 + R_2} \tag{69}$$

The above equation shows us that the resolution is independent of the wavelength (λ), so the resolution obtained from the simulation results are independent of the frequency of the radars considered.

7.3. SAR SIMULATION PACKAGE

In this section, the simulation tool, which was developed to understand the received SAR signals from precipitation targets is explained in detail. Signal simulations and systems simulations are important to understand the design, performance and overall functioning of any system. In this research, the signal simulations which are carried out to understand the SAR signal are important in designing and developing an actual radar system. Signal simulation of SAR for a fixed target for both monostatic and bistatic cases has been developed and used since the initial days of SAR technology. However, signal simulation packages to observe precipitation from SAR platforms are currently under research. There is no standard simulation package for the same. In this research, a SAR simulation code package using the MATLAB programming language is developed.

A block diagram of the overall simulation workflow is shown in Figure 7.6. From this diagram, it can be seen that the blocks are developed in top-down approach. The simulation code can carry out simulations for both monostatic and bistatic SAR in stripmap and pseudo-spotlight mode of SAR scans. The initial input parameters for the simulations are carefully selected and loaded onto the input parameter file. This file is read by the main SAR simulation code, where the various SAR computations required are carried out, such as the Doppler rate and synthetic aperture time. The SAR input parameters can be specified for the airborne and spaceborne parameters based on the simulation scenario required.

The IQ signal generation block is the heart of the simulation code for creating weather returns from the SAR signals in the geometry considered. The I and Q data is the real and complex part of the complex received voltage signal from the radars. This is the raw data which is received by all radars systems and given as the input for the moment generation stage where various moments such as reflectivity and velocity are computed. Currently, two methods of IQ signal generation is possible for the signal simulations.

The IQ data simulation packages developed at the CSU radar group use an asymptotic method and a direct volume of particles backscattering method. The asymptotic method is well documented in the literature, whereas the direct volume of particles backscattering method is relatively new. In the asymptotic method, the timeseries simulation uses the frequency domain algorithm to generate dual-polarized echoes. Here, the primary motivation is to generate the time series corresponding to a specified correlation structure. More details of this simulation method can be found in [27].

Another IQ simulator is based on the direct volume of particles backscattering. We can also consider the bistatic geometry in this simulator and generate the IQ data accordingly. Also, this simulation code considers the drop size distribution of the precipitation particles present on the radar resolution volume. The IQ signal generator block is interfaced with the main SAR simulation code. The appropriate weather parameters required for the simulation are sent and the IQ signal is received from this block.

The main SAR simulation code block is the core of the simulation package. The appropriate equations discussed in the previous section are coded. Some main functions include creating the range reference function, creating the azimuth reference function and creating the raw data based on the sensing geometry. In the process of creating the raw data, each pulse in the synthetic aperture time is considered. The locations of the transmit and receive platforms along with the target locations are considered and the received signal is constructed. The antenna pattern weighing is also handled while creating the received raw SAR signals. Once the signal is constructed, it is passed on to the next block, where the SAR received signal is constructed for all the targets. When considering a volume of targets for precipitation data, IQ data from each resolution volume have to be considered and the simulation is computationally expensive. More work on making the current simulation code faster can be looked at in the future.

The next block of the simulation code package is the SAR processing block. Once the received SAR signal is generated, this signal is passed on to the SAR processing block, where the range and azimuth compression of the received SAR signals are carried out. There are various algorithms to perform the azimuth compression of the SAR signals, such as the 2D FFT method and range migration algorithm. In this research, the azimuth compression is carried out using the 2D FFT method; the range migration algorithm feature is also present in the simulation code package, which can be used for future work.

The next code block is the output block in which the various functions for visualizing the SAR simulations are present. The received SAR signal, processed SAR signal, azimuth cuts of the processed SAR signal and fitting of a Gaussian curve for the azimuth cuts can be handled in the current simulation code package. These functions completes the full chain of the SAR simulation code package. The input parameters can be changed according to the needs of the simulation study and the simulation code can be initiated. The signal generation and processing time for a fixed target case are in the order of a few seconds. When simulating the precipitation target for a single bin, the major chunk of the time is taken by the IQ signal generation code. When simulating a weather resolution volume, the SAR simulation code takes a long time to complete the simulation as signal return from each bin in the azimuth direction has to be computed with respect to the IQ data from the resolution volume.

7.4. Simulations of SAR in monostatic mode for observing precipitation target

The simulation results that are generated using the SAR simulation package described in the previous section are discussed next. For the simulation study presented in this research, we have considered the parameters of a space-borne platform. Simulation results for an airborne platform can be obtained by running the simulation code with airborne platform parameters as the input. First, we present the monostatic SAR simulation results for stripmap and then we present the results for pseudo-spotlight mode of SAR.

7.4.1. Monostatic mode stripmap configuration results.

The spaceborne SAR parameters need to be considered precisely for the simulation of the data. The system parameters of the Global Precipitation Measurement (GPM) Ku radar, which is located on the GPM core satellite are considered for both the transmit and receive platforms to mimic a realistic scenario. Having the reference of an operational remote sensing satellite observing precipitation will aid in specifying the system parameters used for the simulations. The platform parameters which are considered for the simulation are listed in Table 7.1. As mentioned earlier, in the monostatic case, the same platform is used for transmitting and receiving, so the system parameters which is used for the simulations are the same for the transmit and receive platforms.

The transmitter and receiver are located at [5km 0 400km] in [X Y Z] direction. Both the transmit and receive platforms are moving at a velocity of 7670 m/s along the Y direction. The beamwidth for both transmit and receive is considered to be 0.1 degrees. For the simulations, the incidence angle θ of the radar beam was considered based on the geometry of the SAR platforms. Since the satellite is placed in an orbit of 400 km, the slant range

TABLE 7.1. GPM Ku radar parameters.

Parameter	Value
Frequency	13.9 GHz (Ku band)
Height of the platform	400 km
Platform velocity	7670 m/s
Antenna beamwidth	0.71 degrees
Antenna size	1.7404 m
Pulse duration	1 μs
Sampling frequency	200 MHz
Bandwidth	50 MHz
Target	Fixed/Precipitation

to the ground is approximately 400.03 km. The target grid is centered at [0 0 0] in the [Y Y Z] direction. After setting up these parameters, the SAR simulation program was ran in both stripmap and pseudo-spotlight mode of operation. The time of data capture at the SAR receiver with respect to the target (footprint) varies for spotlight and stripmap mode of operation.

The raw SAR received signal is obtained first from the simulation program and then the received SAR signal is sent to the signal processing stage, where the data is processed along the slow-time and fast-time to obtain the output. In this simulation study considered in this research work, no range compression was used for the simulation of the received signal.

Figure 7.7 shows the output of the simulation program for a fixed target in a monostatic configuration. The single fixed target is placed at the target grid center [0 0 0] in [X Y Z] direction. This figure shows plots of the raw received signal as well as the output after signal processing is carried out on the received signal. Figure 7.7 (a) shows the raw received SAR signal generated, All the values are the same as the return from a fixed target is the same as the SAR platform moves in azimuth. Figure 7.7 (b) shows the output after the azimuth compression is carried out on the raw received signal. An azimuth cut along the range of

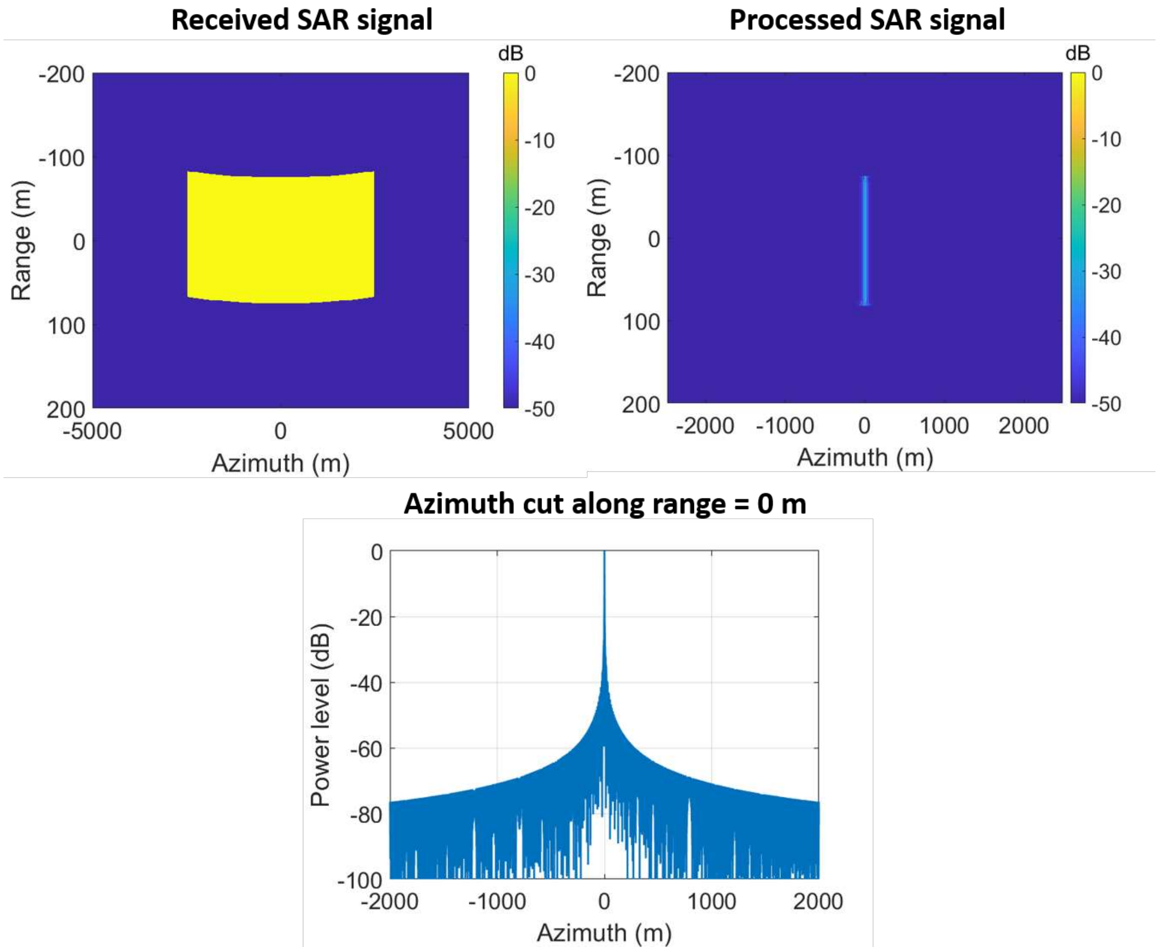
Received SAR signal

Processed SAR signal

Azimuth cut along range = 0 m

Figure 7.7. Monostatic SAR simulation output for a fixed target case, (a) raw received signal (b) Processed SAR signal and (c) Azimuth cut along range 0m of the processed SAR signal.

0 meters is shown in Figure 7.7 (c). From these output plots, it can be seen that we get a sharp peak along the cross-range (azimuth) direction, which is as expected.

Figure 7.8 shows the output of the simulation program for a weather target in a monostatic configuration. A single bin corresponding to the weather target is placed at the target grid center [0 0 0] in [X Y Z] direction. The reflectivity of the precipitation target was set at 40 dBZ, the velocity was set at 0 m/s and the spectral width was set at 1 m/s for this simulation run. Figure 7.8 shows plots of the raw received signal as well as the output after signal processing is carried out on the received signal. Figure 7.8 (a) shows the raw received

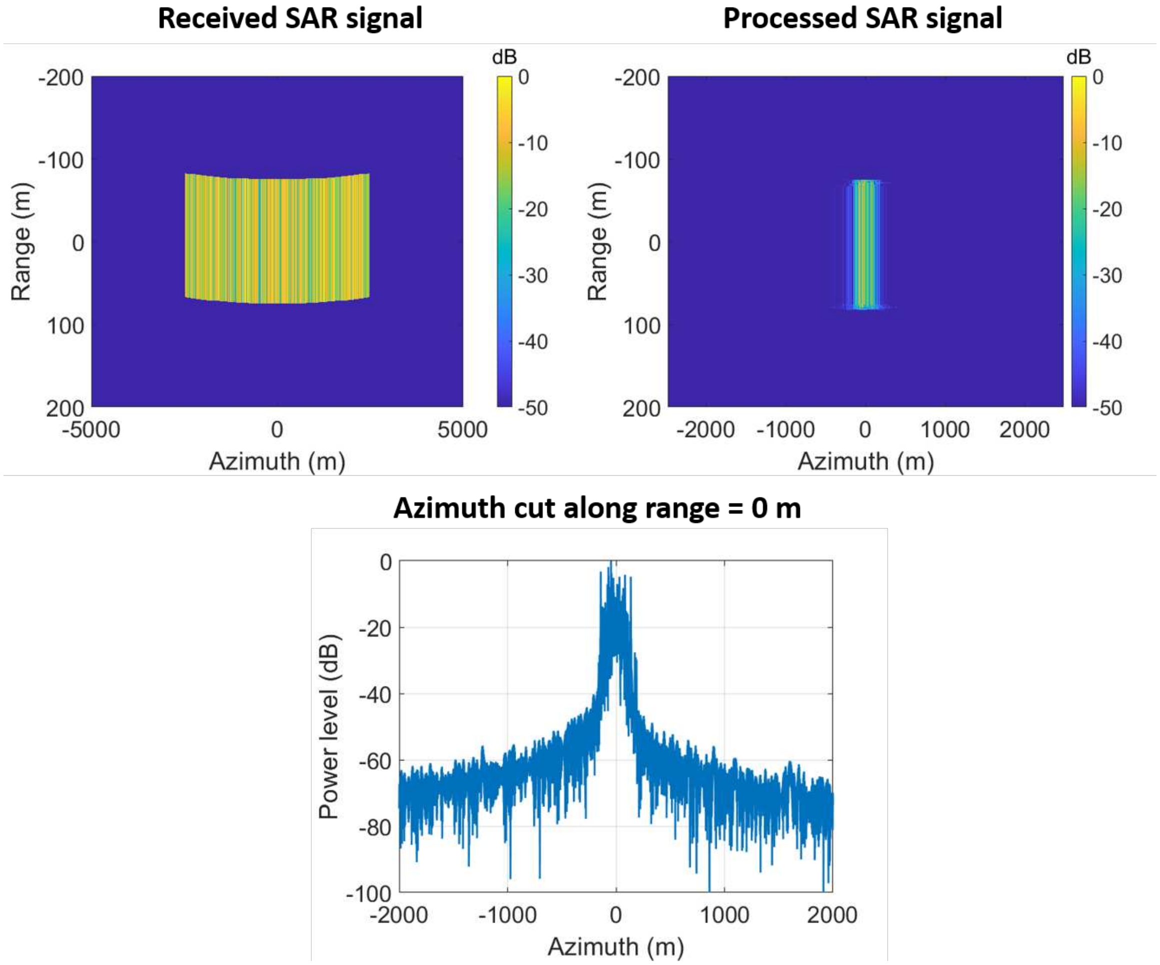

FIGURE 7.8. Monostatic SAR simulation output for a 1 bin weather target case, (a) raw received signal (b) Processed SAR signal and (c) Azimuth cut along range 0m of the processed SAR signal.

SAR signal generated. We see the variation in the returns from a weather target as the SAR platform moves in azimuth, which is generated based on the IQ simulation block. Figure 7.8 (b) shows the output after the azimuth compression is carried out on the raw received signal; an azimuth cut along the range of 0 meters is shown in Figure 7.8 (c). From these output plots it can be seen that the output is spread in cross-range direction. The spread of the output signal along the cross-range direction is expected. This spread is due to the spectral width of the precipitation particles present in the resolution volume.

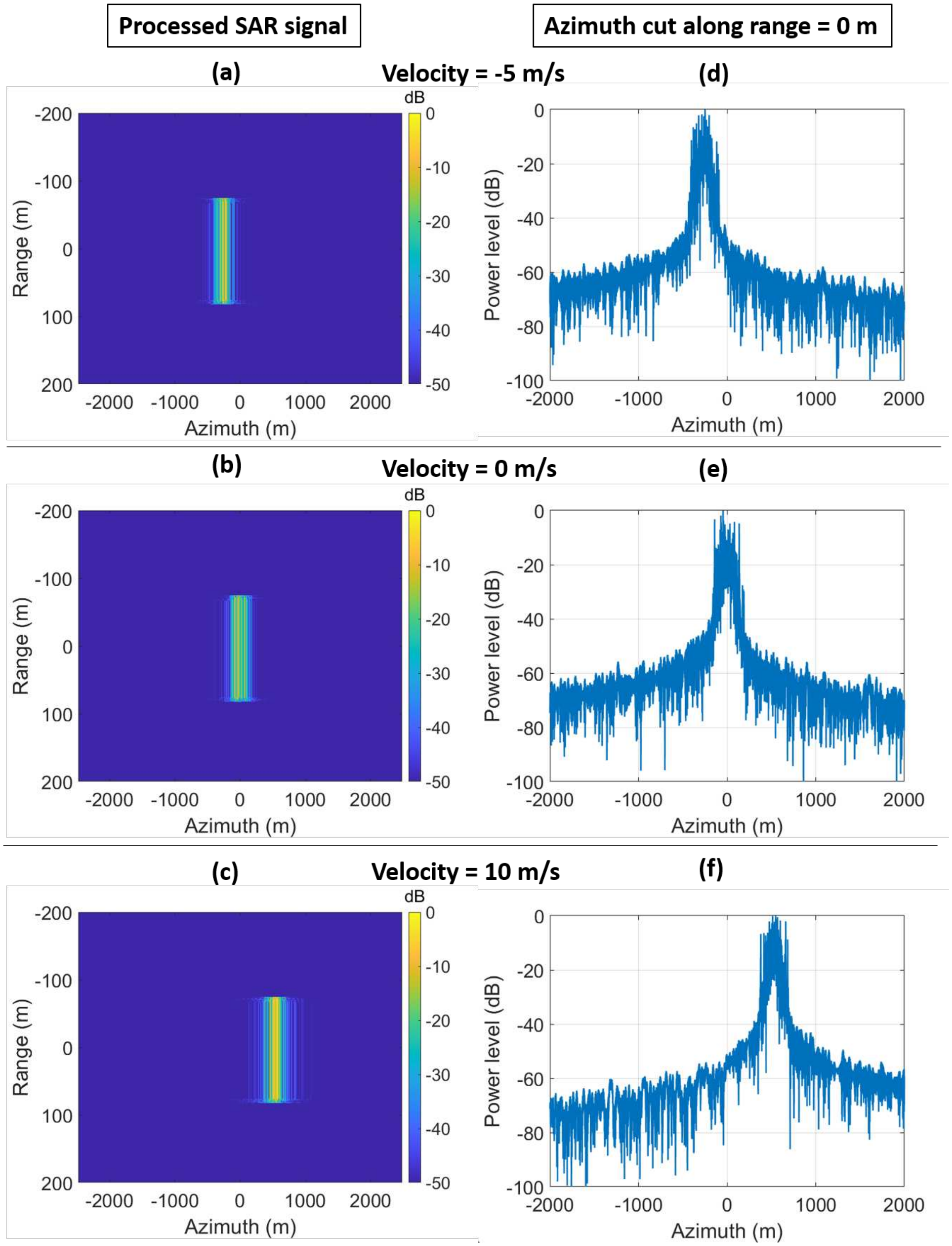

FIGURE 7.9. Monostatic SAR simulation outputs for varying velocity of the precipitation particles. (a), (b) and (c) processed SAR signal corresponding to velocities -5 m/s, 0 m/s and 10 m/s. (d), (e) and (f) Azimuth cuts along range 0m corresponding to velocities -5 m/s, 0 m/s and 10 m/s.

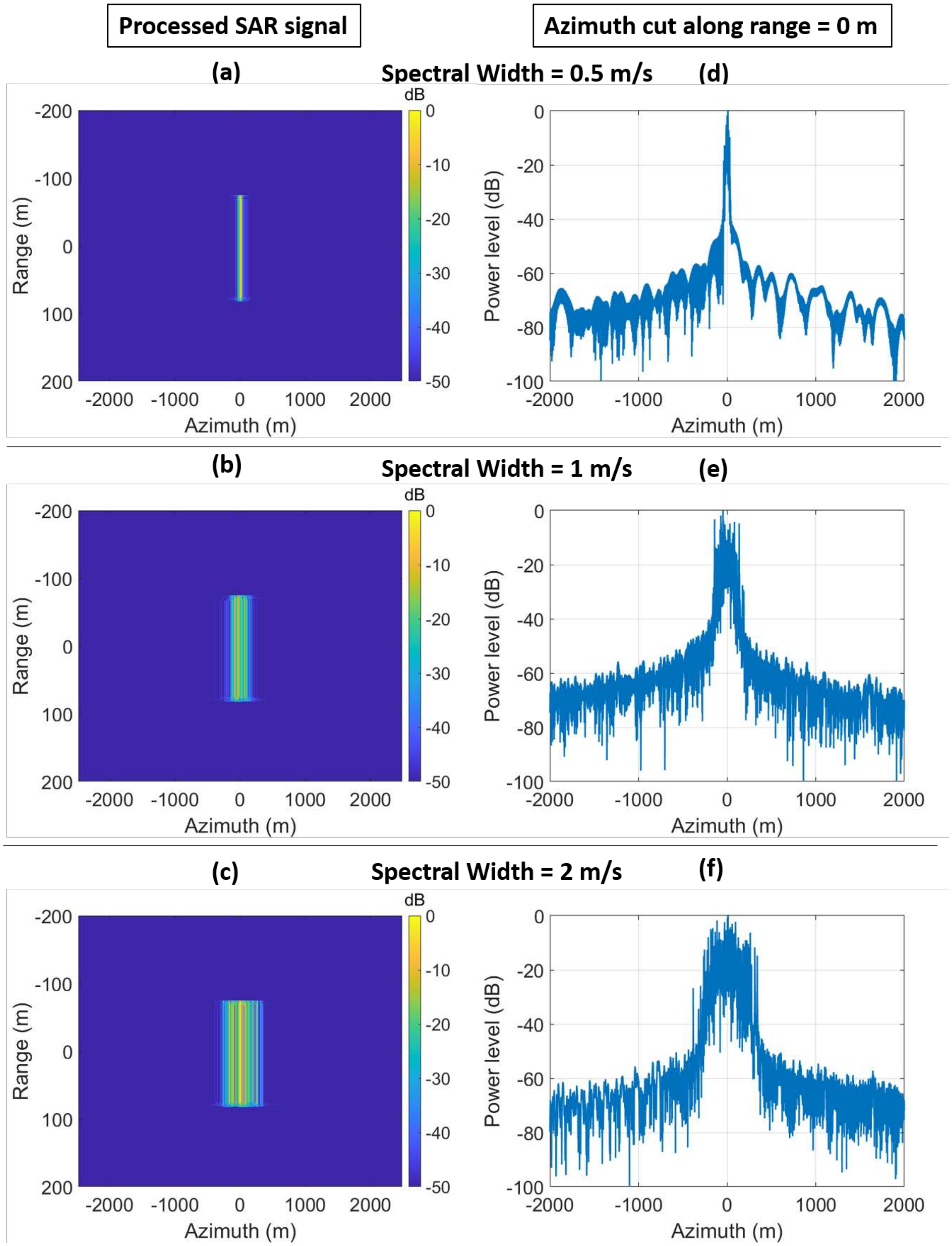

Figure 7.10. Monostatic SAR simulation outputs for varying spectral widths of the precipitation particles. (a), (b) and (c) processed SAR signal corresponding to spectral widths 0.5 m/s, 1 m/s and 2 m/s. (d), (e) and (f) Azimuth cuts along range 0m corresponding to spectral widths 0.5 m/s, 1 m/s and 2 m/s.

To understand the influence of the velocity of the precipitation particles present in the radar resolution volume, the velocity of the precipitation particles considered for the simulation is varied and the simulation results are studied. The velocity of the precipitation particles is translated as a shift in the peak of the processed signal along the cross-range direction (along azimuth). The expected shift due to varying velocity is computed using the Equation 70.

$$\Delta_{shift} = -\frac{v_t R_0}{V_a} \tag{70}$$

Where V_t is the target velocity, V_a is the platform velocity and R_0 is the range to the target. Three velocities of -5 m/s, 0 m/s and 10 m/s are considered and the SAR simulations are carried out. The outputs obtained from the SAR simulation program are shown in Figure 7.9. Considering the simulation parameters, the expected shift along azimuth for the velocity of -5 m/s is -260 meters, it can be seen from Figures 7.9 (a) and (d) that the obtained SAR output is also shifted in azimuth around 260 meters. The error in the location of the peak is in the order of few meters. From the remaining output plots in Figure 7.9, for 0 m/s velocity, we see the output peak around 0 meters (expected azimuth shift is 0 meters). For 10 m/s velocity, we see the output peak around 520 meters (expected output peak is 522 meters).

Next, to understand the influence of the spectral width of the precipitation particles present in the radar resolution volume, the spectral width of the precipitation particles considered for the simulation are varied and the simulation results are studied. The spectral width of the weather is translated as the spread of the main lobe (target) in the peak signal along the cross-range direction (along azimuth).

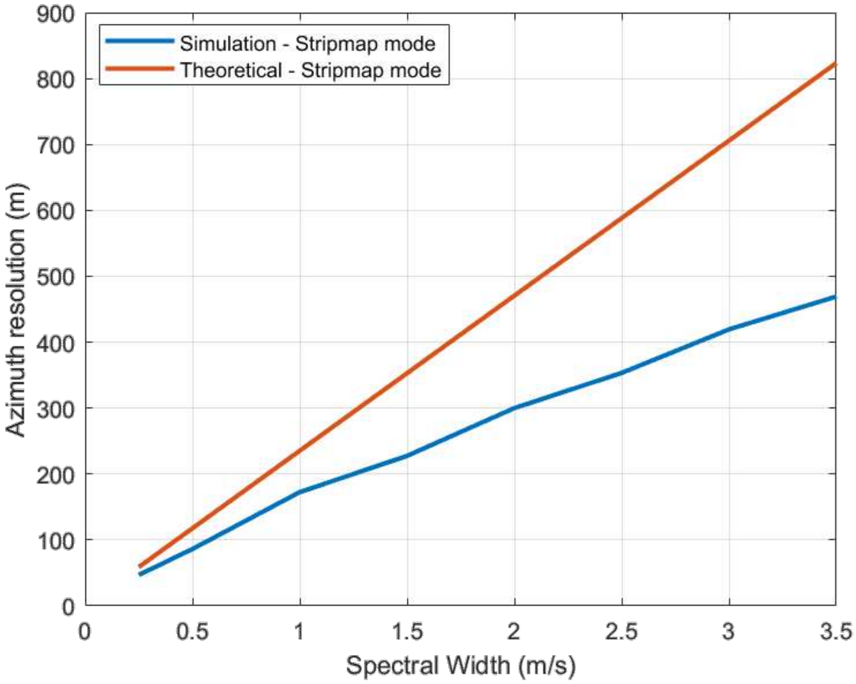

FIGURE 7.11. Theoretical and output values from simulations for azimuth resolution with varying spectral widths for monostatic SAR.

Three spectral widths of 0.5 m/s, 1 m/s and 2 m/s are considered and the SAR simulations are carried out. The outputs obtained from the SAR simulation program are shown in Figure 7.10. It can be seen from Figures 7.10 (a) and (d) that the obtained SAR output has a narrow spread in azimuth around 0 meters for spectral width of 0.5 m/s. From Figures 7.10 (b) and (e), it can be seen that the obtained SAR output has a bit broader spread in azimuth around 0 meters for spectral width of 1 m/s compared to the output obtained for 0.5 m/s spectral width. From Figures 7.10 (c) and (f), we also see a much larger spread in azimuth when considering a spectral width of 2 m/s. From these results, we can infer that as the spectral width of the precipitation particles increases, the width of the main lobe corresponding to the target also increases.

To study the effect of varying spectral width on the azimuth resolution of the output. A Gaussian curve was fitted on the obtained output from the SAR simulations. The 3 dB

TABLE 7.2. Summary of the simulation outputs obtained for stripmap and spotlight mode of SAR.

Simulation mode	Spectral width (m/s)	Footprint (m)	Theoretical resolution expected (m)	Observed 6 dB cutoff resolution (m)
Stripmap	0.25	5033	58.8	32
Stripmap	1	5033	235.3	161
Stripmap	3	5033	705.9	534

cut from the fitted curve will give us the azimuth resolution of the output. The summary of results obtained for the stripmap mode for three different spectral widths corresponding to precipitation particles is given in Table 7.2. From this table, it can be seen that better resolution in the azimuth is obtained for stripmap mode compared to the expected theoretical resolutions. The following spectral width values were considered, 0.25, 0.5, 1, 1.5, 2, 2.5, 3, 3.5, five simulation runs were carried out at each spectral width value and the average azimuth resolution numbers are plotted in Figure 7.11. In this figure, the theoretical value of the expected resolution for the corresponding spectral width is also plotted. From the results, it can be seen that as the spectral width increases, the resolution also increases. Also, the measured resolution from the simulation runs is lower than that of the expected resolutions.

Figure 7.12 shows the output of the simulation program for a weather target in a monostatic configuration. In this simulation case, a resolution of 500 meters is considered and the SAR simulation are carried out considering the size of a resolution bin along the azimuth. A 500 meter resolution corresponding to the weather target ranging from -250 meters to 250 meters is placed with reference to the target grid center [0 0 0] in [X Y Z] direction. The reflectivity of the precipitation target resolution was set at 40 dBZ, the velocity was set at 0 m/s and the spectral width was set at 1 m/s for this simulation run. Figure 7.12 shows plots of the raw received signal as well as the output after signal processing is carried out on the

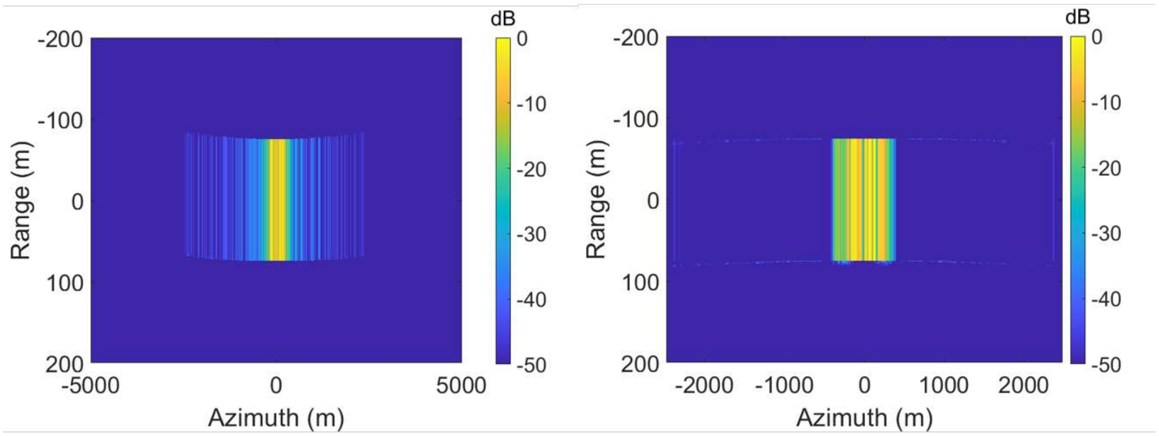

(a) Received SAR signal

(b) Processed SAR signal

(c) Azimuth cut along range = 0 m

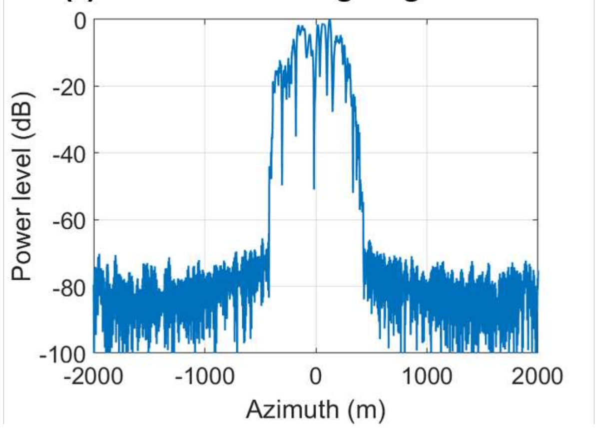

Figure 7.12. Monostatic SAR simulation output for a 1 resolution volume of 500 m weather target case, (a) raw received signal (b) Processed SAR signal and (c) Azimuth cut along range 0m of the processed SAR signal.

received signal. Figure 7.12 (a) shows the raw received SAR signal generated. We see the variation in the returns from a weather target as the SAR platform moves in azimuth which is generated based on the IQ simulation block for all the pulses in the resolution volume. Figure 7.12 (b) shows the output after the azimuth compression is carried out on the raw received signal. An azimuth cut along the range 0 meters is shown in Figure 7.12 (c). From these output plots it can be seen that the output is uniform in the resolution considered and spread in cross-range direction after that. The spread of the output signal along the cross-range once the resolution bin ends is expected, as mentioned earlier, this is due to the spectral width of the precipitation particles in the resolution volume.

7.4.2. MONOSTATIC MODE PSEUDO-SPOTLIGHT CONFIGURATION RESULTS. In this section, the SAR simulation results for a pseudo-spolight mode is carried out and discussed. In the spotlight mode of SAR operation, the receive antenna of the SAR system is focused on a particular area of interest as the platform moves. In traditional SAR systems which map the geodata of Earth, the advantage of using a spotlight mode compared to a stripmap mode of operation is that we get azimuth resolution improvement. The architecture of the spotlight SAR mode is shown in Figure 7.13.

Carrying out SAR signal simulations in the spotlight modes requires the antenna beam to be steered to the region of interest. It is challenging to code up the transmit and receive geometry to handle the spotlight mode of operation. In the current code, we have developed a pseudo-spotlight mode in which the beamwidth of the antenna is varied accordingly, which gives us a larger antenna footprint in turn, a larger synthetic aperture time. For the simulations considered, we have increased the beamwidth by a factor of two, which increases the synthetic aperture time by a factor of two. To understand the pseudo-spotlight simulation mode that is implemented in the simulation code package, an architecture diagram for the same is shown in Figure 7.14.

Figure 7.15 shows the output of the simulation program for a fixed target in pseudo-spotlight mode and monostatic configuration. A single fixed target is placed at the target grid center [0 0 0] in [X Y Z] direction. The figure shows plots of the raw received signal and the output after signal processing which is carried out on the received signal. Figure 7.15 (a) shows the raw received SAR signal generated. All the values are the same as the return from a fixed target is the same as the SAR platform moves in azimuth. It can also be

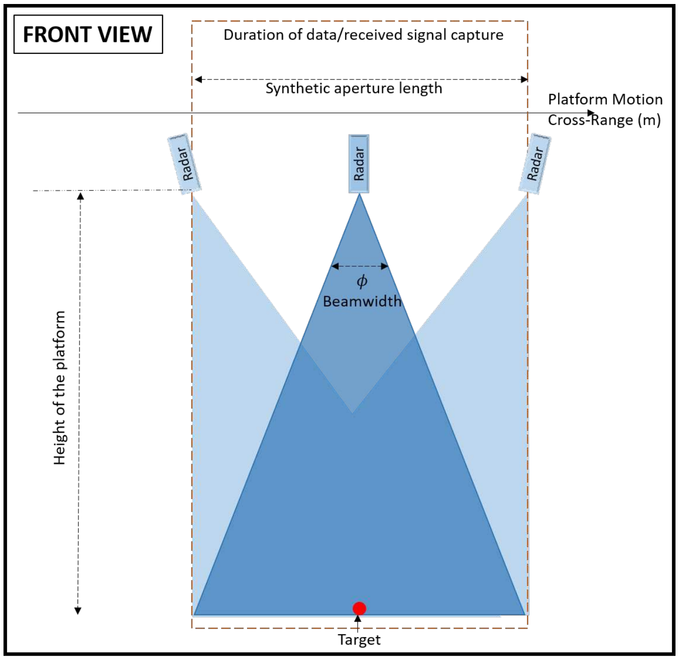

FIGURE 7.13. SAR architecture for spotlight mode - front view.

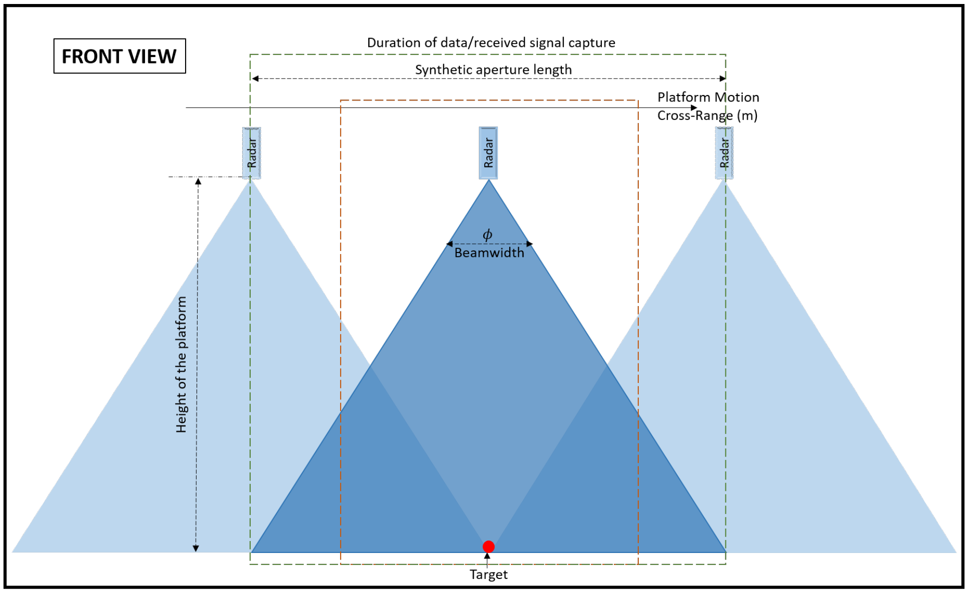

FIGURE 7.14. SAR architecture for pseudo-spotlight mode - front view.

seen that the data is obtained for the entire duration of the simulation window considered. Figure 7.15 (b) shows the output after the azimuth compression is carried out on the raw received signal. An azimuth cut along the range of 0 meters is shown in Figure 7.15 (c).

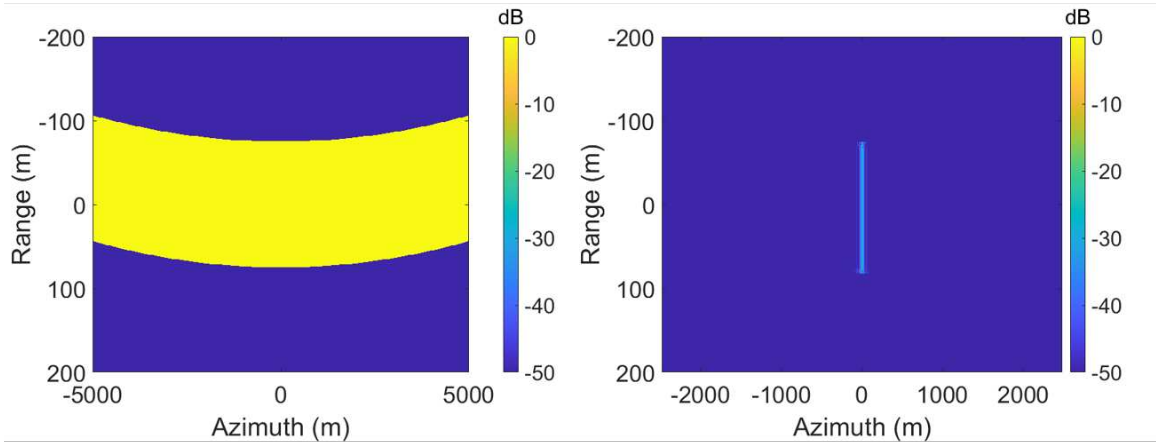
(a) Received SAR signal

(b) Processed SAR signal

(c) Azimuth cut along range = 0 m

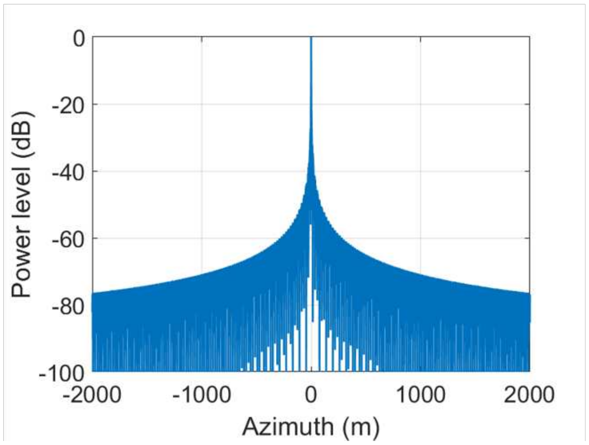

Figure 7.15. Monostatic SAR simulation output for a fixed target case - pseudo-Spotlight mode, (a) raw received signal (b) Processed SAR signal and (c) Azimuth cut along range 0m of the processed SAR signal.

From these output plots, it can be seen that we get a sharp peak along the cross-range (azimuth) direction which is as expected.

Figure 7.16 shows the output of the simulation program for a weather target in pseudo-spotlight mode and monostatic configuration. A single bin corresponding to the weather target is placed at the target grid center [0 0 0] in [X Y Z] direction. For this simulation run, we set the reflectivity of the precipitation target at 40 dBZ, the velocity at 0 m/s, and the spectral width at 1 m/s. Figure 7.16 shows plots of the raw received signal as well as the output after signal processing is carried out on the received signal. Figure 7.16 (a) shows the

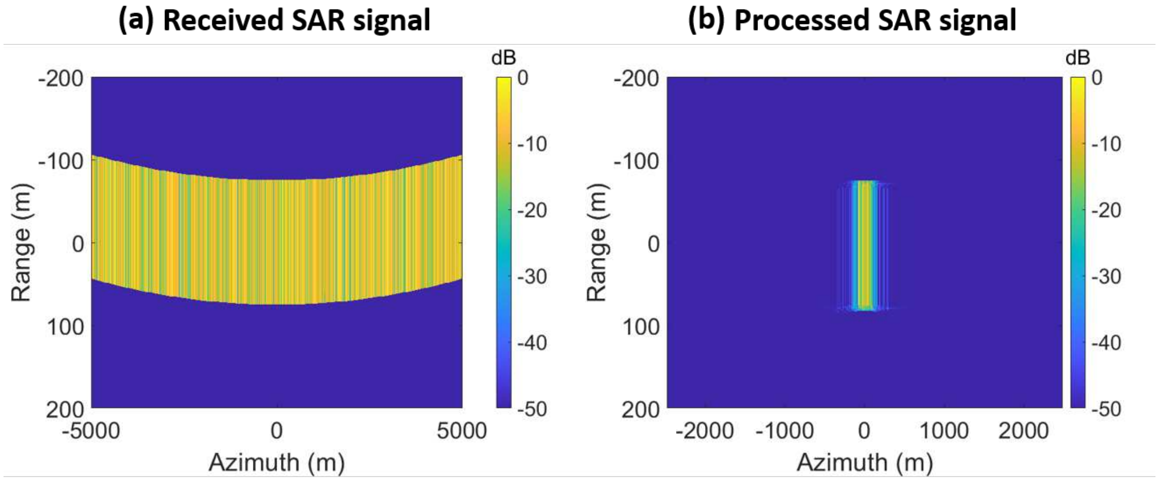
(a) Received SAR signal

(b) Processed SAR signal

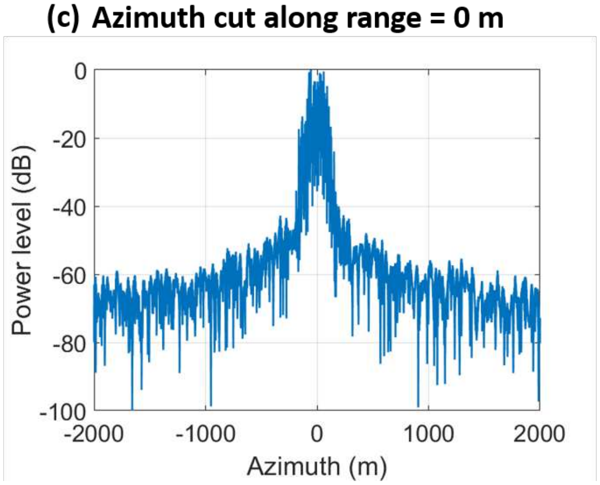
(c) Azimuth cut along range = 0 m

Figure 7.16. Monostatic SAR simulation output for a 1 bin weather target case - pseudo-Spotlight mode, (a) raw received signal (b) Processed SAR signal and (c) Azimuth cut along range 0m of the processed SAR signal.

raw received SAR signal generated. We see the variation in the returns from a weather target as the SAR platform moves in azimuth, generated based on the IQ simulation block. In this case too, we can see that the data is obtained for the entire duration of the simulation window considered. Figure 7.16 (b) shows the output after the azimuth compression is carried out on the raw received signal. An azimuth cut along the range 0 meters is shown in figure Figure 7.16 (c). From these output plots, it can be seen that the output is spread in cross-range direction. The spread of the output signal along the cross-range direction is expected. This is due to the spectral width of the precipitation particles present in the resolution volume. The

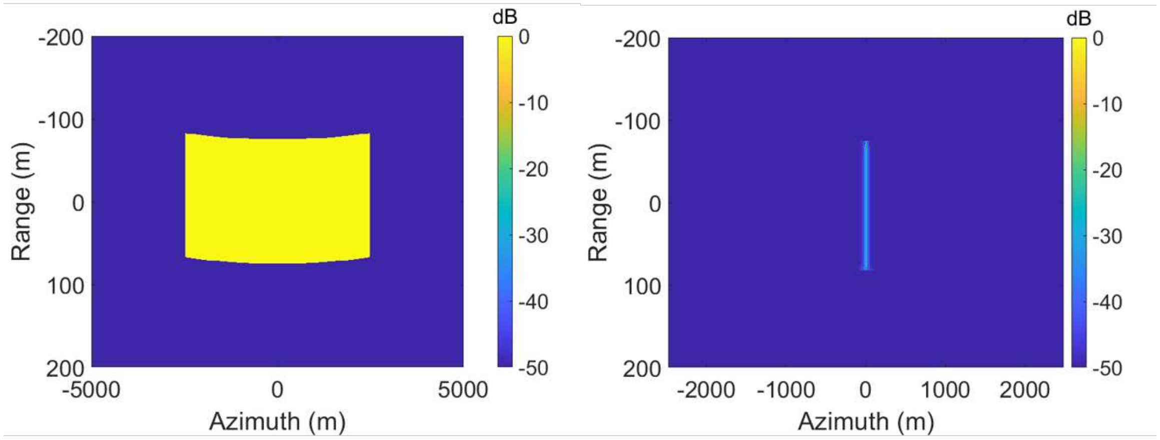
(a) Received SAR signal

(b) Processed SAR signal

(c) Azimuth cut along range = 0 m

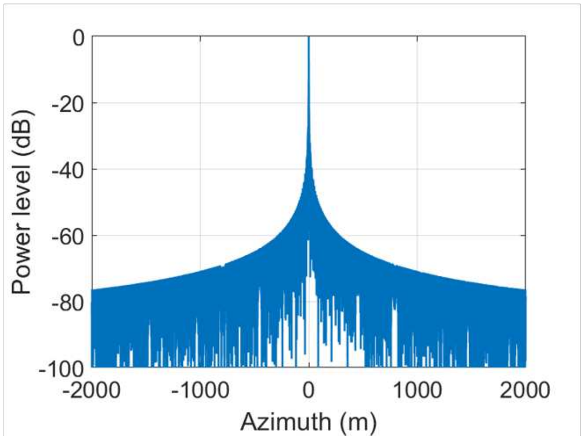

Figure 7.17. Bistatic SAR simulation output for a fixed target case, (a) raw received signal (b) Processed SAR signal and (c) Azimuth cut along range 0m of the processed SAR signal.

output cut has more clarity in the spotlight mode of operation, this is due to the additional data obtained in this SAR operating mode.

7.5. Simulations of SAR in bistatic mode for observing precipitation target

In this section, the SAR simulation results for the bistatic architecture are discussed. The spaceborne SAR platform is considered for the bistatic SAR simulation. The bistatic architecture is shown in Figure 7.5. The transmitter is located at [5km 0 400km] in [X Y Z] direction, and the receiver is located at [-5km 0 400km] in [X Y Z] direction. Both the transmit and receive platforms are moving at a velocity of 7670 m/s along the Y direction. The beamwidth for both transmit and receive antenna is 0.1 degrees. The beta angle is defined as the angle formed between the transmitter-target-receiver. This angle is very small for the simulation case considered. The beta angle value is 1.432 degrees. With this very low beta angle, the simulation results are expected to be closely matching with the monostatic results. For the simulations, the incidence angle θ of the radar beam was considered based on the geometry of the SAR platforms. Since the satellite is placed in an orbit of 400 km, the slant range to the ground is approximately 400.03 km. The target grid is centered at [0 0 0] in the [X Y Z] direction. For the simulations, the baseline distance (the distance between the transmit and receive platforms) is considered as 10 km. This value is small compared to the platform height distance of about 400 km. Similar results corresponding to monostatic results are expected for the bistatic cases too. The pulse repetition frequency was considered as 18 KHz for the simulations. These simulation parameters were set up and the simulation program was run in the stripmap mode of bistatic SAR operation.

Figure 7.17 shows the output of the simulation program for a fixed target in a bistatic configuration. A single fixed target is placed at the target grid center [0 0 0] in [X Y Z] direction. The figure shows plots of the raw received signal and the output after signal processing is carried out on the received signal. Figure 7.17 (a) shows the raw received SAR signal generated. All the values are the same as the return from a fixed target is the same as the SAR platform moves in azimuth. Figure 7.7 (b) shows the output after the azimuth compression is carried out on the raw received signal. An azimuth cut along the range 0 meters is shown in Figure 7.17 (c). From these output plots, it can be seen that we get a sharp peak along the cross-range (azimuth) direction which is as expected.

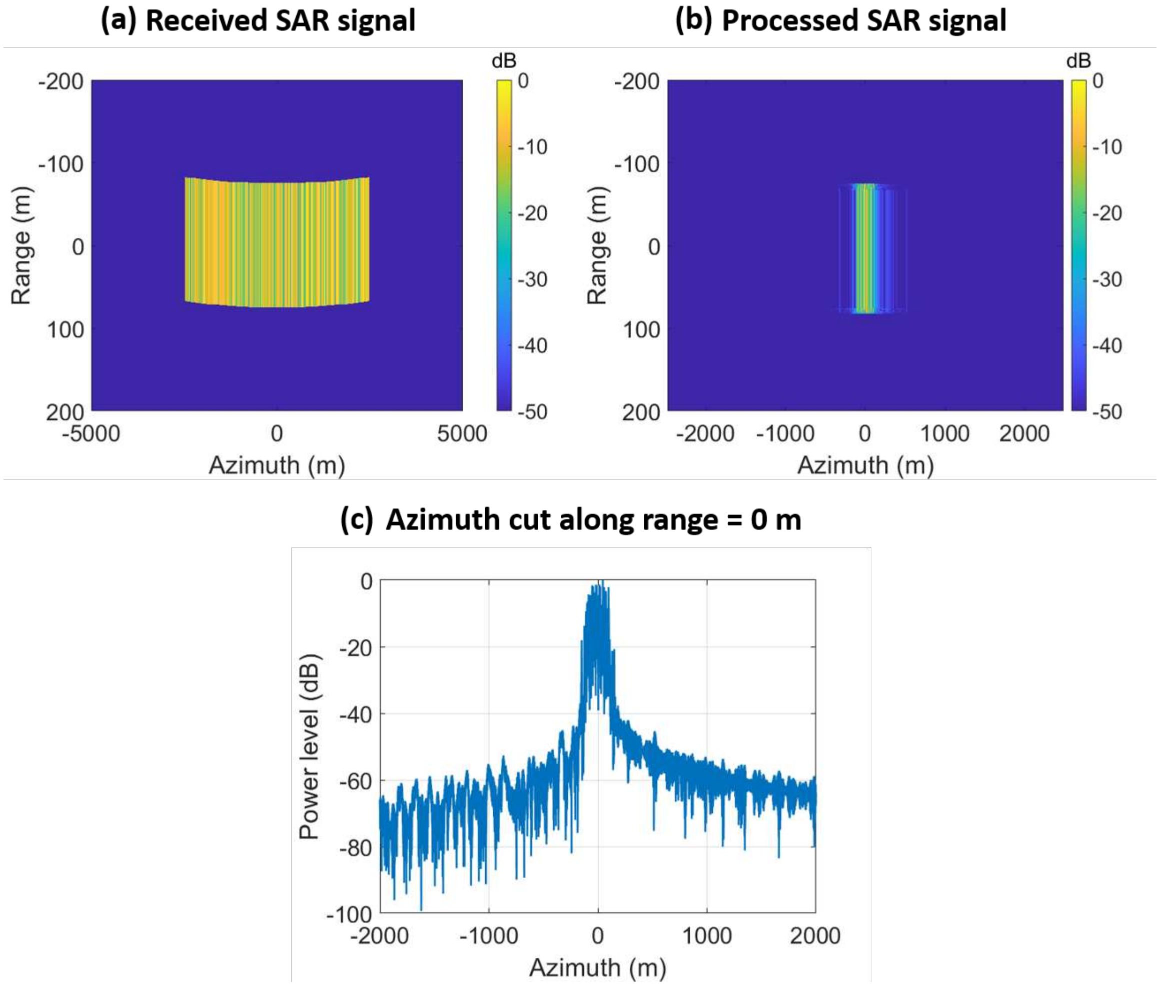

FIGURE 7.18. Bistatic SAR simulation output for a 1 bin weather target case, (a) raw received signal (b) Processed SAR signal and (c) Azimuth cut along range 0m of the processed SAR signal.

Figure 7.18 shows the output of the simulation program for a weather target in a bistatic configuration. A single bin corresponding to the weather target is placed at the target grid center [0 0 0] in [X Y Z] direction. The reflectivity of the precipitation target was set at 40 dBZ, the velocity was set at 0 m/s and the spectral width was set at 1 m/s for this simulation run. Figure 7.18 shows plots of the raw received signal and the output after signal processing is carried out on the received signal. Figure 7.18 (a) shows the raw received SAR signal generated. We see the variation in the returns from a weather target as the SAR platform moves in azimuth, which is generated based on the IQ simulation block. For the

(a) Received SAR signal **(b) Processed SAR signal**

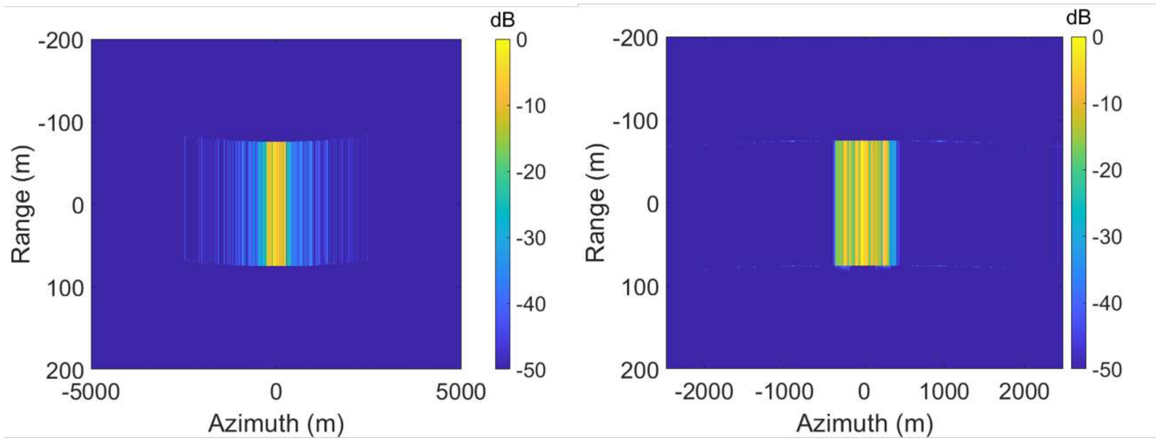

(c) Azimuth cut along range = 0 m

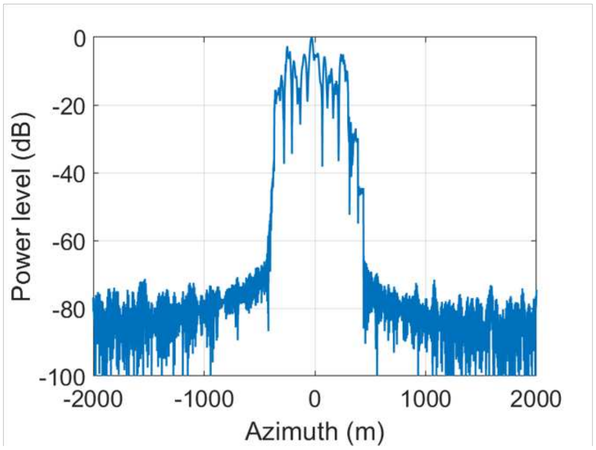

FIGURE 7.19. Bistatic SAR simulation output for a 1 resolution volume of 500 m weather target case, (a) raw received signal (b) Processed SAR signal and (c) Azimuth cut along range 0m of the processed SAR signal.

bistatic simulation case; the IQ signals are generated based on the beta angle. Figure 7.18 (b) shows the output after the azimuth compression is carried out on the raw received signal. An azimuth cut along the range of 0 meters is shown in Figure 7.18 (c). From these output plots it can be seen that the output is spread in cross-range direction. The spread is due to the output signal along the cross-range direction is expected. This is due to the spectral width of the precipitation particles present in the resolution volume. The results are similar to that obtained from the monostatic case because the beta angle is very low for the bistatic SAR architecture considered.

Figure 7.19 shows the output of the simulation program for a weather target in a bistatic configuration. In this simulation case, a resolution of 500 meters is considered and the SAR simulation is carried out considering the size of a resolution bin along the azimuth. A 500 meter resolution corresponding to the weather target ranging from -250 meters to 250 meters is placed with reference to the target grid center [0 0 0] in [X Y Z] direction. The reflectivity of the precipitation target resolution was set at 40 dBZ, the velocity was set at 0 m/s and the spectral width was set at 1 m/s for this simulation run. Figure 7.19 (a) shows the raw received SAR signal generated; we see the variation in the returns from a weather target as the SAR platform moves in azimuth, which is generated based on the IQ simulation block for all the pulses in the resolution volume. Figure 7.19 (b) shows the output after the azimuth compression is carried out on the raw received signal. An azimuth cut along the range 0 meters is shown in Figure 7.19 (c). From these output plots it can be seen that the output is uniform in the resolution considered and spread in cross-range direction after that. The spread of the output signal along the cross-range once the resolution bin ends is expected. As mentioned earlier this is due to the spectral width of the precipitation particles present in the resolution volume.

7.6. SAR SIMULATIONS CONSIDERING INPUT WEATHER RADAR DATA

To have a better understanding of the SAR simulations, actual radar data that was collected by a ground-based weather radar is considered and the SAR simulations are carried out. The values of the weather radar parameters such as reflectivity are given as the input for the IQ data simulation module based on the location of the precipitation event. The current code package can handle data along the azimuth direction and in one range gate above the ground. The range gate closest to the ground is considered and a profile of precipitation event

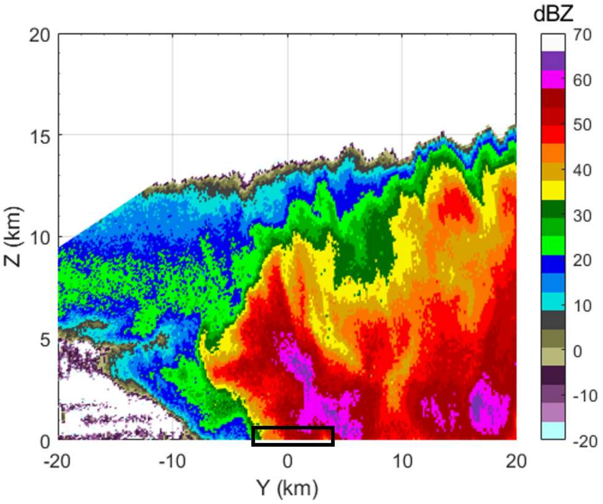

Figure 7.20. RHI plot of CHILL S-band radar data considered for the simulation case.

is simulated. One case of simulation is discussed in this research work. There is potential for more detailed analysis to be carried out. The reflectivity profile for the simulation was considered from an actual precipitation event from the CSU-CHILL S-band radar. A picture of the storm and the region from which reflectivity values were chosen are shown in Figure 7.20.

Considering the computation time of the simulation code, a short region centered around the target grid is considered for the simulations. The input reflectivity profile, which varies from -1km to 1km in the azimuth direction, is shown in the Figure 7.22. It can be seen from this figure that the reflectivity varies by about 10 dBZ. This variation in reflectivity is expected in the output of the SAR processed data. The other parameters for the precipitation were kept at a constant value. The velocity was set at 0 m/s and the spectral width was set at 1 m/s for this simulation case.

The same processing flow is followed for obtaining the results in this case too. The raw data that is generated from the simulation program is sent to the signal processing program, in which the data is processed to obtain the final SAR image. Range compression is not used

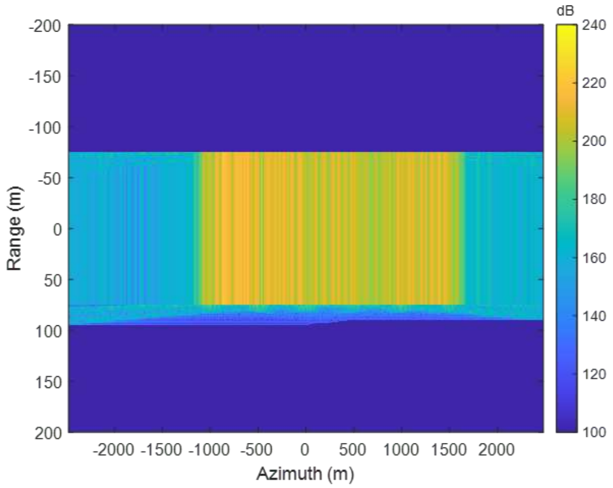

FIGURE 7.21. Azimuth compressed SAR output image for simulation considering profile of reflectivity.

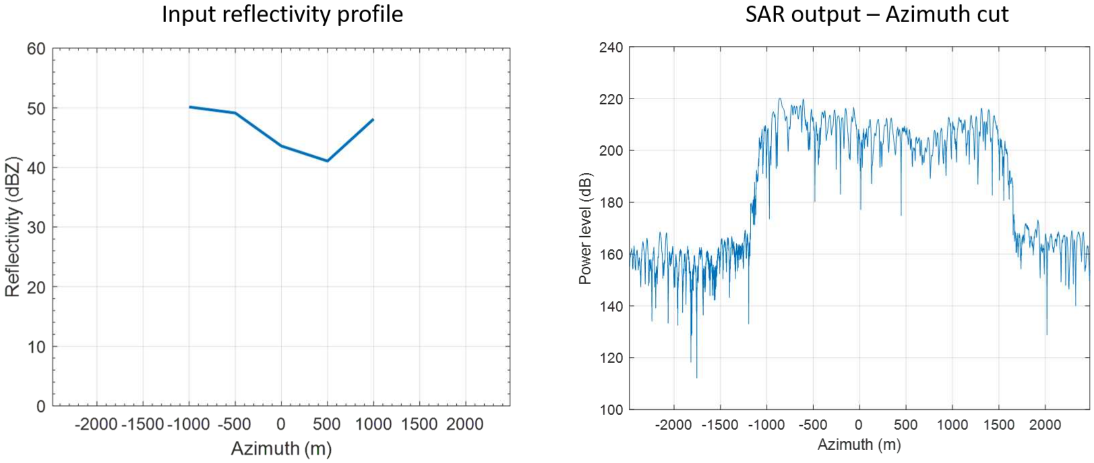

FIGURE 7.22. (left) Azimuth cut of input reflectivity profile and (right) azimuth cut of output SAR processed image corresponding to range 0 meters

for the simulations. Azimuth compression is performed on the SAR data and the results are studied. The azimuth compressed output for this simulation case is shown in Figure 7.21.

The azimuth or cross-rage cut along range 0 meters is shown in Figure 7.22. From this figure, it can be seen that the same trend of the input reflectivity profile is observed in the output reflectivity profile. More detailed analysis and optimization of the code have to be done for accurate simulation and interpretation of the data.

CHAPTER 8

SUMMARY AND FUTURE WORK

8.1. SUMMARY

This research work focuses on improving precipitation mapping at local, regional and global scales. At the local scale, the concept of using millimeter wave frequency band radars to estimate precipitation information was introduced. At the regional scale, a new attenuation correction algorithm to correct attenuation for rain and ice particles is discussed. The attenuation corrected data will improve the accuracy of the precipitation estimates. A proposed system of using a network of automobile radars for regional precipitation mapping is also discussed. At the global scale, simulation studies of spaceborne synthetic aperture radars (SAR) for mapping precipitation is discussed.

A brief introduction to the different instruments which are currently available for remote sensing of the atmosphere was discussed in Chapter 1. Next, in this chapter, the current precipitation measurement methods in the urban regions is discussed. A brief overview of the rise in urbanization and the rise in global water cycle is discussed. The challenges of measuring precipitation in urban areas and the need for improving it was also discussed in this chapter. Some of the issues include radar beam blockage due to structures, observation gaps due to the radar beam propagation and spatial gaps in surface level precipitation data. Finally, the objectives of this research were described with specific goals.

In chapter 2, the remote sensing instruments which collect data at a specific geolocation are introduced. The various types of rain gauges and disdrometers are discussed. Data from a rain gauge deployed at the Colorado State University campus is discussed considering four year data from the instrument, A Parsivel disdrometer dataset taken from the ICE-POP field campaign is discussed considering rain and snow events. The variation of the particle size distributions for rain and snow was studied. For the data set considered, the drop diameters of the rain particles were concentrated below 2 mm and had velocity values up to 7 m/s. The snow particles were having a larger spread in the distribution of drop diameters with the maximum diameter going up to 6 mm, but had lower velocity values compared to rain particles.

In chapter 3 starts with a brief introduction to automobile radars. Next in this chapter, the frequency bands and the various applications of the automobile radars were briefly introduced. The key parts of the 77 GHz automobile radar was discussed with the help of a simple block diagram. Next, in this chapter, the use of automobile radars as a rain gauge was introduced. The various considerations and design specifications for using the W-band (77 GHz) radars to measure rain rate is explained in detail with supporting equations. Theoretical simulations were carried out at 77 GHz and the relationships between rain rate, reflectivity and attenuation were obtained.

The technology aspect of the millimeter wave radars is also discussed in chapter 3. The need for a timeseries IQ data simulation tool is introduced. The different approaches for generating a timeseries signal is briefly introduced. A timeseries IQ signal simulation code is developed, which accounts for all precipitation particles in the radar resolution volume individually. The various aspects considered for signal simulation such as the distribution of precipitation particles and the radar backscattering are discussed in detail. The steps of the simulation code are discussed with the help of a block diagram. A signal simulation is carried out at 77 GHz, the output signals are analyzed and the signal statistics are discussed which are consistent with the prior literature. The current state-of-the-art automobile sensors are introduced. An evaluation board TI AWR1642 which has the TI automobile radar on a chip is briefly introduced, this board is used for rain rate estimation experiments. The experiments of using millimeter wave radars for measuring precipitation is discussed in detail. The reflectivity value of approximately 52 dB was obtained for a precipitation event using the automobile radar evaluation module, this value is in close agreement with the NWS reflectivity value considered at the location of the experiment.

Weather radars play a prominent role in the remote sensing of the atmosphere. In Chapter 4, a brief introduction to weather radars was discussed. This information will serve as a foundation for understanding the various radar moments obtained from the received radar signal. The received radar signal was explained in detail with the help of range-time axis and sample-time axis diagram. The scattering matrix of the dual-polarization radar was explained. The two orthogonally transmitted horizontal and vertical signals, which will give useful information regarding the particle size, shape and orientation of the hydrometeors are explained. The various radar moments which are obtained from the received radar signal along with the computational equations were explained. Precipitation estimates obtained using weather radars are discussed. Radar data from S, X and Ku bands are considered and the rain rate estimation methods are discussed. The Ku band radar data from ICE-POP campaign is considered and the method of obtaining snow rate is also briefly discussed. The next section in this chapter discusses the current systems which are used for mapping precipitation. Three different systems which are used for obtaining the precipitation information are introduced.

As mentioned earlier, the attenuation of radar signals has been a well-known issue since the beginning of radar technology. While numerous research is available in the literature for attenuation correction for rain particles, only a few look into attenuation correction for ice hydrometeors. The attenuation encounters by ice hydrometeors are small compared to rain, but they should be accounted for and corrected in radar data to get accurate retrievals such as the precipitation rate. Chapter 5 starts with an introduction to attenuation in weather radars. The DROPS1.0 and DROPS2.0 algorithms, which process the radar data and give quality corrected, rain attenuation corrected and hydrometeor classification outputs were explained in detail with examples. A brief introduction of attenuation correction for ice hydrometeors was discussed. The simulation procedure for obtaining the relationship between specific attenuation and radar moments was discussed. It was also seen that various parameters associated with ice hydrometeors need to be considered for simulations. The simulation results obtained for X and Ku frequencies at horizontal and vertical polarizations were discussed in detail and the relationships were obtained accordingly. The numerical values for the attenuation relationships were also provided.

Next in chpater 5, the algorithm proposed for attenuation correction of all hydrometeors is explained in detail. The algorithm uses the specific phase and hydrometeor classification outputs from DROPS2.0 algorithm along with theoretical simulation relationships to correct attenuation. The relationship between specific attenuation and path integrated attenuation was also explained. The Ku band radar data collected during the 2018 ICE-POP field campaign from D3R weather radar and X-band radars deployed in Santa Clara, California and Mt. Crested Butte, Colorado are used to study the performance of the algorithm. The radar data set from ICE-POP campaign has data from both rain and snow events. A maximum PIA of 8 dB was seen in D3R Ku data during an intense snow storm. The PIA at X band was relatively low compared to the Ku band data, a maximum PIA of 2 dB was observed with the X band dataset. The performance of the proposed algorithm for attenuation correction visually looks good. The results of Ku band were compared with data from a nearby disdrometer from which it was seen that attenuation correction improves the quality of the corrected data.

Chapter 6 discusses the system analysis of using a network of automobile radars for precipitation mapping. The simulation results of using automobile radars for generating precipitation map in urban regions are discussed in detail in this chapter. The Dallas-Fort Worth urban region is considered for the simulation study. Since this concept is new, the simulation steps are explained one step at a time and the results are presented. The road map data is obtained for the region and then the simulation points resembling automobile radars are generated using the rain rate obtained from the CASA radar network. Different interpolation methods are studied to generate the precipitation map using the simulated points. The natural neighbour interpolation method gives the best result. The performance of the output is studied. Various factors which will influence the generation of precipitation maps are briefly discussed. These simulations show the potential of using automobile radars in meteorological applications on a regional scale. A potential future system that can be implemented by using a network of automobile radars for precipitation mapping is also discussed.

Obtaining precipitation information using spaceborne synthetic aperture radar (SAR) is an emerging field of study. Chapter 7 starts with an introduction to the current technology for precipitation mapping from satellites. Next in this chapter, introduction for SAR for mapping precipitation is given. Detailed mathematical framework for monostatic and bistatic SAR was discussed in detail with the specific architecture considered. For the bistatic case, a specific architecture with a baseline distance of 10 km was considered. A simulation system for SAR signals which models precipitation volumes is developed. The GPM Ku band radar parameters were considered and the simulations were carried out in stripmap mode for monostatic and bistatic SAR architecture. The pseudo-spotlight mode of simulations was carried out for the monostatic architecture. From the simulation results, it was seen that the azimuth resolution is affected by the spectral width of the precipitation particles. The bistatic simulation results look similar to the monostatic results because of the short baseline distance compared to the platform height in the architecture considered. Variation of mean velocity translates as a shift of the signal in the azimuth direction. Variation of spectral width has a influence on the spread of the output signal, larger the spectral width, larger the spread of the output signal.

8.2. FUTURE WORK

The research on using millimeter wave automobile radars for precipitation mapping showed promising results. Further research of the various automobile radars available currently in the market can be done. The use of automobile radar for precipitation measurement can to be studied further. This will aid in efficiently designing the radar system in the future. More field experiments using a millimeter wave radar for mapping precipitation information should be carried out. The precipitation results obtained can be studied for the correctness and compared with rain rates obtained from other instruments such as weather radars. Additional constraints and features can be developed for the simulations of obtaining precipitation maps using a network of automobile radars.

The research related to the attenuation correction for ice hydrometeors can be explored further. The proposed attenuation correction algorithm can work well when the radar backscattered signal is in the Rayleigh scattering region. At higher frequency, the appropriate signal simulations considering Mie scattering must be carried out to implement this algorithm. Attenuation correction at higher frequency bands is not simple. Currently limited literature is available regarding attenuation correction for rain at higher frequency bands such as Ka and W-band radars. The attenuation correction for the D3R Ka-band can be looked into and using the attenuation information at Ku band, a new attenuation correction method can be developed for D3R Ka band. The proposed attenuation correction method discussed in this research can be merged with DROPS2.0 algorithm and a new package of post-processing algorithms can be developed and released. More case studies on a large dataset has to be carried out to validate the attenuation correction research.

The simulation tool for observing precipitation from the spaceborne SAR platform can be upgraded to accommodate various architectures in the bistatic case. Currently, the code can perform simulation for a single range profile. Code package that can handle multiple range profiles in a 3D sense can be developed. Simulation studies can be carried out to study the effects of varying radar parameters on the output signal.

Bibliography

[1] U. Nations, “World urbanization prospects: The 2018 edition highlights,” *Department of Economic and Social Affairs*, 2018.

[2] S. M. Patole, M. Torlak, D. Wang, and M. Ali, “Automotive radars: A review of signal processing techniques,” *IEEE Signal Processing Magazine*, vol. 34, no. 2, pp. 22–35, 2017.

[3] S. Montanari, *Fabrication and characterization of planar Gunn diodes for Monolithic Microwave Integrated Circuits*, vol. 9. Forschungszentrum, Zentralbibliothek, 2005.

[4] T. Instruments, *AWR1642 Evaluation Module (AWR1642BOOST) Single-Chip mmWave Sensing Solution.*, 2020.

[5] H. Chen, V. Chandrasekar, and R. Bechini, “An improved dual-polarization radar rainfall algorithm (drops2. 0): Application in nasa ifloods field campaign,” *Journal of Hydrometeorology*, vol. 18, no. 4, pp. 917–937, 2017.

[6] B. Cutt and R. Lawrence, “Managing data quality in a terabyte-scale sensor archive,” in *Proceedings of the 2008 ACM symposium on Applied computing*, pp. 982–986, 2008.

[7] L. J. Battan, “Radar attenuation by wet ice spheres,” *Journal of Applied Meteorology*, vol. 10, no. 2, pp. 247–252, 1971.

[8] R. Bechini and V. Chandrasekar, “A semisupervised robust hydrometeor classification method for dual-polarization radar applications,” *Journal of Atmospheric and Oceanic Technology*, vol. 32, no. 1, pp. 22–47, 2015.

[9] Snowcrystals.com, *The morphology diagram.*, Accessed May 29, 2020.

[10] NWS and NOAA, *National Weather Service, Advanced Hydrology Prediction Service*, Accessed May 30, 2020.

[11] NASA, *NASA Global Precipitation Measurement.*, Accessed May 30, 2022.

[12] H. Chen, *Radar and satellite observations of precipitation: space time variability, cross-validation, and fusion.* PhD thesis, Colorado State University. Libraries, 2017.

[13] T.-i. Wang and S. Clifford, “Use of rainfall-induced optical scintillations to measure path-averaged rain parameters,” *JOSA*, vol. 65, no. 8, pp. 927–937, 1975.

[14] J. Holmes, B. Case, and E. Michelena, “Rain gauge for noaa data buoys,” in *OCEANS 81*, pp. 463–467, IEEE, 1981.

[15] J. A. Nystuen, J. R. Proni, P. G. Black, and J. C. Wilkerson, “A comparison of automatic rain gauges,” *Journal of Atmospheric and Oceanic Technology*, vol. 13, no. 1, pp. 62–73, 1996.

[16] J. A. Nystuen, “Listening to raindrops from underwater: An acoustic disdrometer,” *Journal of Atmospheric and Oceanic Technology*, vol. 18, no. 10, pp. 1640–1657, 2001.

[17] X. Liu, B. He, S. Zhao, S. Hu, and L. Liu, “Comparative measurement of rainfall with a precipitation micro-physical characteristics sensor, a 2d video disdrometer, an ott parsivel disdrometer, and a rain gauge,” *Atmospheric Research*, vol. 229, pp. 100–114, 2019.

[18] V. Winkler, “Range doppler detection for automotive fmcw radars,” in *2007 European Radar Conference*, pp. 166–169, IEEE, 2007.

[19] Altera Corporation, *Implementing Digital Processing for Automotive Radar Using SoCs.*

[20] F. Lalezari, “Orthogonal linear transmit receive array radar,” Aug. 21 2012. US Patent 8,248,298.

[21] S. Wang, H. Chen, V. M. Patel, and A. Petropulu, “Two-dimensional beamforming automotive radar with orthogonal linear arrays,” in *2019 IEEE Radar Conference (RadarConf)*, pp. 1–6, IEEE, 2019.

[22] R. I.-R. P.-. ITU, *Specific attenuation model for rain for use in prediction methods.*, 2005.

[23] S. Bertoldo, C. Lucianaz, and M. Allegretti, "On the use of a 77 ghz automotive radar as a microwave rain gauge," *Engineering, Technology & Applied Science Research*, vol. 8, no. 1, pp. 2356–2360, 2018.

[24] G. Mie, "Beitage zur optic truber medien, speziell kolloidaler metalllosungen," *Ann. Physik.*, vol. 25, pp. 1–377, 1908.

[25] C. Mätzler, "Matlab functions for mie scattering and absorption, version 2," *IAP Res. Rep*, vol. 8, no. 1, p. 9, 2002.

[26] G. Galati and G. Pavan, "Computer simulation of weather radar signals," *Simulation Practice and Theory*, vol. 3, no. 1, pp. 17–44, 1995.

[27] S. Choudhury and N. Bharadwaj, "Computer simulation of weather radar signals," *Department of Electrical & Computer Engineering, Colorado University*, pp. 1–6, 2002.

[28] G. Zhang, M. Xue, Q. Cao, and D. Dawson, "Diagnosing the intercept parameter for exponential raindrop size distribution based on video disdrometer observations: Model development," *Journal of applied meteorology and climatology*, vol. 47, no. 11, pp. 2983–2992, 2008.

[29] V. N. Bringi and V. Chandrasekar, *Polarimetric Doppler Weather Radar: Principles and applications.* Cambridge University Press, first ed., 2001.

[30] A. Devices, *EV - TINYRAD24G User Guide.*, 2020.

[31] S. S. Joshil, R. M. Beauchamp, and V. Chandrasekar, "Recent advancements on range ambiguity characterization and mitigation for the nasa d3r," in *2017 IEEE International Geoscience and Remote Sensing Symposium (IGARSS)*, pp. 4413–4416, 2017.

[32] Y. Wang and V. Chandrasekar, “Algorithm for estimation of the specific differential phase,” *Journal of Atmospheric and Oceanic Technology*, vol. 26, no. 12, pp. 2565–2578, 2009.

[33] R. Cifelli, V. Chandrasekar, H. Chen, and L. E. Johnson, “High resolution radar quantitative precipitation estimation in the san francisco bay area: Rainfall monitoring for the urban environment,” *Journal of the Meteorological Society of Japan. Ser. II*, vol. 96, pp. 141–155, 2018.

[34] T. Yu, V. Chandrasekar, H. Xiao, and S. S. Joshil, “Snowfall estimation using dual-wavelength radar during the pyeongchang 2018 olympics and paralympic winter games,” *Journal of the Meteorological Society of Japan. Ser. II*, 2021.

[35] D. McLaughlin, D. Pepyne, V. Chandrasekar, B. Philips, J. Kurose, M. Zink, K. Droegemeier, S. Cruz-Pol, F. Junyent, J. Brotzge, *et al.*, “Short-wavelength technology and the potential for distributed networks of small radar systems,” *Bulletin of the American Meteorological Society*, vol. 90, no. 12, pp. 1797–1818, 2009.

[36] J. Brotzge, V. Chandresakar, K. Droegemeier, J. Kurose, D. McLaughlin, B. Philips, M. Preston, and S. Sekelsky, “Distributed collaborative adaptive sensing for hazardous weather detection, tracking, and predicting,” in *International Conference on Computational Science*, pp. 670–677, Springer, 2004.

[37] Y. Song, D. Han, and M. A. Rico-Ramirez, “High temporal resolution rainfall information retrieval from tipping-bucket rain gauge measurements,” *Procedia Engineering*, vol. 154, pp. 1193–1200, 2016.

[38] N. S. A. Salleh, M. K. B. M. Aziz, and N. Adzhar, “Optimal design of a rain gauge network models,” in *Journal of Physics: Conference Series*, vol. 1366, p. 012072, IOP Publishing, 2019.

[39] A. K. Mishra and P. Coulibaly, "Developments in hydrometric network design: A review," *Reviews of Geophysics*, vol. 47, no. 2, 2009.

[40] S. S. Joshil and C. V. Chandrasekar, "Calibration of d3r weather radar using uav-hosted target," *Remote Sensing*, vol. 14, no. 15, p. 3534, 2022.

[41] K. L. S. Gunn and T. W. R. East, "The microwave properties of precipitation particles," *Quarterly Journal of the Royal Meteorological Society*, vol. 80, no. 346, pp. 522–545, 1954.

[42] R. M. Rasmussen, J. Vivekanandan, J. Cole, B. Myers, and C. Masters, "The estimation of snowfall rate using visibility," *Journal of Applied Meteorology*, vol. 38, no. 10, pp. 1542–1563, 1999.

[43] J.-J. Fernández-Durán and G. Upton, "Statistical problems with weather-radar images, ii: Attenuation detection," in *AIP Conference Proceedings*, vol. 659, pp. 198–207, American Institute of Physics, 2003.

[44] A. Ryzhkov and D. Zrnic, "Precipitation and attenuation measurements at a 10-cm wavelength," *Journal of Applied Meteorology and Climatology*, vol. 34, no. 10, pp. 2121–2134, 1995.

[45] M. R. Kumjian, "Principles and applications of dual-polarization weather radar. part i: Description of the polarimetric radar variables.," *Journal of Operational Meteorology*, vol. 1, 2013.

[46] E. Gorgucci, G. Scarchilli, and V. Chandrasekar, "Error structure of radar rainfall measurement at c-band frequencies with dual polarization algorithm for attenuation correction," *Journal of Geophysical Research: Atmospheres*, vol. 101, no. D21, pp. 26461–26471, 1996.

[47] K. Aydin, Y. Zhao, and T. A. Seliga, "Rain-induced attenuation effects on c-band dual-polarization meteorological radars," *IEEE transactions on geoscience and remote sensing*, vol. 27, no. 1, pp. 57–66, 1989.

[48] L. Wang, P. Liu, Z. Heng, and H. Wang, "Improving c-band weather radar reflectivity attenuation based on two-dimensional video disdrometer data," *Journal of Applied Remote Sensing*, vol. 14, no. 2, p. 024521, 2020.

[49] V. Bringi, V. Chandrasekar, N. Balakrishnan, and D. Zrnić, "An examination of propagation effects in rainfall on radar measurements at microwave frequencies," *Journal of Atmospheric and Oceanic Technology*, vol. 7, no. 6, pp. 829–840, 1990.

[50] V. N. Bringi, T. Keenan, and V. Chandrasekar, "Correcting c-band radar reflectivity and differential reflectivity data for rain attenuation: A self-consistent method with constraints," *IEEE transactions on geoscience and remote sensing*, vol. 39, no. 9, pp. 1906–1915, 2001.

[51] Y. Gou, H. Chen, and J. Zheng, "An improved self-consistent approach to attenuation correction for c-band polarimetric radar measurements and its impact on quantitative precipitation estimation," *Atmospheric Research*, vol. 226, pp. 32–48, 2019.

[52] E. Gorgucci and V. Chandrasekar, "Evaluation of attenuation correction methodology for dual-polarization radars: Application to x-band systems," *Journal of Atmospheric and Oceanic Technology*, vol. 22, no. 8, pp. 1195–1206, 2005.

[53] R. F. Rincon, R. Lang, R. Meneghini, S. Bidwell, and A. Tokay, "Estimation of path-average rain drop size distribution using the nasa/trmm microwave link," in *IGARSS 2001. Scanning the Present and Resolving the Future. Proceedings. IEEE 2001 International Geoscience and Remote Sensing Symposium (Cat. No. 01CH37217)*, vol. 3, pp. 1038–1040, IEEE, 2001.

[54] P. Zhang, X. Liu, Z. Li, Z. Zhou, K. Song, and P. Yang, "Attenuation correction of weather radar reflectivity with arbitrary oriented microwave link," *Advances in Meteorology*, vol. 2017, 2017.

[55] R. Cifelli, V. Chandrasekar, S. Lim, P. Kennedy, Y. Wang, and S. Rutledge, "A new dual-polarization radar rainfall algorithm: Application in colorado precipitation events," *Journal of Atmospheric and Oceanic Technology*, vol. 28, no. 3, pp. 352–364, 2011.

[56] H. Liu and V. Chandrasekar, "Classification of hydrometeors based on polarimetric radar measurements: Development of fuzzy logic and neuro-fuzzy systems, and in situ verification," *Journal of Atmospheric and Oceanic Technology*, vol. 17, no. 2, pp. 140–164, 2000.

[57] R. C. Gonzales and R. E. Woods, "Digital image processing," 2002.

[58] Y. Lu, Z. Jiang, K. Aydin, J. Verlinde, E. E. Clothiaux, and G. Botta, "A polarimetric scattering database for non-spherical ice particles at microwave wavelengths," *Atmospheric Measurement Techniques*, vol. 9, no. 10, pp. 5119–5134, 2016.

[59] E. A. Brandes, K. Ikeda, G. Zhang, M. Schönhuber, and R. M. Rasmussen, "A statistical and physical description of hydrometeor distributions in colorado snowstorms using a video disdrometer," *Journal of applied meteorology and climatology*, vol. 46, no. 5, pp. 634–650, 2007.

[60] H. R. Pruppacher and J. D. Klett, "Microphysics of clouds and precipitation," *Nature*, vol. 284, no. 5751, pp. 88–88, 1980.

[61] S. Y. Matrosov, A. Heymsfield, and Z. Wang, "Dual-frequency radar ratio of nonspherical atmospheric hydrometeors," *Geophysical research letters*, vol. 32, no. 13, 2005.

[62] M. I. Mishchenko, L. D. Travis, and D. W. Mackowski, "T-matrix computations of light scattering by nonspherical particles: a review," *Journal of Quantitative Spectroscopy and Radiative Transfer*, vol. 55, no. 5, pp. 535–575, 1996.

[63] S. S. Joshil, "Salient features of the d3r radar enhancements," Colorado State University. Libraries, 2018.

[64] V. Chandrasekar, R. M. Beauchamp, M. Vega, H. Chen, M. Kumar, S. Joshil, M. Schwaller, W. Petersen, and D. Wolff, "Meteorological observations and system performance from the nasa d3r's first 5 years," in *2017 IEEE International Geoscience and Remote Sensing Symposium (IGARSS)*, pp. 2734–2736, IEEE, 2017.

[65] V. Chandrasekar, S. S. Joshil, M. Kumar, M. A. Vega, D. Wolff, and W. Petersen, "Snowfall observations during the winter olympics of 2018 campaign using the d3r radar," in *IGARSS 2019-2019 IEEE International Geoscience and Remote Sensing Symposium*, pp. 4561–4564, IEEE, 2019.

[66] E. Ruzanski, V. Chandrasekar, and Y. Wang, "The casa nowcasting system," *Journal of Atmospheric and Oceanic Technology*, vol. 28, no. 5, pp. 640–655, 2011.

[67] S. Pulkkinen, V. Chandrasekar, and A.-M. Harri, "Nowcasting of precipitation in the high-resolution dallas–fort worth (dfw) urban radar remote sensing network," *IEEE Journal of Selected Topics in Applied Earth Observations and Remote Sensing*, vol. 11, no. 8, pp. 2773–2787, 2018.

[68] A. A. Organization, *State facts: Autos drive Texas Forward.*, Accessed May 30, 2020.

[69] V. Chandrasekar, Y. Wang, H. Chen, and H. Pohjola, "The casa quantitative precipitation estimation system: a five year validation study.," *Natural Hazards & Earth System Sciences*, vol. 12, no. 9, 2012.

[70] U. S. census Bureau, *2019 TIGER/Line Shapefiles: Roads*, Accessed December 20, 2019.

[71] G. A. Vicente, R. A. Scofield, and W. P. Menzel, “The operational goes infrared rainfall estimation technique,” *Bulletin of the American Meteorological Society*, vol. 79, no. 9, pp. 1883–1898, 1998.

[72] NOAA, *NOAA - Precipitation CMORPH CDR.*, Accessed May 30, 2022.

[73] A. Moreira, P. Prats-Iraola, M. Younis, G. Krieger, I. Hajnsek, and K. P. Papathanassiou, “A tutorial on synthetic aperture radar,” *IEEE Geoscience and remote sensing magazine*, vol. 1, no. 1, pp. 6–43, 2013.

[74] D. Atlas and R. K. Moore, “The measurement of precipitation with synthetic aperture radar,” *Journal of atmospheric and oceanic technology*, vol. 4, no. 3, pp. 368–376, 1987.

[75] J. P. Fritz and V. Chandrasekar, “Simultaneous observations and analysis of severe storms using polarimetric x-band sar and ground-based weather radar,” *IEEE transactions on geoscience and remote sensing*, vol. 48, no. 10, pp. 3622–3637, 2010.

Appendix A

Parameters for relationship between specific phase and specific attenuation for different hydrometeors at X band

Table A.1. X band, horizontal polarization - Values for a and b from 0° elevation to 45° elevation

Particle	par	0	5	10	15	20	25	30	35	40	45
Rain	a	0.298	0.302	0.311	0.325	0.344	0.372	0.409	0.460	0.529	0.627
Rain	b	1.027	1.027	1.027	1.027	1.028	1.028	1.028	1.028	1.029	1.029
Hail	a	0.8	0.8	0.9	0.9	1.0	1.1	1.3	1.5	1.8	2.2
Hail	b	1.329	1.329	1.329	1.329	1.328	1.328	1.328	1.327	1.330	1.327
Graupel	a	0.150	0.153	0.160	0.170	0.185	0.207	0.237	0.280	0.341	0.433
Graupel	b	1.341	1.341	1.341	1.341	1.341	1.341	1.340	1.340	1.340	1.340
Aggregates	a	0.088	0.090	0.094	0.100	0.110	0.123	0.141	0.168	0.205	0.261
Aggregates	b	1.363	1.363	1.363	1.363	1.363	1.363	1.363	1.364	1.364	1.364
Crystals	a	0.002	0.002	0.002	0.002	0.002	0.002	0.003	0.003	0.004	0.006
Crystals	b	1.623	1.630	1.631	1.633	1.634	1.636	1.638	1.641	1.643	1.645

Table A.2. X band, vertical polarization - Values for a and b from 0° elevation to 45° elevation

Particle	par	0	5	10	15	20	25	30	35	40	45
Rain	a	0.250	0.254	0.263	0.276	0.295	0.322	0.358	0.408	0.476	0.572
Rain	b	0.997	0.998	0.999	1.000	1.002	1.005	1.007	1.010	1.013	1.016
Hail	a	0.7	0.7	0.8	0.8	0.9	1.0	1.2	1.4	1.7	2.1
Hail	b	1.331	1.331	1.331	1.331	1.330	1.330	1.329	1.329	1.328	1.327
Graupel	a	0.125	0.128	0.134	0.144	0.159	0.179	0.209	0.250	0.309	0.398
Graupel	b	1.336	1.336	1.336	1.336	1.336	1.336	1.336	1.337	1.336	1.337
Aggregates	a	0.082	0.084	0.088	0.094	0.103	0.116	0.134	0.160	0.197	0.253
Aggregates	b	1.359	1.359	1.359	1.359	1.360	1.360	1.360	1.361	1.361	1.362
Crystals	a	0.0002	0.0003	0.0003	0.0004	0.0005	0.0007	0.001	0.002	0.002	0.004
Crystals	b	1.418	1.423	1.428	1.435	1.442	1.450	1.466	1.636	1.639	1.642

Appendix B

Parameters for relationship between specific phase and specific attenuation for different hydrometeors at Ku band

Table B.1. Ku band, horizontal polarization - Values for a and b from 0° elevation to 45° elevation

Particle	par	0	5	10	15	20	25	30	35	40	45
Rain	a	0.463	0.470	0.483	0.505	0.537	0.580	0.639	0.719	0.828	0.981
Rain	b	0.995	0.995	0.995	0.995	0.996	0.996	0.996	0.997	0.997	0.998
Hail	a	2	2	2	2	3	3	4	4	5	7
Hail	b	1.571	1.571	1.572	1.572	1.574	1.575	1.576	1.577	1.578	1.579
Graupel	a	0.275	0.281	0.293	0.311	0.337	0.375	0.427	0.500	0.604	0.756
Graupel	b	1.315	1.315	1.315	1.314	1.313	1.312	1.311	1.310	1.309	1.307
Aggregates	a	0.160	0.163	0.170	0.181	0.197	0.220	0.252	0.296	0.360	0.454
Aggregates	b	1.324	1.324	1.324	1.323	1.323	1.322	1.322	1.321	1.320	1.319
Crystals	a	0.003	0.003	0.003	0.003	0.004	0.005	0.006	0.007	0.009	0.012
Crystals	b	1.647	1.647	1.647	1.649	1.650	1.651	1.652	1.654	1.656	1.658

Table B.2. Ku band, vertical polarization - Values for a and b from 0° elevation to 45° elevation

Particle	par	0	5	10	15	20	25	30	35	40	45
Rain	a	0.391	0.398	0.411	0.432	0.462	0.504	0.561	0.639	0.746	0.896
Rain	b	0.955	0.956	0.958	0.960	0.963	0.966	0.970	0.974	0.978	0.982
Hail	a	2	2	2	2	2	3	3	4	5	7
Hail	b	1.581	1.581	1.581	1.581	1.582	1.582	1.583	1.583	1.583	1.583
Graupel	a	0.229	0.234	0.245	0.262	0.287	0.323	0.373	0.443	0.543	0.691
Graupel	b	1.313	1.313	1.312	1.312	1.311	1.310	1.308	1.307	1.306	1.305
Aggregates	a	0.148	0.151	0.158	0.168	0.184	0.206	0.237	0.281	0.344	0.436
Aggregates	b	1.319	1.319	1.319	1.319	1.318	1.318	1.317	1.317	1.317	1.316
Crystals	a	0.0006	0.0006	0.0007	0.0009	0.001	0.002	0.002	0.003	0.005	0.008
Crystals	b	1.592	1.592	1.597	1.606	1.614	1.630	1.648	1.643	1.646	1.650